Theory of Ultrafast Exciton Dynamics in Photosynthetic Antenna Systems

DISSERTATION

zur Erlangung des akademischen Grades
doctor rerum naturalium
(Dr. rer. nat.)
im Fach Physik

eingereicht an der
Mathematisch-Naturwissenschaftlichen Fakultät I
Humboldt-Universität zu Berlin

von
Herrn Dipl.-Phys. Ben Brüggemann
geboren am 23.01.1973 in Bad Hersfeld

Präsident der Humboldt-Universität zu Berlin:
Prof. Dr. Jürgen Mlynek

Dekan der Mathematisch-Naturwissenschaftlichen Fakultät I:
Prof. Thomas Buckhout, PhD

Gutachter:

1. PD Dr. Volkhard May
2. Prof. Dr. Rienk van Grondelle
3. PD Dr. Oliver Kühn

eingereicht am:	1. April 2004
Tag der mündlichen Prüfung:	2. Juli 2004

Abstract

The multi-exciton description of excitation energy transfer in chromophore complexes and biological light harvesting antenna systems is extended to include the exciton-exciton annihilation processes. To achieve a complete microscopic description the approach is based on intra–chromophore internal conversion processes which leads to non-radiative transitions from higher to lower lying exciton manifolds. Besides an inclusion of exciton-exciton annihilation the used multi-exciton density matrix theory also accounts for a coupling to low-frequency vibrational modes and the radiation field. Concentrating on transitions from the two- to the single-exciton manifold exact and approximate expressions for the annihilation rate are derived.

A first application of the introduced extended multi-exciton density matrix theory is given by the computation of ultrafast transient absorption spectra. To elucidate the process of exciton-exciton annihilation in intensity dependent transient absorption data the approach is applied to the B850 ring of the LH2 found in *rhodobacter sphaeroides.* The signatures of exciton-exciton annihilation as well as the influence of static disorder are discussed in detail. The simulations of transient absorption including static disorder and orientational averaging are in good agreement with experimental data.

The recently published structure of the Photosystem I (PS1) of *Synechococcus elongatus* made it for the first time possible to introduce an excitonic model for the 96 chlorophylls embedded in the protein matrix of that core-antenna system, as presented in this work. The challenge has been to reproduce linear frequency domain spectra in a wide temperature range as well as the time resolved fluorescence. The couplings and the dipole-moments of the chlorophylls are extracted from the x-ray crystal structure. Since the position of the energetic levels of the chlorophylls depend on the respective surrounding their determination is achieved by fitting low temperature absorption, linear dichroism and circular dichroism at the same time. After assigning some chromophores to the red-most states, an evolutionary algorithm is used to get the best fit. The quality of the resulting PS1 model (additionally accounting for inhomogeneous line broadening) is confirmed in calculating time dependent fluorescence spectra which show a good agreement with recent experimental results. The outlined method is also applicable to other photosynthetic antenna systems.

The above described exciton models successfully explain the respective measurements. In a second step, they will be used to propose a new type of experiment, the exciton control experiment. Based on an exciton model for the FMO complex of *Prosthecochloris aestuarii* and the proposed PS1 model of *Synechococcus elongatus* one studies the laser pulse formation of excitonic wavepackets, i.e. a coherent superposition of excitonic states similar to vibrational wavepackets.

Optimal Control theory is used to calculate the shape of femtosecond laser pulses that leads to a spatial localization of excitation energy. The possibility to populate such a localized target state is demonstrated, even in the presence of disorder or exciton-exciton annihilation, and it is shown that the efficiency of localization as well as the length the most suited pulses strongly depend on temperature.

Keywords:
photosynthetic antenna systems, multi-exciton density matrix theory, exciton-exciton annihilation, optimal control of excitonic wavepackets, photosystem I

Zusammenfassung

Die Multiexzitonen-Theorie des Anregungsenergie–Transfers in Farbstoff–Protein–Komplexen und biologischen Antennensystemen wird um den Prozess der Exziton–Exziton–Vernichtung erweitert. Um eine mikroskopische Beschreibung zu erzielen, wird eine Herangehensweise benutzt, die auf der Internen Konversion der Anregungsenergie innerhalb der Farbstoffmoleküle basiert. Diese Interne Konversion führt zu nicht strahlenden Übergängen von höheren zu niedrigeren Exziton–Mannigfaltigkeiten. Neben der Einbeziehung der Exziton–Exziton–Vernichtung beinhaltet die hier verwendete Multiexziton–Dichtematrixtheorie auch die Kopplung zu niedrig–energetischen Schwingungs–Freiheitsgraden und dem elektrischen Feld. Für den Übergang von der Zwei- zu der Einexzitonen –Mannigfaltigkeit werden exakte und genäherte Ausdrücke hergeleitet.

Die erste Anwendung der erweiterten Multiexziton–Dichtematrixtheorie ist die Berechnung von ultra-schnellen differentiellen Absoptionsspektren. Um den Prozess der Exziton-Exziton-Vernichtung in intensitätsabhängigen differenziellen Absorptionsspektren näher zu untersuchen, wird diese Herangehensweise auf den B850 Ring des LH2 von *rhodobacter sphaeroides* angewendet. Die Bedeutung der Exziton-Exziton-Vernichtung und der Einfluss von statischer Unordnung werden detailiert diskutiert. Die Simulationen der differentiellen Absorptionsspektren mit statischer Unordnung und Orientierungsmittelung zeigen gute Übereinstimmung mit experimentellen Beobachtngen.

Durch die Veröffentlichung der Strukturdaten des Photosystem I (PS1) von *Synechococcus elongatus* wurde es zum ersten Mal möglich, ein Exziton-Modell für die 96 Chorophyllmoleküle einzuführen, die in die Proteinmatrix dieses Antennensystems eingebettet sind. Das Ziel dabei ist, sowohl die linearen Spektren in einem weiten Temperaturbereich, als auch die zeitaufgelöste Fluoreszenz zu reproduzieren. Die Kopplungen und die Dipolmomente der Chlorophyllmoleküle wurden den Strukturdaten entnommen. Da die Energien der einzelnen Farbstoffe stark von deren unmittelbarer Umgebung abhängt, werden diese bestimmt, indem simulierte Absorption, Lineardichroismus und Zirkulardichroismus bei niedrigen Temperaturen den experimentellen Spektren angepasst werden. Nachdem einige Chlorophyllmoleküle den Zuständen mit den niedrigsten Energien zugeordnet wurden, werden die Energien mit Hilfe eines evolutionären Algorithmus angepasst. Die Qualität des PS1 Modells wird durch die Berechnung der zeitabhängigen Fluoreszenz untermauert (mit zusätzlicher inhomogener Linienbreite), die Simulationen stimmen gut mit aktuellen experimentellen Resultaten überein.

Die oben erwähnten Exziton-Modelle beschreiben die jeweiligen Experimente erfolgreich. Der nächste Schritt ist, diese Modelle zu nutzen, um einen neuen Typ von Experiment vorzuschlagen, das Exciton-Steuerungs-Experiment. Auf dem Exciton-Modell des FMO Komplexes von *Prosthecochloris aestuarii* und dem oben erwähnten PS1 Modell von *Synechococcus elongatus* aufbauend wird die Bildung von exzitonischen Wellenpaketen durch Laser-Anregung studiert. Diese stellen eine kohärente Überlagerung exzitonischer Zustände dar, ähnlich der bei Schwingungs-Wellenpaketen. Um die spezielle Form des Femtosekunden-Laserpulses zu bestimmen, der zu einer räumlichen Lokalisierung der Anregungsenergie führt, wird die Theorie der optimalen Steuerung verwendet. Die Möglichkeit, solch einen lokalisierten Zielzustand zu erreichen, wird aufgezeigt, auch unter dem Einfluss von energetischer Unordnung und Exziton-Exziton Vernichtung. Ferner wird gezeigt, dass die Effizienz der Lokalisierung und die Länge des optimalen Pulses stark von der Temperatur abhängen.

Schlagwörter:
Photosynthetische Antennensysteme, Multiexziton-Dichtematrixtheorie, Exziton-Exziton-Vernichtung, Kontrolle exzitonischer Wellenpakete, Photosystem I

Contents

Introduction

The understanding of the processes leading to photosynthesis in bacteria, algae and higher plants has been a main topic of research in biology as well as in chemistry and physics over the last century. Whereas earlier only the slower processes could be studied with the upcoming femtosecond lasers also the investigation of fast energy and charge transfer process became feasible. Besides studying the reaction center where the charge transfer chain starts the research activity focused on another group of pigment-protein complexes, the so called antenna systems. They include a number of chromophores like chlorophyll (Chl) or bacteriochlorophyll (BChl) embedded into a protein matrix. Often also carotenoids have been found, which are used to increase the absorption and for photo-protection (Ref. [vAVvG00]). The antenna systems are used to enlarge the possibility of catching light quanta, later the excitation is transfered to the reaction center. As it turned out, the structure of these complexes is very well defined. That made it possible to crystallize some of the complexes and perform x-ray scattering experiments. Such an experiment is then repeated for complexes which have been changed at certain positions to extract the phases. The result is an electron density map into which the protein backbone with its amino-acids and the chromophores have been fitted. To bridge the gap between the structural information and the ultrafast optical experiments theoretical modeling and simulations become necessary.

The theoretical description is based on the theory of open quantum systems and on the Frenkel-exciton concept, i.e. the local excitation of electrons within a single chromophore and no charge transfer to another molecule. An introduction to the theory of dissipative quantum systems is given in Refs. [LAI$^+$91, Muk95, Blu96, MK00a]. The application of the exciton concept to photosynthetic antenna systems is discussed e.g. in Ref. [vAVvG00], whereas the multi-exciton density matrix theory and its application is given in Ref. [RMK01]. The latter will be the starting point for this work. A different approach would be given by quantum chemical calculations, but due to the huge size of the antenna systems this approach is restricted to small parts of the complex. First principle calculations have been applied to the single chromophores (e.g. [PG00]), whereas semiempirical methods could be used for single chromophores (e.g. [DVFF02, TM$^+$00]) and pairs of chromophores (e.g. Ref. [TM$^+$00]) with their respective protein surroundings. Even if a close pair of chromophores is considered [TM$^+$00], there is no charge transfer between the chromophores for lowest exited state Q_y of Bacteriochlorophyll. Therefore an Frenkel-exciton model for the spectroscopy in the spectral region of the Q_y state results even from the quantum chemical calculations.

The photosynthetic antenna systems are optimized to absorb light quanta. Therefore even the application of moderate laser intensities often leads to more than one excitation per complex. Usually the light intensity is reduced until the possibility of two excitations becomes neglectable. However that may not be always appropriate, e.g. in the case of a control scenario as discussed later. But since even in nature the probability of two excitons in one complex is not vanishing it is interesting how this twofold excitation is handled without damaging the complex. The theoretical description is given by the exciton-exciton annihilation process, where the two excitations are used to excite a higher excited state of one chromophore, which subsequently relaxes to the first excited state by ultrafast internal conversion. This process is included in the present work into the multi-exciton density matrix theory of Ref. [RMK01], and comparisons with intensity dependent transient absorption experiments for the LH2 antenna system are made.

The process of exciton-exciton annihilation becomes also important for a different type of experiments, where one uses shaped laser pulses with medium intensity to control the energy transfer. The application to the excitons of photosynthetic antenna systems will be discussed in this work. The idea of coherent control of quantum systems evolved first in theory, but with the development of complementary experimental methods as liquid-crystal pulse shapers the application to e.g. molecules in gas phase became feasible. The main concept is to build up an vibrational wavepacket on one of the potential energy surfaces of the molecule and lead it to a special region, sometimes including the breaking of some bonds, and thus initiating new chemistry. The product is probed e.g. by a second laser beam or a mass spectrometer. In this work a similar approach is developed for excitonic wavepackets, they represent a coherent superpositions of delocalized exciton states. This has to be done with care, because the fast dephasing processes as well as the spectral inhomogeneity in this complexes has to be included for a realistic description.

Different antenna systems are addressed during this work. For the bacteriochlorophyll containing antenna systems LH2 and FMO a long tradition of exciton models can be found in literature. The structure has been known for several years now, and the models used here are based on recent descriptions. The story is different for the PS1 complex as the structure has only recently been published, and just two different approaches have been made to set up an exciton-model system. In this work a third approach will be made since the assignments of both earlier approaches were not able to resemble the low temperature absorption and linear dichroism spectra which have been measured during this work. Additionally, the nature of the states with the lowest energy, the so called red chlorophylls, is still not clarified.

As it has been discussed, one aim of this work is to give the theoretical foundations to control excitonic wavepackets in photosynthetic antenna systems. The application of the Optimal Control theory as given in Part I, Chapter 4 will be discussed later in Part II, Chapter 7. The earlier Chapters in the respective Parts may be seen as extensive preparations to reach this goal. Higher excited states and exciton-exciton annihilation had to be included, as the respective control experiments usually are done in a medium field intensity regime, where the probability of two excitations per complex cannot be neglected. The work is organized as follows. As a starting point and an introduction, a short overview about bacterial photosynthesis and different antenna complexes is given in Chapter 1. In particular the antenna systems which will be used throughout this work are presented.

Part I follows which deals with the presentation and further development of the multi-exciton density matrix. In Chapter 2 the multi-exciton density matrix theory (see e.g. [RMK01]) is extended to the introduction of higher excited states of the chromophores, and to the inclusion of exciton-exciton annihilation caused by internal conversion between the higher excited state and the first excited state. A whole range of optical spectroscopy, both of linear and nonlinear nature, is presented in the Chapter 3, based on the multi-exciton density matrix theory. The calculation of these optical properties will be used in Part II for the comparison with respective experiments. The last Chapter of the theory part (Chapter 4) deals with the description of the Optimal Control theory. Where appropriate, details of the calculations have been moved to the Appendix.

In the Part II of this work the theory as given in Part I is applied to different photosynthetic antenna systems. For most simulations also experimental data were available, and the comparison between both are used to prove the general correctness of the approach. First, in Chapter 5 the multi-exciton density matrix theory is used to describe the signatures of exciton-exciton annihilation in the LH2 complex. The internal conversion rate will be discussed, and homogeneous as well as inhomogeneous broadening are studied. The model for the chromophores developed in this Chapter is also used with small changes in the later Chapters. For the chlorophylls in the PS1 an exciton model is proposed in Chapter 6 using the following approach. The orientations of the Chl dipole moments are extracted from the recently published structure, and the Chl energies are shifted by an evolutionary algorithm to fit linear low temperature spectra. In a second step the time resolved fluorescence is calculated, and compared to the respective experiment.

The possibilities of controlling the exciton motion in photosynthetic antenna systems are discussed in Chapter 7. Starting with simple models one shifts to the relatively small FMO complex which turned out to be most suitable for the proposed control task. Combining the PS1 model from Chapter 6 with the insight gained from the exciton control in the FMO complex, a Coherent Control experiment is proposed. It is based on the transient anisotropy as feedback signal.

This work is concluded with Chapter 8 where an outlook on further developments in this field as well as possible experimental realizations is given.

Chapter 1

Bacterial Photosynthesis

1.1 Introduction

Photosynthesis, i.e. the conversion of light to cellular energy, is one of the main basics of life on earth. This work deals with the theoretical modeling of photosynthetic antenna systems or more general chromophore complexes (CC), thus first an short introduction into the biological function of these systems is given. The process of photosynthesis starts with the light induced excitation of certain molecules, the chromophores. The most important chromophores are Chlorophyll (Chl) and Bacteriochlorophyll (BChl) with a strong absorption in the red region of the light spectrum, and the carotenoids which absorb in the blue region. The chromophores are arranged in protein complexes, the antenna systems and the reaction center, within the membrane. The excitation energy is then transfered to a special pair of (B)Chl in the reaction center, which is the starting point of an electron transfer chain. During the cyclic electron transfer a proton gradient is build up, which is used by another membrane protein for the synthesis of ATP, the main energy carrier of a cell. For the cell grow, a different process is necessary, which includes an noncyclic electron transfer to transform NADP to NADPH (Calvin cycle). As a last step, the transfered electron has to be replaced, and different sources of electrons are used in nature e.g. water or hydrogen sulfide. Depending on the electron source, two different types of photosynthetic organisms exist [Bri04a].

One group of photosynthetic organisms includes cyanobacteria, algae, and higher plants. All these organism use different Chlorophylls as chromophore. Water is used as electron source, and Oxygen is released during the process. Since cyanobacteria and its predecessors are present on earth since more than two billion years, they are thought to be responsible for the early oxygen production, which was a prerequisite for higher forms of life. To raise the energy level of the electrons from water to NADP, two steps are necessary. Therefore, two different reaction centers are present in these organisms. The photosystem I (PS1) is used

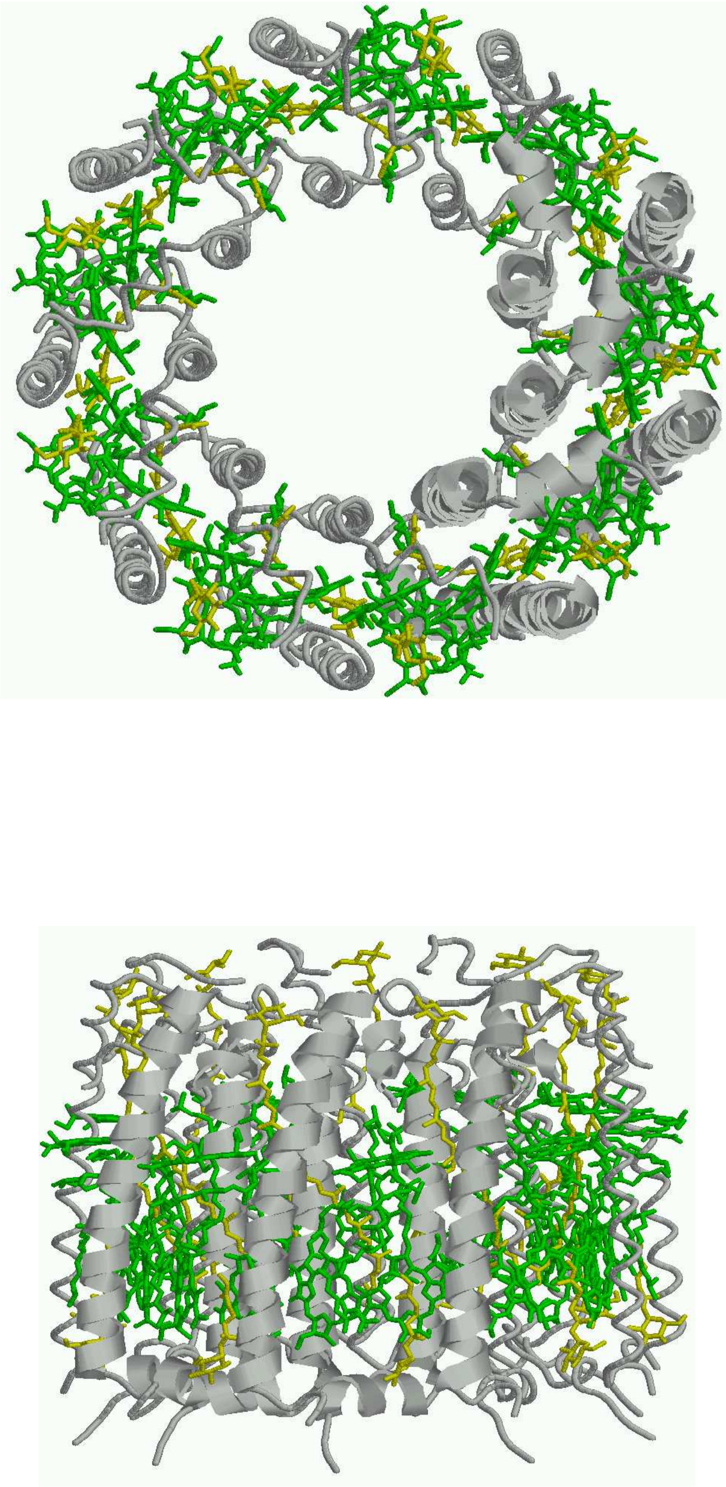

Figure 1.1: The light harvesting complex LH2 from *Rhodopseudomonas acidophila*, Ref. [PPF$^+$97] (identifier 1kzu in the protein data bank). Plotted with `rasmol`. Top and side view, beside a sketch of the protein backbone the BChls (green) and the carotenoids (yellow) are shown.

both for the cyclic energy creation (ATP synthesis) and in a noncyclic way to produce NADPH. For the noncyclic process the other photosystem comes into play. The photosystem II (PS2) is able to use water as electron donor after photo-excitation and produces oxygen. The electron, which is now at a higher energetic level due to the work of the PS2, is then transfered to the PS1 to replace the one which was used for the NADPH creation. The photosynthetic system is contained in an sag-like, folded intracellular membrane, called thylakoid membrane. Cyanobacteria are the progenitors of chloroplasts in plants.

The other groups of photosynthetic bacteria work with various bacteriochlorophylls as chromophore. Additionally, different electron donors are used, like hydrogen sulfide (green bacteria, purple sulfur bacteria) or hydrogen (purple nonsulfur bacteria), and therefore no oxygen is produced. Only one photosystem (or reaction center) is present in these organisms, the one of green bacteria is related to the PS1, whereas the one of purple bacteria is related to PS2.

In the following Sections of this Chapter the photosynthetic antenna systems which will be addressed in this work are presented, and an overview is given about the progress of x-ray structure analysis in this field. For the simulations of optical properties of the antenna systems it is important to know the orientation of all (B)Chls in the complex. This becomes possible, if the resolution of the x-ray structure is approximately 2.5 Å. At somewhat lower resolution (e.g. 4.4 Å) only the plane of the (B)Chls is given, and different orientations are still possible. The characteristics of the chromophores BChl and Chl will be addressed in the Sections 5.2 and 6.2 where the modeling of the photosynthetic antenna systems is done, because the proper description of the chromophores is crucial for that procedure.

1.2 Purple Nonsulfur Bacteria and LH2

The photosynthetic apparatus of purple nonsulfur bacteria consists of the periphery light harvesting complex LH2 and the core antenna complex LH1 which surrounds the bacterial reaction center. A recent review on structure and function can be found in Ref. [HRD$^+$02]. The structure of these different parts has been resolved by x-ray diffraction, at least for one species. The spatial position of the atoms in two different LH2 complexes have been published. The LH2 complex of *Rhodopseudomonas acidophila* [PPF$^+$97, PPH$^+$03] (Resolution 2.5Å and 2.0Å, new name: *Rhodoblastus acidophila*) inhibits a 9-fold rotational symmetry (cf. Fig. 1.1) whereas the LH2 complex of *Rhodosphirillum molischianum* (Resolution 2.0Å, new name: *Phaeospirillum molischianum*) looks similar, but with an 8-fold symmetry. Both have two different rings of BChl molecules, called B850 (16/18 BChl*a*) and B800 (8/9 BChl*a*) after their main absorption line. The core antenna LH1 uses similar building blocks, but without the B800 ring. It has a 16 fold symmetry if measured alone. Current structural data of *Rhodopseudomonas* *pallustris* suggest that the LH1 including the reaction center has a broken symmetry with an opening instead of the 16th segment [RHS+03] (resolution 4.8 Å). And, the structure of the reaction center of *Rhodobacter sphaeroides* is given in Ref. [FKD+02] (resolution 2.0 Å) for two different states. The B850 ring of the LH2 of *Rhodopseudomonas acidophila* will be used in Chapter 5 as a reference system for the discussion of exciton-exciton annihilation.

1.3 Green Bacteria and FMO

Green sulfur Bacteria which are common in freshwater and marine sediments are capable of photosynthesis even under very dim conditions. Beside one other group they are the only bacteria which contain the so called Chlorosome, a special light harvesting antenna. It consists of a bag of rod-like stapled BChl*c*, which are not as usual embedded into a protein matrix. This results in a maximal light absorption. Between the Chlorosome and the cell membrane into which the reaction center is embedded lies an arrangement of a special chromophore-protein complex, called Fenna-Matthews-Olson (FMO) complex (Fig.1.2). It consists beside the protein of 7 BChl*a* (Fig. 7.5). This was the first photosynthetic antenna system, whose structure was resolved by x-ray diffraction. Up to now the arrangement of the BChls in the FMO Complex of two different species is known, *Chlorobium tepidum* [LZBA97, CABA03] (Resolution 2.5Å and 2.2Å) and *Prosthecochloris aestuarii* [TM93] (Resolution 1.9Å). Since it has a well known structure and just a few chromophores it is used as a prototype of a photosynthetic antenna system. The FMO complex of *Prosthecochloris aestuarii* will be used for the applications of the Optimal Control theory in Chapter 7.

1.4 Cyanobacteria and PS1

Cyanobacteria contain only one form of Chlorophyll, Chl*a*. They live nearly everywhere, but are most common in fresh water [Bri04b]. Especially in nitrogen polluted lakes an exponential grow, called blooming, can happen. Other species form together with fungi the composite organism of lichens, or live in the soil down to a depth of 1 m. As it has been stated in the introduction, the cyanobacteria have already the same photosynthetic system as algae and higher plants. It consists of two photosynthetic reaction centers, PS1 and PS2.

The structure of the energy producing PS1 has been resolved for the cyanobacteria *Synechococcus elongatus* [JFK+01] (Resolution 2.5Å, Fig. 1.3, note that the name has recently been changed from *Synechococcus* to *Thermosynechococcus*) and the green plant *Pisum sativum* [BSFN03] (Resolution 4.4Å, the structure of the PS1 of *Synechococcus elongatus* has been used to describe the central part of the complex). It consists of a huge Chl containing antenna which sur-

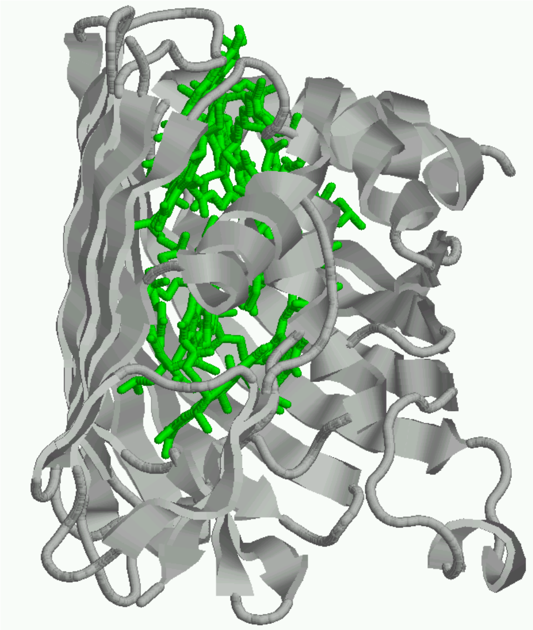

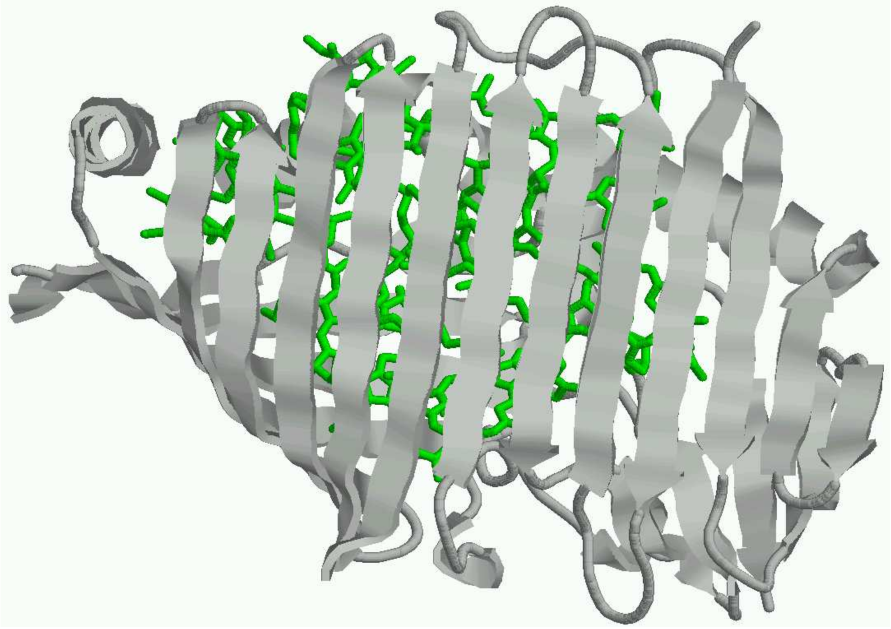

Figure 1.2: The light harvesting complex FMO from *Prosthecochloris aestuarii*, Ref. [TM93] (identifier 4bcl in the protein data bank). Plotted with `rasmol`. Two different views, beside a sketch of the protein backbone the BChls (green) are shown.

rounds the actual reaction center. The oxygen producing PS2 has been resolved for *Synechococcus elongatus* [ZWK+01, FIM+04] (Resolution 3.8 and 3.5 Å) and *Thermosynechococcus vulcanus* [KS03](Resolution 3.7 Å). Based on the new PS1 structure of *Synechococcus elongatus* an exciton model for this complex is introduced in Chapter 6 which can describe linear spectra as well as the time resolved fluorescence. This model is used again in Section 7.4 to propose a control experiment.

1.5 Summary

After a short introduction to Photosynthesis in Bacteria, some typical antenna systems have been presented. Besides an overview about the current state of structural information gained by x-ray scattering, a detailed picture of the three antenna complexes which will be addressed in this work is given. The LH2 antenna of *Rhodopseudomonas acidophila* will be used for calculations of higher excited states and exciton-exciton annihilation in Chapter 5. The recently published structure of the PS1 of *Synechococcus elongatus* opened the task of constructing a proper model system of this complex, which can describe recent experiments (Chapter 6) and can be used to propose new ones (Section 7.4). The FMO Complex of *Prosthecochloris aestuarii* with its small amount of BChl is a kind of prototype of an antenna system, the ideas of exciton control will be derived with regard to this complex in Chapter 7.

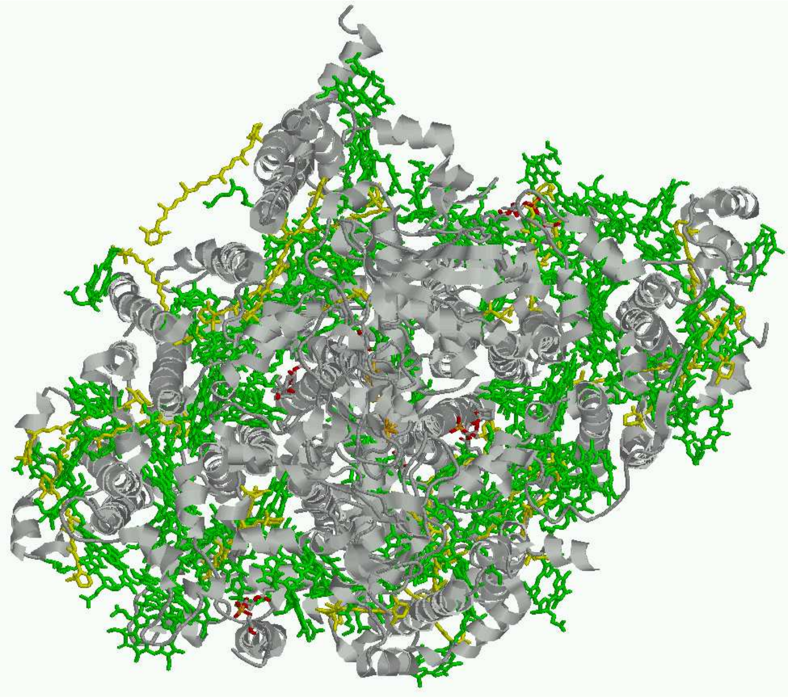

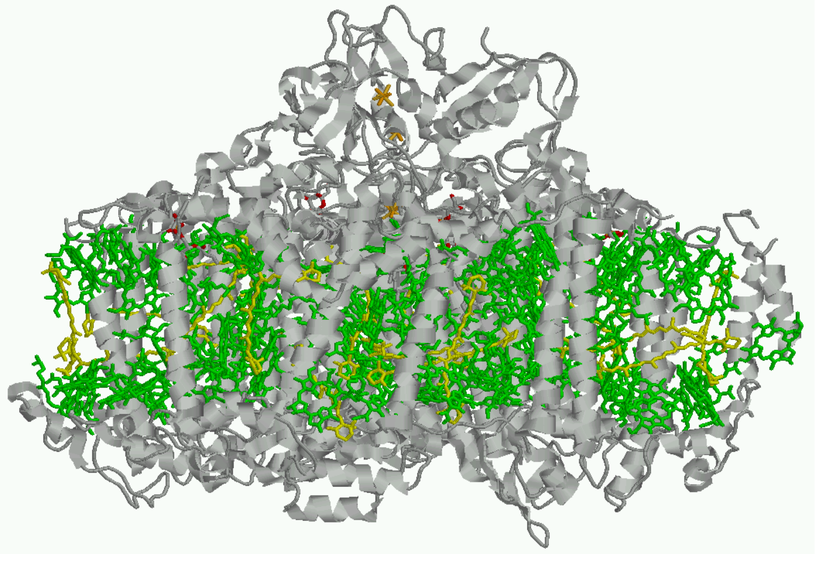

Figure 1.3: The light harvesting complex PS1 from *Synechococcus elongatus*, Ref. [JFK$^+$01](identifier 1jb0 in the protein data bank). Plotted with `rasmol`. Top and side view, beside a sketch of the protein backbone the Chls (green) and the carotenoids (yellow) are shown.

Part I

Theory

Chapter 2

The Multi-Exciton Density Matrix Theory

2.1 Introduction

The theoretical description of photosynthetic antenna systems is based on the Frenkel-Exciton concept [Fre31a, Fre31b]. It has been developed for insulating crystals and consists of local excitations of the respective atoms. These local excitations couple via e.g. dipole coupling and form exciton bands. A different exciton concept has been given by Wannier and Mott [Wan37, Mot38] which has been extensively used for the description of optical properties of semiconductor crystals. It describes an electron in the coulomb potential of a hole (i.e. the place where the electron has been before the excitation), with a finite distance between them. These different concepts have been shown later to be two special cases of an uniform exciton theory by Knox [Kno63]. At the same time Davydov developed the exciton theory for molecular crystals [Dav62].

The description of open quantum systems, like photosynthetic antenna systems, started with the projection operator technique of Nakajima and Zwanzig [Nak58, Zwa64], where the projector removes the bath degrees of freedom and keeps only the system coordinates. This is done in the framework of the density matrix in Liouville space [Fan63], where a Liouville equation of motion has been developed in close analogy to that of the statistical mechanics. For the dissipative part, resulting from the system-bath interaction in lowest order the Redfield-theory [Red63] is used. Recent books on the application and development of the density matrix theory include [MK00a, Muk95, LAI$^+$91, Blu96].

Another approach is the incoherent transfer of excitation energy between different chromophores, it has been developed by Förster [För48]. It is valid for systems with small excitonic couplings and fast vibrational relaxation. An extension to the transfer between different arrays of chromophores with strong excitonic coupling has been made in Ref. [SJF01].

An intermediate regime is addressed by the modified Redfield approach developed in Ref. [ZMCM98]. Comparisons between the different approaches have been made in [YF02], where the modified Redfield approach turned out to include both the Förster and the Redfield approaches in the respective limiting cases.

Among the first applications of the exciton theory to chromophore complexes was the application to J-Aggregates (e.g. Ref. [KS96]), the application to photosynthetic systems has been reviewed in Ref. [vAVvG00].

The starting point for this work is the extension of the density matrix theory to higher excited states and multiple excitations in one complex as it is has been published in Ref. [RMK01]. A review of the formalism is given in this Chapter and the Appendix. The main focus of this Chapter is the proper integration of the process of exciton-exciton annihilation (EEA) into the multi-exciton (MX) density matrix theory of Ref. [RMK01]. This turned out to be necessary because in experiments a fast decay of the main bleaching which depends on the pulse intensity has been found. Additionally, in the later Chapters of this work the possibility to control the exciton motion in photosynthetic antenna systems is evaluated, and the impact of the ultrafast EEA process on the controllability is important for realistic simulations.

First, some key points of the model are explained. For the incorporation of EEA into the MX approach it is essential to work, at least, with an electronic three level model for every single chromophore positioned at site m. This three–level model comprises the ground–state φ_{mg} with energy ϵ_{mg}, the first excited state φ_{me} with energy ϵ_{me} and a higher excited state φ_{mf} with energy ϵ_{mf}. In most cases the state φ_{me} may correspond to the first excited singlet state S_1 whereas the state φ_{mf} represents one of the higher–excited singlet states S_n $(n > 1)$ (cf. Fig. 2.1). However, the latter is fixed by the demand to have an energetic distance to the first excited state similar to that between the first excited state and the ground–state. Excitations within these levels are coupled by the Coulomb interaction leading to excitation energy motion and the formation of delocalized MX states. The relevance of this three-level model for the actual chromophores in photosynthetic antenna systems will be discussed in Chapter 5.

EEA in chromophore complexes (CC) or dye aggregates is usually characterized as a two step process. First, two S_1-excitations at different chromophores have to move close together (Fig. 2.1, upper panel) so that their excitation energy can be used to create a higher excited S_n–state $(n > 1)$ at one chromophore (Fig. 2.1, middle). This step leaves the other chromophore in the S_0 ground–state and is usually named exciton fusion. In a second step an ultrafast internal conversion (IC) process transfers the chromophore which is in the higher excited S_n–state to the S_1–state (Fig. 2.1, lower panel). The result is only one S_1-excitation. Of course, the S_1 state of the chromophore should have a much longer lifetime than the S_n- state and the S_n-state is chosen to have approximately twice the energy of the S_1-state. To describe both the intra manifold relaxation and the IC process two different kinds of vibrational degrees of freedom (DOF) will be used. The

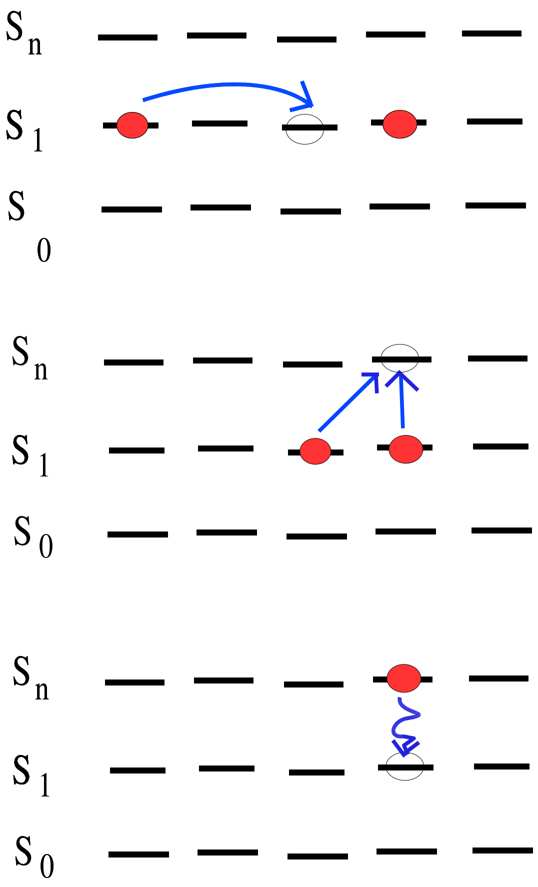

Figure 2.1: Sketch of the EEA process for five chromophores, each described as a three-level system: First the movement of two S_1 excitons towards each other (upper panel) and the creation of a single S_n excitation (middle). Then, the radiationless relaxation from the S_n state to the S_1 state by internal conversion (lower panel).

IC process is mediated by high frequency intra-molecular vibrations, the surplus energy is transfered to these modes.

If the view on EEA mentioned above is embedded into the MX theory, the description automatically accounts for the first step of EEA – the exciton fusion. For example, the two–exciton states already incorporate the mixture of two S_1–excitations and a single S_n–excitation. Accordingly, EEA is obtained as a radiation–less transition from the two–exciton to the single–exciton manifold.

But before explaining this in detail, the next section spends some time on the correct derivation of the CC Hamiltonian, including the coupling between the electronic states and the protein vibrations as well as the intra–molecular vibrations. A diagonalization with respect to the electronic interaction between the different chromophores results in the delocalized MX states, they are introduced in Section 2.3. The MX density matrix theory is explained in Section 2.4 incorporating all mechanisms of exciton relaxations (cf. Appendix B). The discussion of the EEA process is given in Section 2.5, including the respective rate expressions used the integration into the MX density matrix theory. At the end of that section the EEA rates between the two-exciton and the one-exciton manifold are developed. The more technical details can be found in Appendices A,B and C.

2.2 Multi-Exciton Hamiltonian

Some remarks on the MX picture have been already made in the introductory part of this Chapter. In particular the notation for the intramolecular states φ_{ma} of chromophore m with respective energies ϵ_{ma} ($a = g, e, f$ denotes the three electronic levels of interest) has been fixed. All these excitation energies as well as the Coulomb coupling functions are modulated by the variety of vibrational DOF. These vibrational DOF (mainly the inter-molecular protein vibrations) are responsible for electronic excitation energy dissipation within a given exciton manifold. Additionally, intra–molecular (intra–chromophore) vibrational modes participate in the IC–process which is the prerequisite of EEA.

All these types of couplings will written in a representation with respect to the MX–states $|\alpha_N\rangle$ (α is the MX quantum number and N indicates to which manifold the state belongs). The results is given by the multi-exciton–vibrational coupling. So far this type of coupling cannot be specified by quantum chemical calculations and different types of assumptions become necessary.

The details related to the derivation of the MX Hamiltonian including the coupling to vibrational DOF and the radiation field can be found in Appendix C and A.2, respectively (cf. also [MK00a, RMK01]). In this Chapter emphasis is placed on the contributions of intra–molecular vibrations and nonadiabatic transitions both necessary to account for internal conversion processes.

2.2.1 Unity Operator

The derivation of the CC–Hamiltonian can be best demonstrated by introducing electronic product states $\prod_m \varphi_{ma}$ of the whole CC which are built up by the single chromophore states

$$
|\,\{me\}_{\mathcal{M}};\{nf\}_{\mathcal{N}}\rangle = \prod_{m=1}^{N_C} \varphi_{ma}, \begin{cases} a=e, & m\in\{me\}_{\mathcal{M}} \\ a=f, & m\in\{nf\}_{\mathcal{N}} \\ a=g, & \text{else} \end{cases}, \tag{2.1}
$$

where the number of chromophores is given by N_C. The multi-index $\{me\}_{\mathcal{M}}$ indicates the $\mathcal{M}$ chromophores at sites $m_1,...,m_{\mathcal{M}}$ which are in the first excited state S_1, and $\{nf\}_{\mathcal{N}}$ stands for the *different* set of $\mathcal{N}$ chromophores at sites $n_1,...,n_{\mathcal{N}}$ which are in the higher excited state S_n, all *other* chromophores are in the ground state. The higher excitations count twice to the total number of excitations, as they have approximately twice the energy. This results in the total number of excitations $N=\mathcal{M}+2\mathcal{N}$, in the following the Hamiltonian and the states will be ordered with respect to this number. Although excited states with large N will be rarely produced in the experiment it is useful to derive expressions which are valid for an arbitrary N (of course less than twice the whole number N_{C} of considered chromophores).

The introduction of product states, Eq. 2.1, makes it possible to write the unity operator of the electronic CC state space as

$$
\begin{aligned}
1_{\mathrm{CC}} &= \sum_{N=0}^{2N_{\mathrm{C}}}\sum_{\mathcal{M}=0}^{N_C}\sum_{\mathcal{N}=0}^{N_C}\delta_{N,\mathcal{M}+2\mathcal{N}}\sum_{\{me\}_{\mathcal{M}}}\sum_{\{nf\}_{\mathcal{N}}} \\
&\quad \times|\{me\}_{\mathcal{M}},\{nf\}_{\mathcal{N}}\rangle\langle\{me\}_{\mathcal{M}},\{nf\}_{\mathcal{N}}|\,.
\end{aligned} \tag{2.2}
$$

The ordering with respect to the number N of elementary excitations is done by Kronecker's δ–function. This correct notation is somewhat lengthly. Whenever possible the abbreviated version $|\{me,nf\}_N\rangle$ for the state vector will be used, indicating the presence of N excitation but mixed in the way described above (any summation with respect to these states has to be of the type of Eq. 2.2). Note that the summation is over all *different* states, e.g. $\sum\limits_{\{me\}_{\in}} = \sum_{m=1}^{N_C}\sum_{n=1}^{m-1}$, and thus avoids the multiple counting of the same state, and the normalization condition holds.

The quantity n_{states} of N-exciton states, which is important for estimating the computational effort, is given by

$$
n_{\mathrm{states}}(N) = \sum_{\mathcal{M}=0}^{N_C}\sum_{\mathcal{N}=0}^{N_C}\delta_{N,\mathcal{M}+2\mathcal{N}}\frac{N_C!}{(N_C-\mathcal{M}-\mathcal{N})!(\mathcal{M}+\mathcal{N})!}\,. \tag{2.3}
$$

2.2.2 Chromophore Complex Hamiltonian

Before presenting the CC–Hamiltonian it is noted that the quantities mentioned so far depend on the set of all vibrational coordinates R incorporating intra–chromophore coordinates R_{intra} and inter–chromophore coordinates R_{inter}. The consideration of vibrational DOF leads to an introduction of potential energy surfaces (PES) $U(\{me,nf\}_N;R)$ of the N–fold excited state into the Hamiltonian instead of pure electronic energies, and one may write

$$\begin{aligned} H_{\text{CC}} &= \sum_N \Big\{ \sum_{\{me,nf\}_N} (T_{\text{nuc}} + U(\{me,nf\}_N;R)) \\ &\quad \times |\{me,nf\}_N\rangle\langle\{me,nf\}_N| + V^{(N)}_{\text{el-el}} \Big\} \\ &\quad + \sum_m (\Theta_{me,mf}|\varphi_{me}\rangle\langle\varphi_{mf}| + \text{h.c.}) - \mathbf{E}(t)\hat{\mu}_{\text{CC}} \; . \qquad (2.4) \end{aligned}$$

Besides the kinetic energy operator T_{nuc} of the nuclei this expression contains the inter–chromophore electronic interaction $V^{(N)}_{\text{el-el}}$. The second part describes the nonadiabatic coupling between the state φ_{mf} and φ_{me} of every chromophore where the coupling matrix element is given by $\Theta_{me,mf}$. The action of the radiation field with electric field–strength $\mathbf{E}(t)$ is accounted for in the last part ($\hat{\mu}_{\text{CC}}$ is the CC dipole operator comprising contributions from every chromophore).

2.2.3 Electronic Interaction

The calculations of the electronic interactions of the different chromophores using a two level approach of the chromophore has often been done, e.g. [vAVvG00]. Here, this approach is extended to the three level description of the chromophores resulting in

$$\begin{aligned} V_{\text{el-el}} = & \sum_{m,n} J_{me,ne}|\varphi_{mg}\rangle\langle\varphi_{me}| \otimes |\varphi_{ne}\rangle\langle\varphi_{ng}| \\ + & \sum_{m,n} J_{me,nf}|\varphi_{mg}\rangle\langle\varphi_{me}| \otimes |\varphi_{nf}\rangle\langle\varphi_{ne}| + c.c. \\ + & \sum_{m,n} J_{mf,nf}|\varphi_{me}\rangle\langle\varphi_{mf}| \otimes |\varphi_{nf}\rangle\langle\varphi_{ne}| \, . \qquad (2.5) \end{aligned}$$

The first part describes the transition $S_0 \rightarrow S_1$ of chromophore n from the ground state to the first excited state and chromophore m from the first excited state to the ground-state ($S_1 \rightarrow S_0$) with the coupling constant $J_{me,ne}$. The second part describes transitions where the two S_1 excitations of chromophore m and n are used to form a single S_n excitation at chromophore n, leaving chromophore m in the ground-state S_0(coupling constant $J_{me,nf}$). Also the reverse process is possible, with the coupling constant $J_{nf,me}$. The last is the interaction between two excited chromophores where chromophore n makes the transition $S_1 \rightarrow S_n$ to the higher excited state and chromophore m $S_n \rightarrow S_1$ to the first excited state with the coupling constant $J_{mf,nf}$. As these couplings preserve the manifold index N, the electronic coupling operator can be written as $V_{\text{el-el}} = \sum_N V_{\text{el-el}}^{(N)}$, where

$$V_{\text{el-el}}^{(N)} = \sum_{\{me,nf\}_N} \sum_{\{\bar{m}e,\bar{n}f\}_N} V_{\text{el-el}}^{(N)}(\{me,nf\}_N, \{\bar{m}e,\bar{n}f\}_N) |\{me,nf\}_N\rangle\langle\{\bar{m}e,\bar{n}f\}_N| \, . \tag{2.6}$$

One possible realization of the interaction is given by the dipole-dipole interaction approximation, which often has been used for photosynthetic antenna systems. It is given by

$$J_{me,ne} = \frac{\mathbf{d}_{eg}^{(m)}\mathbf{d}_{eg}^{(n)} - 3(\mathbf{d}_{eg}^{(n)}\mathbf{n}_{mn})(\mathbf{d}_{eg}^{(m)}\mathbf{n}_{mn})}{|\mathbf{r}_m - \mathbf{r}_n|^3} \, , \tag{2.7}$$

using the $S_0 \rightarrow S_1$ transition dipole moments $\mathbf{d}_{eg}^{(m)}$and the spatial position $\mathbf{r}_m$ of chromophore m, and the normalized vector from molecule m to molecule n, $\mathbf{n}_{mn} = (\mathbf{r}_n - \mathbf{r}_m)/|\mathbf{r}_n - \mathbf{r}_m|$. The coupling factors $J_{me,nf}$, $J_{mf,ne}$, and $J_{mf,nf}$ are similarly calculated using the respective dipole moments. If the distances of the chromophores become too small, the dipole-dipole coupling approach is no longer valid. This will be discussed in the respective sections.

2.2.4 Coupling to Vibrational States

The following discussion focuses on the electron–vibrational coupling. The potential energy surface (PES) introduced in H_{CC} may be written in detail as

$$\begin{aligned} &U(\{me,nf\}_N;R) = U_0(R) \\ &+(1-\delta_{N,0})\Big(\sum_{k\in\{me\}_\mathcal{M}} \epsilon_k(eg;R) + \sum_{k\in\{nf\}_\mathcal{N}} \epsilon_k(fg;R)\Big)_{|N=\mathcal{M}+2\mathcal{N}}, \end{aligned} \tag{2.8}$$

where the quantities $\epsilon_k(ag;R)$, $a = e, f$, are given as the single chromophore excitation energies $\epsilon_{ka}(R) - \epsilon_{kg}(R)$. They appear since the complete ground–state PES has been introduced as $U_0(R) = \sum_m \epsilon_{mg}(R) + V_{\text{nuc-nuc}}$, where the repulsive Coulomb interaction between different atoms has been denoted by $V_{\text{nuc-nuc}}$. The introduction of the excitation energies $\epsilon_k(ag;R)$ is not obligatory but in the present approach necessary to introduce MX states. To compute these quantities one provides that $U_0(R)$ possesses a global minimum at the set $R = R_0$ of vibrational coordinates. Eq.2.8 can be written as

$$U(\{me,nf\}_N;R) \;\; = \;\; U(\{me,nf\}_N;R_0) \; + \Delta U(\{me,nf\}_N;R) \, , \tag{2.9}$$

where the $U(\{me,nf\}_N;R_0)$ are the Franck–Condon transition energies to the particular N–fold excitations and the $\Delta U(\{me,nf\}_N;R)$ define the PES related to this excited state.

2.3 Multi-Exciton States

The picture which will be stressed in the following is that of MX–states of the whole CC where one changes from the locally excited electronic chromophore states to delocalized (or partially delocalized) states. These states can be ordered within the various exciton manifolds. The ordering scheme starts with the CC electronic ground–state denoted by $|0\rangle$. It is followed by the single exciton manifold, the two exciton manifold and so on (Fig. 2.2). All these states will be named MX–states and will be written as $|\alpha_N\rangle$, where α_N is the quantum number of the exciton state in the N–exciton manifold. The number N corresponds to the number of basic excitations roughly given by the S_0–S_1–transition energy of a single chromophore. For example, the single exciton state $|\alpha_1\rangle$ follows from the presence of a single S_1–excitation whereas the two–exciton state $|\alpha_2\rangle$ may be formed by two S_1–excitations or alternatively by a single S_n–excitation. Transitions between the different manifolds are initiated by the external electric field and, from higher to lower manifolds, by the EEA process. Low frequency protein vibrational modes are responsible for the relaxation within the different manifolds.

The reason to formulate the MX–theory for an arbitrary number of excitations present in the CC is the fact that when considering EEA processes a population of the two–exciton manifold comes into play. Furthermore, e.g. for calculating pump-probe spectra the transition amplitudes between the two– and the three–exciton manifold may become important, too. And if the pump–intensity is further increased even higher exciton manifolds have to be taken into account. Such a MX–theory has been developed in [RMK01]. Here, this approach is generalized to the case where any chromophore is described by an electronic three–level model with internal conversion between the two excited levels.

To introduce the MX states the CC Hamiltonian, Eq. 2.4 has been rewritten using Eq. 2.9, and the part defined by the excitation energies $U(\{me,nf\}_N;R_0)$ and the coupling $V^{(N)}_{\text{el}-\text{el}}$ (Eq. 2.6) is diagonalized, both related to the N'th excited state of the CC. In other words, the eigenvalues and eigenvectors for the excitonic Hamiltonian are calculated separately for every exciton manifold. The respective N–exciton states can be written as

$$|\alpha_N\rangle \;=\; \sum_{\{me,nf\}_N} C_{\alpha_N}(\{me,nf\}_N)|\{me,nf\}_N\rangle\ . \qquad (2.10)$$

The $C_{\alpha_N}(\{me,nf\}_N)$ are the exciton expansion coefficients, i.e. the eigenvec-

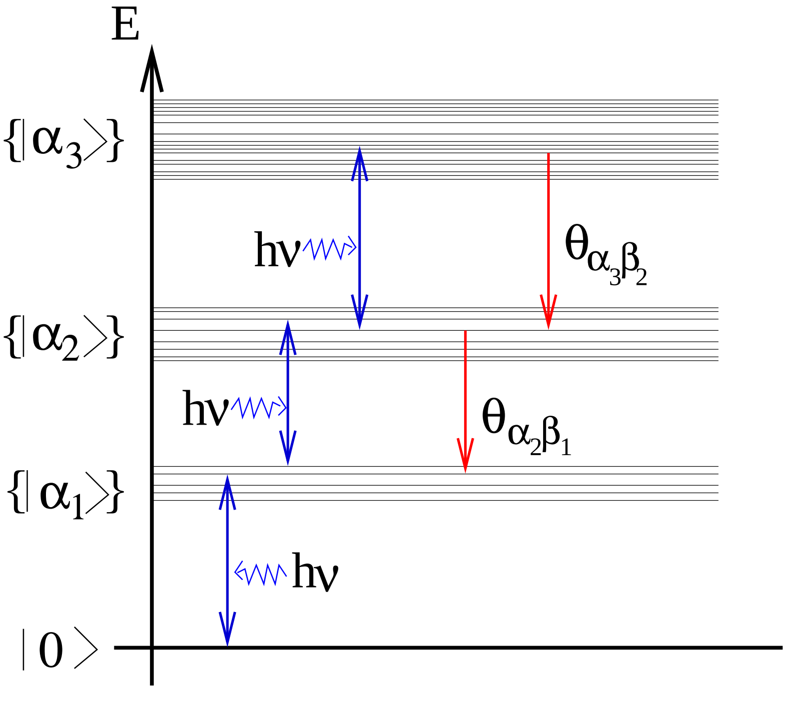

Figure 2.2: The exciton energies of the CC, ordered by their respective energies into the ground-state $|0\rangle$, the one-exciton manifold $\{|\alpha_1\rangle\}$, the two- and three exciton manifolds $\{|\alpha_2\rangle\}$ and $\{|\alpha_3\rangle\}$. Transitions between the different exciton manifolds are due to an external field and the EEA process.

tors gained by the above mentioned diagonalization. The respective eigenvalues $E(\alpha_N)$ give the energies of the multi-exciton states. According to the normalization of the states $|\{me, nf\}_N\rangle$ one easily verifies the normalization condition $\sum_{\{me,nf\}_N} |C_{\alpha_N}(\{me, nf\}_N)|^2 = 1$. Resulting from Eq. 2.10 the MX representation of the CC Hamiltonian is introduced (cf. Fig. 2.2),

$$\begin{aligned} H_{\mathrm{CC}} &= \sum_N \Big(\sum_{\alpha_N} E(\alpha_N)|\alpha_N\rangle\langle\alpha_N| + \sum_{\alpha_N,\beta_N} H_{\mathrm{vib}}(\alpha_N, \beta_N)|\alpha_N\rangle\langle\beta_N| \Big) \\ &\quad + \sum_{N>1} \sum_{\alpha_{N-1}} \sum_{\beta_N} (\Theta(\alpha_{N-1}, \beta_N)|\alpha_{N-1}\rangle\langle\beta_N| + \text{h.c.}) - \mathbf{E}(t)\hat{\mu}_{\mathrm{CC}}. \end{aligned} \tag{2.11}$$

Details on the MX matrix elements of the nonadiabatic coupling can be found in Appendix A.1. The coupling to the external field is given in Appendix A.2.

2.3.1 The Vibrational Hamiltonian

The vibrational Hamiltonian $H_{\mathrm{vib}}(\alpha_N, \beta_N)$ depending two–fold on the MX quantum numbers is obtained as the MX matrix element of the sum of T_{nuc} as well as $\Delta U(\{me, nf\}_N; R)$, Eq. 2.9. If both quantum numbers are related to the CC electronic ground–state one can write $H_{\mathrm{vib}}(0, 0) \equiv H^{(0)}_{\mathrm{vib}} = T_{\mathrm{nuc}} + [U_0(R) - U_0(R_0)]$. This expression may separate into the intra–chromophore contribution $H^{(0,\mathrm{intra})}_{\mathrm{vib}}$ and into the contribution $H^{(0,\mathrm{pro})}_{\mathrm{vib}}$ depending on the protein coordinates, and for the kinetic energy $T_{\mathrm{nuc}} = T_{\mathrm{pro}} + T_{\mathrm{intra}}$. The vibrational Hamiltonian which belongs to excited CC states reads ($N > 0$)

$$\begin{aligned} H_{\mathrm{vib}}(\alpha_N, \beta_N) &= \delta_{N,0} H^{(0)}_{\mathrm{vib}} + (1 - \delta_{N,0}) \Big(T_{\mathrm{nuc}} \qquad (2.12) \\ &+ \sum_{\{me,nf\}_N} C^*_{\alpha_N}(\{me, nf\}_N)\, \Delta U(\{me, nf\}_N; R)\, C_{\beta_N}(\{me, nf\}_N) \Big). \end{aligned}$$

For simplicity it is provided that there is no mode–coupling between the inter–chromophore vibrations and the intra–chromophore vibrations and one separates

$$\begin{aligned} \Delta U(\{me, nf\}_N; R) &= \Delta U_{\mathrm{intra}}(\{me, nf\}_N; R_{\mathrm{intra}}) \\ &\quad + \Delta U_{\mathrm{pro}}(\{me, nf\}_N; R_{\mathrm{pro}}) \end{aligned} \tag{2.13}$$

into an intra–molecular part and into a part depending on the vibrations of the protein complex. This separation results in the contribution $H^{(\mathrm{intra})}_{\mathrm{vib}}(\alpha_N, \beta_N)$ and in the contribution $H^{(\mathrm{pro})}_{\mathrm{vib}}(\alpha_N, \beta_N)$, respectively.

2.3.2 Coupling to Protein Vibrations

As it is standard in literature (see e. g. [RMK01, MK00a]) the low–frequency protein vibrations can be accounted for in a manner where all deviations from the electronic ground–state vibrations are considered as perturbations. Starting with the Hamiltonian for the protein vibrations

$$H_{\text{vib}}^{(\text{pro})}(\alpha_N,\beta_N) = \delta_{N,0} H_{\text{vib}}^{(0,\text{pro})} + (1-\delta_{N,0})\Big(T_{\text{pro}} + \sum_{\{me,nf\}_N} \times C_{\alpha_N}^{*}(\{me,nf\}_N)\Delta U_{\text{pro}}(\{me,nf\}_N;R)\; C_{\beta_N}(\{me,nf\}_N)\Big)\ . \qquad (2.14)$$

in Appendix C.1 a linear linear expansion of the PES is made. The respective form of the linear multi-exciton–vibrational coupling reads

$$H_{\text{vib}}^{(\text{pro})}(\alpha_N,\beta_N) = H_{\text{vib}}^{(0,\text{pro})} + \sum_{\xi} \hbar\omega_\xi g_\xi^{(\text{pro})}(\alpha_N,\beta_N) Q_\xi\,, \qquad (2.15)$$

where the dimensionless vibrational coordinate is given by harmonic oscillator operators (with mode index ξ) according to $Q_\xi = c_\xi + c_\xi^{+}$. The related vibrational frequency is denoted by ω_ξ, and $g_\xi^{(\text{pro})}(\alpha_N,\beta_N)$ is the dimensionless coupling matrix. Additionally, modulations of the inter–chromophore electronic coupling $V_{\text{el–el}}^{(N)}$ (cf Eq. 2.4) may be taken into account, but have been neglected here.

2.4 Multi-Exciton Density Matrix

The photoinduced kinetics of the MX system has often been described within a version of the density matrix theory usually called multilevel Redfield theory. The MX density matrix $\rho(\alpha_M,\beta_N;t)$ represents the central quantity to be determined. The diagonal elements $\rho(\alpha_M,\alpha_M;t)$ give the MX level populations $P(\alpha_M;t)$, whereas off–diagonal elements define the various coherences. Those can be arranged with respect to intra–manifold coherences indicating the presence of excitonic wavepackets in the particular manifold, and inter–manifold coherences reflecting optical excitations and thus the presence of transition polarizations in the system.

The main assumption of the standard approach is a second–order perturbation theory with respect to the MX vibrational coupling. In the present case, however, the mentioned approach needs an extension to account for EEA in a proper way. In particular the MX- vibrational coupling for the intra-chromophore modes which are responsible for the IC has to be included beyond second order perturbation theory. The respective calculations are presented in Section 2.5.

The approach is most flexible formulated in the state representation. Since the model comprises two types of exciton–vibration couplings, the one related to (low–frequency) protein vibrations, and the other referring to (high–frequency) intra–molecular vibrations the complete MX vibrational states read

$$|A\rangle = |\alpha_M\rangle|\chi_\mu\rangle|\bar{\chi}_{\alpha_M\bar{\mu}}\rangle. \tag{2.16}$$

Beside the MX states $|\alpha_M\rangle$ the expression contains the vibrational states $|\chi_\mu\rangle$ of the inter–molecular vibrations. These states are *eigenstates* of the Hamiltonian $H_{\text{vib}}^{(0,\text{pro})}$ introduced in the foregoing section (Eq. 2.15). They factorize with respect to the different modes, and the respective *eigenenergies* are denoted as $\hbar\Omega_\mu$. The vibrational states of the intra–chromophore modes $|\bar{\chi}_{\alpha_M\bar{\mu}}\rangle$ depend on the exciton quantum number and have to be understood as *eigenstates* of the Hamiltonian $H_{\text{vib}}^{(\text{intra})}(\alpha_M,\alpha_M)$, Eq. A.9. The respective *eigenvalues* are denoted as $\hbar\bar{\Omega}_{\alpha_M\bar{\mu}}$. If all PES involved are approximated by displaced parabola the *eigenvalues* can be written as $\bar{\Omega}_{\alpha_M\bar{\mu}} = \bar{\Omega}_{\bar{\mu}} + \triangle\Omega(\alpha_M)$ (cf. Appendix A.3.2). Such an independency of all intra–molecular vibrational frequencies $\bar{\Omega}_{\bar{\mu}}$ on the actual multi-exciton state is essential for the following. The part $\Delta\Omega(\alpha_M)$ which represents a MX–state dependent energetic shift collects all contributions of $H_{\text{vib}}^{(\text{intra})}(\alpha_M,\alpha_M)$ (reorganization energies, see Appendix A.3.1 and A.3.2).

Since the whole density matrix theory (see Appendix A.4) is based on a representation using the general MX vibrational states $|A\rangle$ the (reduced) MX density matrix has to be determined from the total time-dependent statistical operator $\hat{W}(t)$ as follows:

$$\begin{aligned} \rho(\alpha_M,\beta_N;t) &= \langle\alpha_M|\hat{\rho}(t)|\beta_N\rangle \\ &= \sum_{\mu,\bar{\mu}}\langle\alpha_M|\langle\chi_\mu|\langle\bar{\chi}_{\alpha_M\bar{\mu}}|\hat{W}(t)|\bar{\chi}_{\beta_N\bar{\mu}}\rangle|\chi_\mu\rangle|\beta_N\rangle\ . \end{aligned} \tag{2.17}$$

The problems which arise from the dependence of the intra-chromophore vibrations from the excitonic state are discussed in Appendix A.4. In that Appendix, a mean field approach could be used to connect the above given reduced density matrix with the usual one

$$\bar{\rho}(\alpha_M,\beta_N;t) = \sum_{\mu,\bar{\mu}}\langle\alpha_M|\langle\chi_\mu|\langle\bar{\chi}_{\alpha_M\bar{\mu}}|\hat{W}(t)|\bar{\chi}_{\alpha_N\bar{\mu}}\rangle|\chi_\mu\rangle|\beta_N\rangle \tag{2.18}$$

which is diagonal in the vibrational modes and useful for further calculations. The mean field approach results in

$$\bar{\rho}(\alpha_M,\beta_N;t) = S(\alpha_M,\beta_N)\rho(\alpha_M,\beta_N;t)\ . \tag{2.19}$$

with $S(\alpha_M,\beta_N) = \sum_\mu f(\mu)\langle\bar{\chi}_{\alpha_M\mu}|\bar{\chi}_{\beta_N\mu}\rangle$ and the thermal distribution function $f(\mu)$. Having this translation in mind one concentrates again on the initial density matrix $\rho(\alpha_M,\beta_N;t)$. For the calculations of Part II it is assumed for reasons of simplicity that $S(\alpha_M,\beta_N)=1$.

2.4.1 Equations of Motion for the Reduced Multi-Exciton Density Matrix

The multi-exciton representation of the CC–Hamiltonian, Eq. 2.4 is given in Appendix A.5. Once this representation has been introduced equations of motion can be set up. This has been done in in Appendix B by applying a projection operator technique to the full statistical operator. Furthermore the Markov and Bloch approximations have been made (see e.g. [Muk95, MK00a]). A short notation for the equation of motion of the reduced density matrix is achieved using Liouville superoperators, it is given by

$$\frac{\partial}{\partial t}\hat{\rho}(t) = (-i\mathcal{L}_0 - \mathcal{D} - i\mathcal{L}_{\text{field}}(t))\hat{\rho}(t)\ . \tag{2.20}$$

Here, $\mathcal{L}_0$ stands for the oscillatory part, $\mathcal{D}$ for the dissipative part, and $\mathcal{L}_{\text{field}}$ for the interaction with the field. The resulting equation of motion reads in mode detail (cf. Eqs. B.15,B.16 and B.18)

$$\begin{aligned}
&\frac{\partial}{\partial t}\rho(\alpha_M,\beta_N;t) = -i\Omega(\alpha_M,\beta_N)\ \rho(\alpha_M,\beta_N;t)\\
&-i\sum_{\gamma_K}\Big(<v_{\alpha_M;\gamma_K}>\rho(\gamma_K,\beta_N;t) - <v_{\gamma_K\beta_N}>\rho(\alpha_M,\gamma_K;t)\Big)\\
&-\delta_{\alpha_M,\beta_N}\sum_{K,\gamma_K}\Big(k(\alpha_M\to\gamma_K)\rho(\alpha_M,\alpha_M;t) - k(\gamma_K\to\alpha_M)\rho(\gamma_K,\gamma_K;t)\Big)\\
&-(1-\delta_{\alpha_M,\beta_N})\Big(\Gamma(\alpha_M)+\Gamma(\beta_N)+\tilde{\Gamma}(\alpha_M,\beta_N)\Big)\rho(\alpha_M,\beta_N;t)\\
&-\frac{i}{\hbar}\mathbf{E}(t)\sum_{K,\gamma_K}\Big(\boldsymbol{\mu}(\alpha_M,\gamma_K)\rho(\gamma_K,\beta_N;t) - \boldsymbol{\mu}(\gamma_K,\beta_M)\rho(\alpha_M,\gamma_K;t)\Big)\,.
\end{aligned} \tag{2.21}$$

The equation of motion Eq. 2.21 consist of different parts which will now be discussed.

First, an oscillatory part (symbolized by $\mathcal{L}_0$) for the coherences is given which includes the pure MX transition frequencies, which are defined according to

$$\Omega(\alpha_M,\beta_N) \ = \ E(\alpha_M)/\hbar + \Delta\Omega(\alpha_M) - E(\beta_N)/\hbar - \Delta\Omega(\beta_N)\,. \tag{2.22}$$

Also in the oscillatory part are the thermal averages with respect to the vibrational DOF $< v_{\alpha_M;\gamma_K} >$ (see Eq. B.8) of the full coupling matrix elements $V_{A,B} = \langle A|\hat{V}|B\rangle$. Here, $\hat{V}$ denotes any type of coupling Hamiltonian appearing in Eq. 2.11, and $|A\rangle$ as well $|B\rangle$ represent the complete MX–vibrational states. The contributions proportional to $< v_{\alpha_M;\gamma_K} >$ form the so–called mean–field terms (Eq. B.8). They enter the reversible part of the density matrix equation. Further on, they describe dissipation via the factorized part of the second–order correlation function (see Eqs. B.11 and B.14). It should be noted that these mean field contributions vanish, if linear exciton-vibrational interaction is provided. This is the case for the protein vibrations, and it is also assumed in Part II for the intra-chromophore vibrations. The role of the mean field part of the nonadiabatic coupling will be discussed in Section 2.5.3.

The second part describes the influence of dissipation (symbolized by $\mathcal{D}$). It consists of rate expressions for the populations and the dephasing of the coherences. All transition rates which are of the second order with respect to the coupling matrix $V_{A,B}$ follow from the relaxation matrix according to Eqs. B.17 and B.14, and the population transfer part is derived

$$k(\alpha_M \to \beta_N) \;=\; 2\Gamma(\alpha_M \beta_N, \beta_N \alpha_M; \Omega(\alpha_M, \beta_N))\,. \tag{2.23}$$

The definition of the relaxation matrix $\Gamma(\alpha_M \beta_N, \beta_N \alpha_M; \Omega(\alpha_M, \beta_N))$ can be found in Appendix B, Eq. B.14. The dephasing of the coherences, is given by the relaxation part

$$\Gamma(\alpha_M) = \frac{1}{2} \sum_{K} \sum_{\gamma_K} k(\alpha_M \to \gamma_K)\,, \tag{2.24}$$

and the pure dephasing part $\tilde{\Gamma}(\alpha_M, \beta_N)$, the details can be found in Appendix B, Eq. B.19 and B.20.

The last part gives the coupling to the external field (symbolized by $\mathcal{L}_{\text{field}}$), the calculation of the multi-exciton dipole moments using the respective expansion coefficients has been done in Appendix A.2.

2.4.2 The Relaxation Matrix

Next, it is specified how to tackle the different contributions to the relaxation matrix resulting from the various parts of coupling potentials which enter $V_{A,B}$, Eq. A.37. The part $V^{(\text{mx}-\text{pro})}$ following from the coupling to protein vibrations will be considered in the complete second–order form and is discussed in Appendix C (cf. [RMK01]). The next part of $V_{A,B}$ stems from the off–diagonal part of the intra–molecular vibrations represented by the coupling $V^{(\text{mx}-\text{intra})}$, Eq. A.39. Since a specification of both contributions needs a fit to experimental data it is assumed that it is possible to include intra–molecular multi-exciton–vibrational couplings into the excitation energy dissipation described by delocalized (inter–molecular) vibrations. As a further contribution the nonadiabatic coupling $V^{(\text{na})}$, Eq. A.40 is considered up to the second–order. However, the latter expression will not be discussed here but in Section 2.5.

Finally one focuses on the second–order correlation functions which are formed by different parts of the coupling matrix, i.e. which lead to cross–correlations. A first set of such cross–correlation functions is given by $V^{(\text{mx}-\text{pro})}$, on the one–hand, and on the other hand by $V^{(\text{mx}-\text{intra})}$and $V^{(\text{na})}$. Since no difference is made between protein vibrations and intra–molecular vibrations as long as excitation energy dissipation is concerned, there is no need to deal with the combination of $V^{(\mathrm{mx-inter})}$ and $V^{(\mathrm{mx-pro})}$. It remains the contribution including $V^{(\mathrm{na})}$. It is obvious that the respective terms in the density matrix equations only represent small corrections to the used Bloch–approximation. This results from the fact that a coupling potential acting within a given exciton–manifold is combined with a coupling which relates different manifolds.

According to the foregoing discussion the complete relaxation matrix, Eq. B.14 and thus the general transition rate splits off into a part referring to inter–molecular vibrations and into a part following from nonadiabatic couplings,

$$\begin{aligned} k(\alpha_M \quad \rightarrow \quad & \beta_N) \\ & \equiv 2\Gamma(\alpha_M\beta_N, \beta_N\alpha_M; \Omega(\alpha_M, \beta_N)) \\ & = \delta_{M,N} 2\Gamma^{(\mathrm{mx-pro})}(\alpha_N\beta_N, \beta_N\alpha_N; \Omega(\alpha_N, \beta_N)) \\ & +(\delta_{M+1,N} + \delta_{M-1,N}) 2\Gamma^{(\mathrm{na})}(\alpha_M\beta_N, \beta_N\alpha_M; \Omega(\alpha_M, \beta_N)) \; . \end{aligned} \tag{2.25}$$

Details on both contributions are given in the following sections.

2.4.3 Relaxation Matrix Caused by a Coupling to Protein Vibrations

The inter–molecular part of the relaxation matrix follows in more detail as (cf. Eq. A.38, although the intramolecular vibrations give an additional time dependent factor to the integral, this has been neglected here)

$$\begin{aligned} \Gamma^{(\mathrm{mx-pro})} \quad & (\alpha_N\beta_N, \beta_N\alpha_N; \Omega(\alpha_N, \beta_N)) \\ & = \ \mathrm{Re} \int_0^\infty dt \ \exp\left(i\Omega(\alpha_N, \beta_N)t\right) \\ & \times \sum_{\mu\nu} f(\mu) e^{i\Omega_{\mu\nu}\tau} \sum_{\xi} \omega_\xi g_\xi(\alpha_N\beta_N) \langle\chi_\mu| c_\xi^+ + c_\xi |\chi_\nu\rangle \\ & \times \sum_{\bar\xi} \omega_{\bar\xi} g_{\bar\xi}(\beta_N\alpha_N) \langle\chi_\nu| c_{\bar\xi}^+ + c_{\bar\xi} |\chi_\mu\rangle \; . \end{aligned} \tag{2.26}$$

For simplicity the index ”mx-pro” at the frequencies and coupling constants is removed here and in the following. In a further step one transfers the terms oscillating with transition frequency $\Omega_{\mu\nu}$ into two time–evolution operators embedding the oscillator operators.

The completeness relation for the χ_ν makes it possible to remove the respective states and the related summation. The μ–summation together with the thermal distribution function $f(\mu)$ is replaced by a trace–formula including the respective equilibrium statistical operator. This finally leads to an expression including the spectral density $\mathcal{J}$ of the MX inter–molecular vibrational coupling. One replaces $\Gamma^{(\text{mx}-\text{pro})}$ by the respective rate and gets ($n(\Omega)$ denotes the Bose–Einstein distribution),

$$k^{(\text{mx}-\text{pro})}(\alpha_N \to \beta_N) = 2\pi\Omega^2(\alpha_N, \beta_N)\Big(1 + n(\Omega(\alpha_N, \beta_N))\Big) \qquad (2.27)$$
$$\times\Big(\mathcal{J}(\alpha_N\beta_N, \beta_N\alpha_N; \Omega(\alpha_N, \beta_N)) \;-\mathcal{J}(\alpha_N\beta_N, \beta_N\alpha_N; -\Omega(\alpha_N, \beta_N))\Big)\,.$$

A further treatment of this expression together with an explanation of the spectral densities and the introduction of some useful approximations can be found in Appendix C.

2.5 Exciton-Exciton Annihilation

So far, EEA has often been described by the rate equation $\partial n(\mathbf{r}, t)/\partial t \;= -\gamma n(\mathbf{r}, t)^2$, with the exciton density $n(\mathbf{r}, t)$ at the spatial position $\mathbf{r}$ and the annihilation rate constant γ (for a recent overview see [vAVvG00]). Besides such a macroscopic description valid for larger aggregates (and organic semiconductors), where exciton diffusion may take place various microscopic theories have been presented [GFG95, RKMK01, MGF99, Sun70]. A density matrix hierarchy has been derived in [Sun70] which refers to the multiple presence of intra–chromophore excitations (concrete estimations concentrated on single and two–exciton contributions). The studies on EEA kinetics in [GFG95, RKMK01, MGF99] have been based on microscopic computations of the annihilation rate constant γ. Using ”Golden Rule” arguments γ follows as the square of the transition matrix element between a state of two delocalized excitons and a state of a localized higher intra–molecular excitation multiplied by the (constant) density of final states.

If interested in phenomena on a sub-picosecond time–scale coherences between different exciton levels become important which are best described in the framework of the density matrix theory. Consequently, it is essential to include the EEA into an exciton density matrix theory. Different approaches have been presented in the past (see [RM97a, RM97b, RM97c, RMSK00, RMK01]). Concentrating on a chlorophyll dimer EEA has been described by means of a direct derivation of nonadiabatic transitions. They are characterized by simple microscopic internal conversion rates if the limit of instantaneous nonadiabatic transitions is taken. The possible incorporation of EEA into the anharmonic oscillator description of Frenkel excitons has been demonstrated in [RMSK00], and a derivation of rate equations including EEA rates can be found in [RMK01]. In this Section it is explained in detail how to generalize the multi-exciton (MX) density matrix theory for an inclusion of EEA processes and, in this way, the concepts on EEA

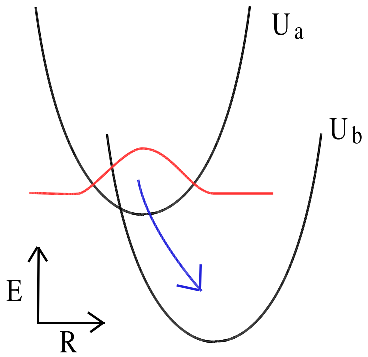

Figure 2.3: Sketch of the internal conversion process for a single two state chromophore as discussed in Ref. [RMK01, MK00a]. The potential energy surfaces U_a and U_b and the state φ_a are shown.

of [RM97a, RM97b, RM97c] have been combined with the MX approach of Ref. [RMK01].

For the description of the nonadiabatic transition process one expects the incorporation of transition rates which are in a certain sense the MX representation of standard internal conversion rates. The standard IC rate describes a transition from the (adiabatic) state φ_a to state φ_b (Fig. 2.3, Ref. [RMK01, MK00a])

$$k^{(\mathrm{IC})}_{a\to b} = \frac{2\pi}{\hbar}|\Theta_{a,b}|^2 D_{ab}(\omega_{ab}). \tag{2.28}$$

Here, the dependence of the nonadiabatic coupling $\Theta_{a,b}$ on the vibrational coordinates has been neglected and ω_{ab} is discussed below. As a result, the so-called Franck-Condon weighted and thermal averaged combined density of states (DOS) could be introduced,

$$D_{ab}(\omega_{ab}) = \frac{1}{2\pi\hbar}\int dt\; e^{i\omega_{ab}t} tr_{\mathrm{vib}}\{\hat{R}_a U_a^+(t) U_b(t)\}\,. \tag{2.29}$$

In the given expressions $\hbar\omega_{ab} = U_a^{(0)} - U_b^{(0)}$ denotes the difference of the minima of both potential energy surfaces (PES) at the respective equilibrium configuration of the nuclear coordinates. Accordingly, the time–evolution operators $U_a^+(t)$ and $U_b(t)$ are defined by the vibrational Hamiltonian H_a and H_b belonging to state φ_a and φ_b, respectively (both starting at the energy minimum of the PES) and $\hat{R}_a$ is the vibrational equilibrium operator for state φ_a. The vibrational degrees of freedom (DOF) addressed in the trace are of the intra–molecular type and act as accepting modes for the non-radiative transition.

As it is well–known the rate expression Eq. 2.28 contains the coupling between the electronic DOF and the intra–molecular vibrations beyond the standard second–order perturbation theory. The development of a density matrix theory which may take notice of all orders of the exciton vibrational coupling has been demonstrated in Appendix B (cf. also [KMS94]). As a result one can derive equations of motion for the density matrix $\rho(\alpha_M, \beta_N; t)$ but now including the correct expressions of the IC–rates. This has been achieved by incorporating the diagonal part Eq. A.9 of $H_{\text{vib}}^{(\text{intra})}$ into the time–evolution operator.

2.5.1 Coupling to Intra–Molecular Vibrations

Now, one concentrates on the coupling between the multi-exciton states and the intra–molecular vibrations which is essential for a correct description of EEA. To end up with formulas similar to standard IC–rates [MK00a] a part of the complete coupling has to be treated beyond a simple second–order perturbation theory. Within the present MX scheme such a non–perturbative description becomes possible for the diagonal part of the intra–molecular contribution $H_{\text{vib}}^{(\text{intra})}(\alpha_N, \alpha_N)$ to the complete vibrational Hamiltonian, Eq. 2.12. The off–diagonal contributions will be handled as a perturbation and can be included into the expression valid for protein vibrations. The details are available in Appendix A.3.

The MX representation, Eq. A.9 of the intra–chromophore vibrational Hamiltonian introduces a mixing of all local vibrations as it would be also the case if one changes from a diabatic representation of a molecular Hamiltonian to the adiabatic representation. Here such an electronically induced vibrational mode mixing is originated by the inter–molecular Coulomb forces (leading to the MX states). It results in a new arrangement of local modes as demonstrated in Appendix A.3.

2.5.2 Relaxation Matrix of Exciton-Exciton Annihilation

The contribution from the nonadiabatic coupling is handled in the same manner as demonstrated in Section 2.4.3. Starting from an expression similar to Eq. 2.26 a trace, now, defined with respect to all intra-chromophore vibrational DOF is introduced (cf. Eq. A.40). The rate of EEA is obtained from the non–factorized part of the complete relaxation matrix. Again here and in the following the index ”mx-intra” is removed at frequencies, coupling constants, etc., and one obtains

$$
\begin{aligned}
k^{(\text{EEA})}(\alpha_N \;\to\; \beta_{N-1}) = \frac{2}{\hbar^2}\,\text{Re}\int\limits_0^\infty dt\; e^{i\Omega(\alpha_N,\beta_{N-1})t} \qquad (2.30)\\
tr_{\text{intra}}\{\hat{R}(\alpha_N)U^{+}(\alpha_N,t)\Theta(\alpha_N\beta_{N-1})U(\beta_{N-1},t)\Theta(\beta_{N-1}\alpha_N)\}\;.
\end{aligned}
$$

Since transitions from a lower to a higher exciton manifold are thermally excluded, the respective rates will not be shown.

The trace in Eq. 2.30 represents the correlation function formulated with the MX–representation of the nonadiabatic coupling operator Θ and has to be taken with respect to the intra–molecular vibrational DOF of the CC (for transition frequencies $\Omega(\alpha_N, \beta_{N-1})$, see Eq.2.22). It incorporates the equilibrium statistical operator $\hat{R}(\alpha_N)$ of the intra–molecular vibrations in the MX state $|\alpha_N\rangle$. And, vibrational time–evolution operators U^+ and U referring to the initial and the final MX state appear. These operators read (cf. Eq. A.9, and note $N > 0$)

$$U^+(\alpha_N, t) \quad = \quad \exp\{\frac{i}{\hbar}(H_{\text{vib}}^{(\text{intra})}(\alpha_N, \alpha_N)t\} \ . \tag{2.31}$$

If an approximation is made where the dependence of the $\Theta(\alpha_N \beta_{N-1})$ on the vibrational DOF is neglected, it becomes useful to introduce an notation similar to that in Eq.2.28. Therefore, Eq. 2.30 is split into the square of the nonadiabatic coupling matrix element and the combined DOS,

$$k^{(\text{EEA})}(\alpha_N \to \beta_{N-1}) \quad = \quad \frac{2\pi}{\hbar}|\Theta(\alpha_N \beta_{N-1})|^2 \mathcal{D}(\alpha_N, \beta_{N-1}; \Omega(\alpha_N, \beta_{N-1})) . \tag{2.32}$$

The DOS reads

$$\mathcal{D}(\alpha_N, \beta_{N-1}; \omega) \quad = \quad \frac{1}{2\pi\hbar} \int dt\ e^{i\omega t} tr_{\text{intra}}\{\hat{R}(\alpha_N) U^+(\alpha_N, t) U(\beta_{N-1}, t)\} \tag{2.33}$$

The time–integration from$-\infty$ to ∞ is simply derived by taking the real part of Eq. 2.30. It is obvious that $k^{(\text{EEA})}$, Eq.2.32 resembles the internal conversion rate $k_m^{(\text{IC})}$ introduced in Eq. 2.28. The difference here is that the initial state φ_{mf} and the final state φ_{me} defining $k_m^{(\text{IC})}$ have been replaced by the MX states $|\alpha_N\rangle$ and $|\beta_{N-1}\rangle$, respectively.

2.5.3 Discussion of the Mean Field Part

Beside $k^{(\text{EEA})}$ the complete nonadiabatic relaxation matrix includes the factorized part into which the quantities

$$\hbar < v_{\alpha_M \beta_N}^{(\text{na})} > \quad = \quad (\delta_{M+1,N} + \delta_{M-1,N}) \Theta(\alpha_M \beta_N) S(\alpha_M \beta_N) \ , \tag{2.34}$$

with

$$S(\alpha_M \beta_N) \quad = \quad \sum_{\bar{\mu}} f(\bar{\mu}) \langle \bar{\chi}_{\alpha_M, \bar{\mu}} | \bar{\chi}_{\beta_N, \bar{\mu}} \rangle \tag{2.35}$$

enter. Note that the quantity $S(\alpha_M\beta_N)$ also appears in the definition of the MX density matrix (Eq. 2.19, cf. Appendix A.4). As a pure coupling term in the reversible part of the density matrix equations it relates two different exciton manifolds which are extremely off–resonant. Therefore this term can be neglected.

It remains to discuss how to handle the factorized part of the relaxation matrix. A general way of treating such contributions is given in Ref. [MM01a]. It is based on the introduction of an auxiliary density matrix which partly replaces the factorized part of Γ and obeys an equation of motion free of any dissipative contribution but with the mean–field term. Since it gives off–resonance contribution all those terms will be neglected including the expression in Eq. 2.34.

2.5.4 The Two-Exciton Annihilation Rate

This section is devoted to a detailed analysis of the EEA rate, Eq. 2.30 if specified to the transition from the two to the single-exciton manifold. Since the concrete expression is of basic importance for the numerical calculations given in Chapter 5 the existence of a rate formula similar to Eq. 2.32 is demonstrated in detail but with a DOS valid for single chromophores. Such an expression can be obtained if the combined DOS is calculated for the limiting case of vanishing electronic inter–chromophore coupling (neglect of $V^{(N)}_{\text{el-el}}$ in Eq. 2.4). A rate expression which is improved by incorporating MX effects into combined DOS is derived in Appendix A.6.

The approximation including the single chromophore DOS is achieved discussing the trace expression in Eq. 2.30 (note the specification to a transition from a two to a single-exciton state),

$$k^{(\text{EEA})}(\alpha_2 \;\to\; \beta_1) = \frac{2}{\hbar^2}\,\text{Re}\int\limits_0^\infty dt\; e^{i\Omega(\alpha_2,\beta_1)t} \qquad (2.36)$$
$$tr_{\text{intra}}\{\hat{R}(\alpha_2)U^+(\alpha_2,t)\Theta(\alpha_2\beta_1)U(\beta_1,t)\Theta(\beta_1\alpha_N)\}\;.$$

Once the MX states $|\beta_1\rangle$ and $|\alpha_2\rangle$ are expanded according to Eq. 2.10 the required approximation follows in taking the remaining trace in the zeroth order with respect to inter–chromophore electronic coupling $V^{(N)}_{\text{el-el}}$.

Since the time evolution operators and $\tilde{R}$ are only defined by the diagonal (intramolecular) part, Eq. A.9, of the complete MX vibrational coupling, Eq. 2.12, the correct time evolution operators in the absence of inter–chromophore electronic coupling are not automatically gained. However, a detailed inspection of this limit shows (see Appendix A.3.1) that the product of $\exp(i\Omega(\alpha_2)t)$ with $U^+(\alpha_2,t)$ as well as the product of $\exp(-i\Omega(\beta_1)t)$ with $U(\beta_1,t)$ can be identified by respective time evolution operators U_0 for the whole CC but with electronically decoupled chromophores (first contribution to H_{CC}, Eq. 2.4). Therefore, one can write the trace expression in Eq. 2.36 as (note the expansion of the MX states as well as the nonadiabatic coupling Hamiltonian H_{na})

$$\begin{aligned}
& \text{tr}_{\text{intra}}\{\hat{R}(\alpha_2)U^+(\alpha_2,t)\Theta(\alpha_2\beta_1)U(\beta_1,t)\Theta(\beta_1\alpha_2)\} \\
\approx\ & e^{-i\Omega(\alpha_2,\beta_1)t}\text{tr}_{\text{intra}}\{\langle\alpha_2|\hat{R}_0 U_0^+ H_{\text{na}}|\beta_1\rangle\langle\beta_1|U_0(t)H_{\text{na}}|\alpha_1\rangle\} \\
=\ & e^{-i\Omega(\alpha_2,\beta_1)t}\sum_{m,\bar{m}}\sum_{n,\bar{n}} C^*_{\alpha_2}(mf)C_{\beta_1}(ne)C_{\beta_1}(\bar{n}e)C_{\alpha_2}(\bar{m}f) \\
& \times\sum_{k,l}\Theta_{kfe}\Theta_{lfe}\text{tr}_{\text{intra}}\{\langle mf|\hat{R}_0 U_0^+(t)|\varphi_{kf}\rangle\langle\varphi_{ke}|ne\rangle \\
& \times\langle\bar{n}e|U_0(t)|\varphi_{le}\rangle\langle\varphi_{lf}|\bar{m}f\rangle\}\,. \qquad (2.37)
\end{aligned}$$

To get this expression it has been already taken into account that the part of the two-exciton state expansion which contains the presence of two singly excited chromophores does not contribute. Instead, it remains $\langle mf|$ at the left part of the trace, Eq. 2.37 as well as $|\bar{m}f\rangle$ at the right part. Further it is noted $|\varphi_{kf}\rangle\langle\varphi_{ke}|ne\rangle = \delta_{k,n}|kf\rangle$, as well as $|\varphi_{le}\rangle\langle\varphi_{lf}|\bar{m}f\rangle = \delta_{l,\bar{m}}|le\rangle$ and the whole EEA rate, Eq. 2.30 is written as

$$\begin{aligned}
k^{(\text{EEA})}(\alpha_2 \quad\rightarrow\quad & \beta_1) \\
& \approx \frac{2}{\hbar^2}\,\text{Re}\,\sum_{m,\bar{m}}\sum_{n,\bar{n}} C^*_{\alpha_2}(mf)C_{\beta_!}(ne)C_{\beta_1}(\bar{n}e)C_{\alpha_2}(\bar{m}f)\Theta_{nfe}\Theta_{\bar{m}fe} \\
& \times\int_0^\infty dt\,\text{tr}_{\text{intra}}\{\langle mf|\hat{R}_0 U_0^+(t)|nf\rangle\langle\bar{n}e|U_0(t)|\bar{m}e\rangle\}\,. \qquad (2.38)
\end{aligned}$$

This expression further simplifies since only the diagonal electronic matrix elements contribute ($m = n$ and $\bar{n} = \bar{m}$). One obtains $\langle mf|\hat{R}_0 U_0^+(t)|mf\rangle = e^{i\omega_{mf}t}\hat{R}_{mf}U^+_{mf}(t)\prod_{k\neq m}\hat{R}_{kg}U^+_{kg}(t)$ and $\langle\bar{m}e|U_0(t)|\bar{m}e\rangle = e^{-i\omega_{\bar{m}e}t}U_{\bar{m}e}(t)\prod_{k\neq\bar{m}}U_{kg}(t)$. The respective single-chromophore energies $\hbar\omega_{ma}$, equilibrium statistical operators $\hat{R}_{ma}$, and time evolution operators U_{ma} have been introduced in Eq. 2.29 and in Appendix A.3.1.

Both foregoing formulas give the whole trace (note the replacement of $\bar{m}$ by n),

$$\begin{aligned}
& \text{tr}_{\text{intra}}\{\langle mf|\hat{R}_0 U_0^+(t)|nf\rangle\langle\bar{n}e|U_0(t)|\bar{m}e\rangle\} \qquad (2.39) \\
=\ & \delta_{m,n}e^{i\omega_{mfe}t}tr_m\{\hat{R}_{mf}U^+_{mf}(t)U_{me}(t)\} \\
& +(1-\delta_{m,n})e^{i\omega_{mfg}t}tr_m\{\hat{R}_{mf}U^+_{mf}U_{mg}\}e^{-i\omega_{neg}t}tr_n\{\hat{R}_{ng}U^+_{ng}(t)U_{ne}(t)\}.
\end{aligned}$$

The newly introduced trace expressions $tr_m\{\ldots\}$ only refer to those vibrational DOF which belong to chromophore m. They lead to the type of correlation function which are typical for nonadiabatic transitions and which determine, for example, the IC-rate Eq. 2.28. And indeed the term of Eq. 2.39 proportional to $\delta_{m,n}$ just corresponds to an IC-process at chromophore m from state φ_f to state φ_e. In the second term of Eq. 2.39 a transition from φ_f to φ_g(at chromophore m) is combined with a transition from φ_g to φ_e(at chromophore n). If expression Eq. 2.39 is inserted into the rate expression Eq. 2.38 the term proportional to $\delta_{m,n}$ can be expressed by the DOS of the type of Eq. 2.29 $D_{mfe}(\omega_{mfe})$(now additionally labeled by the site index m). In contrast, the second term can be written as a frequency integral with respect to $D_{mfg}(\omega_{mfg})$ and $D_{nge}(\omega_{nge})$. Accordingly, the whole EEA rate reads

$$\begin{aligned} k^{(\mathrm{EEA})}(\alpha_2 \to \beta_1) \;&\approx\; \frac{2\pi}{\hbar}\sum_{m,n} C^*_{\alpha_2}(mf)C_{\beta_1}(me)C_{\beta_1}(ne)C_{\alpha_2}(nf)\Theta_{mfe}\Theta_{nef} \\ &\times\Big(\delta_{m,n}D_{mfe}(\omega_{mf,me}) + (1-\delta_{m.n}) \\ &\times\int d\hbar\omega D_{mfg}(\omega_{mfg}-\omega)D_{nge}(\omega-\omega_{neg})\Big)\,. \end{aligned} \tag{2.40}$$

It would be an acceptable approximation to assume that the vibrational structure of all chromophores is identical. Therefore, the intra-chromophore nonadiabatic coupling as well as single chromophore combined DOS become independent of the site indices.

To achieve an quantitative estimate for the rate an additionally restriction to the high-temperature case is made and one replaces all DOS $D_{mab}(\omega_{mab})$ by

$$D(\omega_{ab};\lambda_{ab}) \;=\; \sqrt{\frac{\pi}{\hbar^2 k_B T\lambda_{ab}}}exp\left\{-\frac{(\hbar\omega_{ab}-\lambda_{ab})^2}{4\lambda_{ab}k_BT}\right\} \tag{2.41}$$

These quantities are only characterized (beside temperature) by the transition frequency ω_{ab} and the reorganization energy λ_{ab}. The expression, Eq. 2.41 simply allows to carry out the frequency integral in the second part of Eq.2.40 which leads to $D(\omega_{fg};\lambda_{fg}+\lambda_{ge})$. This DOS has to be distinguished from the DOS $D(\omega_{fg};\lambda_{fe})$ entering the first term in Eq.2.40.

The first term will become maximal if $\hbar\omega_{fe}=\lambda_{fe}$ (activation-less case). If at the same time $\lambda_{fg}+\lambda_{ge}$ is much smaller or much larger than λ_{fe}, the second part of the rate expression 2.40 remains small and the whole expression is dominated by the first term (Fig.2.4 a) It results in

$$k^{(\mathrm{EEA})}(\alpha_2 \to \beta_1) \;\approx\; \sum_m |C_{\alpha_2}(mf)C_{\beta_1}(me)|^2 k^{(\mathrm{IC})}_{f\to e} \tag{2.42}$$

with the (single chromophore) internal conversion rate $k^{(IC)}_{f\to e}$ introduced in Eq. 2.28. The complete EEA rate has been obtained by the uniform single chromophore internal conversion rate times the overlap (with respect to all sites)

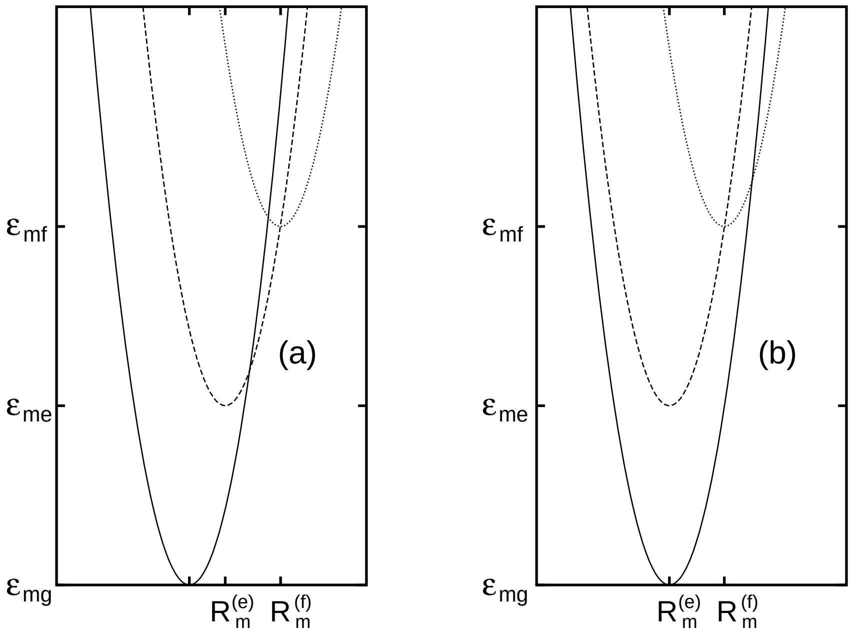

Figure 2.4: The two different limiting cases for the respective positions of the chromophore PES. Part (a) is related to Eq. 2.42, part (b) to Eq. 2.43.

between the probability $|C_{\alpha_2}(mf)|^2$ to have a double excitation at site m and the probability $|C_{\beta_1}(me)|^2$ to have a single excitation at site m.

The obtained formula is ready for an application in the MX density matrix theory since it correctly describes the transition from a two-exciton to a single-exciton state. The use of single chromophore IC-rates, of course, may be improved if one includes MX effects. (Some details how to include MX effects into the combined DOS are given in Appendix A.6.) The EEA rate of Eq. 2.42 can be reduced to the rate for a transition from the doubly excited state $|me, ne\rangle$ to the singly excited state $|me\rangle$ if $|C_{\alpha_2}(mf)C_{\beta_1}(me)|^2$ is expanded up to the second order in the inter–chromophore electronic coupling. Then it describes the fusion process of two local single excitations to the doubly excited state (S_n-state) at a single chromophore.

Another limiting case for the EEA rate Eq. 2.40 is found if $\lambda_{fe} = \lambda_{fg} + \lambda_{ge}$(Fig.2.4 b) . Now the first and the second type of the DOS in the EEA rate become equal and the whole rate reads

$$k^{(\mathrm{EEA})}(\alpha_2 \to \beta_1) \approx \left| \sum_m C_{\alpha_2}(mf) C_{\beta_1}(me) \right|^2 k^{(\mathrm{IC})}_{f \to e} . \tag{2.43}$$

In contrast to Eq. 2.42, the rate after Eq. 2.43 results from the combination of two different IC processes at two different chromophores. Since such transition processes enter which couple different sites via the transition from state φ_f to φ_g at site m with the transition from φ_g to φ_e at site n the EEA rate incorporates the square of an expansion coefficient overlap. It is given by the overlap between the probability amplitude $C^*_{\alpha_2}(mf)$ to have a double excitation at site m and the probability amplitude $C_{\beta_1}(me)$ to have a single excitation at the same site m.

The relation among the different reorganization energies necessary to get $k^{(\text{EEA})}(\alpha_2 \to \beta_1)$ from Eq. 2.43 might be fulfilled if either $\lambda_{fg} = 0$ or $\lambda_{ge} = 0$. Discussing this in terms of PES, either U_f and U_g, or U_g and U_e should be not shifted horizontal to another.

Adopting this simple picture of the PES for e.g. BChl, it is noted first that the transfer time between U_f and U_e is of the order of 100 fs, i.e. nearly activationless ($\hbar\omega_{fe} \approx \lambda_{fe}$). When further a lifetime of the first excited state of ~ 1 ns is taken into account, the PES of the ground-state U_g and the first excited state U_e are also considerably shifted towards each other and the case leading to Eq. 2.42 applies. Therefore, Eq. 2.42 will be used for the study of EEA in the B850 ring of LH2 in Chapter 5.

2.6 Summary

The multi-exciton description of chromophore complexes and biological antenna systems has been supplemented by the inclusion of exciton-exciton annihilation processes. This became possible by allowing for nonadiabatic transitions from a higher intra–chromophore level to the first excited electronic level. If translated into the multi-exciton picture exciton-exciton annihilation proceeds as the following two–step process. First there appears the exciton fusion where the single excitations of two different chromophores are transformed into a higher excitation of one chromophore. This is a process which introduces an internal rearrangement of the concrete N–exciton wavefunction but takes place without changing the actual exciton manifold. Afterwards the internal conversion process moves the higher excited chromophore back to its first excited state. This corresponds to a radiationless transition from the N–exciton to the $(N-1)$–exciton manifold.

To incorporate exciton exciton annihilation into the multi-exciton density matrix theory an approach has been chosen which was used earlier for the description of electron transfer reactions [KMS94]. If the internal conversion is considered as a process which proceeds instantaneously on the time–scale on which all other multi-exciton processes take place, the radiationless transitions can be described by respective rate expressions. These expressions resemble the standard form of internal conversion rates but carry certain informations on the presence of multi-exciton states. A prerequisite has been the correct derivation of a coupling between the multi-exciton states and the intra–chromophore vibrations which act as accepting modes within the internal conversion process.

A detailed analysis has been given for the exciton-exciton annihilation rate entering the multi-exciton density matrix equations. The actual form of the annihilation rate depends on the chromophore PES. Providing a uniform internal conversion rate for all chromophores in the complex two limiting cases for the annihilation rate based on transitions from the two– to the single–exciton manifold have been presented.

Using such types of expressions the whole theory is ready for an application to concrete systems. In Chapter 5 the theory as described here is applied to simulate intensity dependent transient absorption spectra taken at the B850 ring of the LH2 complex of *Rb. sphaeroides* [THP$^+$01]. It is also used in Chapter 7 where the exciton control in the presence of EEA is discussed for the FMO complex. However in Chapter 6 and the most part of Chapter 7 only the one-exciton version could be used due to computational restrictions.

Chapter 3

Simulation of Optical Properties

3.1 Introduction

In this chapter the calculation of linear and nonlinear spectra is presented, using the general theoretical approach given in Chapter 2. The well known expressions for linear absorption, which will be given at the end of this Chapter, can be found e.g. in Refs [MK00a, vAVvG00, SBRM02] and for linear and circular dichroism in Ref. [vAVvG00].

It has been explained at different places how to compute femtosecond transient absorption (see, for example [Muk95, NvG02, LAI$^+$91, SM95, KS96, MCM97, KS97, BK99, DMC$^+$00]). But as shortly discussed in Chapter 2 the description has to go beyond any theory based on a third–order expansion in the field–strength. Since a fifth-order description seemed to be rather demanding with respect to the computations, a different approach that avoids perturbation theory for the action of the pump–field [SSD95, WSSD97] has been chosen. For the probe field perturbative and nonperturbative expressions are given.

Where appropriate and computationally possible an averaging over spatial configurations as well as spectral inhomogeneity has been carried out. The former is introduced by rotating each molecule with respect to the polarized pump pulse using the three Euler's angles with random values [Muk95]. The latter has been taken into account by adding Gaussian distributed disorder to the chromophore energies (diagonal disorder).

The starting point will be the discussion of transient absorption spectra in the following Section. The linearization with respect to the probe field will be gained in Section 3.3, the time resolved Fluorescence is given in Section 3.4. Later the linear spectra are given as a special case of the transient absorption with vanishing pump field (Section 3.5).

3.2 Transient Absorption

When discussing a pump probe experiment the applied field contains a pump as well as a probe part (abbreviated in the following by "pu" and "pr", respectively) and reads

$$\begin{aligned} \mathbf{E}(\mathbf{r},t) &= \sum_{p=\mathrm{pu,pr}} \mathbf{e}_p E_p(t) e^{i(\mathbf{k}_p\mathbf{r}-\omega_p t)} + \mathrm{c.c.} \\ &= \sum_{p=\mathrm{pu,pr}} \mathbf{e}_p \tilde{E}_p(t) e^{i\mathbf{k}_p\mathbf{r}} + \mathrm{c.c.}\,. \end{aligned} \tag{3.1}$$

The unity vectors of the field polarization are denoted by $\mathbf{e}_p$, $E_p(t)$ are the field amplitudes, and the wave-vectors and frequencies are given by $\mathbf{k}_p$ and ω_p , respectively. The electric fields $\tilde{E}(t)$ also include the time dependence due to the carrier wave. In the general case the induced polarization may cover any mixture of these partial waves

$$\begin{aligned} \mathbf{P}(\mathbf{r},t) &= \sum_{m,n} \mathbf{e}_{m,n} P_{m,n}(t) e^{i((m\mathbf{k}_{\mathrm{pu}}+n\mathbf{k}_{\mathrm{pr}})\mathbf{r}-(m\omega_{\mathrm{pu}}+n\omega_{\mathrm{pr}})t)} + c.c. \\ &= \sum_{m,n} \mathbf{e}_{m,n} \tilde{P}_{m,n}(t) e^{i(m\mathbf{k}_{\mathrm{pu}}\mathbf{r}+n\mathbf{k}_{\mathrm{pr}}\mathbf{r})} + c.c.\ , \end{aligned} \tag{3.2}$$

Here, m and n determine the spatial direction into which the polarization $\tilde{P}_{m,n}(t)$ is emitted, and $\mathbf{e}_{m,n}$ denote the polarization unity vectors. Again, $\tilde{P}_{m,n}(t)$ includes all time dependencies.

To get the probe pulse absorption one has to determine the probe pulse induced polarization $\tilde{P}_{\mathrm{pr}}(t,\mathbf{E}_{\mathrm{pu}}) = \tilde{P}_{0,1}(t)$ which is given by the part of the complete polarization $\mathbf{P}(\mathbf{r},t)$ propagating into the direction $\mathbf{k}_{\mathrm{pr}}$. Once this has been done the frequency dispersed absorption signal $A_{\mathrm{pr}}(\omega)$ can be deduced from the Fourier transform of $\tilde{P}_{\mathrm{pr}}(t,\mathbf{E}_{\mathrm{pu}})$ and $\tilde{E}_{\mathrm{pr}}(t)$ according to

$$A_{\mathrm{pr}}(\omega,\mathbf{E}_{\mathrm{pu}}) = \frac{4\pi\omega}{c}\mathrm{Im}\frac{\tilde{P}_{\mathrm{pr}}(\omega,\mathbf{E}_{\mathrm{pu}})}{\tilde{E}_{\mathrm{pr}}(\omega)}\ . \tag{3.3}$$

In defining A_{pr} the dependence on the pump field is indicated. The differential absorption signal simply follows as

$$\Delta A_{\mathrm{pr}}(\omega,\mathbf{E}_{\mathrm{pu}}) = A_{\mathrm{pr}}(\omega,\mathbf{E}_{\mathrm{pu}}) - A_{\mathrm{pr}}(\omega,\mathbf{E}_{\mathrm{pu}}=0)\,. \tag{3.4}$$

Different treatments exist to select the contribution P_{pr} from the overall polarization. If the medium response is described in the framework of a third–order response function a direct selection becomes possible [Muk95]. However, this standard treatment cannot be used in the present case since it does not incorporate EEA. To include the necessary two–exciton populations at least a fifth–order response function theory would become necessary. In such a case it sees more appropriate to calculate the polarization directly without any perturbation expansion with respect to the applied pump and probe pulses. Therefore, one has to start from the following expression for the total polarization

$$\mathbf{P}(\mathbf{r},t) \;=\; \frac{1}{\Delta V(\mathbf{r})}\sum_{CC\in\Delta V(\mathbf{r})} \mathrm{tr}_{\mathrm{mx}}\{\hat{\mu}_{CC}\hat{\rho}(t)\}\ . \tag{3.5}$$

The formula describes a spatial averaging of the polarization contributions of all CC contained in the volume $\Delta V(\mathbf{r})$ around the spatial point $\mathbf{r}$ where the (macroscopic) polarization should be determined. The single CC polarization follows from the MX trace expression defined via the CC dipole operator and the MX density matrix. Therefore, the polarization and in particular $\mathbf{P}_{\mathrm{pr}}$ can be determined via a direct computation of the MX density matrix accounting for both field contributions directly in the respective equations of motion Eq. 2.21.

The selection of $\tilde{P}_{\mathrm{pr}}$ from Eq. 3.5 follows [WSSD97, SSD95]. The dependence of the polarization on the pump and probe pulse propagation direction in Eq. 3.2 is transformed to a phase factor $\phi_p = \mathbf{k}_p\mathbf{r}$. Note that this description suggests that the same field is applied to all CC in the probe volume.

$$\mathbf{P}(\phi_{\mathrm{pu}},\phi_{\mathrm{pr}},t) \;=\; \sum_{m,n}\tilde{\mathbf{P}}_{m,n}(t)e^{i(m\phi_{\mathrm{pu}}+n\phi_{\mathrm{pr}})} + c.c.\ . \tag{3.6}$$

In Ref. [SSD95] it has been shown, that concentrating on resonant transitions and with the restriction to the one-exciton manifold and the ground state only phases with $j(\phi_{\mathrm{pr}}-\phi_{\mathrm{pu}})$ $+\phi_{\mathrm{pr}}$ exist, with $-(l+1)\leq j \leq l$ for $(2l+1)$th order. This results in $m=-j$ and $n=j+1$. A close inspection shows, that the result is also valid if the two-exciton manifold is included. Setting $\phi_{\mathrm{pr}}=0$ one gains for the third order polarization

$$\begin{aligned}\mathbf{P}(\phi_{\mathrm{pu}},t) \;=\;& \tilde{\mathbf{P}}_{1,0}(t)e^{i\phi_{\mathrm{pu}}} + \tilde{\mathbf{P}}_{0,1}(t)\\ &+\tilde{\mathbf{P}}_{-1,2}(t)e^{-i\phi_{\mathrm{pu}}} + \tilde{\mathbf{P}}_{2,-1}(t)e^{2i\phi_{\mathrm{pu}}} + c.c.\ .\end{aligned} \tag{3.7}$$

For the fifth order polarization, additional processes become possible

$$\begin{aligned}\mathbf{P}(\phi_{\mathrm{pu}},t) \;=\;& \tilde{\mathbf{P}}_{1,0}(t)e^{i\phi_{\mathrm{pu}}} + \tilde{\mathbf{P}}_{0,1}(t)\\ &+\tilde{\mathbf{P}}_{-1,2}(t)e^{-i\phi_{\mathrm{pu}}} + \tilde{\mathbf{P}}_{2,-1}(t)e^{2i\phi_{\mathrm{pu}}}\\ &+\tilde{\mathbf{P}}_{-2,3}(t)e^{-2i\phi_{\mathrm{pu}}} + \tilde{\mathbf{P}}_{3,-2}(t)e^{3i\phi_{\mathrm{pu}}} + c.c.\ .\end{aligned} \tag{3.8}$$

Now the density matrix is propagated for different relative phases $\phi_{\rm pu}$ of the pump and probe pulse. Note that the above equations also hold for the Fourier-transformed polarizations. If the combination

$$\tilde{\mathbf{P}}_{\rm pr}(\omega, \mathbf{E}_{\rm pu}) = \mathbf{e}_{\rm pr}\tilde{P}_{\rm pr}(\omega, \mathbf{E}_{\rm pu}) = \frac{1}{4}\sum_{l=0}^{3}\mathbf{P}(\frac{\pi}{2}l, \omega) \tag{3.9}$$

is chosen the polarization in the direction of the probe field $\mathbf{k}_{\rm pr}$ is obtained in both cases. Of course to meet the requirements of a pump–probe experiment a sufficient weak probe field compared to the pump field has to be used. Higher order contributions of the polarization are at least third order in the probe-field and can be neglected when a weak probe field is provided. It results that Eq. 3.9 holds even for arbitrary order in the pump field.

If $\Delta A_{\rm pr}$ should be determined in dependence on the delay time $\tau_{\rm del}$ between the pump and the probe pulse, for each delay time four propagations of the whole density matrix equations (at least during the action of the probe pulse) are necessary. This becomes computational very expensive if static disorder has to be accounted for. Since a direct disorder averaging requires the consideration of many different representatives of the disordered ensemble of CC one applies an approach where only a single density matrix propagation per ensemble representative becomes necessary, and will be given in the next section. Unfortunately, it is only valid for such a delay between the pump and the probe pulse where any direct pulse overlapping is already absent.

3.3 Weak Probe Field

A single density matrix propagations to determine $\Delta A_{\rm pr}$ in dependence on $\tau_{\rm del}$ becomes sufficient if $\tilde{P}_{\rm pr}$ in Eq. 3.3 is linearized with respect to the weak probe field, i.e. if $\Delta A_{\rm pr}$ becomes independent on the probe field. This treatment is somewhat standard (see, for example [RMK01, SM95]), but here the approach of [SM95] is generalized to an inclusion of MX energy dissipation and dephasing as well as to the inclusion of a finite pump–pulse duration.

The general expression for $\Delta A_{\rm pr}$ derived in Appendix D is valid for all exciton manifolds and includes diagonal as well as off–diagonal MX density matrix elements. It has been achieved by propagating the density matrix in the presence of the pump pulse and then using a first order perturbation approach with respect to a δ-like probe field using the assumption of non-overlapping pulses. For the concrete computations discussed in the following it suffices to confine to the two–exciton manifold. Furthermore, to remain sufficient simple one concentrates on the part $A_{\rm pr}^{\rm (pop)}$ of the whole expression which exclusively is determined by MX–level populations. The expression determined by off–diagonal MX density matrix elements can be found in Appendix D. One gets

$$
\begin{aligned}
&A_{\mathrm{pr}}(\omega,\tau_{\mathrm{del}}) = \frac{4\pi\omega n_{\mathrm{CC}}}{\hbar c} \\
&\Big(\sum_{\beta_1} \mid d(0,\beta_1) \mid^2 G(\beta_1,0;\omega)(P(0;\tau_{\mathrm{del}},\mathbf{E}_{\mathrm{pu}}) - P(\beta_1;\tau_{\mathrm{del}},\mathbf{E}_{\mathrm{pu}})) \\
&-\sum_{\alpha_1,\beta_2} \mid d(\alpha_1,\beta_2) \mid^2 G(\beta_2,\alpha_1;\omega)(P(\alpha_1;\tau_{\mathrm{del}},\mathbf{E}_{\mathrm{pu}}) - P(\beta_2;\tau_{\mathrm{del}},\mathbf{E}_{\mathrm{pu}}) \\
&-\sum_{\alpha_2,\beta_3} \mid d(\alpha_2,\beta_3) \mid^2 G(\beta_3,\alpha_2;\omega)P(\alpha_2;\tau_{\mathrm{del}},\mathbf{E}_{\mathrm{pu}})\Big)\,. \qquad (3.10)
\end{aligned}
$$

The expression for the absorption consists of the various transition dipole moments $d(\alpha_N,\beta_{N+1})$, the Fourier-transformed $G(\beta_{N+1},\alpha_N)$ of the time evolution operator without interaction with the field and the respective MX-state populations $P(\alpha_N;\tau_{\mathrm{del}},\mathbf{E}_{\mathrm{pu}})$, which have been gained by propagating the whole density matrix under the influence of the pump pulse until τ_{del}. The density of the chromophore complexes in the probe volume is denoted by n_{CC}, and the labeling "pop" has been removed. The dipole matrix elements follow from those introduced in Appendix A.2 but multiplied with the polarization unity vector of the probe–pulse field

$$
d(\alpha_N,\beta_{N-1}) = \mathbf{d}(\boldsymbol{\alpha}_{\mathbf{N}},\boldsymbol{\beta}_{\mathbf{N-1}})\mathbf{e}_{\mathrm{pr}}\,. \qquad (3.11)
$$

The various G–functions, i.e. the Fourier-transformed of the field-free time evolution operators

$$
\begin{aligned}
&G(\alpha_M,\beta_N;\omega) \\
&= \mathrm{Im}\,\frac{1}{\omega - \Omega(\alpha_M,\beta_N) - \Gamma(\alpha_M) - \Gamma(\beta_N) - \tilde{\Gamma}(\alpha_M,\beta_N)} \\
&= \frac{\Gamma(\alpha_M) + \Gamma(\beta_N) + \tilde{\Gamma}(\alpha_M,\beta_N)}{(\omega - \Omega(\alpha_M,\beta_N))^2 + (\Gamma(\alpha_M) + \Gamma(\beta_N) - \tilde{\Gamma}(\alpha_M,\beta_N))^2} \qquad (3.12)
\end{aligned}
$$

determine the Lorentzian line shape of the different inter–manifold transitions (cf. Eq. 3.12). It is centered at the transition frequency between the both states, $\Omega(\alpha_M,\beta_N)$, and the broadening is determined by the various dephasing rates Γ after Eqs. 2.24 and B.20.

Now the different terms of Eq. 3.10 are discussed. The first term on the right–hand side of Eq. 3.10 covers the ground–state bleaching contribution ($\sim P(0;\tau_{\mathrm{del}},\mathbf{E}_{\mathrm{pu}})$) and the stimulated emission part $\sim P(\beta_1;\tau_{\mathrm{del}},\mathbf{E}_{\mathrm{pu}})$, whereas excited–state absorption (from the single–exciton states) is given by the part $\sim P(\alpha_1;\tau_{\mathrm{del}},\mathbf{E}_{\mathrm{pu}})$ of the second term. It also contains stimulated emission via transitions from two–exciton states to single–exciton states ($\sim P(\beta_2;\tau_{\mathrm{del}},\mathbf{E}_{\mathrm{pu}})$). Excited state absorption from the two–exciton to the three–exciton states is given by the last term. However, since $P(\beta_3;\tau_{\mathrm{del}},\mathbf{E}_{\mathrm{pu}}) = 0$ is provided this last term does not contain a three–exciton population. Unfortunately, it cannot precisely answered if one is really working in such a pump–intensity regime where $P(\beta_3; \tau_{\rm del}, \mathbf{E}_{\rm pu})$ remains small.

The standard linear absorption into the single–exciton manifold follows if the second and third summation are removed and if in the first one the population difference $P(0; \tau_{\rm del}, E_{\rm pu}) - P(\beta_1; \tau_{\rm del}, E_{\rm pu})$ is replaced by 1, i.e. the ground–state equilibrium distribution (cf. Section 3.5). Therefore, the differential absorption $\Delta A_{\rm pr}$ (Eq. 3.4) can be deduced from $A_{\rm pr}$ by replacing $P(0; \tau_{\rm del}, E_{\rm pu})$ by $P(0; \tau_{\rm del}, E_{\rm pu}) - 1$. Eq. 3.10 is a well known formula for calculating transient absorption spectra [LAI+91, SM95, KS96, BK99] and will be compared in Chapter 5 with a description where both pulses are considered non–perturbatively.

For further use in the following section the asymptotic form of $\Delta A_{\rm pr}$ is given, i. e. for $\tau_{\rm del} \to \infty$ (of course in the present context this means that $\tau_{\rm del}$ enters the range of some picoseconds). The asymptotic form reads

$$\begin{aligned} \Delta A_{\rm pr}(\omega, \infty) \;=\; & \frac{4\pi\omega n_{\rm CC}}{\hbar c} \Big(P(0; \infty, E_{\rm pu}) - 1 \Big) \\ & \times \sum_{\alpha_1} \Big(\mid d(\alpha_1, 0) \mid^2 G(\alpha_1, 0; \omega)(1 + f(E(\alpha_1)) \\ & - \sum_{\beta_2} \mid d(\beta_2, \alpha_1) \mid^2 G(\beta_2, \alpha_1; \omega) f(E(\alpha_1)) \Big) \,. \end{aligned} \tag{3.13}$$

The expression provides that for $\tau_{\rm del} \to \infty$ any population of the two–exciton levels has been disappeared according to EEA. However, a thermal distribution $f(E(\alpha_1))$ among the single–exciton states could be formed since any recombination from the single–exciton levels to the ground–state can be neglected at the considered time–scale. Note that $f(E)$ is normalized to 1 and that $1 - P(0) = \sum_{\alpha_1} P(\alpha_1)$. Both relations allow a complete expression of $\Delta A_{\rm pr}(\omega, \infty)$ by the pump–field dependent ground–state population $P(0)$.

3.4 Fluorescence

To compare the simulations of laser driven dynamics with experimental data, the time and spectrally resolved fluorescence will be calculated in Chapter 6. The usual approach is to make an expansion including the second order of the pump field and the quantized probe field [Muk95]. Again, another approach has been chosen. Following the calculation of the transient absorption in the last Section, the complete dynamics of the system including the pump pulse is calculated. An expansion with respect to the quantized fluorescence field with $d(\alpha_N, \beta_{N-1}) = \mathbf{e}_F \mathbf{d}(\alpha_N, \beta_{N-1})$, and written for excitations up to the two-exciton manifold, gives (see, e.g. [Muk95, LAI+91])

$$\begin{aligned} F(\omega,t) &= -\frac{\omega^3 n_{\mathrm{CC}}}{\pi\hbar c^3}\Big(\sum_{\beta_1}|d(\beta_1,0)|^2 G(\alpha_1,0;\omega)P(\alpha_1;t,\mathbf{E}_{\mathrm{pu}}(t)) \\ &\quad + \sum_{\alpha_1,\beta_2}|d(\beta_2,\alpha_1)|^2 G(\beta_2,\alpha_1;\omega)P(\beta_2;t,\mathbf{E}_{\mathrm{pu}}(t)) \end{aligned} \qquad (3.14)$$

This equation has been derived in analogy to the absorption of a weak probe pulse in the last section. Besides the pre-factor the main difference between Eq.3.10 and Eq. 3.14 is the missing of an excitation process. Similar as in the proceeding section the following approximations have been made: (a) pump pulse and fluorescence are well separated in time, (b) all intra-manifold coherences have been neglected, and (c) the fluorescence lifetime is large compared to the observation time, i.e. the depopulation of the excited state *due to fluorescence* is small, and can be neglected while calculating the dynamics. Whereas the approximation (a) is intrinsic to this approach, (b) and (c) can be released easily. The chosen experimental polarization of the fluorescence is represented by the unit vector $\mathbf{e}_F$, and the linewidth is calculated after Eq. 3.12.

3.5 Calculation of Linear Spectra

For the calculation of linear spectra different combinations of the single chromophore dipole moments μ_m are used, depending on the experimental realization of the respective technique. Besides this geometrical factor, the formulas in this section represent a special case of the transient absorption of a weak probe pulse where no pump pulse has been applied, Eq. 3.10.

3.5.1 Absorption

The linear absorption $A(\omega)$ is gained using Eq. 3.10

$$A(\omega) = \frac{4\pi\omega n_{\mathrm{CC}}}{\hbar c}\sum_{\alpha_1}|\mathbf{d}(\alpha_1,0)|^2 G(\alpha_1,0;\omega)\,, \qquad (3.15)$$

with the dipole moment

$$\mathbf{d}(\alpha_1,0) = (d_{\alpha_1,x}, d_{\alpha_1,y}, d_{\alpha_1,z}) = \sum_m C_{\alpha_1}(m)\boldsymbol{\mu}_m\,. \qquad (3.16)$$

Note that the notation could be simplified with regard to Eq. 3.10 caused by the omission of the pump pulse.

3.5.2 Linear Dichroism

The linear dichroism $LD(\omega)$ is the difference in absorption parallel and perpendicular to a certain symmetry axis, here denoted as the z-axis. One obtains:

$$LD(\omega) = -\frac{4\pi\omega n_{\mathrm{CC}}}{\hbar c} \sum_{\alpha_1} (d^2_{\alpha_1,z} - \frac{1}{2}(d^2_{\alpha_1,x} + d^2_{\alpha_1,y})) G(\alpha_1, 0; \omega) \,. \tag{3.17}$$

The symmetry around the z-axis is used to orient the molecules in the probe volume.

3.5.3 Circular Dichroism

The circular dichroism $CD(\omega)$, i.e. the difference of the absorption of circular polarized light of different polarization, is given by

$$CD(\omega) = -\frac{4\pi\omega n_{\mathrm{CC}}}{\hbar c} \sum_{\alpha_1} (CD_{\alpha_1} + CD^{(chr.)}_{\alpha_1}) G(\alpha_1, 0; \omega) \,, \tag{3.18}$$

with the geometry factor

$$CD_{\alpha_1} = \sum_{mn} C_{\alpha_1}(m) C_{\alpha_1}(n) \, \mathbf{r}_{m,n} \cdot (\boldsymbol{\mu}_m \times \boldsymbol{\mu}_n) \,. \tag{3.19}$$

Here $\mathbf{r}_{m,n}$ connects the center of the m-th and the n-th chromophore. For the calculation of the CD spectra it is important to notice that certain chromophores exhibits an intrinsic CD spectrum due to mixing with higher excited states [vAVvG00]. This has been included by the introduction of $CD^{(chr.)}_{\alpha_1}$ in Eq. 3.18.

3.6 Summary

In this Chapter, a broad range of spectroscopical methods have been adopted to the multi-exciton density matrix formalism developed in Chapter 2. Both linear spectroscopy like absorption, linear dichroism and circular dichroism and nonlinear processes like transient absorption and time resolved fluorescence have been described. The respective simulations of optical properties will be done in Chapter 5 for the transient absorption of LH2 and in Chapter 6 for the linear spectra and the time resolved fluorescence of PS1.

Chapter 4

Optimal Control Theory

4.1 Introduction

The laser pulse control of molecular dynamics has made a huge development over the last two decades (a recent overview has been given in Refs.[RZ00, SB03]). The pioneering theoretical works of Tannor, Kosloff, and Rice [TKR86] and Brumer and Shapiro [BS86] gave rise to different control scenarios using a set of coherent excitation pulses. Due to the work of Rabitz, the optimal control (OC) theory has been applied to this field [PDR88, SWR88] and arbitrary pump pulses have been gained. The general approach of the optimal control theory is to find an optimized pulse with an iterative scheme to move the system to a target state at a given target time. The formulation of the OC theory which will be used in this work is based on the iterative scheme given in Ref. [ZBR97] and, for dissipative systems, in Ref. [OZR99]. The OC theory has been later refined to account for the experimental conditions of the pulse formation in Ref. [SdVR99] and, for the density matrix description, in Refs. [MM01b, MKM02]. The relevance of the pulse shape that is gained by the OC theory to the experimental conditions of a liquid-crystal pulse shaper has been shown in Ref. [MM02]. Approaches which release the condition of a fixed target time and deal with a target interval have been developed in Ref. [MR01, SR90a, SR90b]. Besides these optimization approaches analytical expressions can be gained for certain quantum control problems (e.g. [KAS02] and [CMW96]).

In this Chapter, similar to the case of vibrational wavepackets a coherent superposition $\sum_N \sum_\alpha A_{tar}(\alpha_N)|\alpha_N\rangle$ of electronic eigenstates $|\alpha_N\rangle$ will be the target state, an objective which has not been addressed in the literature so far. The corresponding optimal control theory will be deduced in the following section. An extension to include static disorder is made in Section 4.3, and an approach which releases the condition of a fixed target time is given in Sec. 4.4. The last Section of this Chapter deals with an analytical solution for the optimal pulse in a weak field approach with small dissipation.

4.2 Optimal Control of Excitonic Wavepackets

The Optimal Control (OC) theory is used to find a particular electric field, which guides the system from the ground state $|0\rangle$ (or any other given state) at $t = t_0$ to a given target state

$$|\phi_{\text{tar}}\rangle = \sum_{N,\alpha_N} A_{\text{tar}}(\alpha_N)|\alpha_N\rangle \tag{4.1}$$

at $t = t_f$ (see, e.g. [RZ00]). The pulse is calculated self-consistently using an iterative scheme. For open quantum systems the OC theory is described in [MKM02, OZR99], the discussion in this section will follow this approach, but explicitly use the multi-exciton description as described in Chapter 2. Starting with the objective functional

$$\begin{aligned} J &= \text{tr}_{\text{mx}}\{P_{\text{tar}}\hat{\rho}(t_f)\} - \frac{1}{2\hbar\Lambda_0\lambda}\int_{t_0}^{t_f} dt \frac{1}{f(t)}|E(t)|^2 \\ &\quad + \int_{t_0}^{t_f} dt\, \text{tr}_{\text{mx}}\Big\{\hat{\sigma}(t)\Big(\frac{\partial}{\partial t} + i\mathcal{L}\Big)\hat{\rho}(t)\} \end{aligned} \tag{4.2}$$

with the initial condition $\hat{\rho}(t_0) = |0\rangle\langle 0|$ and the target state $P_{\text{tar}} = |\phi_{\text{tar}}\rangle\langle\phi_{\text{tar}}|$, as given above. The trace expression on the right–hand side has to be taken with respect to the particular states of the involved excitonic manifolds. This functional consists of three parts, which will now be discussed in detail. Its maximization will give the optimal field. First, the expectation value of the target operator $P_{\text{tar}} = |\phi_{\text{tar}}\rangle\langle\phi_{\text{tar}}|$ at the target time is given. The next part is the condition to minimize the electric field. To guarantee that the field vanishes at $t = t_0$ and $t = t_f$ a time dependent Lagrangian multiplier $(\lambda f(t))^{-1}$ is used. The constant $\Lambda_0 = \frac{1eV}{|\mu_{chr.}|^2}$ where $\mu_{chr.}$ is the dipole moment of a single chromophore accounts for the unit conversion. The last condition ensures that the equation of motion is fulfilled by $\hat{\rho}(t)$ and as it will become clear soon also by $\hat{\sigma}(t)$, but in a modified form.

The maximization process of Eq. 4.2 leads to one of two possible solutions. Depending on the actual values of the first trace, the Lagrangian parameter $(\lambda f(t))^{-1}$, the dissipation, and the complexity of the system either the optimal solution will be found, or the solution with vanishing electric field.

Now the variational procedure is applied, giving two equations of motion, and a coupling term. First, variation with regard to $\hat{\sigma}(t)$ results in the ordinary equation of motion for the density matrix (cf. Eq. 2.20)

$$\frac{\partial}{\partial t}\hat{\rho}(t) = -i\mathcal{L}\hat{\rho}(t) = (-i\mathcal{L}_0 - \mathcal{D} - i\mathcal{L}_{\text{field}}(t))\hat{\rho}(t)\ . \tag{4.3}$$

The Liouville superoperators $\mathcal{L}_0$, $\mathcal{D}$, and $\mathcal{L}_{\text{field}}(t)$ are responsible for the free exciton motion, dissipation, and coupling to the laser pulse, respectively. The dissipative part of the equation of motion $\left(\frac{\partial}{\partial t}\hat{\rho}(t)\right)_{diss} = -\mathcal{D}\hat{\rho}(t)$ is written as usual (cf. Eq. 2.21)

$$\begin{aligned}
&\left(\frac{\partial}{\partial t}\rho(\alpha_M,\beta_N;t)\right)_{diss} = \\
&\quad -\delta_{\alpha_M,\beta_N}\sum_{K,\gamma_K}\Big(k(\alpha_M\to\gamma_K)\rho(\alpha_M,\alpha_M;t) - k(\gamma_K\to\alpha_M)\rho(\gamma_K,\gamma_K;t)\Big) \\
&\quad -(1-\delta_{\alpha_M,\beta_N})\Big(\Gamma(\alpha_M)+\Gamma(\beta_N)+\tilde{\Gamma}(\alpha_M,\beta_N)\Big)\rho(\alpha_M,\beta_N;t) \qquad (4.4)
\end{aligned}$$

Variation with respect to $\hat{\rho}(t)$ and a partial integration to move the time derivative to $\hat{\sigma}(t)$ result in

$$\frac{\partial}{\partial t}\hat{\sigma}(t) = -i\mathcal{L}^{\dagger}\hat{\sigma}(t) = (-i\mathcal{L}_0 + \mathcal{D}^{\dagger} - i\mathcal{L}_{\text{field}}(t))\hat{\sigma}(t)\ , \qquad (4.5)$$

where † denotes the Hermitian conjugation in the Liouville space $A^{\dagger}_{ab,cd} = A^{*}_{cd,ab}$ (cf. Ref. [Muk95]). Additional the final condition $\hat{\sigma}(t_f) = P_{tar} = |\phi_{tar}\rangle\langle\phi_{tar}|$ is gained. The dissipative part $\left(\frac{\partial}{\partial t}\hat{\sigma}(t)\right)_{diss} = +\mathcal{D}^{\dagger}\hat{\sigma}(t)$ is given by the negative transposed of Eq. 4.4

$$\begin{aligned}
&\left(\frac{\partial}{\partial t}\sigma(\alpha_M,\beta_N;t)\right)_{diss} = \\
&\quad +\delta_{\alpha_M,\beta_N}\sum_{K,\gamma_K}\Big(k(\gamma_K\to\alpha_M)\sigma(\alpha_M,\alpha_M;t) - k(\alpha_M\to\gamma_K)\sigma(\gamma_K,\gamma_K;t)\Big) \\
&\quad +(1-\delta_{\alpha_M,\beta_N})\Big(\Gamma(\alpha_M)+\Gamma(\beta_N)+\tilde{\Gamma}(\alpha_M,\beta_N)\Big)\sigma(\alpha_M,\beta_N;t) \qquad (4.6)
\end{aligned}$$

Note that beside the sign the rates between the populations have been exchanged. The last equation results from the variation with respect to $\mathbf{E}(t)$ leading to a coupling term for both previous derived equations

$$\mathbf{E}(t) = i\lambda\Lambda_0 f(t)\text{tr}_{\text{mx}}\{\hat{\sigma}(t)[\hat{\mu},\hat{\rho}(t)]_-\}\ . \qquad (4.7)$$

Besides the total dipole operator $\hat{\mu}$ of all chromophores of the CC the trace includes the two density operators $\hat{\sigma}(t)$ and $\hat{\rho}(t)$. As an initial state for the density operator one takes $\hat{\rho}(t_0) = |0\rangle\langle 0|$, i.e. before the presence of the laser pulse the system is in its electronic ground–state $|0\rangle$. In contrast to the ordinary propagation of $\hat{\rho}$ starting at t_0 and ending at t_f the operator $\hat{\sigma}(t)$ is propagated backwards in time starting at t_f with the final condition $\hat{\sigma}(t_f) = |\phi_{\text{tar}}\rangle\langle\phi_{\text{tar}}|$. The respective equation of motion is similar to that for $\hat{\rho}$ but with -$\mathcal{D}$ replaced by $+\mathcal{D}^{\dagger}$. For the chosen equation of motion in Bloch approximation the result has been given in Eq. 4.6 (For more general types see [MKM02]). The propagation of the two density operators is coupled via the electric field strength. If it is replaced by the expression on the right–hand side of Eq. 4.7 two coupled nonlinear equations are received which can be solved iteratively.

To carry out the iteration one starts with a Gaussian shaped field at a certain guessed wavelength for the first backward propagation. Then, one can iterate the set of equation back and forth until a certain convergence has been reached. The field amplitude is determined by the Lagrangian parameter $\lambda f(t)$ which time dependence is given by

$$f(t) = \exp(-(\frac{(t-t_0)-\tau_c/2}{\tau_c/5})^2)\,, \tag{4.8}$$

where the field duration $\tau_c = t_f - t_0$ has been introduced. It results in a Gaussian envelope centered at $t_0 + \tau_c/2$ with the full width half maximum (FWHM) of $\tau_c/3$.

4.3 Inclusion of Structural and Energetic Disorder

Naturally, finding an optimal pulse should not be restricted only to ordered systems, but should also deal with the different orientations and inhomogeneities. Therefore the approach as described in the foregoing section is extended to simultaneously account for N_{CC} individual chromophore complexes. Again the objective functional gives the staring point

$$\begin{aligned} J \;= \textstyle\sum_{k=1}^{N_{CC}} \quad & \mathrm{tr}_{\mathrm{mx}}\{P^{(k)}_{\mathrm{tar}}\hat{\rho}^{(k)}(t_f)\} - \frac{1}{2\hbar\Lambda_0\lambda}\int_{t_0}^{t_f} dt\, \frac{1}{f(t)}|E(t)|^2 \\ & + \int_{t_0}^{t_f} dt\, \mathrm{tr}_{\mathrm{mx}}\Big\{\hat{\sigma}^{(k)}(t)\Big(\frac{\partial}{\partial t} + i\mathcal{L}^{(k)}\Big)\hat{\rho}^{(k)}(t)\Big\}\,, \end{aligned} \tag{4.9}$$

but now $\hat{\rho}^{(k)}(t)$ and $\hat{\sigma}^{(k)}(t)$ have an additionally CC index as well a the Liouvillian $\mathcal{L}^{(k)}$ belonging to the k-th CC with its specific energetic disorder and spatial orientation. The initial conditions are given by $\hat{\rho}^{(k)}(t_0) = |0^{(k)}\rangle\langle 0^{(k)}|$, the target states by $\hat{\sigma}^{(k)}(t_f) = P^{(k)}_{\mathrm{tar}} = |\phi^{(k)}_{\mathrm{tar}}\rangle\langle\phi^{(k)}_{\mathrm{tar}}|$. They denote the target state similar as without disorder, but now with an index for the specific the CC. Notice that the equations for all different k are coupled only by the electric field part.

$$\mathbf{E}(t) = i\frac{\lambda\Lambda_0 f(t)}{N_{CC}}\sum_{k=1}^{N_{CC}} \mathrm{tr}_{\mathrm{mx}}\{\hat{\sigma}^{(k)}(t)[\hat{\mu}^{(k)}, \hat{\rho}^{(k)}(t)]_-\}\;. \tag{4.10}$$

Since the equations of motion as given in the previous section must be solved for all N_{CC} chromophore complexes simultaneously to extract the field Eq. 4.10, this approach is rather time consuming and restricted to only a few CC.

4.4 Matching a Time-Dependent Target State in an Target Interval

To determine the state of the system not only at a given time t_f but during the whole time interval between t_0 and t_f a modified objective functional can be used (a more involved discussion can be found in Ref. [KM04])

$$\begin{aligned} J &= \int_{t_0}^{t_f} dt\, \mathrm{tr}_{\mathrm{mx}}\{\hat{\phi}(t)\hat{\rho}(t)\} - \frac{1}{2\hbar\Lambda_0\lambda}\int_{t_0}^{t_f} dt \frac{1}{f(t)}|E(t)|^2 \\ &+ \int_{t_0}^{t_f} dt\, \mathrm{tr}_{\mathrm{mx}}\Big\{\hat{\sigma}(t)\Big(\frac{\partial}{\partial t} + i\mathcal{L}\Big)\hat{\rho}(t)\Big\}, \end{aligned} \tag{4.11}$$

with the initial conditions $\hat{\rho}(t_0) = |0\rangle\langle 0|$. A target function $\hat{\phi}(t)$ has been introduced, it determines the objective of the optimal pulse during the whole propagation interval.

Now the variational procedure is applied, giving two equations of motion, and a coupling term. First, variation with respect to $\hat{\sigma}(t)$ results in the ordinary equation of motion for the density matrix, resulting in Eq. 4.3. The variation with regard to $\hat{\rho}(t)$ and a partial integration result in (cf. 4.6)

$$\begin{aligned} \frac{\partial}{\partial t}\hat{\sigma}(t) &= -i\mathcal{L}^\dagger\hat{\sigma}(t) - \hat{\phi}(t) \\ &= (-i\mathcal{L}_0 + \mathcal{D}^\dagger - i\mathcal{L}_{\mathrm{field}}(t))\hat{\sigma}(t) - \hat{\phi}(t)\ , \end{aligned} \tag{4.12}$$

and the final condition and $\hat{\sigma}(t_f) = |0\rangle\langle 0|$. This result differs from Eq. 4.6 because an additional time dependent external force $\hat{\phi}(t)$ is applied. The last equation is given by the variation with regard to $\mathbf{E}(t)$, it couples both previous equations, and gives Eq. 4.7

4.5 Construction of an Optimal Pulse

Besides the approach used in the previous section, under certain conditions an optimal pulse can also be constructed as a superposition of a few single-frequency pulses, i.e. there is an analytical solution to the optimization problem (see, e.g. [KAS02]). The main drawback of this approach is that the pulse has to be long enough to allow the addressing of the individual exciton states in the frequency domain. An estimation of this duration is given below. On the other hand during this time the influence of dissipation has to be small.

In the following a weak field approach (i.e. linear in the pump field) will be used, and dissipation will be neglected (or will be regarded as small on the timescale of the pulse). Naturally only a small population in the one-exciton manifold will be achieved, and the target state must be within that manifold. Using a specific target state

$$|\phi_{\mathrm{tar}}\rangle = \sum_{\alpha_1} A_{\mathrm{tar}}(\alpha_1)|\alpha_1\rangle\,, \tag{4.13}$$

which could be e.g. a localized state at a certain chromophore, the electric field to create this state is given by

$$E(t) = E_0 f(t) \sum_{\alpha_1} \cos\Big(\Omega(\alpha_1,0)(t-t_f)\Big)\frac{A_{\mathrm{tar}}(\alpha_1)}{d(\alpha_1,0)}\,, \tag{4.14}$$

using $\mathbf{E}(t) = \mathbf{e}_{\mathrm{pu}}E(t)$ and $d(\alpha_M,\beta_N) = \mathbf{e}_{\mathrm{pu}}\mathbf{d}(\alpha_M,\beta_N)$. Note that for better comparison with the approach of the last section and caused by the experimental conditions, a Gaussian pulse envelope $f(t)$ has been chosen after Eq. 4.8, which is small at $t = t_0$ and $t = t_f$ and has its maximum at $t = t_0 + \tau_c/2$, with $\tau_c = t_f - t_0$.

Now the minimal duration τ_c for the optimized pulse will be discussed. The Gaussian envelope leads to a broadening of the Fourier stick spectrum at each energy $\hbar\Omega(\alpha_1,0)$, which is not critical as long as the spectra for different one exciton states do not overlap. Being more precise, the Fourier-transform

$$E(\omega) = E_0 \sum_{\alpha_1} f(\omega - \Omega(\alpha_1,0))\frac{A_{\mathrm{tar}}(\alpha_1)}{d(\alpha_1,0)} \tag{4.15}$$

should fulfill

$$E(\Omega(\alpha_1,0)) = \bar{E}_0\frac{A_{\mathrm{tar}}(\alpha_1)}{d(\alpha_1,0)}\,, \tag{4.16}$$

with the constant $\bar{E}_0$ for all one-exciton states $|\alpha_1\rangle$. The same equation should hold for any other state $|\beta_1\rangle$, this results in

$$f(\Omega(\alpha_1,\beta_1)) \sim \delta_{\alpha_1,\beta_1}. \tag{4.17}$$

Using Eq. 4.8 one finds

$$f(\omega) = \sqrt{\pi}\frac{\tau_c}{5}e^{-\frac{\omega^2\tau_c^2}{100}}, \tag{4.18}$$

which is, of course, again a Gaussian function, with $\sigma = \sqrt{50}/\tau_c$. At a distance of 3σ the function has decreased to 0.01, which will be sufficient for the present case. This results in the relationship

$$\tau_c \geq \frac{3\sqrt{50}}{\Omega(\alpha_1,\beta_1)}\,, \tag{4.19}$$

which should hold for any two different one-exciton states $|\alpha_1\rangle$ and $|\beta_1\rangle$. Using shorter time intervals, the optimal control theory of the previous section will find better solutions, even in a weak field approach (cf. Chapter 7).

4.6 Summary

In this Chapter, the optimal control theory has been adopted to the multi-exciton density matrix formalism developed in Chapter 2. Extensions to disordered systems have been given, and one possibility to release the restriction to a specific target time has been shown. Additionally the construction of an optimal pulses has been described, and the time range where it is appropriate. The application of the optimal control theory on PS1 and FMO will be given in Chapter 7. Additionally the optimal control theory which accounts for disorder, and the constructive approach will be applied to the FMO complex in that Chapter.

Part II

Application

Chapter 5

Exciton-Exciton Annihilation in LH2

5.1 Introduction

It is of ongoing interest to reveal details of excitation energy transfer dynamics in the various light harvesting antennas of bacteria as well as higher plants (A recent overview can be found in [si02]). To apply intensive laser pulses represents a particular approach although it touches non–physiological conditions. However, in this way it becomes possible to study higher excited states and new relaxation channels such as exciton exciton annihilation (EEA). Additionally, when thinking about control experiments (cf. Chapter 7) the effect of EEA has to be taken into account for a realistic description. Originally, experiments considering EEA have been carried out on dye aggregates (see for example [SDT88, SGGP88]. But there are some recent works where EEA has been demonstrated for different photosynthetic antenna systems. The FMO-Complex has been studied in [GVK$^+$96], EEA could be described for the LH1 in [BJvM$^+$95, VAPS96], and the Refs. [MCG97, SGGP88] dealt with the LH2 (Fig. 5.1). Besides these specific experiments, it should be noted that EEA also may happen in an natural environment, and that the ability to handle higher excitations without much damage (besides heating) is crucial for the antenna complex.

It has been explained in detail in Section 2 how to embed this mechanism of EEA into a description based on delocalized (or partially delocalized) exciton states. As a main result of Chapter 2 besides correct formulas an approximate version of this rate which is most appropriate for numerical simulations has been obtained. This rate expression is obtained as a product of an IC rate (identical for all chromophores) and of an overlap expression between the probability to have a double excitation at a certain chromophore and the probability to have a singly excited chromophore.

With this EEA density matrix theory available the present Chapter discusses

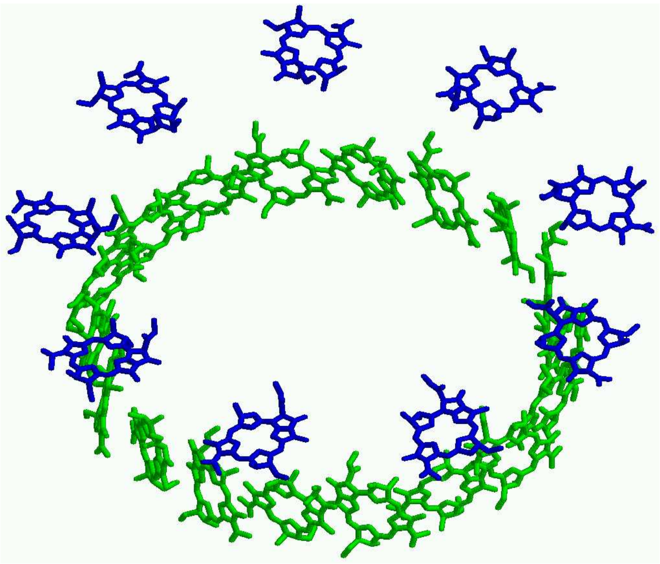

Figure 5.1: The light harvesting complex LH2 from *Rhodopseudomonas acidophila*, Ref. [PPF$^+$97] (identifier 1kzu in the protein data bank). Plotted with `rasmol`. The two rings of BChl*a*s B850 (lower ring) and B800 (upper ring), named after their main absorption line (in nm), are shown.

simulations of transient absorption spectra. The computations concentrate on the B850 ring of the LH2 of *rhodobacter sphaeroides* (for a recent overview see [SPvG99]). To account properly for EEA the 18 Bacteriochlorophylls (BChls) which form the B850 ring have to be modeled as three–level systems (Fig. 5.2). Therefore, beside the Q_y–excitation a higher excited state is introduced which should be separated from the first excited Q_y–state by the same energetic distance as the first excited state from the ground state. The delocalized MX states are formed by the electronic inter–chromophore coupling. In the simulations the ground state, the single exciton manifold and the two exciton manifold are included. Energetic relaxation in the one and the two–exciton manifold is caused by the coupling to the protein environment, whereas the EEA is mainly determined by local vibrations participating in the IC process. Furthermore, as it is well–accepted and has been demonstrated recently by single molecule spectroscopy [vOKK$^+$99, vOKK$^+$00, MKvO$^+$01, BSH$^+$99, TCD$^+$99, TGJW00] any light harvesting complex is characterized by a certain amount of static disorder, i. e. each complex has a slightly different spectrum caused by a differing microscopic surrounding. This phenomenon will also be considered, and frequency dispersed transient absorption spectra will be computed.

The different views of single molecule spectroscopy and time dependent spectroscopy for photosynthetic antenna systems are combined in Section 5.5. With the use of a multi-exciton density matrix theory including the exciton-exciton an-

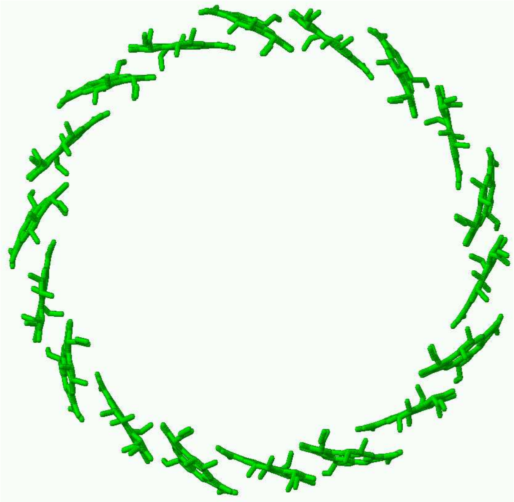

Figure 5.2: The B850 ring of LH2 of *Rps. acidophila* after Ref. [PPF$^+$97].

nihilation (EEA) process one gets insight into the dynamics of single molecules. It is shown that the static disorder slows down the EEA process by a factor of two, and that therefore the internal conversion rate from a higher excited to the first excited state of BChl has to be modified to match the experiment. It results in a two times faster decay constant, i.e. 35 fs, than in the case without disorder.

Computations on pump–probe spectra for dye aggregates and antenna systems, in particular for the LH2 have been published at different places [LAI$^+$91, Muk95, SM95, KS96, MCM97, KS97, BK99, DMC$^+$00, RMK01, NvG02]. However, all these approaches (at least within the numerical calculations) stay on a description which is of third–order in the field–strength. As it is well known (cf., e.g. Ref. [MCM97]) such an treatment does not include two–exciton state population but only coherences among them and the single exciton states. This fact indicates that the present approach which describes EEA and thus requires the incorporation of two–exciton (and even higher manifold) populations has to go beyond all theses standard theories based on third–order response functions.

This Chapter is organized as follows. In the next section the B850 model system is defined, followed by calculations of transient absorption under the influence of EEA. Then static energetic disorder is introduced, first for single B850 rings, and later transient spectroscopy of an disordered ensemble of B850 rings will be calculated. Whenever experimental results were available, a comparison with the simulations will be made.

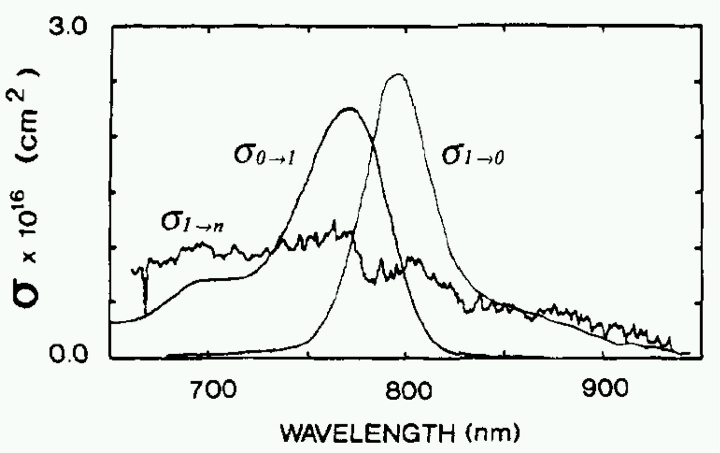

Figure 5.3: Ground-state absorption spectrum ($\sigma_{0\to1}$), stimulated-emission spectrum ($\sigma_{1\to0}$), and excited state absorption spectrum ($\sigma_{1\to n}$) of BChl$a$ in MeOH. Taken from Ref. [BNP13].

5.2 Defining the LH2 Model System

Before presenting the results of the simulations all parameters entering the model have to be fixed. The LH2 of *rhodobacter sphaeroides* inhibits a water wheel like arrangement of 18 strongly coupled BChl$a$s (Ref.[PPF$^+$97] and Fig. 5.2). They are paired to nine dimers and absorbing at 850 nm thus forming the so–called B850 part [vAVvG00, SPvG99]. 9 additional BChl$a$ are positioned in a second concentric ring and absorb at 800 nm (the B800 part, cf Fig. 5.1). Since only BChl$a$ is present in this complex the a is neglected in the following. In contrast to the B850 part it is characterized by a weaker inter–BChl coupling.

Since it is not the aim to give a comprehensive description of the LH2 a model is chosen which is simple enough but includes EEA and can reproduce the respective part of the measured transient absorption spectra. Therefore, the B800 part is removed and thus the possible relaxation from it to the B850 part and one concentrates exclusively on the B850 ring.

Now, the three states of the BChl molecule, which will be used within this work are discussed. Besides the ground state (S_0) the lowest excited state (S_1) of the BChl is used. It is the so called Q_y–state of the BChl (the state with energy ε_e) and for the energy the indisputable value located at 799 nm is used. As already discussed in various papers (see e.g. [RMK01]) the concrete assignment of the higher excited state (S_n–state, here with energy denoted by ε_f) is impossible. This uncertainty, of course, is related to the fact that a dense spectrum of electron–vibrational excitations exists in the energetic range of a doubled Q_y–excitation (cf. Fig. 5.3) in the BChl monomer. Due to couplings to other BChls, even charge transfer states may come into play. However, since the higher excited state decays very fast due to IC, the exact nature of this state is not that important. Therefore the excited state absorption spectrum is replaced by a single effective level. Its concrete energetic positions is influenced by the density of states related to the original spectrum. But the introduction of ε_f becomes only important if the related transition dipole moments are large enough to allow for a noticeable strong coupling to delocalized two–exciton states formed by two Q_y–excitation. That the transition dipole moments are large enough for an efficient coupling has been already confirmed by the early measurements of [BNP13] (Fig. 5.3). Note that the broadening of the excited state absorption makes a direct comparison of the dipole moments difficult. Therefore, the dipole–moment of the $S_1 \rightarrow S_n$ transition of BChl has been assigned a similar magnitude as the dipole–moment of the $S_0 \rightarrow S_1$ transition, both are set equal to 6.32 Debye (cf. [vAVvG00]). Furthermore, a blue shift of $100\,cm^{-1}$ for the $S_1 \rightarrow S_n$ transition energy of each chromophore is introduced with regard to the $S_0 \rightarrow S_1$ transition (cf. Fig 5.3).

The earlier debate about the concrete values of the electronic inter–BChl coupling more or less settled now. Here one follows the suggestion of Ref. [SPvG99] and the nearest neighbor Q_y-coupling is taken as alternating between the two values $322\,cm^{-1}$ and $288\,cm^{-1}$, and all other couplings have been neglected. Because of the close packing of the chromophores these values are beyond the dipole–dipole approximation. This makes the application of quantum chemical calculations necessary, as it has been done for each pair of BChl in the LH2 in Ref. [TM$^+$00] resulting in similar coupling values for the main couplings.

The coupling processes with the transition $\varphi_e \rightarrow \varphi_f$ at one BChl and the transitions $\varphi_f \rightarrow \varphi_e$ or $\varphi_e \rightarrow \varphi_g$ at a nearest neighbor BChl (as well as all reverse processes) are described by the coupling energy of $305 cm^{-1}$(the mean value of the basic couplings among the Q_y–excitations).

The depopulation of the higher excited state at a single chromophore which is the last step of the EEA occurs via internal conversion to the first excited state. The IC rate enters the EEA transition rate $k^{(\mathrm{EEA})}$, Eq. 2.42. The respective time constant is taken as $1/k_{IC} = 70\,fs$ for simulations excluding disorder as it will be discussed in the next section.

The model for the LH2 which has been described above is, besides the important inclusion of the higher excited state, rather simple. More complex models have been set up e.g. in Ref. [NWvG03] including the B800 to B850 transfer to describe linear and nonlinear spectra, and in Ref. [DKKS02] with an combined molecular dynamics and quantum chemistry approach, leading to a polaron model for the excitations.

Finally some comments on the used description of the intra–manifold transition rates $k^{(\mathrm{mx-pro})}$, Eq. 2.27 which are caused by the coupling to the protein vibrations (details can be found in Appendix C). Since nearly nothing is known of the details of these vibrations it has been tried to reduce the number of possible additional parameters as much as possible. This is achieved by assuming any influence is absent of extended (nonlocal) vibrations of the protein body correlating different BChl. The assumption results in local BChl spectral densities which should be equal one to another. Furthermore, one restricts the appearance of spectral densities on a modulation of the Q_y–state. It remains the single chromophore spectral density (which has been adopted to experimental data in [OKP02]):

$$J_e(\omega) \;=\; j_e \sum_{\nu=1}^{5} \frac{\omega^2}{2\omega_\nu^3} \exp(-\omega/\omega_\nu) \; . \tag{5.1}$$

The various frequencies are given by $\omega_1 = 10.5\,cm^{-1}$, $\omega_2 = 25\,cm^{-1}$, $\omega_3 = 50\,cm^{-1}$, $\omega_4 = 120\,cm^{-1}$ and $\omega_5 = 350\,cm^{-1}$. The overall coupling factor j_e is finally used to achieve a fine–tuning of the computed spectra to the measured ones. Since the IC channel is much faster than the intra–manifold relaxation caused by $k^{(\mathrm{mx-pro})}$ the coupling of the higher excited MX–states to protein vibrations has been neglected. All computations have been carried out for room temperature conditions.

5.3 Simulation of Transient Absorption

The transient absorption was calculated by Eqs. 3.4, 3.3 and 3.9. According to the experiment, in the simulations for both the pump and the probe field linearly polarized electric fields of 100 fs duration with a Gaussian envelope are used, with the magic angle (54.7°) between the polarization directions. The orientational average has been taken into account in the simplest way by multiplying the transient absorption by a factor of $\frac{1}{3}$. The value of the coupling to the reservoir DOF has been set to $j_e = 2.0$. The inclusion of static disorder will be discussed in one of the next sections.

To determine the internal conversion rate, the measured transient absorption decay at early times has been fitted for the highest excitation intensities. The respective time constant for the internal conversion is 70 ± 5 fs. Using this time constant and the above mentioned parameters the experimental transient absorption kinetics at different excitation intensities of the experiment could be simulated very well (Fig. 5.4). In a recent article [THP$^+$01], it was estimated that for the highest excitation intensities used here, the average number of excitations in the LH2 is 2-3. This justifies the neglect of higher excited states beyond the two-exciton manifold, at least for the lower intensities. Nevertheless, there is some deviation from the measured data at the two highest intensities, indicating that excited-state absorption from the two-exciton to the three-exciton state becomes important. (Its neglect leads to an overestimation of the signals.)

Fig. 5.5 shows the overall populations $P_M(t) = \sum_{\alpha_M} |\rho(\alpha_M, \alpha_M; t)|$ ($M = 0, 1, 2$) with $\sum_{M=0,1,2} P_M(t) = 1$ calculated for the different pump intensities of

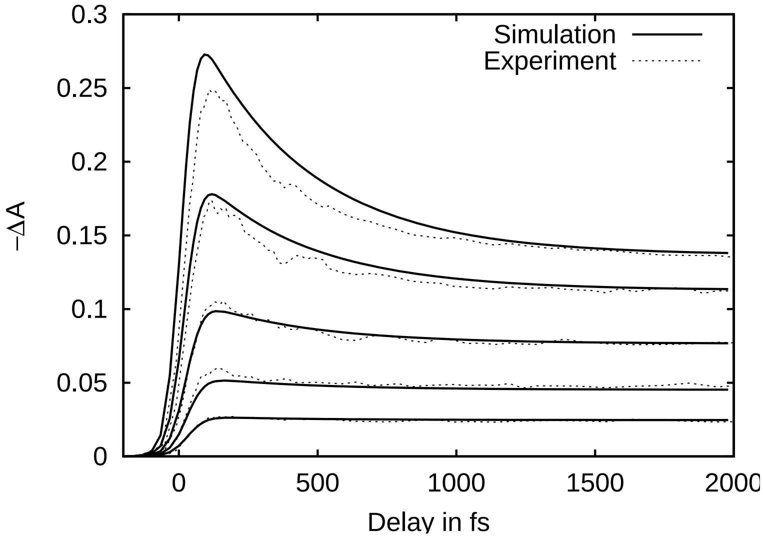

Figure 5.4: Transient absorption kinetics versus delay time for pump pulse with 100 fs duration and energies of 128, 64, 32, 16 and 8 $\mu J/cm^2$ (from top to bottom). Pump pulse wavelength 850 nm, probe pulse wavelength 860 nm. Experimental (dotted, Ref.[THP$^+$01]) and simulated (solid) values.

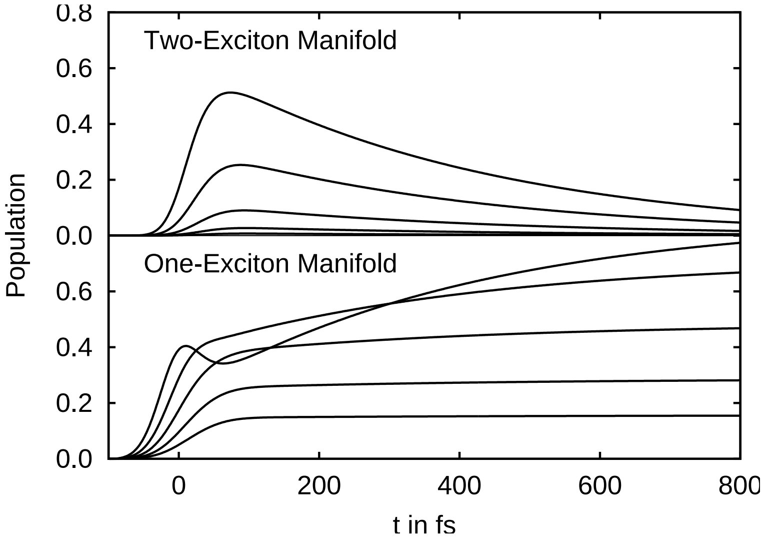

Figure 5.5: Population of the one and two-exciton manifold for pump pulse energies and wavelengths as in Fig. 5.4.

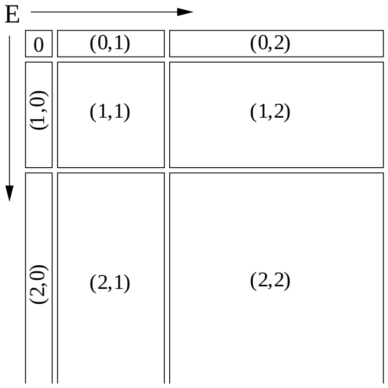

Figure 5.6: Scheme of the multi-exciton spectrogram. The elements of the multi-exciton density matrix are ordered by the corresponding eigenenergies, increasing from left to right and top to bottom. Parts with different manifold indices M, $N = 0$, 1, 2 are separated as shown.

Fig. 5.4. The population decay from the two-exciton manifold into the single-exciton manifold through the EEA process can be clearly identified. During the pump pulse action, processes such as ground state absorption, excited state absorption, and stimulated emission occur. At the highest pump energy there is a decrease in the one-exciton manifold at the end of the pump pulse, which is caused by a combination of ground state depletion and excited state absorption.

Having fixed the parameters one can visualize some otherwise unmeasurable internal dynamics of the system. In the multi-exciton spectrogram, the absolute value of each element of the multi-exciton density matrix $|\rho(\alpha_N, \beta_M; t)|$ is plotted, ordered by energy as shown in Fig. 5.6 with a logarithmic color scale (Fig. 5.7). The elements $|\rho(\alpha_N, \beta_N; t)|$ (N =1, 2, 3) belonging to the same manifold represent populations (diagonal part, $\alpha_N = \beta_N$) and coherences (off diagonal part) of the N-exciton states α_N and β_N. In contrast the elements $|\rho(\alpha_N, \beta_M)|$ with $N \neq M$ describe coherences between the different manifolds caused by the coupling to the external field. The pictures provide the basis for a quantitative discussion of the main features of the dissipative dynamics. The pump pulse excites both populations and coherences. Looking at the coherences between the ground and one-exciton state one can distinguish the two strongly allowed transitions (marked “a” in Fig. 5.7) and two weaker ones at higher energies (marked ”c” in Fig. 5.7), which are well known from other studies of the ideal symmetric system [SPvG99]. The two transitions marked as “b” in Fig. 5.7 are mediated by the two exciton manifold, as could be clarified by a detailed inspection of the time evolution. Between the one-exciton and the two-exciton manifold, quite a number of transitions are allowed. Both the coherences and populations relax to the low energy side of the corresponding manifold. After a while the coherences die out, and the populations thermalize.

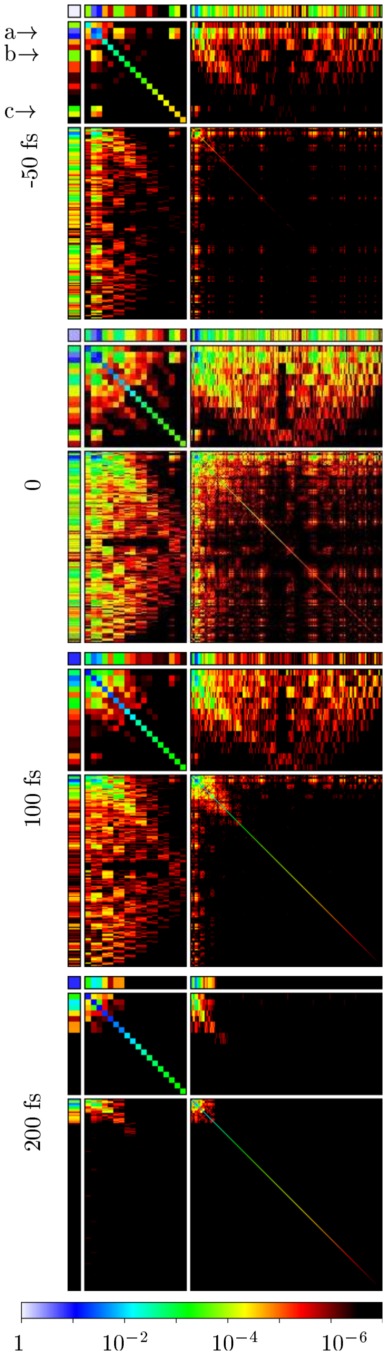

Figure 5.7: Multi-exciton spectrogram for the highest pump intensity of Fig. 5.4 at -50 fs, pump pulse maximum, 100 fs and 200 fs delay time (from top to bottom). The absolute value of each density-matrix element $|\rho(\alpha_N, \beta_M; t)|$ is shown by a logarithmic color scale. See also Fig. 5.6. The coherences labeled a, b , and c are discussed in the text.

5.4 Simulation of Frequency Resolved Transient Absorption

To have a clear assignment of EEA in the frequency resolved transient absorption spectra the calculations of this Section neglect disorder, the two following sections will deal with this topic. Of course these results cannot be compared directly with the experiment. But to achieve similar spectra like the measured ones (of e.g. [FJLW98]) the energies are slightly red-shifted (the Q_y–state equals 810 nm). The value of the reservoir coupling constant is set in this section to $j_e = 1.5$. As usual in the experiments linearly polarized pump and probe pulses are used with the magic angle (54.7°) between the two polarization directions. Both pulses are applied at a wavelength of 850 nm and have a Gaussian envelope with a duration of 100 fs for the pump–pulse and with a shorter duration of 25 fs for the probe–pulse. The shorter duration has been taken to cover the frequency range of interest when calculating frequency resolved transient absorption.

Since $\Delta A_{\rm pr}(\omega, \infty)$ has a pronounced minimum at 850 nm its value at long times $\Delta A_{\rm pr}(\lambda = 850{\rm nm}, \infty)$ is taken to introduce normalized transient absorption spectra (for the pump-probe delay time $\tau_{\rm del}$)

$$\Delta A_{\rm pr}^{({\rm norm})}(\omega, \tau_{\rm del}) \;=\; \frac{\Delta A_{\rm pr}(\omega, \tau_{\rm del})}{\Delta A_{\rm pr}(\lambda = 850{\rm nm}, \infty)} \,. \tag{5.2}$$

The introduction of such a normalized absorption has the advantage that all curves presented in the following have the same minimum for large delay times irrespective of the applied pump beam intensity. Furthermore, if disorder is neglected, for large delay times the curves completely coincide since the dependence on the ground–state population is canceled by the normalization. This easily allows to find signatures of EEA in the spectra.

The Figs. 5.8 and 5.9 display the normalized frequency resolved transient absorption (of the B850 part of the LH2) according to Eqs. 3.3 and 5.2 and at different delay times. Therefore, the spectra are calculated by treating the action of the pump and the probe–field beyond a perturbative expansion, and it has been set $E_{\rm pu} = 50 E_{\rm pr}$. The time–evolution of the total one–exciton and two–exciton population is shown in the insets of Fig. 5.8 and Fig. 5.8. Since the spectra of Fig. 5.8 have been computed for a eight times weaker pump–pulse intensity leading to a negligible two–exciton population, they have to be considered as reference spectra unaffected by EEA.

At 850 nm the transient absorption of Fig. 5.8 shows a pronounced bleaching. The sharp structure is caused by the fact that at the absence of disorder only the two degenerated states of the one–exciton manifold often denoted as $k \pm 1$ are optically allowed from the ground–state. The transient absorption becomes stationary after $\tau_{\rm delay} = 700$ fs what is also obvious by the time–evolution of

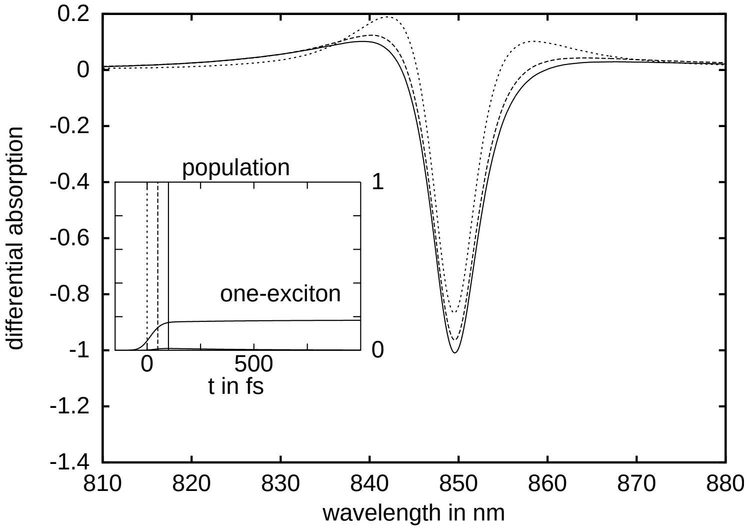

Figure 5.8: Normalized frequency resolved transient absorption of the B850 part of the LH2 at different delay times τ_{del} according to Eq. 5.2 and for the absence of disorder. The pump and the probe pulses are applied at a wavelength of 850 nm and with a duration of 100 fs and 25 fs, respectively. The pump–pulse energy density amounts $8\mu J/cm^2$. Dotted curve: $\tau_{\mathrm{del}} = 0$, dashed curve: $\tau_{\mathrm{del}} = 50fs$, full curve: $\tau_{\mathrm{del}} = 100fs$. The inset shows the time evolution of the total population of the one– and the two–exciton manifold. Vertical lines mark the delay times at which the transient absorption has been calculated.

the one–exciton population. (Of course the relaxed single–exciton distribution is removed by other processes not involved in the present description.)

The behavior is different if the pump–pulse intensity is increased (Fig. 5.9). First the MX–dynamics shown by the insets of Fig. 5.9 is considered. Here, the strong pumping induces a two–exciton population comparable to the one–exciton population. And according to EEA there is rise a of the latter population at the expense of the two–exciton population. The notable population of the two–exciton levels up to about 500 fs changes the transient absorption strongly when compared with the case drawn in Fig. 5.8. At later times, however, $\Delta A_{\rm pr}^{(\rm norm)}$ matches the the (quasi–) stationary curve of Fig. 5.8 (because of drawing spectra normalized according to Eq. 5.2). The intermediate change of the transient absorption by two–exciton populations results in the absence of the two shoulders around the main minimum at 850 nm. Between 50 fs and 500 fs, $\Delta A_{\rm pr}^{(\rm norm)}$ remains very small outside the minimum. Only if the two–exciton populations has been decayed due to EEA these positive structure reappears. This intermediate behavior is considered as a strong indication for notable two–exciton populations and the action of EEA. As a completion to the discussion lead so far Fig. 5.10 displays the single–exciton population subdivided with respect to the different energies. First the dipole–allowed state becomes populated by the pump–pulse but simultaneously a fast redistribution takes place ending up with a thermal population of all levels.

A further insight into the time–evolution of the transient absorption given in Fig. 5.9 is achieved when separating it into the different contributions contained in Eq. 3.10. Since the mentioned formula is only valid for a non–overlapping pump and probe pulse Fig. 5.11 starts at a delay–time of 100 fs (part a). Furthermore it is noted that a complete reproduction of the results of Fig. 5.9 is impossible because Eq. 3.10 provides an impulsive action of the probe–pulse. Besides the total value of $\Delta A_{\rm pr}^{(\rm norm)}$ Fig. 5.11 displays the ground–state bleaching, the excited state absorption from the one–exciton into the two–exciton manifold, and stimulated emission from the two–exciton state to the one–exciton state, as well as from the one–exciton state to the ground–state. Comparing all curves for the four chosen delay times (100 fs, 300 fs, 700 fs and 1500 fs) one first notices the stationary behavior of the ground–state bleaching. This is due to the fact that after the action of the pump–pulse the ground—state depletion has been finished (within the present approach) and population redistribution only appears between the one– and the two–exciton manifold. Because of a decreasing two–exciton population the contribution of the stimulated emission from the two–to the one–exciton states to $\Delta A_{\rm pr}^{(\rm norm)}$ disappears relatively fast. But this process together with the stimulated emission from the one–exciton to the ground–state is responsible for a decrease of the shoulders of the total transient absorption around 850 nm in the delay–time interval up to about 500 fs. For later times $\Delta A_{\rm pr}^{(\rm norm)}$ is only dominated by the excited–state absorption (from the one–exciton to the two–exciton manifold) and, of course, by the ground–state bleaching.

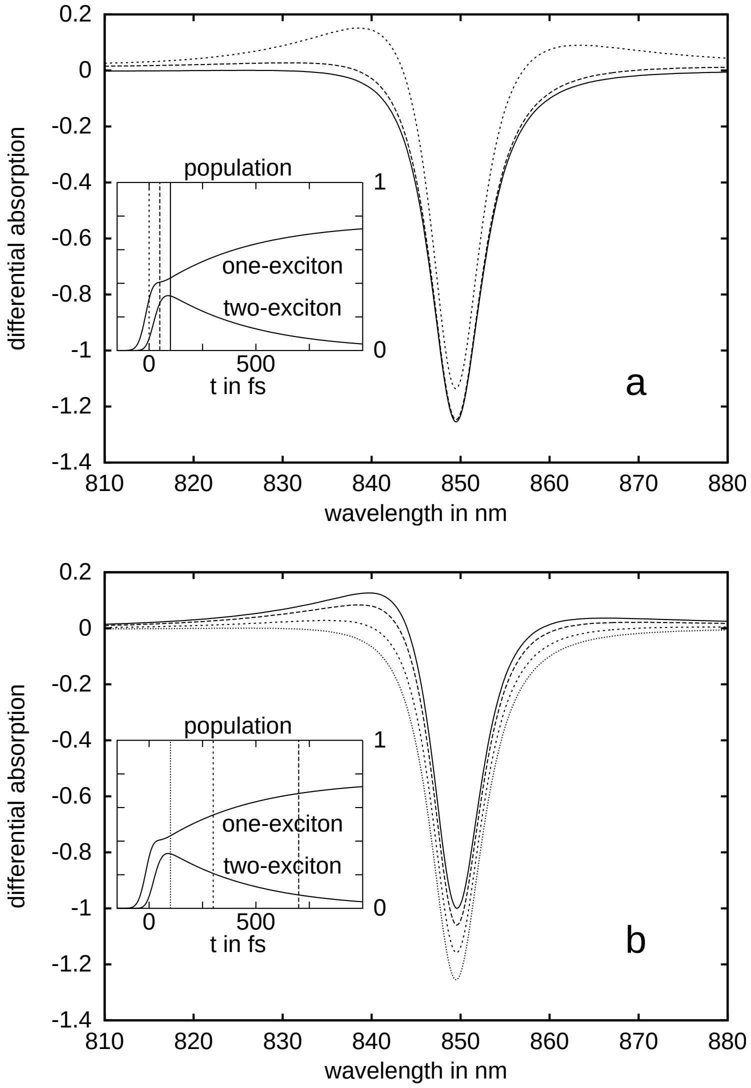

Figure 5.9: Normalized frequency resolved transient absorption of the B850 part of the LH2 at different delay times $\tau_{\rm del}$ according to Eq. 5.2 and for the absence of disorder. The pump and the probe pulses are applied at a wavelength of 850 nm and with a duration of 100 fs and 25 fs, respectively. The pump–pulse energy density amounts $64\mu J/cm^2$. Part a: dotted curve: $\tau_{\rm del} = 0$, dashed curve: $\tau_{\rm del} = 50fs$, full curve: $\tau_{\rm del} = 100fs$. Part b: dotted curve: $\tau_{\rm del} = 100$, short dashed curve: $\tau_{\rm del} = 300fs$, dashed curve: $\tau_{\rm del} = 700fs$, full curve: $\tau_{\rm del} = 1500fs$. The insets shows the time evolution of the total population of the one and the two–exciton manifold. Vertical lines mark the delay times at which the transient absorption has been calculated.

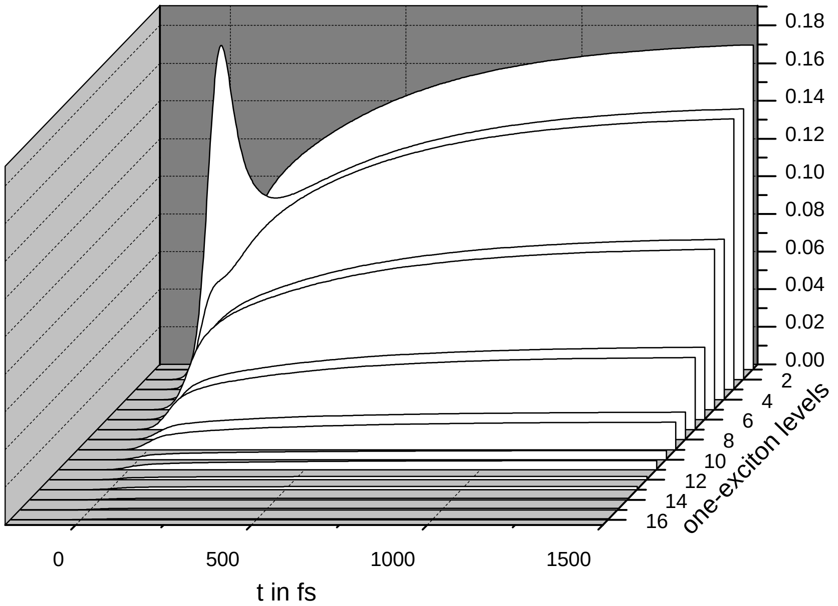

Figure 5.10: One–exciton populations of the B850 part of the LH2 versus time after a pump–pulse action at 850 nm, with a duration of 100 fs and with an energy density of $64 \mu J/cm^2$.

5.5 Single-Molecule Results with Disorder

It is known, that in photosynthetic antenna systems the interaction with the surrounding plays an important role in the dynamics. Due to different timescales this interaction is divided into static and dynamic disorder. The static (energetic) disorder does not change during the time of the experiment, but between different complexes (cf. Fig. 5.12). In contrast the dynamic disorder, which is the quantum-mechanical system-reservoir interaction is the same for all samples and leads to an energetic relaxation of the system. With the development of the single molecule spectroscopy [vOKK$^+$99, vOKK$^+$00, TCD$^+$99, TGJW00, BSH$^+$99, MKvO$^+$01] where these different types of disorder are distinguishable, it is now possible to set up a detailed model. In particular the consequences of static disorder to the EEA process which has been studied in the last Section are of interest. Here, medium intensity pump-pulses are used, which are strong enough to excite both the one-and the two-exciton manifold.

The successful reproduction of the measured transient absorption spectra for the B850 ring of the LH2 of *rhodobacter sphaeroides* in the previous Section offers an access to a more detailed visualization of the internal ultrafast and dissipative excitation energy dynamics connected with the EEA. The same parameters as in the previous section have been used. The overall system bath coupling factor has been chosen as $j_e = 2.0$ as in the first Section without static disorder. If

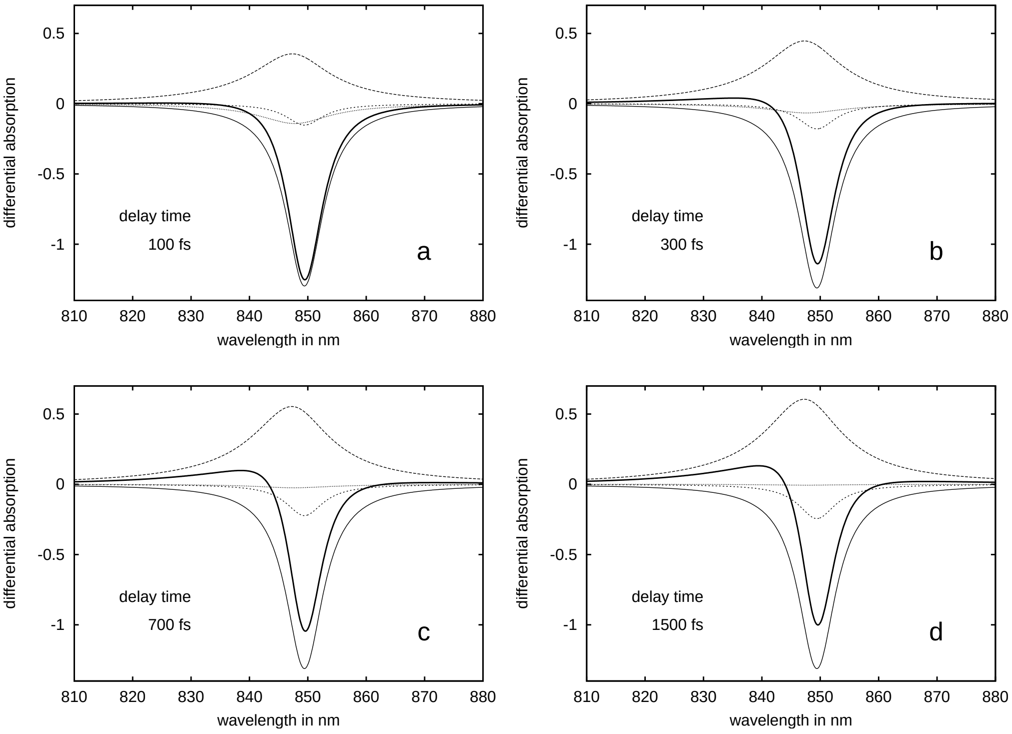

Figure 5.11: Separation of the normalized frequency resolved transient absorption of the B850 part of the LH2 into different contributions according to Eqs. 3.10 and 5.2 (absence of disorder). The pump and the probe pulses are applied at a wavelength of 850 nm. The pump pulse duration amounts 100 fs and the energy density 64 $\mu J/cm^2$. Thick full curve: complete transient absorption, thin full curve: ground–state bleaching, short dashed curve: stimulated emission (from the one–exciton manifold), dashed curve: excited state absorption (from the one–exciton manifold), dotted curve: stimulated emission (from the two–exciton manifold). Part a: $\tau_{\mathrm{del}} = 100$ fs, part b: $\tau_{\mathrm{del}} = 300$ fs, part c: $\tau_{\mathrm{del}} = 700$ fs, part d: $\tau_{\mathrm{del}} = 1500$ fs.

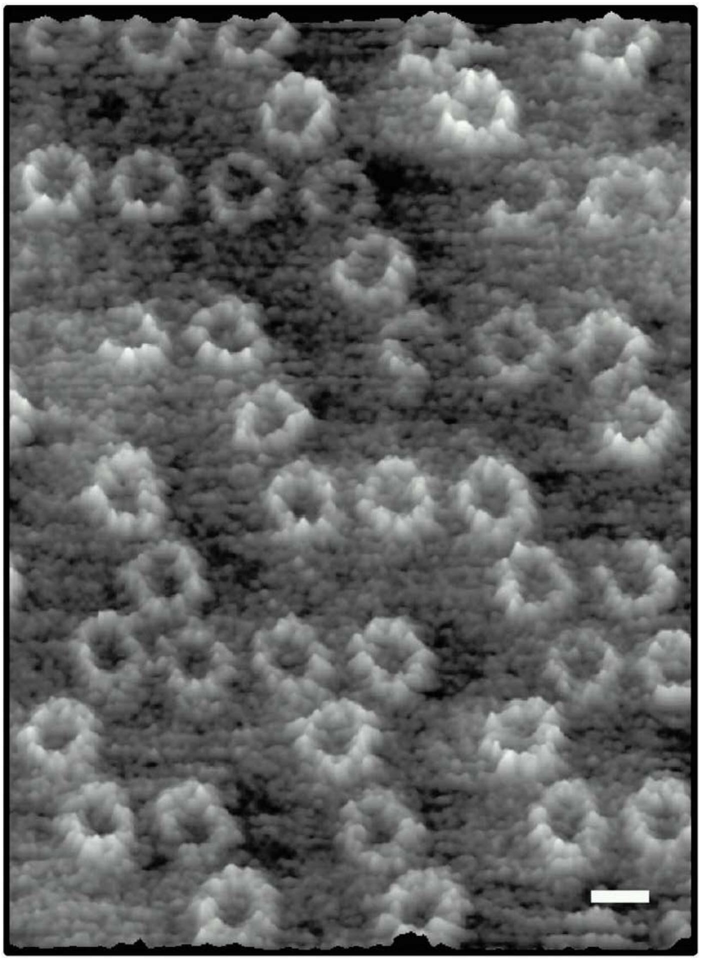

Figure 5.12: LH2 of *Rubrivivax gleatinosum* are comprised of 9 $\alpha/\ \beta$-heterodimers. The topograph recorded with an atomic force microscope (AFM9 in buffer solution under optimum conditions reveals rings that show 9 distinct protrusions that have a height of 14 Å. The scale bar is 50 Å (taken from Ref. [SFS$^+$01]).

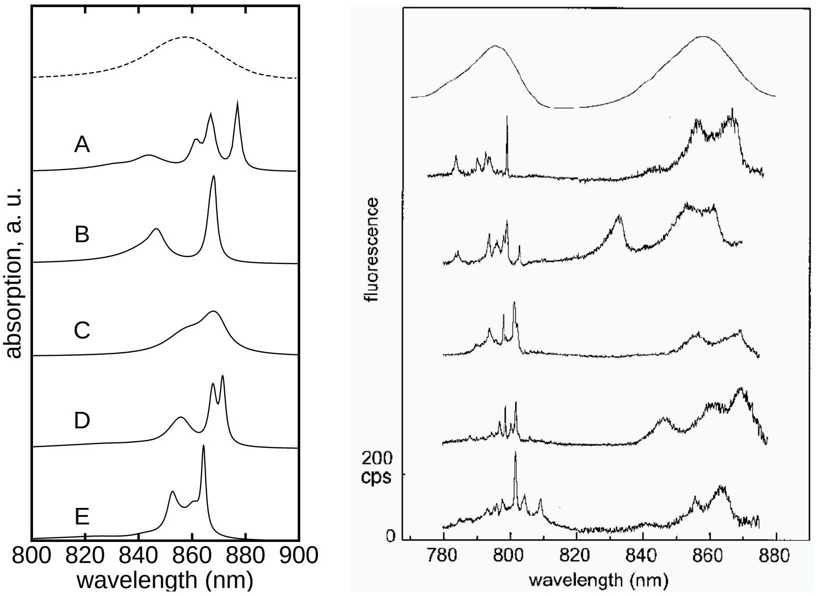

Figure 5.13: Simulated single-molecular linear absorption spectra (left, curves A-E) calculated for such disorder configurations which roughly reproduce the the experimental single-molecule fluorescence excitation spectra (right, taken from Ref. [vOKK$^+$99]). The first spectrum in both pictures gives the ensemble average.

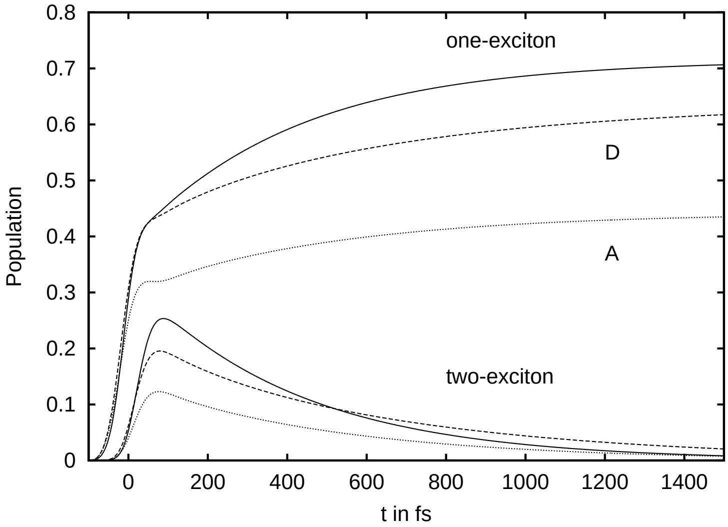

Figure 5.14: Comparison of the population of the one and two-exciton without disorder and for the disorder configurations marked A (dashed) and D (dotted) in fig. 5.13. Pump pulse with 100 fs duration and $64\mu J/cm^2$ energy at 850 nm.

now Gaussian energetic disorder of $\sigma = 300\,cm^{-1}$ is included representatives can be found easily that have a similar linear absorption spectrum [SBRM02] in the B850 region as the single LH2 molecules measured in Ref. [vOKK^{+}99] (5.13). In the literature there is a discussion about an elliptic deformation of the ring [vOKK^{+}99, NvG02] and also about inter-complex disorder, see e. g. [MK00b]. However here the simpler model is used which also was capable to explain the transient absorption experiments, and fewer parameters were necessary. In the following the molecules labeled A and D in Fig.5.13 will be used.

The redistribution of the overall populations $P_N(t) = \sum_{\alpha_N} \rho(\alpha_N, \alpha_N; t)$ referring to different multi–exciton states has been given in the previous section for the ideal symmetric case. As it can be seen in Fig. 5.14 for the complexes A and D, the EEA process is hindered by the inclusion of disorder. The decay of the two-exciton manifold to the one-exciton manifold becomes slower. As a result the internal conversion time $1/k_{IC} = 70\,fs$, which could reproduce the experimental data without disorder, seems to be just an upper boundary for this time constant. To come to a quantitative statement the averaged decay of the two exciton manifold for 100 different realizations of disordered LH2 has been calculated. If now a time constant of $35\,fs$ is used, the averaged and normalized two-exciton decay reproduces the result without disorder, with some minor deviations (Fig. 5.15). The decay is no longer mono-exponential. In the beginning the disordered LH2 relax faster, and at the end slower than the ideal symmetric ones. This is in good correspondence with experimental findings [THP^{+}01]. Another change that has been made in Fig. 5.15 is the assignment of the experimental pulse energies to

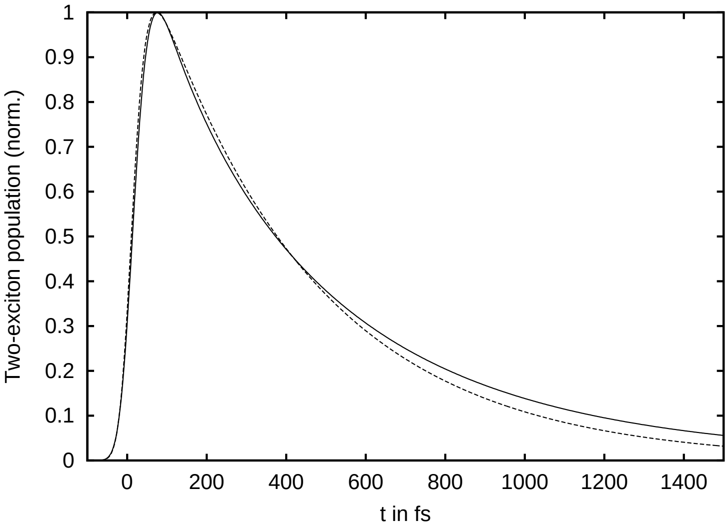

Figure 5.15: Comparison of the decay of the normalized two-exciton manifold without disorder (dashed, $1/k_{IC} = 70$fs) and averaged including disorder ($\sigma = 300cm^{-1}$) with a faster internal conversion rate (solid, $1/k_{IC} = 35$fs). Pump pulse with 100 fs duration and $64\mu J/cm^2$ energy at 850 nm.

the simulated ones. To reach the same two-exciton population twice the pulse energy is necessary in the case with disorder.

Choosing a special disordered configuration one can view the EEA process taking place: The *spatial* redistribution of excitation energy is considered now. Three different types of site–populations (with site–index m) are calculated: The reduced two–exciton population

$$P_m^{(ee)} = \sum_n \sum_{\alpha_2,\beta_2} C_{\alpha_2}(me, ne) C^*_{\beta_2}(me, ne) \rho(\alpha_2, \beta_2; t) \tag{5.3}$$

characterizes the reactant state of the EEA. The population of higher excited chromophores

$$P_m^{(f)} = \sum_{\alpha_2 \beta_2} C_{\alpha_2}(mf) C^*_{\beta_2}(mf) \rho(\alpha_2, \beta_2; t) \tag{5.4}$$

plays the role of the reaction channel and the one–exciton distribution

$$P_m^{(e)} = \sum_{\alpha_1 \beta_1} C_{\alpha_1}(me) C^*_{\beta_1}(me) \rho(\alpha_1, \beta_1; t) \,, \tag{5.5}$$

refers to the EEA product. In Fig. 5.16 these populations are plotted with a color code versus the time after the exciting pulse. Another view is given by Fig. 5.17 for the disorder configurations A and D, where the spatial excitation energy redistribution is depicted. The columns represent the populations $P_m^{(ee)}$ (right part

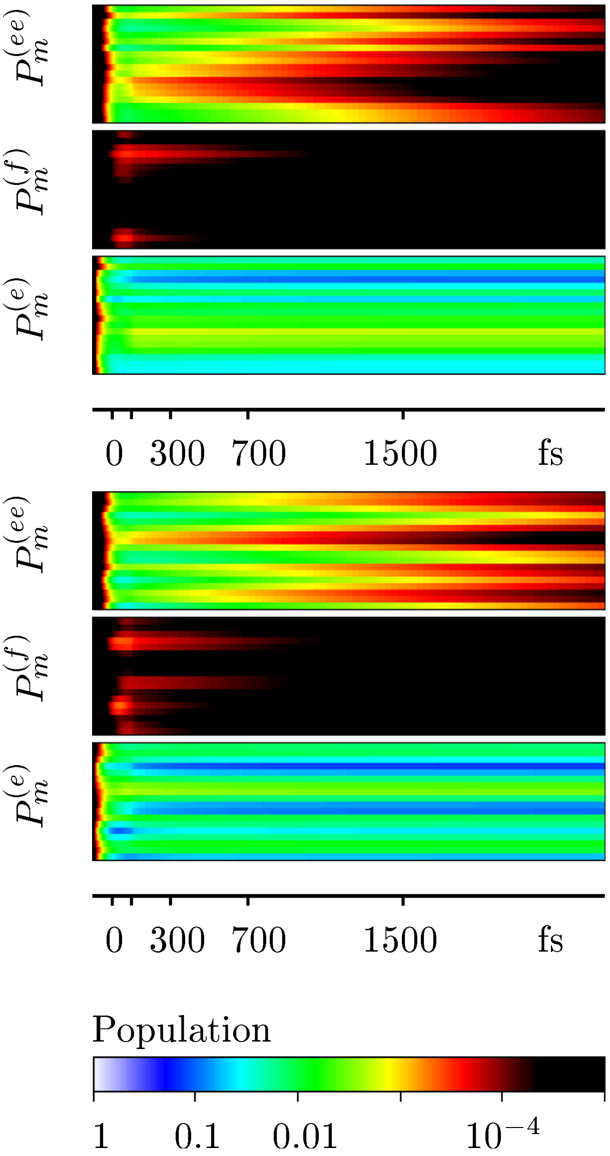

Figure 5.16: Time dependent site-population of the reduced two-exciton state, the doubly excited state at single BChls, and the single-exciton state. Upper and lower panel for the disorder configuration results in the single molecular absorption A (left) and D (right) of Fig. 5.13, respectively. Pump pulse with 100 fs duration and $64 \mu J/cm^2$ energy at 850 nm.

of each column) and $P_m^{(e)}$(left part of each column) whereas the spatial position of the columns resembles the BChls of the B850 ring. Pictures for different times up to 1500 fs after optical excitation corresponding to the $64\mu J/cm^2$pump-pulse of Fig. 5.4 are shown. The highest column for configuration A at 0 fs equals a population of 0.043. The comparison of the population distribution after 1500 fs and the deviations of the BChl energies as depicted in the lower panels of Fig. 5.17 shows a good correspondence and resembles the relaxation process (the largest positive deviation for configuration A corresponds to $436cm^{-1}$). After a population of the one– and two–exciton states in the course of the optical excitation (0 fs and 100 fs–picture in Fig. 5.17) there is a disproportionate increase of the one–exciton population at those sites with negative deviations of their energies form the mean value (300 fs and 1500 fs–picture in Fig. 5.17). This behavior gives a clear indication for the ongoing EEA. In conclusion, the present computations offer an impressive picture of sub–ps excitation energy dynamics and demonstrate how the chosen disorder configurations favor or disfavor the EEA process.

5.6 Simulation of Transient Absorption of a Disordered Ensemble of LH2

In order to simulate experimental spectra one has to consider the random orientation of the LH2 in the probe and the fact that structural and energetic disorder is present. This is taken into account by, first, rotating each ring antenna with randomly chosen Euler's angels. Note that the rotation with three different axes has to be used here, caused by the three-dimensional structure of the LH2 and the use of linear polarized laser pulses (cf. [Muk95]). Second, energetic disorder is considered by randomly distributed Q_y–energies according to a Gaussian distribution with variance $\sigma = 275\ cm^{-1}$. The disorder leads to a redshift of the absorption spectrum that is compensated by using a higher mean energy of the BChls which now equals 799 nm. The overall vibronic coupling factor has been set to $j_e = 1.5$ in order to fit the experimental data. The energy of the $S_1 \rightarrow S_n$ transitions have been retained unchanged. The averaged spectra have been obtained from Eq. 3.10 but with $n_{\rm CC}$ replaced by a summation over 10000 different LH2 divided by the probe volume. Of course, the MX–populations of Eq. 3.10 have been calculated separately for a given disorder configuration (remember that the use of Eq. 3.3 would be to time–consuming).

In Fig. 5.18 the pump pulse has been placed at 847 nm, i.e. slightly to the blue of the main absorption line. It undergoes only a small spectral shift. But due to two–exciton populations and EEA the shoulder at the short–wavelength side of the main absorption clearly observable at $\tau_{\rm del} = 1.5$ ps is suppressed at intermediate times. As discussed in the Section 5.4 this suppression of the

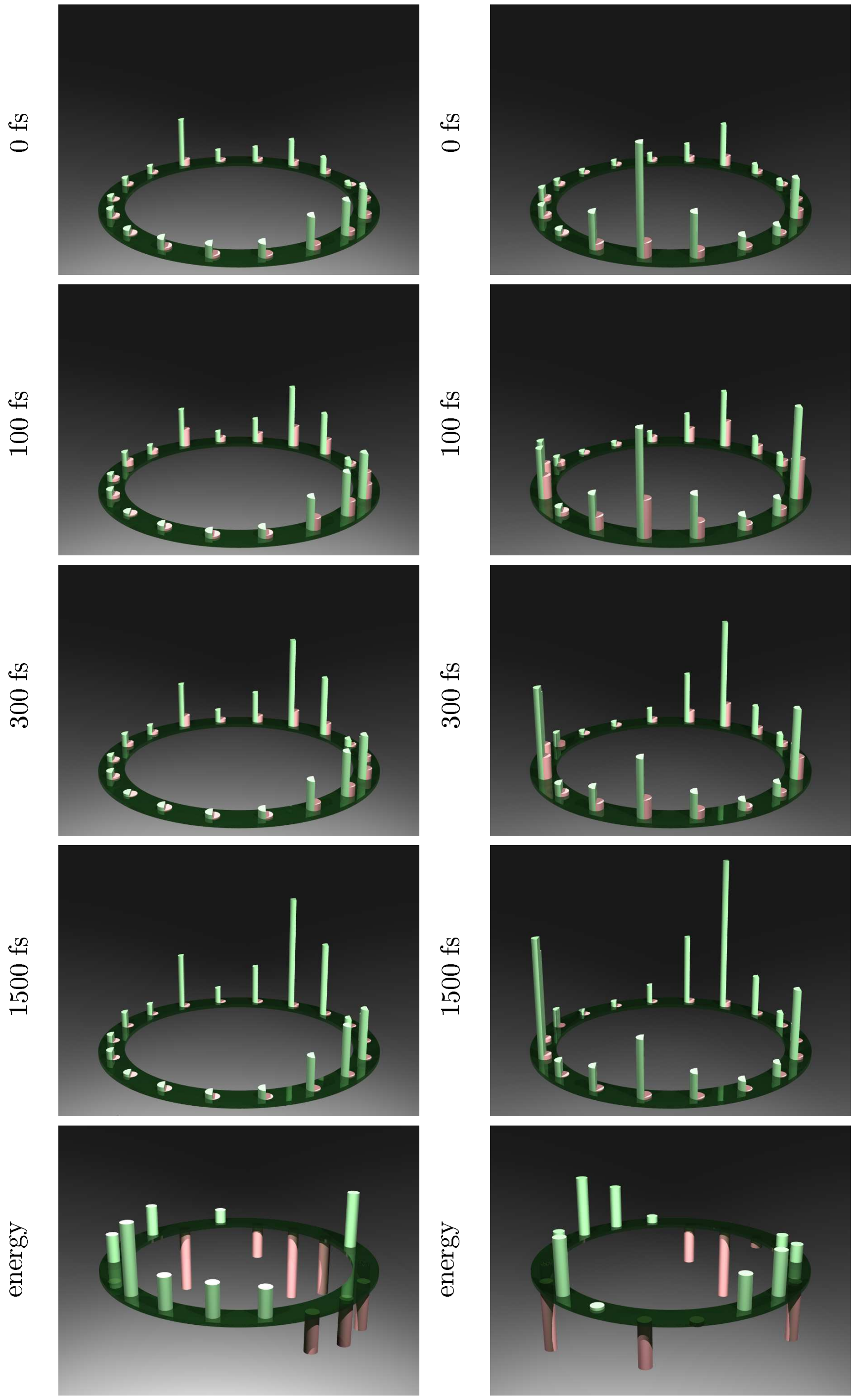

Figure 5.17: Spatial excitation energy redistribution in the B850 part of the LH2 for the two disorder configurations A (left pictures) and D (right pictures). The lowest panel gives the deviations of the BChl energies from the average value (see text).

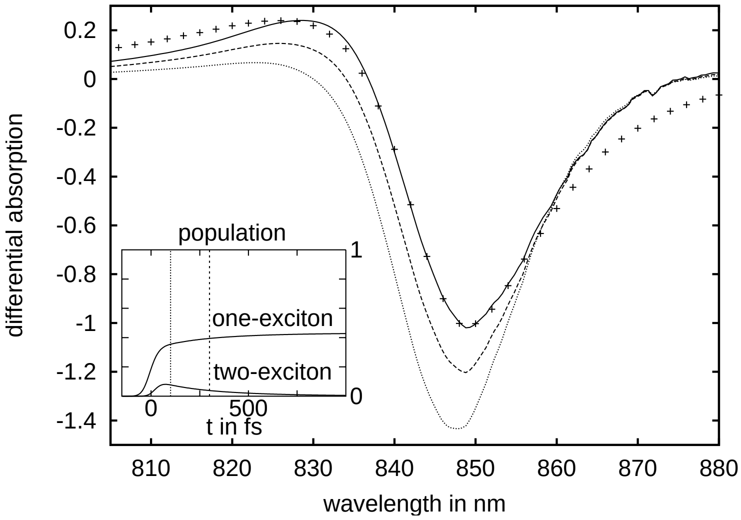

Figure 5.18: Normalized frequency resolved transient absorption of the B850 part of the LH2 according to Eqs. 3.10 as well as 5.2 at different delay times τ_{del}. The pump–pulse acts at 847 nm, with a duration of 100 fs and with an energy density of $64\mu J/cm^2$. Diagonal disorder of $275cm^{-1}$ and orientational averaging have been accounted for by sampling over 10000 configurations. Experimental data (shown by crosses) are taken from Ref. [FJLW98] (for a 150 fs long pump pulse with energy density of 100 $\mu J/cm^2$ and at $\tau_{\mathrm{del}} = 1.1$ ps). Dotted curve: $\tau_{\mathrm{del}} =$ 100, dashed curve: $\tau_{\mathrm{del}} = 300$ fs, full curve: $\tau_{\mathrm{del}} = 1.1$ ps. The inset shows the time evolution of the of population of the one– and two–exciton manifolds.

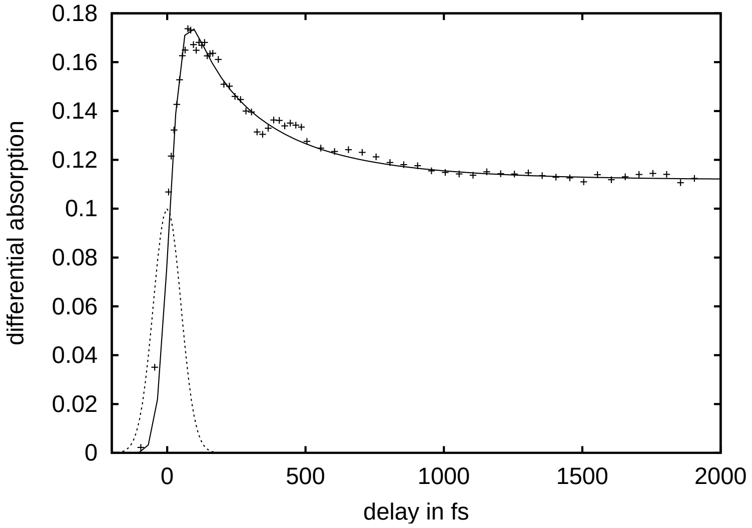

Figure 5.19: Non–normalized transient absorption at 847 nm (according to Eqs. 3.10) versus time after pump–pulse action and the account for disorder (all values like in Fig. 5.18). Experimental data (shown by crosses) are taken from Ref. [THP$^+$01]. The dotted line displays the envelope of the pump–pulse.

shoulder as well as its return at later times is a clear indication for a notable two–exciton population and resulting EEA. The present computations show that the mentioned signature for EEA indeed survives disorder averaging and should be observable in the experiment. To be at the border–line for observing the effect here a somewhat smaller pump–pulse intensity is taken than for the calculations shown in Figs. 5.9 and 5.10.

To underline the importance of the calculations further, the simulation are compared with the experimental data of Ref. [FJLW98] for the delay of 1.1 ps (Similar pump-probe spectra of the B850 ring can be found in Refs. [NAWP96, NJWP99]). In Ref. [FJLW98] a 150 fs pulse with a slightly higher energy density has been used, which should give a higher EEA signal, but this would be without any consequence for the considered large delay–time. The present simulations fit the experimental result quite well. The deviation at the red side of the transient absorption could be reduced by either choosing a bigger value of static disorder, introducing inter–complex disorder or an elliptic deformation. A somewhat different comparison of the computations accounting for disorder with the experimental data of [THP$^+$01] is given in Fig. 5.19 indicating that the present approach may reproduce the whole time–evolution of the transient absorption at a particular frequency.

Using a pump pulse with the wavelength 822 nm and the same intensity as before (Fig. 5.18), the absorption as displayed in Fig. 5.20 is about four times lesser than in Fig. 5.18. Therefore the effect of EEA can hardly be seen. Accord-

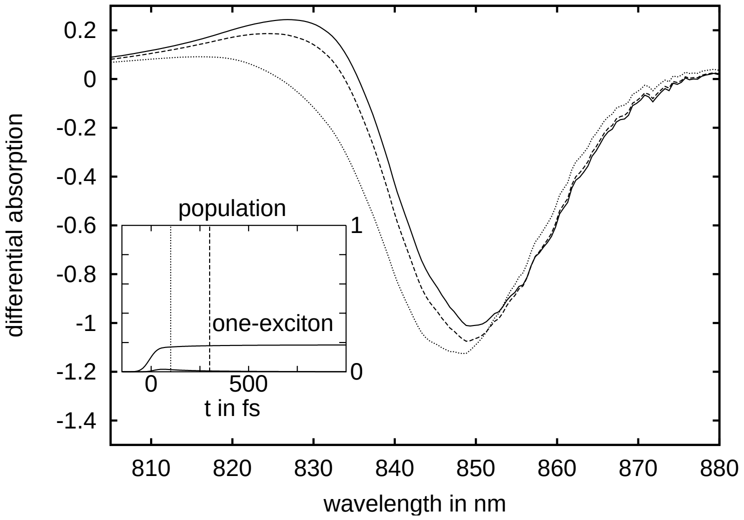

Figure 5.20: Normalized frequency resolved transient absorption of the B850 part of the LH2 according to Eqs. 3.10 as well as 5.2 at different delay times $\tau_{\rm del}$. The pump–pulse acts at 822 nm, with a duration of 100 fs and with an energy density of $64\mu J/cm^2$. Diagonal disorder of $275cm^{-1}$ and orientational averaging have been accounted for by sampling over 10000 configurations. Experimental data (shown by crosses) are taken from Ref. [FJLW98] (for a 150 fs long pump pulse with energy density of 100 $\mu J/cm^2$ and at $\tau_{\rm del} = 1.1$ ps). Dotted curve: $\tau_{\rm del} =$ 100 fs, dashed curve: $\tau_{\rm del} = 300$ fs, full curve: $\tau_{\rm del} = 1.1$ ps. The inset shows the time evolution of the of population of the one– and two–exciton manifolds.

ingly only the rise of the lower wavelength shoulder with increasing delay–time can be observed. Furthermore there is a fast redshift of the bleaching maximum, which is caused by intra manifold relaxation. This calculated redshift agrees very nicely with recent experimental data for the LH1 complexes [NvG02], which inhibit a similar but bigger water wheel like BChl structure called B875. It should be pointed out that caused by the symmetry of the LH2 system this spectral shift can only occur if the system inhibits a considerably amount of static disorder.

5.7 Summary

In continuing the discussion of exciton exciton annihilation (EEA) processes given in Chapter 2 the theory has been applied to the calculation of quantities observable in the experiment. Therefore, the transient absorption measured in an optical pump–probe experiment has been chosen. The need to incorporated two–exciton populations does not allow to apply standard–theories based on third–order response functions. Instead an approach has been taken which accounts for all orders in the pump– and the probe field strength. To understand the time–evolution of the transient absorption in detail an approximate formula has been used which is linear in the probe-pulse. It allows separating the whole spectrum into a ground–state bleaching part, into stimulated emission parts (from the two–exciton to the single–exciton manifold as well as from the single–exciton manifold to the ground–state), and into an excited state absorption part (from the one–exciton to the two–exciton manifold).

In order to elucidate signatures of two–exciton populations and EEA in intensity dependent transient absorption data the approach is applied to the B850 ring of the LH2 found in *Rhodobacter sphaeroides*. The most obvious indication for the EEA is the decay of the main bleaching as it has been discussed in the first Section of this Chapter. With an internal conversion time of 70 fs for a single BChl, intensity dependent pump-probe experiments could be reproduced. Using the frequency resolved simulation as another indication an intermediate suppression was found of the long–wavelength and short–wavelength shoulders of around the dominant single–exciton bleaching structure. The suppression is caused by stimulated emission from the two–exciton to the one–exciton state and the return of the shoulders follows from a depletion of two–exciton population according to EEA. This signature for two–exciton population and resulting EEA survives as a short–wavelength shoulder in the transient absorption if orientational and energetic disorder are taken into account thus indicating the possible observation of this EEA signature when doing frequency resolved transient absorption experiments with sufficiently strong varying pump–pulse intensity.

The EEA process is hindered by static disorder, because the delocalization of the excitons and also their overlap at the single chromophores is smaller. The internal conversion rate has to be increased to 35 fs get a similar dynamics as in the case without disorder. The simulations including averaging over disorder and different orientations were in good agreement with different experiments.

Of course the obtained results are not restricted to the B850 ring of the LH2. They may be also used for experiments at other biological as well as artificial chromophore complexes to give insight into the diversity of relaxation channels at higher optical excitation densities.

Chapter 6

From Structure to Dynamics: Defining the PS1 Model System and Simulation of Exciton Dynamics

6.1 Introduction

Photosynthesis of plants, green algae and cyanobacteria is governed by two large pigment-protein complexes, one of them is the photosystem I (PSI, cf. Section 1.4). The early events of photosynthesis happen on a femtosecond to picosecond timescale. They involve the light induced excitation of chromophore molecules in the antenna system and the subsequent transfer of excitation energy to the reaction center, where a charge separation takes place (for a recent review see [GvG01]).

Recently the three-dimensional structure of the cyanobacterial PSI of *Synechococcus elongatus* has been published with 2.5 Å resolution [JFK$^+$01]. For the first time it gave the spatial orientation and the binding pockets of each chromophore molecule in the core-antenna system. This antenna uses 96 chlorophyll *a* (Chl*a*), and 22 carotenoids as chromophores. Most of the chromophores are arranged in a slightly ring-like structure, which builds the actual antenna, and surround the reaction center (Fig. 6.8). The Chls can be divided into bulk Chls, which absorb around 680 nm and red Chls, absorbing above 700 nm. In the reaction center 6 Chls are arranged, including the special pair (named S1-S2, or P700 according to the main absorption peak) which is the primary electron donor in the charge transfer chain. The red Chls have been spectroscopically well characterized [PDS$^+$96]. Interestingly the spectrum of PS1 complexes of different bacteria shows the biggest diversity in this region [GvG01, GvSR$^+$01, GvAM$^+$94]. The assignment of Chls to the red pool is still under discussion.

The dynamics of excitation transfer and relaxation in the PS1 complex after the application of an ultrafast laser pulse have been measured using transient absorption [ANM00a, ANM00b], and fluorescence [GvSvM$^+$03, PTAG95, GvSR$^+$01, KGvS$^+$01]. These experiments cover a wide dynamical range from intra bulk equilibrium processes to the excitation trapping in the reaction center.

Since the publication of the new structural data several approaches have been made to find a proper microscopic model for the description of the spectroscopic features [DVFF02, BJK$^+$02, SLR$^+$02]. It is the aim of this Chapter to set up an exciton model for the PSI which is closely related to experimental data. The model is confirmed by computing time domain data using density matrix theory.

As a starting point for all further simulations, linear dichroism (LD) as well as absorption spectra were recorded for a wide temperature range. Using a genetic algorithm the best fit of the measured spectra as well as of the CD spectra given in Ref. [BJK$^+$02] determines the proposed PS1 model. In a next step the exciton model is evaluated by studying the kinetics of the system after photo-excitation with a 100 fs laser pulse. It will be shown that the calculated time dependent fluorescence agrees nicely with the experimental data.

6.2 Specification of the PS1-Model

To describe the optical features in the Q_y- absorption region and the fluorescence dynamics of photosynthetic antenna systems it suffices to use a two level model for each chromophore (e .g [vAVvG00]), and to restrict the calculations to the ground state and one-exciton manifold. The Chl$a$ model consists of the ground state and the lowest excited state, Q_y. Due to the protein environment the Q_y excitation energies ε_m of the chlorophylls are individually shifted.

The direction of the Q_y transition dipole moment is not exactly parallel to the y-axis of this molecule (opposite to the observations for the closely related Bacteriochlorophyll) but has an angle smaller than 90 degrees with the x-axis (Fig. 6.3 and 6.1). Here, the x-axis is determined by the vector from the N_A atom to the N_C atom in the Chl$a$ (Fig. 6.3). From LD experiments of Chl$a$ in solution an angle of 70 degrees [FNK88, NFK92] is determined (cf. Fig. 6.1). A simulation based on different experimental spectra of oriented Chl$a$ resulted in an angle of 90 degrees [vZWL$^+$95] for absorption and 107-109 degrees for emission (adopted to the above mentioned definition of the x-axis). Using time resolved fluorescence anisotropy and Förster Energy transfer simulations, an average angle for absorption and emission of 92-97 degrees has been found in peridinin-chlorophyll a-protein [KHG$^+$00]. Theoretical calculations favor an angle of 70 degrees [PG00], and 84.1 degrees [Bed98a, Bed98b]. In this Chapter an angle of 80 degrees will be used, as will be discussed later.

The negative CD of the Chl$a$ in the region of the Q_y absorption line is shown in Fig. 6.2, it is balanced by a positive contribution at higher energies.

The recently published PS1 structure [JFK$^+$01] gave the exact position as well as the orientation of all 96 Chl$a$ molecules for the first time. Their respective

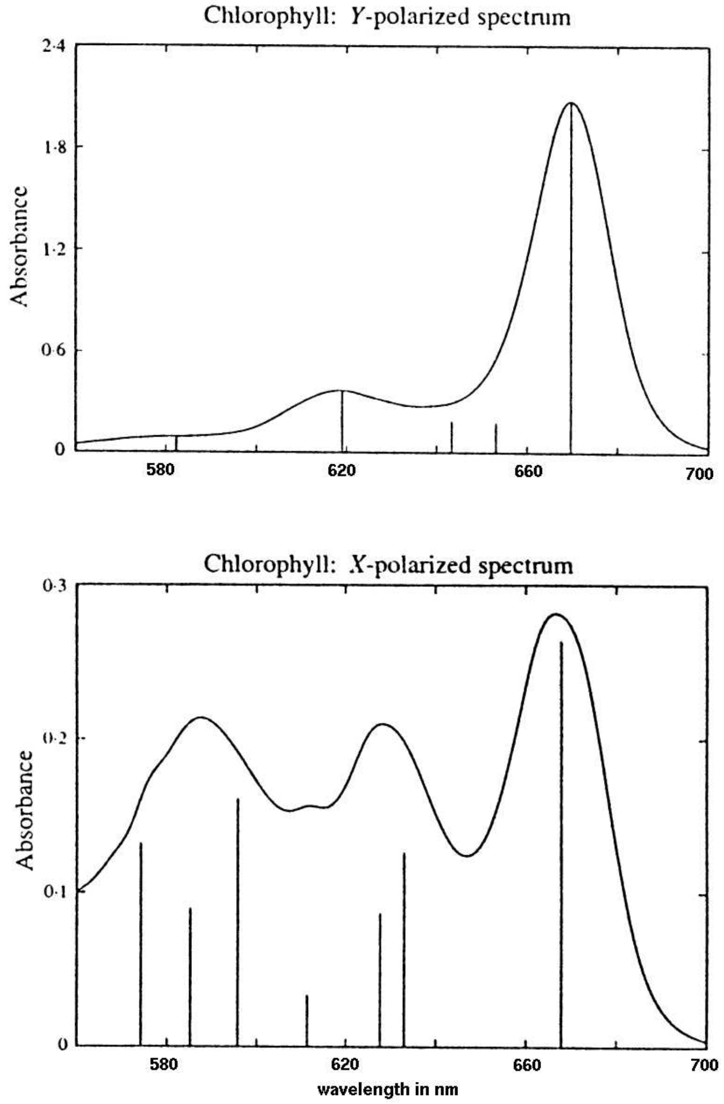

Figure 6.1: Y and X polarized spectra of Chl$a$ and stick spectra of the Gaussians needed to fit the spectra, taken from Ref. [NFK92]. Note the different scales of the absorbance.

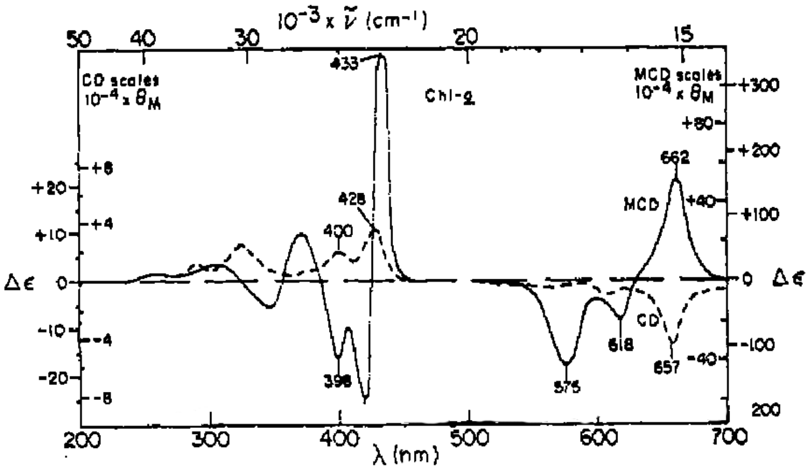

Figure 6.2: Optical activity: CD (dashed) and magnetic circular dichroism (MCD, solid) of Chl *a*, taken from Ref. [HS70].

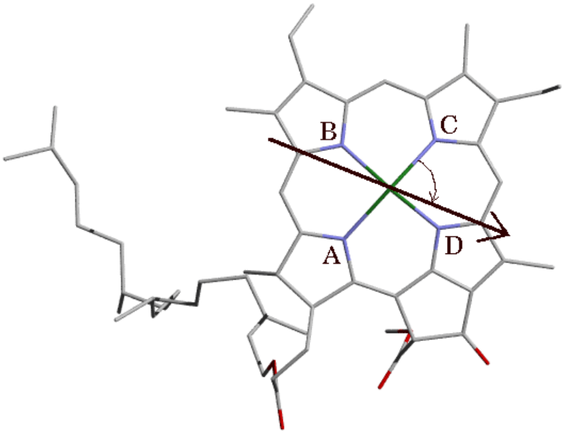

Figure 6.3: The Orientation of the $Q_y$dipole moment in Chl$a$. The positions of the Nitrogen molecules $N_A..N_D$ which are arranged around the central Magnesium atom are given.

dipole moments can be extracted easily. These dipole moments couple to each other and to the electric field. The coupling between different chromophores is described by the dipole-dipole approach [vAVvG00], which is valid if the chromophores are not too close to each other. In particular for the special pair P700 some adjustment due to their compact arrangement needs to be applied. Since only Chl$a$ is present in this complex, the a is neglected in the following.

The coupling of excitonic levels of the chromophores to vibrational levels of the protein surrounding is introduced by a spectral density. This quantity influences both the linear spectra due to line broadening as well as the relaxation in the dynamics.

The spectral density, used for the homogeneous linewidth as well as for the calculation of the energy transfer rates, is based on a fluorescence emission spectrum for the (weakly coupled) lowest energy Chl in the antenna system LHCII [PPvGvA97]. Neglecting any structure, it can be fitted by

$$J_m(\omega) = j_e \sum_{\nu=1}^{5} j_\nu \frac{\omega^2}{2\omega_\nu^3} \exp(-\omega/\omega_\nu)\,. \tag{6.1}$$

with $\omega_1 = 10.5\,cm^{-1}$, $\omega_2 = 25\,cm^{-1}$, $\omega_3 = 50\,cm^{-1}$, $\omega_4 = 120\,cm^{-1}$ and $\omega_5 = 350\,cm^{-1}$. For all Chls $j_v = 0.2$ is chosen. Only for the Chls responsible for the red-most state one uses $j_1 = 0.66$, $j_2 = 0.66$, $j_3 = 2$, $j_4 = 10$ and $j_5 = 0.8$ to reflect the different experimental findings in [GvG01] for the red states of the PS1 of *Synechocystis PCC 6803*. The overall coupling factor is set to $j_e = 0.06$ in order to adjust the dynamics of the whole system.

6.3 Linear Absorption, and Linear and Circular Dichroism

The linear absorption spectra for a wide temperature range are given in Fig. 6.4. They agree with spectra of the same complex reported earlier e.g. in Ref. [BJK$^+$02]. The linear dichroism which has been measured for the first time at low temperatures, is shown in Fig. 6.5. It has a remarkably rich structure, with the most striking feature of missing distinct negative peaks in the spectrum. Taking the arrangement of the antenna complex in the cellular membrane into account, the PS1 is optimized to absorb light which is polarized in the membrane plane rather than that which is polarized perpendicular to it. Additionally the 77K and room temperature CD spectra of Ref. [BJK$^+$02] will be used.

In order to fit all three types of spectra an adjustment of the bulk Chl energies becomes necessary. A special evolutionary algorithm is used, the so called evolution strategy [BS93], see Appendix E. From an initial set of site energies 20 different realizations are generated by the addition of randomly chosen energy deviations. They are normally distributed with a variance of $20\,cm^{-1}$. Then the

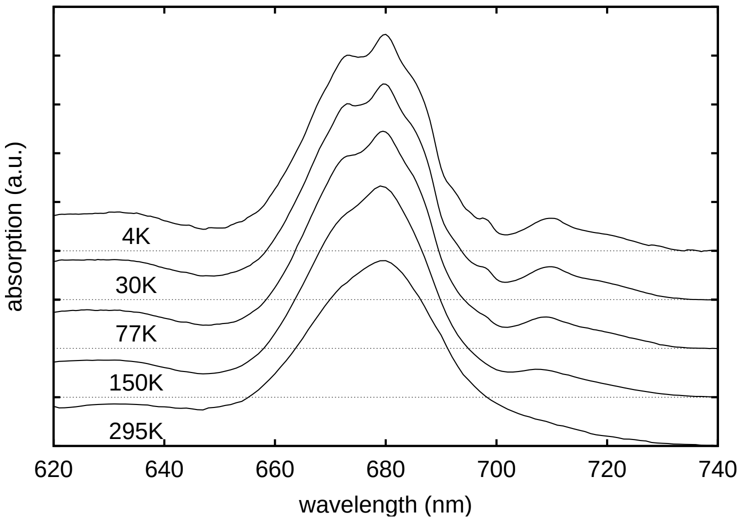

Figure 6.4: Measured absorption spectrum of trimeric PS1 complexes of *Synechococcus elongatus* for temperatures between 4 K and 295 K (as published in Ref. [BSN$^+$04]).

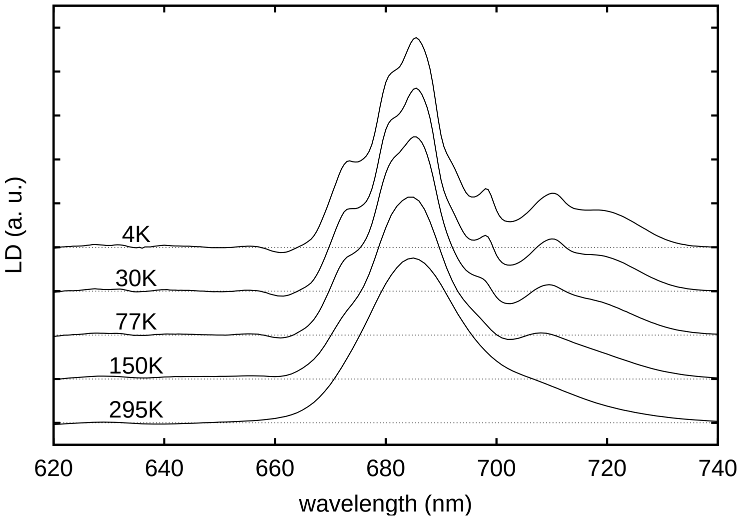

Figure 6.5: Measured linear dichroism of trimeric PS1 complexes of *Synechococcus elongatus* for temperatures between 4 K and 295 K (as published in Ref. [BSN$^+$04]).

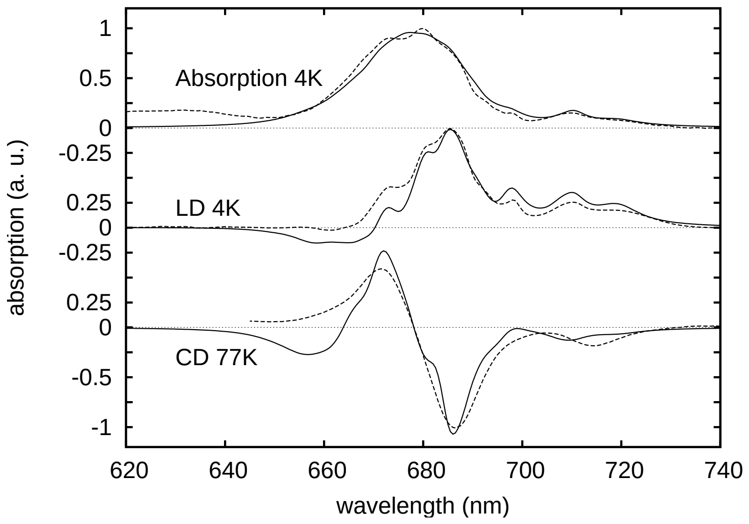

Figure 6.6: Comparison of the calculated broadened homogeneous absorption (see text) and LD at 4 K and CD spectra at 77 K (solid) with experimental data at the same temperatures (dashed, 77 K CD spectrum according to Ref. [BJK$^+$02]).

fitness of each realization is calculated, and the best 5 are used to build up the next generation in the following way. The most important mechanism is called mutation. With a possibility of 20% at each site the energy is added by a randomly chosen value, with a Gaussian energy distribution of a certain variance. The other important mechanism of the algorithm is crossover, i. e. two of the five distributions are chosen randomly and site by site the energy from either of them is taken by chance. As a last mechanism double mutation is introduced, which adds in the same way as described above an amount of energy to two neighbored chromophores. This accounts for the strongly coupled dimers, which may have a similar surrounding, and thus are similarly shifted in energy. One gets 10 new realizations from single mutations, 5 from double mutations and 5 from crossover. With this 20 realizations the procedure is started again, until after 500 generations a certain optimal value of the fitness parameter is reached. Using a greater amount of energy sets has also been tried, but only results in a longer duration of the procedure. The variances of the added random energies are also changed (see Ref. [BS93] and Appendix E).

As a fitness parameter the mean quadratic deviation of the calculated spectra with the experimental ones is used, for absorption (Eq. 3.15), LD (Eq. 3.17) and CD (Eq. 3.18). Additionally the quadratic deviation of the first derivatives of the experimental and simulated spectra is used in order to reproduce the structure of the spectra. The experimental spectra at lowest temperature have been taken, which was 4 K for absorption and LD, and 77 K for CD. The simulations have been done at the respective temperatures. To describe the nonconservative CD

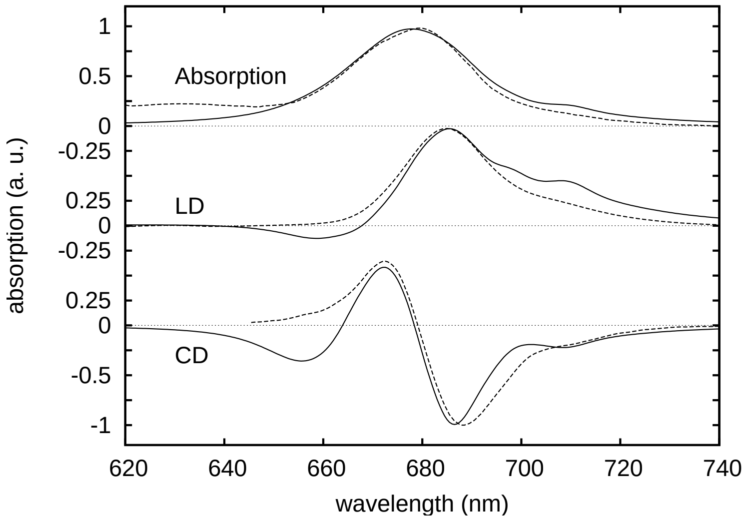

Figure 6.7: Comparison of the calculated broadened homogeneous absorption (see text), LD and CD spectra at 295 K (solid) with experimental data (dashed, same parameters as Fig. 3. The CD spectrum has been taken from Ref. [BJK+02]).

spectrum of the PS1 complex in the Q_y-region, Eq. 3.18 is used, which consists of two parts. One gives the conservative part of the CD due to the coupling between different Chls, the other the intrinsic CD of the Chls, which is proportional to the negative absorption spectrum ($CD_\alpha^{(chr)} = 0.35 \cdot |\mathbf{d}_\alpha|^2$).

Due to computational limitations, it was not possible to average over disorder. Instead, an additional homogeneous broadening of all states is used (included into the pure dephasing $\hat{\Gamma}_\alpha(T) = \hat{\Gamma}(T) = \gamma T^{1.3} + \gamma_0$ with $\gamma_0 = 275 cm^{-1}$ and a higher value for the overall coupling factor $j_e = 0.5$). After an optimal set of site energies has been found with the genetic strategy, this additional homogeneous broadening is removed and a configuration averaging is carried out to account correctly for inhomogeneous broadening.

The huge search space and the large energy difference between the red and the bulk Chls made it impossible for the evolutionary algorithm to assign the red Chls. As initial condition all Chls have the same energy but some needed to be shifted by hand into the red region. Several choices for shifting the energies of certain strongly coupled Chls into the red region have been tried, and the resulting simulated spectra have been compared with the experimental LD, CD and absorption spectra. Using the 4K absorption and LD spectra several combinations are possible. However, a contributing positive CD signal in the respective region only results from A31-A32-B7, A38-A39, and B37-B38. Corresponding to Ref. [GvSvM+03], the lowest exciton state of the trimer B31-B32-B33 has been adjusted to fit the 719 nm absorption (for the identification of the different Chls see Ref. [JFK+01] and Fig. 6.8). For the 710 nm line the pair A38-A39 and

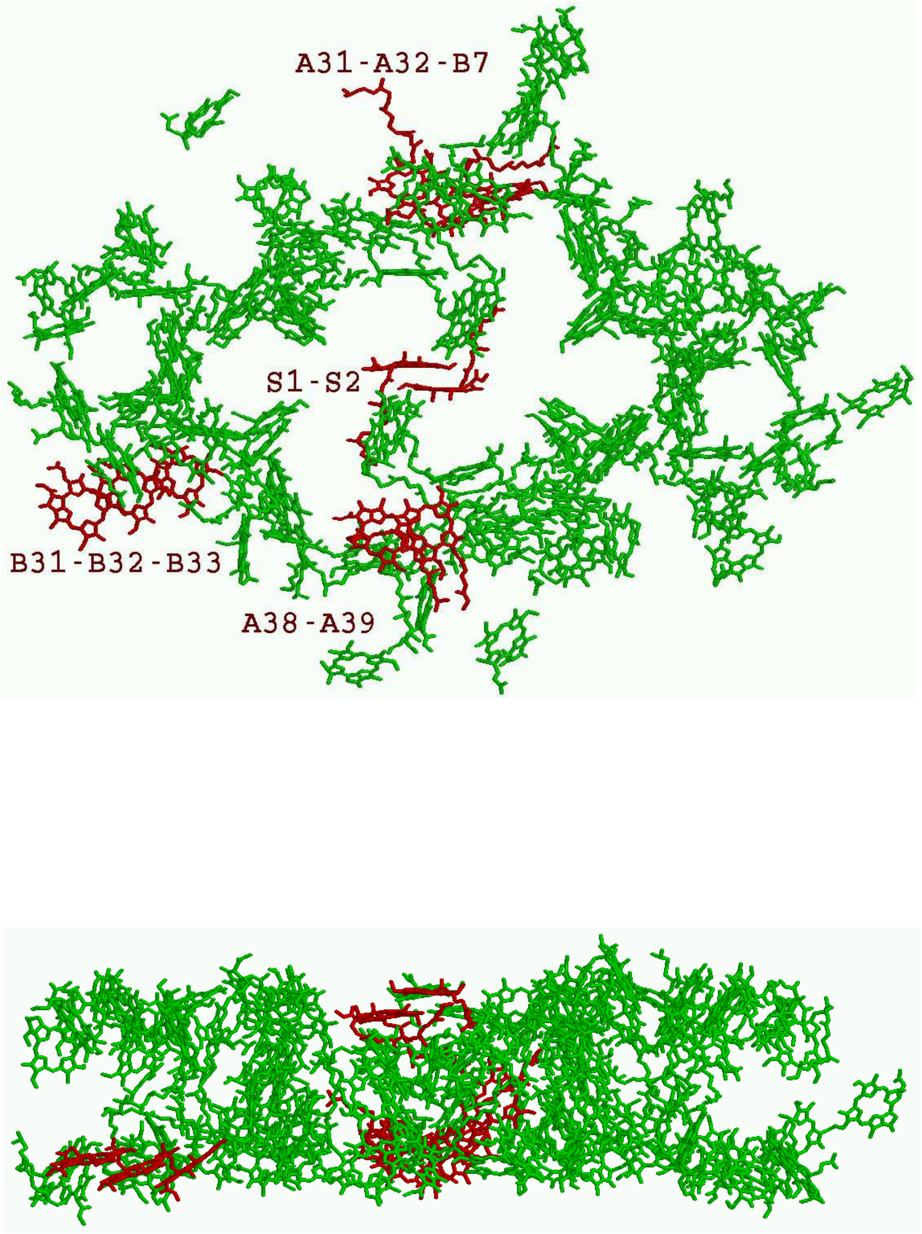

Figure 6.8: The Chls of the PS1 complex after Ref. [JFK$^+$01] (1jb0), the Chls with the red most absorption in the proposed model are marked. Top and side view, plotted with `rasmol`.

	S1	S2	S3	S4	S5	S6
S1(P700 A)	-150 (22)	343 (519)	-109	-44	16	7
S2(P700 B)		-150 (29)	-43	-101	6	14
S3(Acc. A)			-115	33	176	-9
S4(Acc. B)				152	-10	216
S5(A_0 A)					-146	2
S6 (A_0 B)						-129

Table 6.1: Deviations from the mean Chl energy of 14841 cm^{-1}(diagonal boxes) and the mutual coupling constants (off-diagonal boxes) for the Chls in the reaction center. All values are given in cm $^{-1}$. For the special pair (S1,S2) two different sets of energies and coupling constant are given (see text).

the A31-A32-B7 trimer have been chosen. Other choices for the red Chls are also possible, but this combination gave the best fitness value after applying the evolution strategy.

Another possible variation was to shift the angle of the Chl Q_y dipole moment within the molecular frame. Consistent with the present experience, a fit of LD and absorption spectra of a different antenna system called CP 29 could be established using an angle of 70 degrees with respect to the molecular x-axis [RCS+99]. However with the inclusion of the CD spectrum the best fitting angle for the PS1 complex changes to 80±5 degrees.

The result of the fitting procedure is shown in Fig. 6.6. The evolutionary strategy can be used with good results to determine parameters, which do not depend on the spatial environment of the single Chls, like the angle of the dipole moment, or the overall coupling factor. However, the fit of the energies of the bulk Chls by the evolution strategy using linear spectra is not unique. There are other sets of site energies, which give a similar good value for the fitness parameter. But once a set of energies has been established, one can try to simulate other experiments using them, and see if they are described properly.

The neglect of vibrational satellites and higher Chl states (e.g. the Q_x state) results in a slight deviation of the simulations with respect to the experimental data in the blue region (Fig. 6.6). By simply increasing the temperature to 295 K, the room temperature experiments can be described (Fig. 6.7) but without the pronounced bleaching of the red states the experimental spectra show. The experimental observation has been assigned to a blue-shift of the respective red states into the bulk antenna region at higher temperatures (Ref. [GvSR+01]).

The energies and coupling factors of the reaction center (RC) are given in Tab. 6.1. For the special pair, the dipole-dipole coupling approach is known to overestimate the coupling between these Chl molecules (Tab. 6.1, values given in brackets). Additionally, a charge transfer state, which is crucial for the biological function of the complex, has an impact [Bed98a, Bed98b]. As a result the energies of both Chls and their coupling are decreased in such a manner that the lowest state of the special pair remains at 698 nm (see Tab. 6.1, values without brackets). This lowers the upper state of the special pair into the main absorption band and thus the energy transfer from the bulk to the special pair is enhanced. The complete set of Chl energies gained with the above outlined procedure are given in Tab. 6.3. These values will be used in the following for dynamical calculations.

Comparing the present results to previously published ones [DVFF02, BJK+02], the range of the energies in the bulk antenna are the same. In Ref. [DVFF02] highly asymmetric energies in the special pair (710 nm and 674 nm) are favored, whereas similar to Ref. [BJK+02] the present model uses 681 nm for both. Another difference is the assignment of the red states. Whereas in Ref. [DVFF02] the lowest state is localized at the special pair, one exciton state lies below the special pair in in Ref. [BJK+02] (located on the dimer A32-B7 at 715 nm) and additionally some weak coupling monomers (B6, B39, L2, P1). The Chls on which the four lowest exciton states are located in the present model are given in Tab. 6.4. The lowest state of the complex is the lowest state of the trimer B31-B32-B33 at 719 nm, followed by the trimer A31-A32-B7 at 710 nm and the dimer A38-A39 at 708 nm. All these states are below the special pair S1-S2 at 698 nm. Whereas the B31-B32-B33 trimer lies at the periphery of the complex, the other low energy states are located in the vicinity of the reaction center.

The stick spectrum is shown in Fig. 6.9 a. At the respective eigenenergies the dipole moments of the exciton states according to Eq. 3.16 are plotted in units of the Chl dipole moment. Additionally, the simulated absorption spectrum at 4K (arbitrary units) is given for comparison. The states which are partly localized at the special pair (solid lines with crosses) or at the B31-B32-B33 trimer (dashed lines with stars) are plotted in Fig. 6.9 b. For both the lowest lying localized state has the larger part of the dipole strength. The two higher states of the trimer are also localized on it. In contrast the special pair contributes to a number of higher states, all in the upper half of the main absorption band. The delocalized nature of the latter states becomes clear in Fig. 6.10 where the number of Chls over which a state is delocalized $N(\alpha) = 1/\sum_n |C_\alpha(n)|^4$ is plotted versus the energy of the eigenstates $\hbar\Omega_\alpha$. The mean value for this number is 4.99 , with higher numbers in the main absorption band, and lower at the red and blue edges of the spectrum.

From hole burning experiments [ZMJ+02] and single molecule spectroscopy [JTG+00] it is known that the spectra of the PS1 complex are influenced by inhomogeneous line broadening. A possible way to include the broadening is to account for diagonal disorder, i. e. for each site energy a randomly chosen energy is added according to a Gaussian distribution centered at zero with a certain variance σ. This has been done and the spectra have been calculated by averaging over $10^3 - 10^5$ realizations (depending on the needed accuracy and computational time). Other approaches like the variation of the location and direction of the

Chl	ε_n(nm)	ε_n(cm^{-1})	Chl	ε_n(nm)	ε_n(cm^{-1})	Chl	ε_n(nm)	ε_n(cm^{-1})
S1	681	14691	A27	673	14855	B19	657	15225
S2	681	14691	A28	679	14724	B20	666	15019
S3	679	14726	A29	676	14783	B21	673	14853
S4	667	14993	A30	673	14861	B22	679	14730
S5	681	14694	A31	694	14404	B23	659	15176
S6	680	14712	A32	691	14472	B24	665	15043
A1	680	14701	A33	680	14715	B25	663	15077
A2	677	14770	A34	670	14927	B26	671	14906
A3	666	15021	A35	683	14646	B27	670	14921
A4	673	14848	A36	676	14785	B28	672	14891
A5	667	14991	A37	677	14779	B29	671	14895
A6	666	15019	A38	692	14442	B30	671	14911
A7	676	14795	A39	705	14192	B31	697	14355
A8	673	14864	A40	672	14886	B32	699	14304
A9	687	14564	B1	668	14975	B33	699	14300
A10	669	14955	B2	674	14832	B34	673	14865
A11	687	14565	B3	671	14899	B35	671	14909
A12	672	14884	B4	668	14965	B36	674	14843
A13	684	14616	B5	673	14853	B37	683	14651
A14	672	14882	B6	678	14755	B38	673	14855
A15	681	14677	B7	693	14424	B39	668	14969
A16	676	14799	B8	675	14808	J01	674	14829
A17	677	14779	B9	677	14777	J02	678	14751
A18	669	14946	B10	683	14642	J03	675	14805
A19	669	14947	B11	673	14860	K01	674	14844
A20	666	15026	B12	678	14760	K02	667	14993
A21	666	15024	B13	671	14892	L01	671	14914
A22	675	14804	B14	669	14939	L02	694	14406
A23	667	14996	B15	675	14815	L03	675	14805
A24	674	14833	B16	677	14769	M01	674	14842
A25	672	14884	B17	677	14762	X01	678	14744
A26	675	14820	B18	660	15160	PL01	679	14721

Table 6.3: Energies of the Chls in the PS1 complex as they are used in the present simulations. For better comparison with other publications, the values are given both in nm and cm^{-1} .

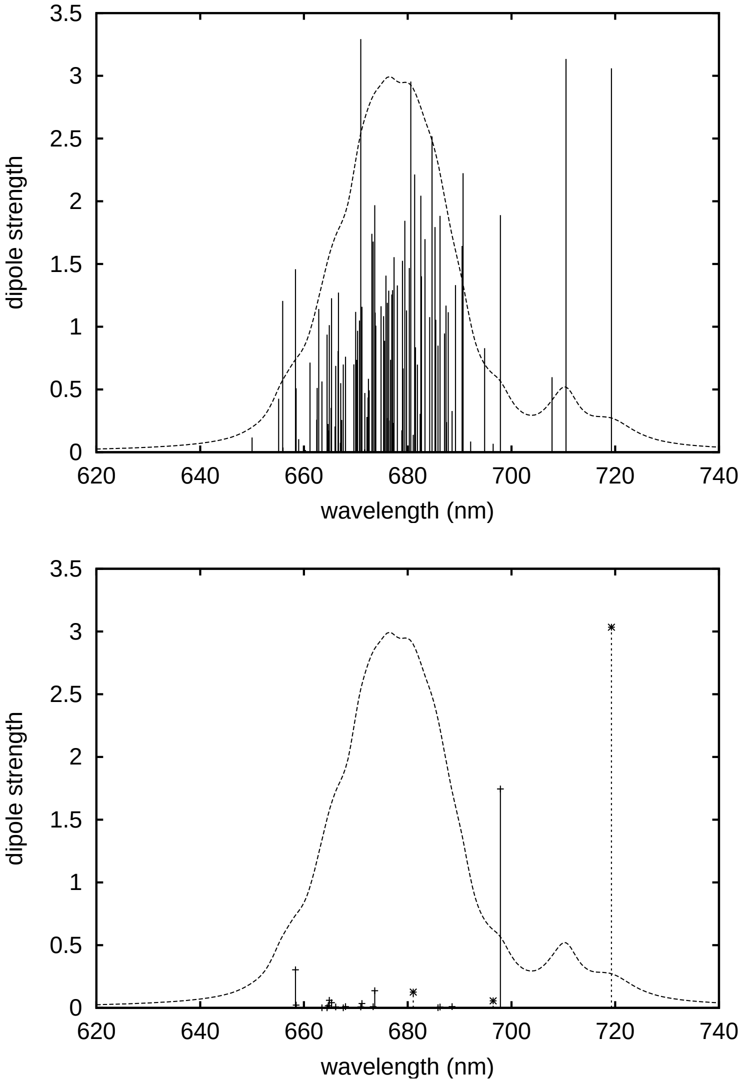

Figure 6.9: Stick spectrum of the PS1 model without disorder (part a). Part b: contribution of the special pair S1-S2 (solid with crosses) and the trimer B31-B32-B33 (dashed with stars) The calculated absorption spectrum at 4 K is shown as a dashed line in both figures.

n	a	b	c	d	$\triangle E$, cm^{-1}
S1	0	0	0	0.48	-150
S2	0	0	0	0.45	-150
A38	0	0	0.15	0	-399
A39	0	0	0.84	0	-649
A31	0	0.23	0	0	-436
A32	0	0.40	0	0	-369
B7	0	0.33	0	0	-417
B31	0.23	0	0	0	-485
B32	0.49	0	0	0	-536
B33	0.27	0	0	0	-541

Table 6.4: The sites contributing to the four lowest excitonic states of the PS1 complex, a (energy equals 719 nm), b (710 nm), c (708 nm), and d (698 nm). The probability $|C_\alpha(n)|^2$ ($\alpha = a, b, c, d$) is given, as well as the deviation from the mean Chl energy 14841 cm^{-1}.

dipole moments are also possible and lead to off-diagonal disorder but have been left for further investigations.

For the static energetic disorder in the present PS1 model a temperature independent Gaussian distribution is used with the variance $\sigma = 100\,cm^{-1}$. This results in a FWHM of the disorder of $235\,cm^{-1}$, which is an upper limit of the disorder in this complex. For the trimer B31-B32-B33, which has been assigned to the red-most lying absorption band, a different spectral density has been used as discussed above, as well as a higher value of the energetic disorder of $\sigma = 150\,cm^{-1}$. Using this inhomogeneous broadening the additionally, for the fitting procedure, introduced homogeneous broadening is removed (i.e. $\gamma_0 = 0$ and $j_e = 0.06$). The results are shown in Figs. 6.11 and 6.12 for 4 K (CD: 77 K) and for room temperature, respectively. The fit of the experimental data is still reasonable but not as good as without static disorder. This could be improved if one would include static disorder into the fitting procedure of the spectra, but at the moment it is still not feasible for such a large system.

6.4 Time Resolved Fluorescence.

Different ultrafast spectroscopic experiments have been reported for the PS1. Among them pump-probe experiments [ANM00a, ANM00b, HSBB93] and time resolved fluorescence [PTAG95, KGvS$^+$01, GvSvM$^+$03, BRS$^+$00, HSBB93] can be found. For calculating the transient absorption spectra of pump-probe experiments the two-exciton states, which give rise to excited state absorption, have to be considered. This has been done for smaller complexes, e.g. the antenna

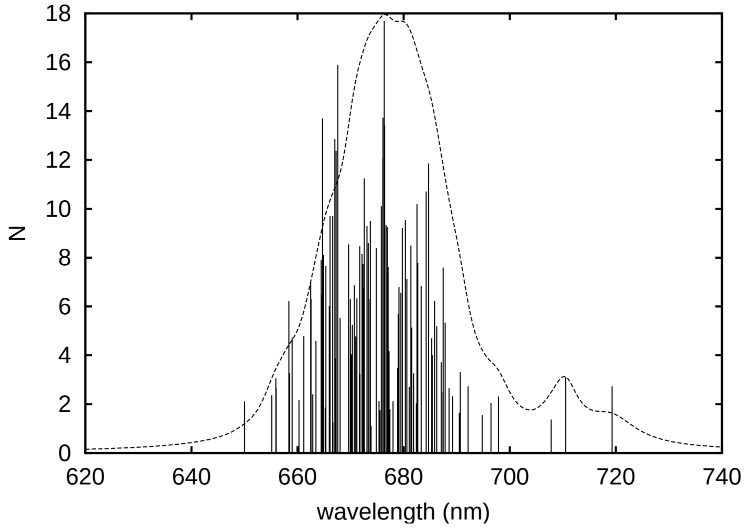

Figure 6.10: Delocalization length $N(\alpha)$ of all excitonic states versus energy, average delocalization length is 4.99 (simulated absorption spectrum at 4K is shown as a dashed line, without disorder).

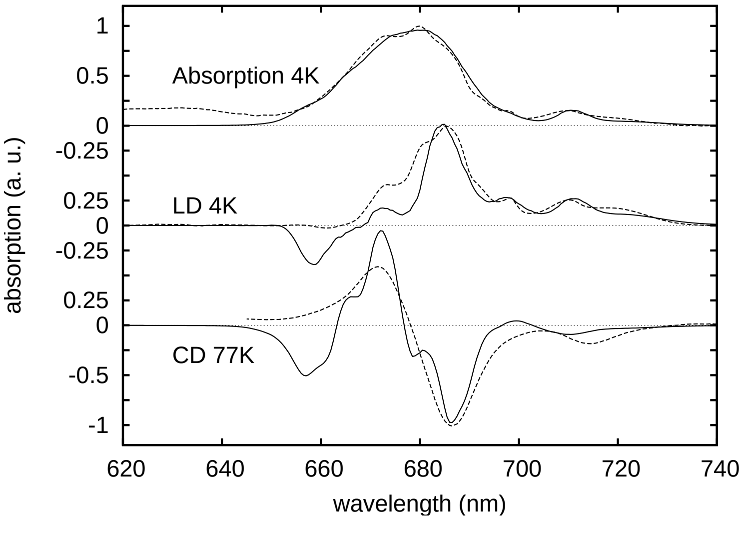

Figure 6.11: Comparison of calculated spectra (solid) including inhomogeneous broadening with experimental data (dashed) at 4 K and 77 K. Gaussian distributed diagonal disorder of $100\,cm^{-1}$ and averaging over 10^5 realizations.

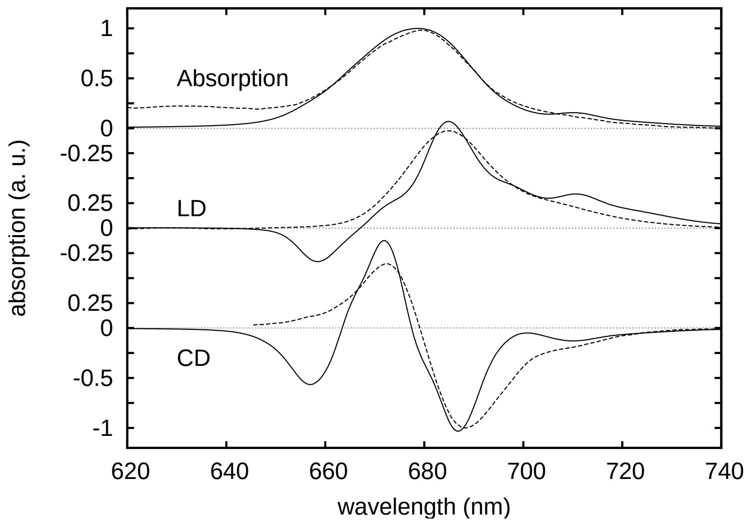

Figure 6.12: Comparison of calculated spectra (solid) including inhomogeneous broadening with experimental data (dashed) at 295 K. Gaussian distributed diagonal disorder of $100\,cm^{-1}$ and averaging over 10^5 realizations.

systems LH1 [NvG02], LH2 [BHS$^+$01, BM04a, NWvG03] (cf. Chapter 5), and LHCII [NSvAvG03] but is still computationally expensive for the PS1 complex. Therefore, the present calculations are restricted to time and spectrally resolved fluorescence which only deals with the one-exciton population and the ground state. Another restriction of the simulation is that one focuses on the excitonic antenna system, and neglects charge separation and transfer processes in the reaction center, i.e. no trapping of excitation takes place.

For the simulation of the dynamics of the PS1 complex after laser excitation static disorder has been included as discussed in the foregoing section as well as oriental averaging. If one uses an expansion with respect to the electric fields, the oriental averaging just gives a certain geometry factor (see, e.g. [NvG02, NSvAvG03, NWvG03]). However in a non-perturbative approach it has to be taken explicitly into account by rotating the molecule using randomly chosen Euler's angles. Only 100 samples are used, but due to the broad absorption bands at room temperature, the deviation from the average for a larger ensemble is not dramatic.

The disorder and orientally averaged populations $< \rho_{\alpha\alpha}(t) >_{DO}$ of the 96 one-exciton eigenstates of the Chls of the PS1 are shown in Fig. 6.13 (sorted by their energies). The populations have been calculated according to Eq. 2.21, after excitation with a linearly polarized 100 fs (FWHM) pulse with a wavelength of 650 nm. The pulse excites a whole range of eigenstates, with the main impact in the respective energy region. This is shown by the excitation of the highest states. With a time range of about 10 ps the system equilibrates. The population

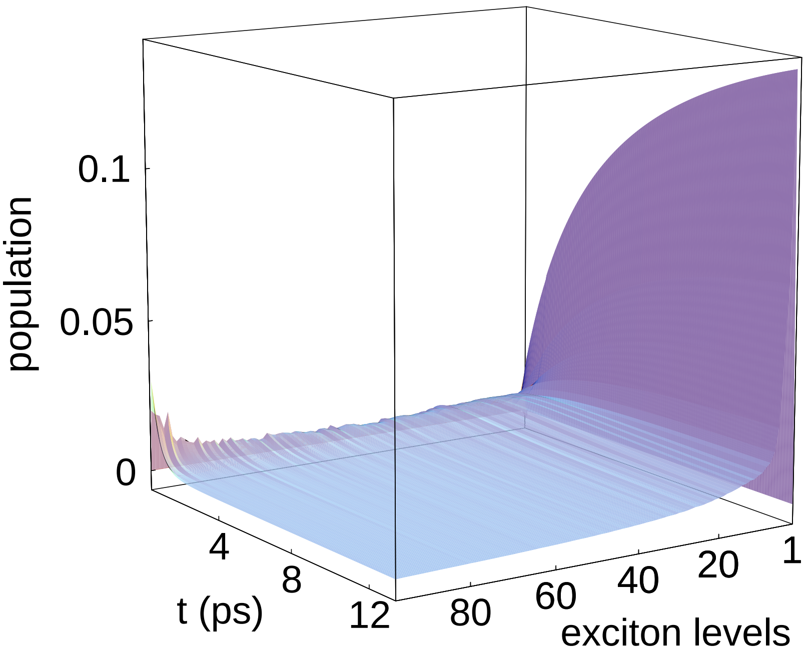

Figure 6.13: Population redistribution of all exciton levels after an excitation with an 100 fs pulse at 650 nm wavelength (T=295 K), averaged over 100 different orientations and realizations of disorder.

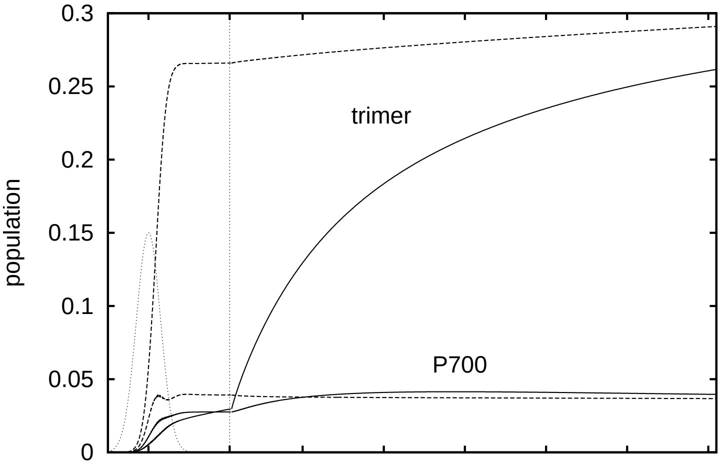

Figure 6.14: Redistribution of normalized site populations at the special pair P700 and the red-lying trimer B31-B32-B33 after an excitation with an 100 fs pulse (light dashed) at 650 nm wavelength (T=295 K, solid) and 710 nm wavelength (T=295 K, dashed), averaged over 100 different orientations and realizations of disorder (two different linear timescales).

of two groups of Chls, the special pair P700 and the trimer B31-B32-B33, which gives rise to the red-most state, is given in Fig. 6.14 for pump pulses with 650 nm and 710 nm wavelength. The populations are normalized after the action of the pulse, i.e. the sum of all one-exciton populations is one. The pulse at 710 nm directly excites the special pair and the trimer. Since the main absorption of the 650 nm pulse is in the bulk Chl region, the trimer and the special pair are mostly populated by transfer of the excitation energy at that pump wavelength.

In a next step, the fluorescence of the PS1 complexes is calculated for the two excitation wavelengths. As in similar experiments, the polarization of the fluorescence is turned 90 degrees with respect to the pump pulse polarization (Eqs. 2.21, 3.14). The time and spectrally resolved calculated fluorescence data are processed in the same way as it is done in the respective experiments [GvSvM$^+$03]. This results in the decay associated spectra (DAS). The key point is to fit the fluorescence data $F(\omega, t)$ at a number of frequencies ω_k with a sum of exponential functions $F(\omega_k, t) = \sum_i F_i(\omega_k) \exp(-t/\tau_i)$, using the time constants τ_i. Here, $F_i(\omega)$ represents the DAS for the time constant τ_i. This procedure is called global analysis, because the time constants become global fitting parameters, i.e. for each ω_k the same set of time constants τ_i is used, but the times are varied globally to get the best fit of the whole frequency and time resolved fluorescence. Numerically such a fitting procedure is done using a nonlinear multidimensional least square fitting algorithm, e.g. the Levenberg-Marquardt algorithm [PTVF92]. The result, the simulated DAS $F_i(\omega)$ for the two excitation wavelengths are shown in Fig. 6.15-6.18, where 20 different frequencies ω_k have been used. The procedure started after the end of the pump pulse.

For the excitation with a 650 nm pulse, six time constants were necessary to achieve a good fit of the simulated fluorescence, the respective DAS are shown in Fig. 6.15. The interpretation is straight forward. The fast components of 414 fs, 438 fs, and 1.0 ps describe the equilibration within the bulk antenna. The two similar components of 414 fs and 438 fs are needed to describe the different lifetimes within the bulk absorption band. Here, only the sum of both is given which represents the energy transfer part. The 1.0 ps component already shows some energy transfer to the red states, mostly by local energy relaxation from the directly excited higher states to the lower exciton states of the red Chls. The 3.4 ps component characterizes the equilibration of the bulk Chls with the red Chls at 710 nm, whereas the 10 ps component shows the equilibration of the bulk Chls with the red Chls at 719 nm. Slower processes could not be found in the simulations, since trapping processes were not included. The equilibrated fluorescence is given by the last component with infinitive lifetime.

In Fig. 6.16 the comparison of the simulated DAS with the experimental ones from Ref. [GvSvM$^+$03] is shown, for the different experimental time constants. Note that the simulated spectra have been shifted to the red by 2 nm to account for fast intramolecular relaxation. The fastest component (after the pulse) in this experiment was 3.4 ps, and the simulation at this time agrees perfectly with

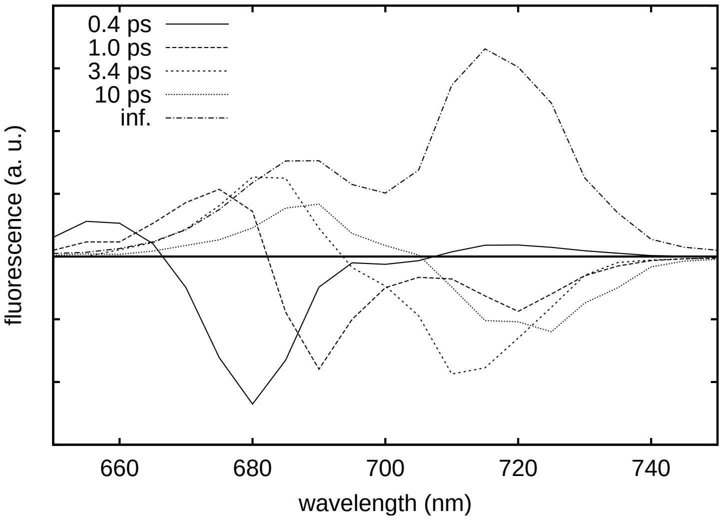

Figure 6.15: Decay associated spectra (DAS) of the fluorescence after excitation at 650 nm at 295 K (averaged over 100 different orientations and realizations of disorder). The 0.4 ps component consists of two different parts with the time-constants 414 fs and 438 fs.

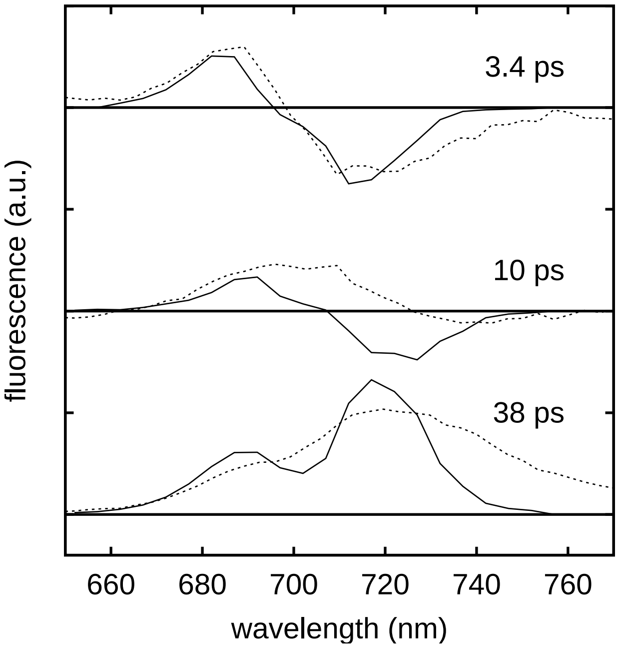

Figure 6.16: Comparison between experimental (dotted) and simulated (solid) DAS of the fluorescence after excitation at 650 nm at 295 K. The experimental DAS for 38 ps is shown with the fluorescence at infinite times in the present simulations. All simulated spectra have been shifted to the red by 2 nm.

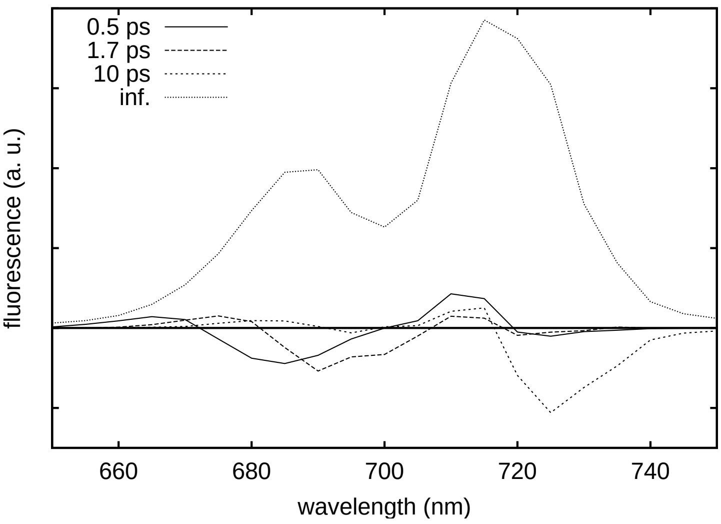

Figure 6.17: Decay associated spectra (DAS) of the fluorescence after excitation at 710 nm at 295 K (averaged over 100 different orientations and realizations of disorder).

the experiment (Fig. 6.16, upper part). Since the vibrational sideband of the Chls were not included, the simulated spectra do not reach as far to the red as the experimental ones. The 10 ps component in the experiment consists of a transfer and a trapping part, and if the trapping part is subtracted (not shown) the simulated DAS corresponds to the experimental one (Fig. 12). The slowest component, which is a 38 ps trapping component in the experiment and the infinitive lifetime component in the simulation is shown in the lower part of Fig. 6.16. The agreement is reasonably good, besides that the experimental DAS extends more to the red, as discussed above, and is broader.

Now the calculations are repeated for a 100 fs pulse with a wavelength of 710 nm in the region of the red Chls. The population dynamics (not shown) gives a sharp rise in that region, and does not change much afterwards. The DAS (Fig. 6.17) have been calculated, using four time constants. A fast energy transfer component with a time constant of 0.5 ps is given by the transfer from the red states to the upper exciton states of these Chls. Then an equilibration process from the 710 nm states to the bulk states with 1.7 ps time constant takes place, followed by a slower equilibration from the 710 nm states to the 719 nm state with 10 ps.

The comparison with the experimental DAS, Fig. 6.18, shows that at 0.7 ps a fast process is present in the experiment which has not been included into the simulations. One possible explanation is that this process is an internal vibrational relaxation of the Chls. Besides this, the agreement is quite reasonable. For the 10 ps component, the agreement could be improved by using an averaging

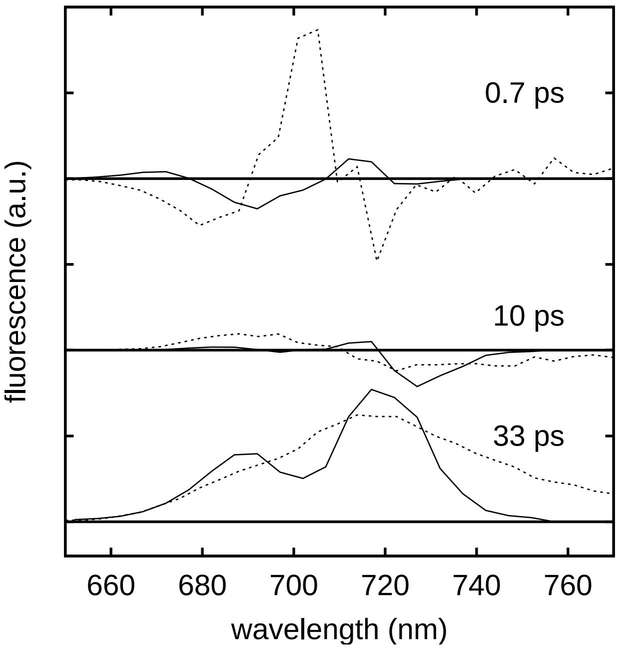

Figure 6.18: Comparison between experimental (dotted) and simulated (solid) DAS after excitation at 710 nm at 295 K. For the fastest experimental time the sum of the simulated DAS with the respective time constants 0.5 ps and 1.7 ps have been used. The experimental DAS for 33 ps is shown with the fluorescence at infinite times in the simulations. All simulated spectra have been shifted to the red by 2 nm.

over more PS1 complexes, whereas the agreement of the 33 ps component is the same as it has been discussed for the 650 ps excitation.

6.5 Summary

The publication of the new structural data of the PS1 complex of *Synechococcus elongatus* [JFK$^+$01] made a microscopic description of the linear spectra as well as the energy transfer pathways possible. Up to now, there have been published different approaches to set up a model for this complex [DVFF02, BJK$^+$02, SLR$^+$02]. All have in common an Frenkel exciton picture where the structural data is used to determine the arrangement of the dipole moments of the single Chls as well as the coupling between the Chls. The differences are how the energies of the single Chls are determined, either by semiempirical quantum chemical calculations [DVFF02], or by fitting linear spectra [BJK$^+$02]. Both earlier approaches fail to describe the low temperature spectra properly. The present PS1 model has been set up by first recording absorption and LD spectra over a broad temperature range, and then fitting the 4K spectra (also including the 77K CD spectrum taken from [BJK$^+$02]) with the aid of an evolutionary strategy [BS93]. As a next step it is used for the simulation of time dependent experiments [GvSvM$^+$03], similar as it has been done in Ref. [YDVF03] for the PS1 model of [DVFF02]. Using a microscopic model for the linewidth of the linear spectra, the extension to a density matrix formalism for calculating time dependent spectra has been straight forward. The time dependent fluorescence after photo-excitation at different wavelength has been simulated, and the results show a good agreement to similar experiments [GvSvM$^+$03]. The present exciton model of the PS1 is used in Section 7.4 to propose an exciton control experiment.

A new method to set up an excitonic model for a photosynthetic antenna system has been developed in this Chapter. The main idea is to use an evolution strategy to fit the low temperature linear spectra simultaneously. This method can be easily applied to other photosynthetic antenna systems, a possible candidate is the photosystem II, where new structural data has been published [FIM$^+$04].

Chapter 7

Towards Control: From Simple Models to Photosynthetic Antenna Systems

7.1 Introduction

It is of ongoing interest to study femtosecond laser pulse control of molecular dynamics. Because an experimental realization could be demonstrated for a variety of systems, the whole field evolved from pure theoretical speculations to a feasible experimental approach (for a recent overview see [RZ00, SB03, (Fe99, dVRRe01]). Originally, laser pulse control has been suggested by theoretical works of Tannor, Kosloff, and Rice [TKR86] and Brumer and Shapiro [BS86]. Then, the theory was put into the universal frame of the so-called Optimal Control Theory by Rabitz [PDR88, SWR88]. However, the experiments were less successful until the use of complex pulse shaping systems. Nowadays, the combination of a liquid–crystal or opto–acoustic femtosecond pulse shaper with a feedback control of the outcome has been introduced as a powerful tool for addressing various control tasks [dVRRe01]. Although originally concentrated on gas–phase systems, meanwhile examples have also been reported for the pulse control of the dynamics of polyatomic systems as well as of condensed phase systems [ZFW$^+$02, BDKG03], and even of biological systems [HWC$^+$02].

In the standard scheme of laser pulse control one tries to form a certain vibrational wavepacket and, in this manner, to move the molecule into the required target state. Typically, this might be a non–bonding electronic state corresponding to a removal of a certain part of the molecule. In the present Chapter, however, a somewhat different type of control task is discussed: the formation of an electronic (excitonic) wavepacket in a chromophore complex and the laser pulse guided spatial localization of the respective excitation energy within one chromophore. It becomes possible to choose certain energy transfer pathways selectively, and thus to gain more insight into the function of the antenna system. The basic idea discussed here is similar to the attempt to localize vibrational energy in a particular bond. Such local vibrational excitations do not represent eigenstates of the respective molecular system, but they might be formed by a certain superposition of eigenstates. The aim of the present Chapter is to show (at least theoretically) that it would be also possible to build up an electronic wavepacket formed by Frenkel excitons and to compress this wavepacket to a spatially localized excitation. In similarity to the case of vibrational wavepackets a coherent superposition $\sum_N \sum_\alpha A_{\rm tar}(\alpha_N)|\alpha_N\rangle$ of electronic eigenstates has to be achieved, in the present case, given by the different exciton states $|\alpha_N\rangle$.

Of course, when considering chromophore complexes under the action of an intensive optical field higher exciton states have to be taken into account, at least the possibility to populate the two–exciton manifold. Now, the formation of an (single–) exciton wavepacket and the excitation energy localization are accompanied by optical transitions into the two–exciton states. One expects the formation of a single–exciton as well as a two–exciton wavepacket, but the whole excitation possibly moves (via stimulated recombination from the two– to the single–exciton state) into a single excited chromophore state. This mechanism will be discussed in detail in the following. However, excitation energy relaxation and dephasing represent a further obstacle. As it is known from different studies (see, for example [MKM02]) environmental effects disturb wavepacket formation and thus reduce the yield of a concrete control task. Nevertheless, laser pulse control is also possible at the presence of dissipation. In the present study such dissipation enters via exciton–vibrational coupling. If it is not to strong it can be described by a density matrix which has been reduced to the electronic (excitonic) degrees of freedom of the system. Such an approach has been developed in Chapter 2 together with exciton exciton annihilation and will be used here.

There have been experiments showing coherent excitonic features in different pigment protein complexes, among them B820 [KPV$^+$96], and FMO [SBS97]. Considering the purified reaction center of *Rhodobacter sphaeroides* at room temperature in Ref. [AMDS99] oscillatory behavior in the time dependent anisotropy could be measured after a 80 fs excitation pulse. This has been assigned to the formation of a coherent superposition of excitonic states at the special pair in the reaction center, using the theoretical framework of Ref. [WH95]. Following this experiment it will be demonstrated that with an appropriately shaped pulse a coherent population of the excitonic states associated with the special pair of the PS1 should be reachable. This will lead to a damped oscillation of the population between the two Chls, and will show up in the anisotropy caused by the different orientations of the respective dipole moments.

To realize an excitonic control task one needs systems where the inter-chromophore coupling overcomes the vibrational relaxation, at least, within a certain time interval. Only for such systems one can expect wavepacket formation and its coherent driving by the externally applied field. Furthermore, a well–balanced distribution of the whole oscillator strength across all exciton levels would be very helpful for a spatial excitation energy localization, as it will be discussed in the following Section.

In the next Section the formalism of Optimal control of excitonic wavepackets will be applied to simple model systems, as a linear chain, or a random network of chromophores. Already these simple models give some insights for choosing the appropriate photosynthetic antenna system for the control task. In the following Section (7.3), the control of spatial localization of excitations in the FMO-complex is considered, applying the multi-exciton density matrix formalism, as it has been developed in Chapter 2. Additionally the effect of disorder and random orientations is investigated. The more theoretical approach on the FMO complex is complemented by calculations using the model of the photosynthetic antenna PS1 as it has been described in Chapter 6 in the last Section (7.4) of this Chapter, where an experimental scheme to detect the motion of excitonic wavepackets is proposed.

7.2 Control in Simple Model Systems and the Role of the Symmetry

First the Optimal Control approach is applied to simple model systems, to learn the general behavior of the algorithm as well as the basic demands of exciton-control. In particular the influence of the symmetry, that a certain spatial configuration of chromophores exhibits, on the success of the control task will be discussed. The chromophores used in this Chapter are simple two-level systems, with an not specified nearest neighbor interaction. No dissipation is included yet.

The first model is a linear chain of 5 chromophores, whose dipole moments are all parallel aligned. All have the same energy and the same nearest neighbor couplings. As the target state a localized excitation at a single chromophore ($n = 2$) is chosen. The result is shown in Fig. 7.1, where the ground state population, the target site population and the optimal pulse are given. The optimal pulse leads to a complete depopulation of the ground state, but the population of the target state is relatively weak. As it will become clear soon this is the result of the high symmetry of the system.

For the excitation of site $n = 2$ a certain linear combination of the exciton states $|\alpha_1\rangle$ has to be used as given in Tab. 7.1, first column. But due to the symmetry, some of these states have vanishing dipole-moments, and thus cannot be addressed by the electric field (Tab. 7.1, second column). To achieve a better control yield, this symmetry is broken by introducing different (random) site energies. This gives all states a certain dipole-moment (Tab. 7.1, last column). The result is shown in Fig. 7.2 where the target site population is indeed higher than in Fig.7.1.

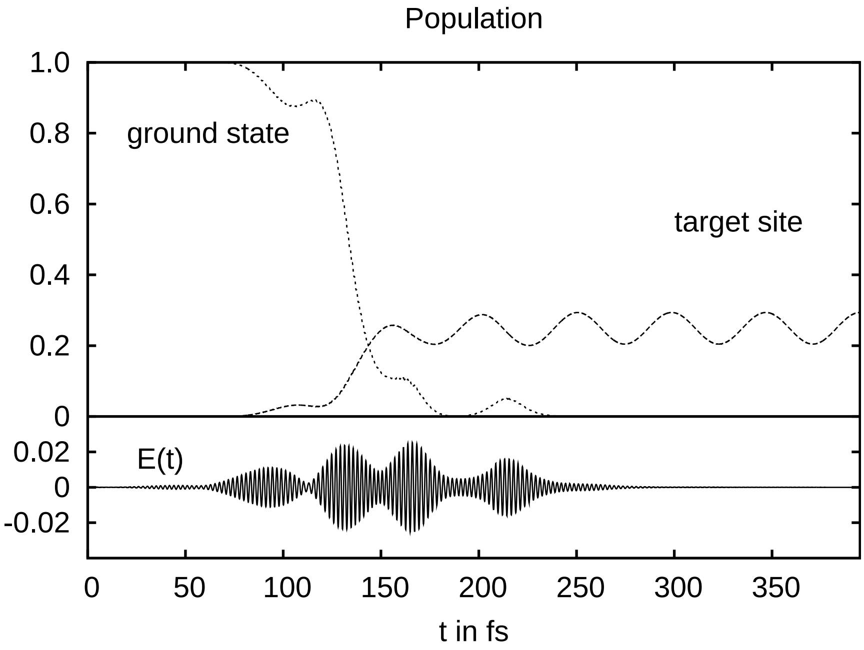

Figure 7.1: Population of the ground state and the target site (n=2) of a linear chain of 5 chromophores with equal energy and nearest-neighbor coupling. The optimal pulse is given in the lower part of the figure.

	$C_{\alpha_1}(n=2)$	$\lvert\mathbf{d}(\alpha_1,0)\rvert$	$\lvert\mathbf{d}(\alpha_1,0)\rvert_{rand.}$
$\alpha_1 = 1$	0.25	0.15	0.1
$\alpha_1 = 2$	0.25	0	0.03
$\alpha_1 = 3$	0	0.5	0.6
$\alpha_1 = 4$	0.25	0	0.4
$\alpha_1 = 5$	0.25	2.0	2.1

Table 7.1: Dipole moment and expansion coefficients of the target site for the linear chain.

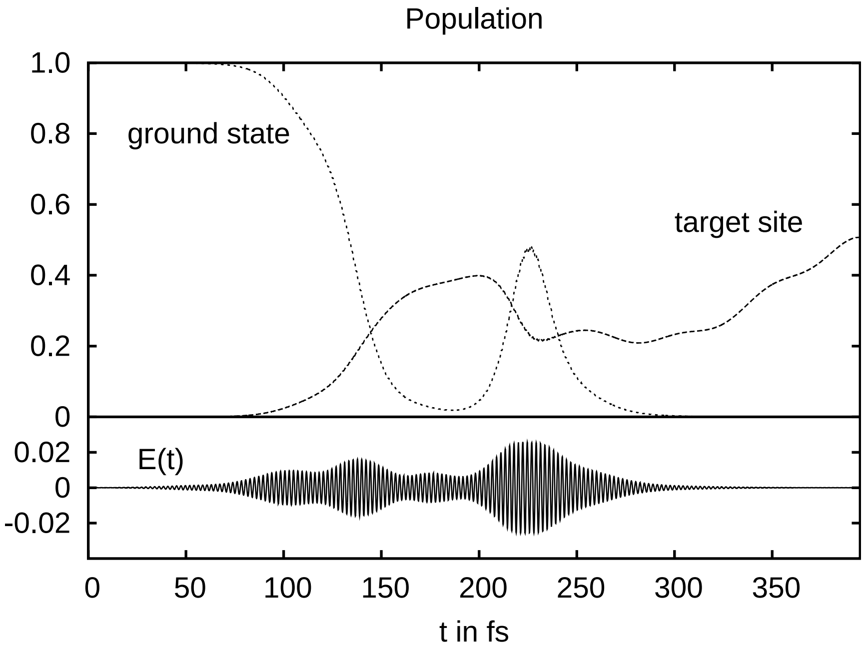

Figure 7.2: Population of the ground state and the target site (n=2) of a linear chain of 5 chromophores with different energies and equal nearest-neighbor coupling. The optimal pulse is given in the lower part of the figure.

This leads to the next model system, which is a configuration of chromophores with random energies and random couplings (not only of the nearest neighbor type). The dipole moments of the chromophores stay parallel to each other. In this configuration all exciton states have comparable dipole-moments.

The result is given in Fig. 7.3, and the target site population reaches nearly 1. To clarify the coherent nature of this population in Fig. 7.4 the population of all sites (left) and all excitonic states (right) is shown. A coherent superposition of the excitonic states $\alpha_1 = 1, 3, 4$ leads to the excitation of site $n = 2$ at the target time. But it is also clear that the site population is not static (as the respective states are not eigenstates of the system) but will oscillate between the chromophores at later times.

Since such a superposition state can only be prepared via optical excitation those systems are of most interest where all exciton levels have a suitable oscillator strength. Regular systems like J–aggregates or the LH2 antenna (cf. Chapter 5) are less suited because the oscillator strength is mainly concentrated to a single state. Instead, complexes with a spatial distribution of chromophores should be taken, for example, the photosynthetic antenna systems FMO or PS1. They represent rather complex systems, but from the present point of view they seem very appropriate because their structure is well defined and only disturbed by a relatively small amount of structural disorder.

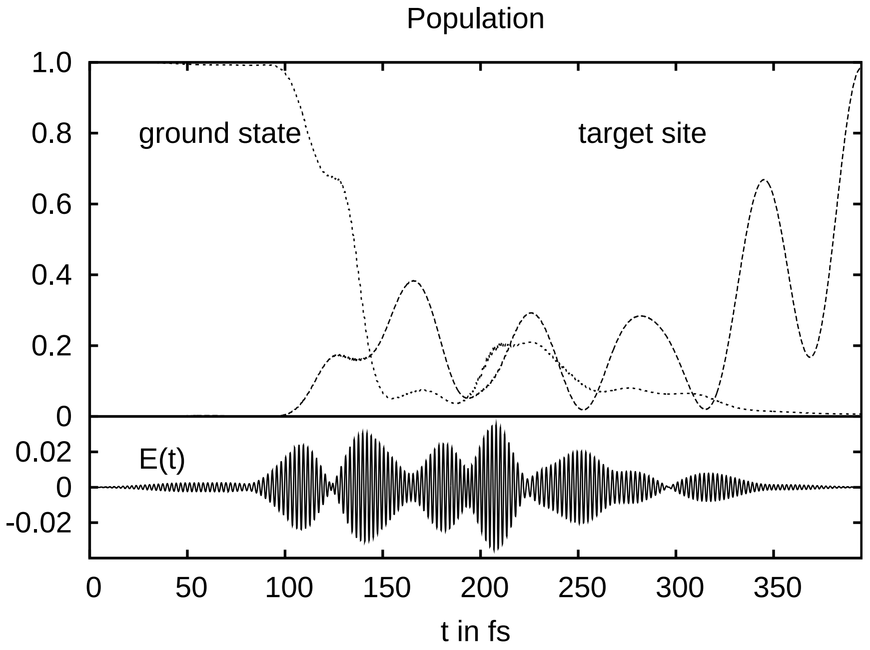

Figure 7.3: Population of the ground state and the target site (n=2) of a random network of 5 chromophores with different energies and different couplings. The optimal pulse is given in the lower part of the figure.

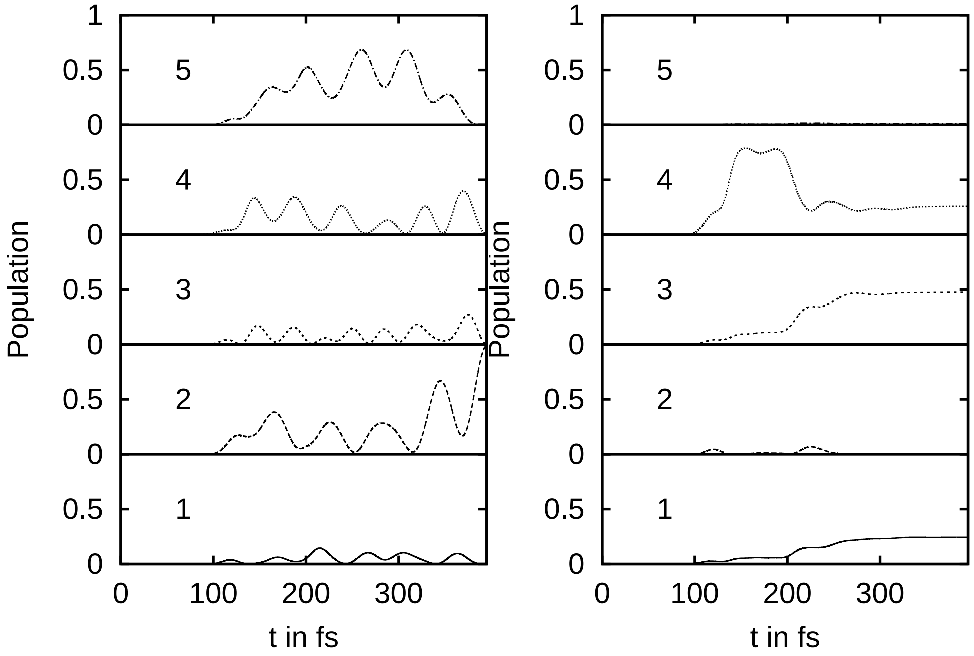

Figure 7.4: Population of all sites ($n = 1...5$, left) and all one-exciton states ($\alpha = 1...5$, right) of a network of five Chls. Target site was site 2.

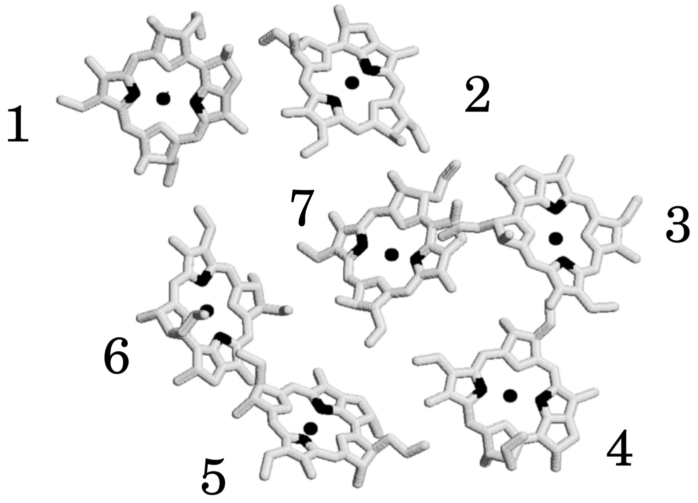

Figure 7.5: Picture of the arrangement of the 7 BChls in FMO using the structural data from Ref. [TM93] (Identifier 4BCL in the Protein Data Bank, rotated for better view). The atoms in the line of the respective Q_y dipole moments are marked (plotted with `rasmol`).

7.3 Coherent Control in the FMO Complex

There are different candidates of chromophore complexes which fulfill the demands of exciton control. Out of several reasons for the main investigations in this Chapter the FMO complex has been chosen. First the structure is well defined [TM93] (see also Section 1.3), and an excitonic model already exists, which reproduces linear low temperature spectra quite well [WPG$^+$02]. It represents a pigment protein complex of the photosynthetic apparatus which belongs to green sulphur bacteria (cf. e.g. the textbook [vAVvG00]). In nature, the FMO complex exists in a trimeric form and includes 21 Bacteriochlorophyll–*a* (BChl*a*) molecules, the monomeric form with 7 BChl*a* is of a modest extend and well suited for the present discussion (the *a* of BChl*a* is suppressed in the following). By the way, the need for a distribution of oscillator strength across all exciton levels favors the FMO complex with its spatially distributed BChl against high–symmetric arrangements of chromophores as in the light harvesting complexes of purple bacteria (LH1 and LH2) or in linear dye aggregates.

In the following the Optimal Control theory of Chapter 4 is applied to the FMO complex. The laser-pulse induced localization of excitation energy is suggested theoretically on a timescale of a few hundred femtoseconds to a few picoseconds. Based on a Frenkel exciton model for the BChl Q_y-excitations the laser pulse driven motion of an excitonic wavepacket into a spatially localized

	ε_n
$n = 1$	12350 (809.7)
$n = 2$	12465 (802.2)
$n = 3$	12160 (822.4)
$n = 4$	12350 (809.7)
$n = 5$	12600 (793.7)
$n = 6$	12480 (801.3)
$n = 7$	12460 (802.6)

Table 7.2: Energies (given in cm^{-1}) and corresponding wavelengths (in nm) of the BChls of FMO (cf. Ref. [WPG$^+$02]).

excitation of a single BChl is discussed in detail. Beside single-exciton states the description also accounts for two exciton levels. It includes excitation energy relaxation and dephasing as well as exciton-exciton annihilation after Chapter 2. The influence of structural and energetic disorder is also considered. Although the latter effects may decrease the efficency of excitation energy localization drastically, it is demonstrated that even under realistic conditions tailored laser pulses may deposit energy in a single BChl of the FMO complex.

7.3.1 FMO-Model System

The FMO model system follows the general approach of this work given already in Section 5.2. The BChl energies have been taken from Ref. [WPG$^+$02] (Tab. 7.2). The dipole-dipole coupling between the 7 BChls has been calculated using the structural data [TM93] and Eq. 2.7. The diagonalization of the respective excitonic Hamiltonian results in the energies and dipole moments of the excitonic states given in Tab. 7.4. The exciton-expansion coefficients are given in Tab. 7.3 and Fig.7.6. It is interesting that the delocalization length (Tab. 7.3, last column) is relatively small, it is between 1.25 and 2.35 for all states. It has been checked that this model describes the low temperature experimental spectra, the linear absorption, the linear dichroism, and, to a lesser extend, the circular dichroism quite well.

7.3.2 Dynamic Wavepacket Localization in FMO

As already indicated in the foregoing sections the discussion will concentrate on laser pulse localization of excitation energy. As a starting point, higher exciton manifolds beside the single–exciton one as well as the influence of orientational and structural disorder are neglected. These restrictions will be released in the following sections.

$\lvert C_\alpha(n)\rvert^2$	$n=1$	$n=2$	$n=3$	$n=4$	$n=5$	$n=6$	$n=7$	l_d
$\alpha=1$	0.005	0.015	**0.896**	0.079	0.002	0.001	0.002	1.24
$\alpha=2$	**0.715**	**0.218**	0.003	0.049	0.000	0.001	0.014	1.78
$\alpha=3$	0.032	0.014	0.083	**0.632**	0.067	0.029	**0.152**	2.35
$\alpha=4$	0.000	0.022	0.014	**0.119**	0.089	**0.684**	0.072	2.02
$\alpha=5$	0.020	**0.110**	0.000	0.074	0.090	0.044	**0.663**	2.14
$\alpha=6$	**0.227**	**0.619**	0.003	0.000	0.039	0.033	0.079	2.25
$\alpha=7$	0.000	0.002	0.000	0.056	**0.713**	**0.210**	0.019	1.80

Table 7.3: The exciton expansion coefficients $|C_\alpha(n)|^2$of the the used model of BChl in FMO, as well as the delocalization length $l_d = (\sum_n C_\alpha(n)^4)^{-1}$ Contributions > 0.1 are printed in bold.

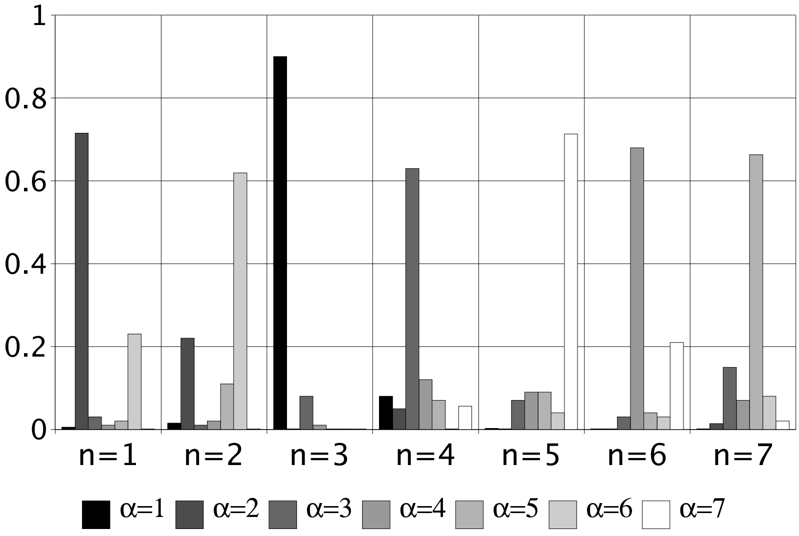

Figure 7.6: The exciton expansion coefficients $|C_\alpha(n)|^2$ of the used FMO exciton model.

	$\|d_{\alpha,x}\|^2$	$\|d_\alpha\|^2$	$\hbar\Omega_\alpha$
$\alpha = 1$	0.64	0.66	12139 (823.8)
$\alpha = 2$	0.16	2.13	12290 (813.7)
$\alpha = 3$	0.01	0.95	12322 (811.5)
$\alpha = 4$	1.21	1.39	12426 (804.7)
$\alpha = 5$	0.61	1.21	12485 (801.0)
$\alpha = 6$	0.09	0.16	12535 (797.8)
$\alpha = 7$	0.07	0.50	12667 (789.4)

Table 7.4: Square of single-exciton dipole moments $\mathbf{d}_\alpha$ and their x-component (in units of the square of single Q_y dipole moments of 40 Debye^2, cf. Ref. [WPG$^+$02]) and the respective excitonic energies (given in cm^{-1}as well as the corresponding wavelengths in nm). The electric field is polarized in the x-direction, if no orientational averaging is applied.

τ_α	4 K	77 K	265 K
$\alpha = 1$	∞	193 ps	8.5 ps
$\alpha = 2$	82 ps	33 ps	3.5 ps
$\alpha = 3$	7.4 ps	5.8 ps	1.8 ps
$\alpha = 4$	8.8 ps	6.6 ps	2.0 ps
$\alpha = 5$	4.0 ps	3.3 ps	1.4 ps
$\alpha = 6$	2.0 ps	1.9 ps	1.1 ps
$\alpha = 7$	1.8 ps	1.8 ps	1.2 ps

Table 7.5: Lifetime of the different excitonic states, $\tau_\alpha = 1/\sum_\beta k(\alpha \to \beta)$.

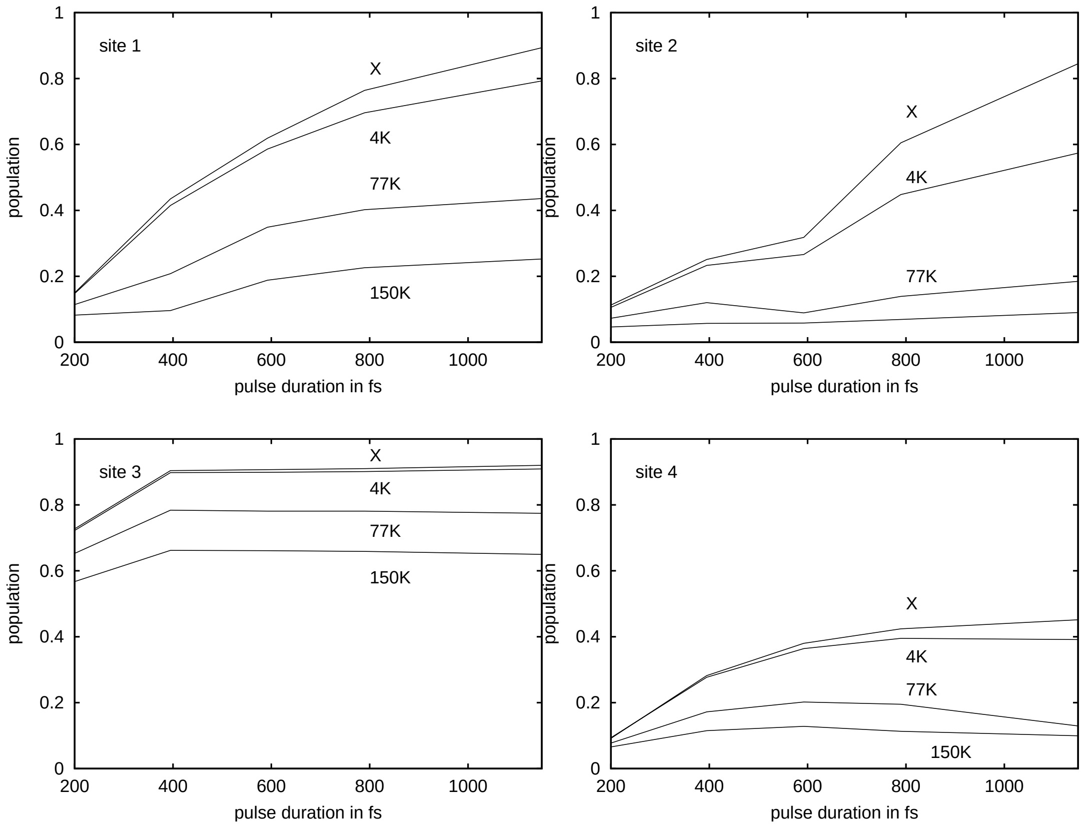

Figure 7.7: Population of a single BChl Q_y-state at site m_{tar} at t_f after excitation with an optimal pulse versus the duration $\tau_c = t_f - t_0$ of the optimal pulse, at different temperatures. Additionally, the populations calculated in the absence of dissipation are given (marked with X). Up to 50 iterations have been used. The penalty factor λ has been set to 0.25.

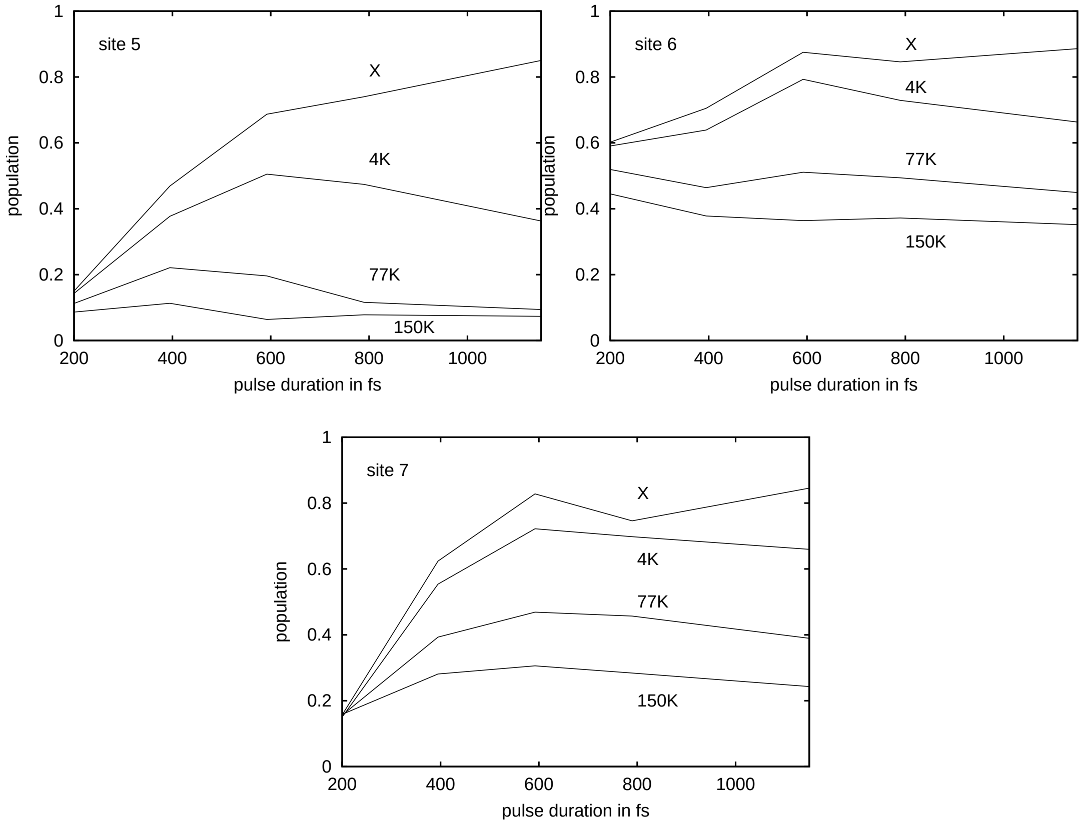

Figure 7.8: Population of a single BChl Q_y-state at site m_{tar} at t_f after excitation with an optimal pulse versus the duration $\tau_c = t_f - t_0$ of the optimal pulse, at different temperatures. Additionally, the populations calculated in the absence of dissipation are given (marked with X). Up to 50 iterations have been used. The penalty factor λ has been set to 0.25.

A completely ordered ensemble of FMO complexes is taken into account with the x–component of the exciton transition dipole matrix element coupling to the electric field–strength of the linearly polarized laser pulse (cf. Table 7.4). In order to analyze the localization of the excitation energy its dependence on the length τ_{c} of the control pulse is studied, as well as the temperature dependence.

According to simulations following the formulation of the Optimal Control theory in Chapter 4 Figs. 7.7, 7.8 show the obtained results for every BChl of the FMO–complex ($m_{\mathrm{tar}} = 1, ..., 7$) and three temperatures and completely without dissipation. The population of the Q_y–state of one of the seven BChl (the target state) is drawn versus the pulse duration $\tau_c = t_f - t_0$. This time varies between 200 and 1200 fs in steps of 200 fs. The drawn values for the site populations are the result of 50 iterations of the forward and backward propagations (cf. Chapter 4). This low value of iterations does not necessarily give already the the optimal result. However these figures can be used to compare the different control tasks, and to find suitable tasks for the further investigations.

The calculations presented in Fig. 7.8 have to be considered as reference calculations for the subsequent discussion. They try to achieve a complete population of the target state $|m_{\mathrm{tar}}e\rangle$. The difference between $P_{\mathrm{tar}}(t_f)$ and 1 may be distributed on other singly excited BChl but also on the ground state (probability conservation in the absence of two–exciton states read $1 = P_0 + \sum_\alpha P_\alpha$). A more involved discussion of this point follows in Section 7.3.3.

As it has to be expected the achieved population of the target state increases with decreasing temperature and increasing pulse length. The behavior is typical for all shown control tasks. However, the achieved total population of the target state depends on the chosen BChl at which excitation energy should be localized. At 4 K the excitation of BChl $m = 2, 4, 5$ stay below 0.6. This result can be explained by the magnitude of the excitonic dipole matrix elements (their component showing in the polarization of the laser pulse). According to Table 7.4 the exciton levels 3, 6, and 7 have the smallest values. As can be directly deduced from Fig. 7.6 those dominate the excitonic wavepacket Eq. 4.1 just for $m = 2$, 4, and 5.

The decrease of the target state population with increasing temperature results from the fact that excitonic energy relaxation and dephasing have an increasing influence when temperature becomes larger. Such an increase of dissipative effects acts counter productive to the external field which tries to form a wavepacket that should become localized in space at $t = t_f$. Of course, the details of these dissipative effects depend on the concrete environment of the BChl and the its coupling strength to the surrounding BChl (cf. Chapter 2).

The way the target state population increases with increasing length of the control pulse is different for different BChl, but first of all reflects the fact, that an increase of τ_{c} offers the possibility to concentrate more probability in the target state. However, if τ_{c} becomes too large the excitonic wavepacket forming the localized state decays during its formation due to dissipative effects. This explains

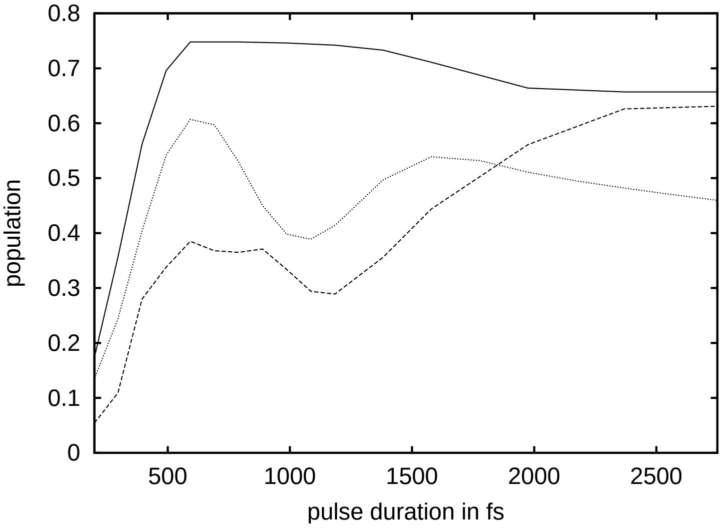

Figure 7.9: Renormalized population (Eq. 7.1) of the target site $m_{tar} = 7$ versus the duration τ_c of the pulse. Solid line: after excitation with an optimal pulse (up to 2000 iterations have been carried out) , dotted line: excitation with an Gaussian pulse, and dashed line: excitation with the approximate optimal pulse after Eq. 4.14 (T = 4 K and $\lambda = 0.25$ for all curves, the Gaussian and the approximate pulse lead only to a small population of the excited states, whereas for the optimal pulse, the ground-state is nearly empty).

the final decrease of the target population with increasing τ_c (this appears in all panels of Figs. 7.7 and 7.8 discussed so far except the panel for $m_\mathrm{tar} = 2$).

The further discussion will concentrate on the excitation energy localization at the BChl at site 7 (cf. Fig. 7.5). According to Fig. 7.6 it is formed by the contributions of different exciton levels, with level 5 dominating the superposition state. To compare the results shown in Fig. 7.8 with the case of weak excitation, as will be discussed below, the renormalized population is introduced

$$p_\mathrm{tar}^{(\mathrm{ren})}(t) = \frac{P_\mathrm{tar}(t)}{\sum\limits_\alpha P_\alpha(t_f)} \equiv \frac{P_\mathrm{tar}(t)}{1 - P_0(t_f)} \ . \tag{7.1}$$

It measures the excitation energy localization in relation to the total excitation (into the single–exciton manifold) and, consequently, represents a quantity which is (at least in the linear regime) independent on the actual degree of excitation.

Fig. 7.9 compares $p_\mathrm{tar}^{(\mathrm{red})}$ versus τ_c with the reduced population achieved by a Gaussian pulse and the ansatz for the control field according to Eq. 4.14. First of all one can state that the pulse determined by the Optimal Control theory leads to the best spatial excitation energy localization (above 75 %). The field pulse according to Eq. 4.14 reaches this result only for large pulse durations. The Gaussian pulse applied with carrier frequency $\omega = \Omega_{\alpha=5}$ never achieves a

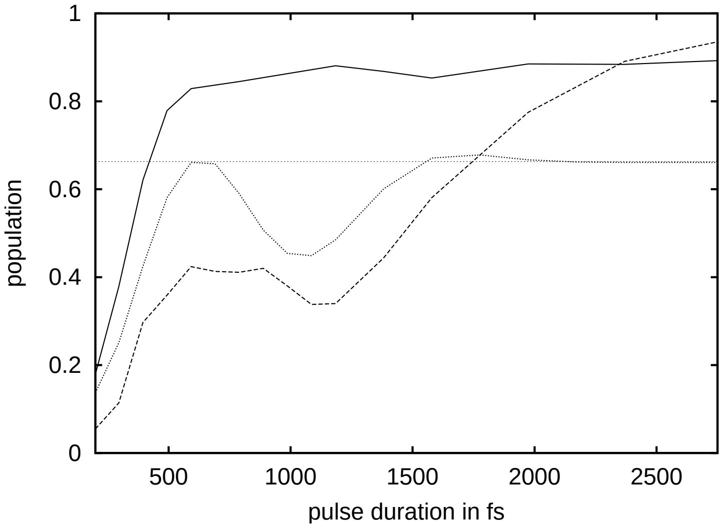

Figure 7.10: The same as Fig. 7.9, but for the absence of dissipation.

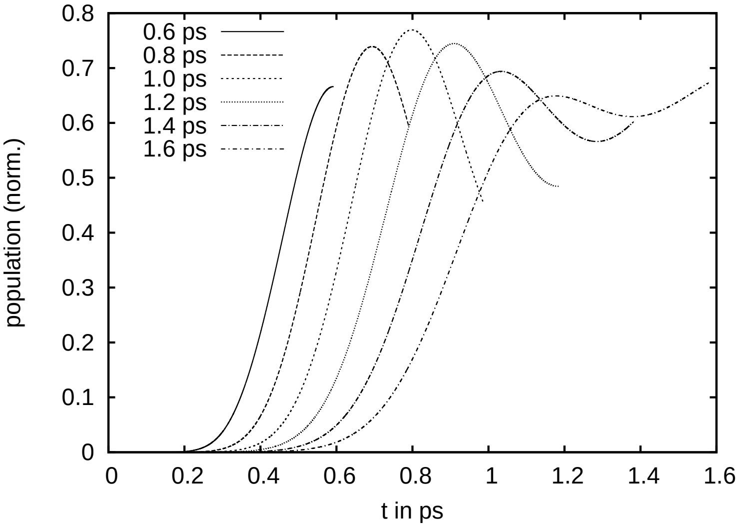

Figure 7.11: Renormalized population, Eq. 7.1 of the target site, $m_{tar} = 7$, versus the time for a Gaussian pulse of different length and for the absence of dissipation (note that the populations have been only drawn up to the respective t_f, $\lambda = 0.25$).

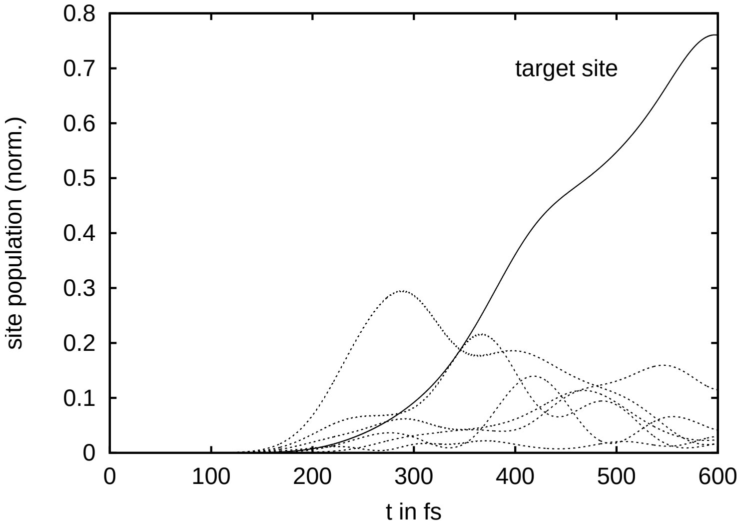

Figure 7.12: Renormalized populations, Eq. 7.1 of all sites including the target site $m_{tar} = 7$ (drawn by the solid line) after excitation with an optimal pulse with τ_C =600 fs duration (T= 4K, $\lambda = 0.25$, to avoid confusion the dotted lines are not assigned to their respective site $m \neq m_{tar}$).

renormalized population above 60 %. The same behavior can be found for the absence of dissipation but with an overall larger control yield (cf. Fig. 7.10). Here, the Gaussian pulse reaches exact the level given by the excitonic expansion coefficient in Tab. 7.3, for longer times (dotted line in Fig. 7.10). To understand the minimum of the target state population obtained when a Gaussian shaped pulse or the pulse according to Eq. 4.14 are applied Fig. 7.11 displays the target state population versus time up to the actual value of t_f for the Gaussian shaped pulse. As it becomes obvious destructive interferences in the excitonic wavepacket decrease the target state population within a certain range of τ_c. This just explains the big dip found in the Figs. 7.9 and 7.10.

The Figs. 7.12 and 7.13 give different views on the population dynamics driven by the optimal pulse of Fig. 7.9 (at τ_c = 600 fs and T= 4 K). The concentration of the most of the excited state population to site $m = 7$ is nicely shown in Fig. 7.12. This comes along with a dominating population of exciton level 5 since site 7 mainly contributes to this exciton state (cf. Table 7.3).

7.3.3 Weak Fields and Exciton-Exciton Annihilation

The purpose of this Section is to extend the application of the Optimal Control theory to the weak field case. Up to now, all control calculations in the present work have neglected the two- and higher exciton manifolds. If one introduces the two-exciton manifold, and this is necessary for a realistic description, the exciton-

exciton annihilation (EEA) process comes into play (cf. 2). The fast relaxation due to this process reduces the success of the control task drastically. To be able to minimize the excitation of the two-exciton manifold and also the influence of the EEA the pump field has to be reduced to a weak field case. Two different approaches are discussed in the following.

First an approach is chosen, which uses a superposition of the excitation of the target site (with weighting factor x) and the ground state (with weighting factor $1 - x$) as target state

$$|\phi_{tar}\rangle = x \sum_{\alpha_1} A'_{tar}(\alpha_1)|\alpha_1\rangle + (1 - x)|0\rangle. \tag{7.2}$$

The total redistribution of population from the FMO ground–state $|0\rangle$ into the target state and the remaining Q_y-states is shown in Fig. 7.13. Since this figure displays results of computations for the type of mixed target state, defined in Eq. 7.2, one has to concentrate on the case $x = 1$ first. Here, more then 70 % of the excited state population is concentrated in the target state. And this appears for a case of a nearly complete ground–state depletion. If x is reduced the target state population stays nearly constant until x goes below the 70 %–value. However the reduced target state population, Eq. 7.1 stays over the whole range of x at 76%. When the optimal pulse which has been gained using the above described approach would be used to propagate the system including two-exciton states and exciton-exciton annihilation the relative population of the target site would drop dramatically for $x > 0.62$.

The second approach to minimize the influence of exciton-annihilation is to fully include the two–exciton states and the EEA process into the equations of motion, and thus to let the algorithm itself find the best solution to this problem. Fig. 7.14 shows different types of populations when using the mixed type of target state, Eq. 7.2, versus the mixing parameter x. As already observed in Fig. 7.13 the best ratio between the target state population ($m_{\mathrm{tar}} = 7$) and the total population of the single exciton manifold, Eq. 7.1 is obtained for a small total excitation ($x = 0.6$). The related ratio of 0.76 decreases to a value 0.59 at $x = 1$. Already at $x = 1$ and the related strong ground–state depletion $P_0 = 0.47$ the maximum of the two–exciton state population $\sum_{\alpha_2} P_{\alpha_2}(t)$ remains small. Note that Fig. 7.14 shows the maximal two–exciton population and not the population present at t_f. The latter is strongly decreased by exciton exciton annihilation processes (cf. Fig. 7.16).

Although the data of Fig. 7.14 have been calculated for the same parameters as those shown in Fig. 7.13 except the inclusion of two–exciton states the results differ remarkably. While in Fig. 7.13 the ground–state is nearly completely depopulated for larger values of the mixing parameter x this is not the case when transitions into two–exciton states become possible. In this case according to the chosen target state the Optimal Control theory tries to reduce the two–exciton

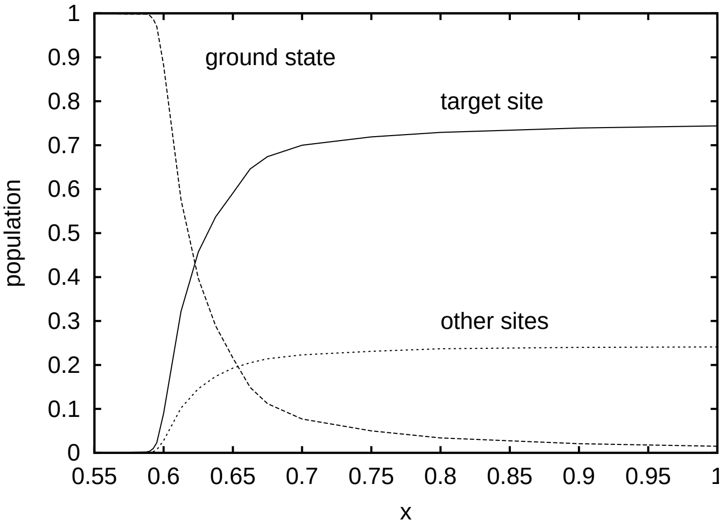

Figure 7.13: Population of the target site $m_{tar} = 7$, of the ground state and of the sum over all other site populations versus the mixing parameter x introduced in Eq. 7.2 (the target state is a linear combination of the ground state and the state, where only BChl No. 7 is excited, with the respective weights $1 - x$ and x). (τ_C =600 fs, T=4K, $\lambda = 0.25$). The renormalized target site population (Eq. 7.1) stays at the value of 0.76 over the whole x-range.

populations as much as possible in accepting a smaller population of the target state. At small values of x both approaches give the same result, because then only a linear interaction with the electric field is probable.

In which way the populations depends on the penalty factor λ (cf. Eq. 4.2) has been shown in Fig. 7.15 (case $x = 1$, including the two-exciton manifold). As it has to be expected an increasing λ initiates an increasing overall field–strength of the optimal pulse and thus the population of the target state increases. Interestingly, this comes along with an decrease of the site–population of all other BChl as well as a very weak increase of the two–exciton population (again the maximal two-exciton population is shown and not the population at t_f).

Details of the temporal state population together with the optimal pulse are shown in Fig. 7.16. The pulse is given by two sub–pulses the later one with an edge extending nearly up to t_f. It becomes obvious from a comparison of the total single–exciton population with the target population that the first sub–pulse mainly results in overall population of the single–exciton states. The population of the target state is achieved by the second sub–pulse which increases the amplitudes of the single–exciton states (in line with an increase of the total single–exciton population) and moves the wavepacket into the target state. Within the action of this second sub–pulse an intermediate two–exciton state population appears. However, because of exciton exciton annihilation and stimulated

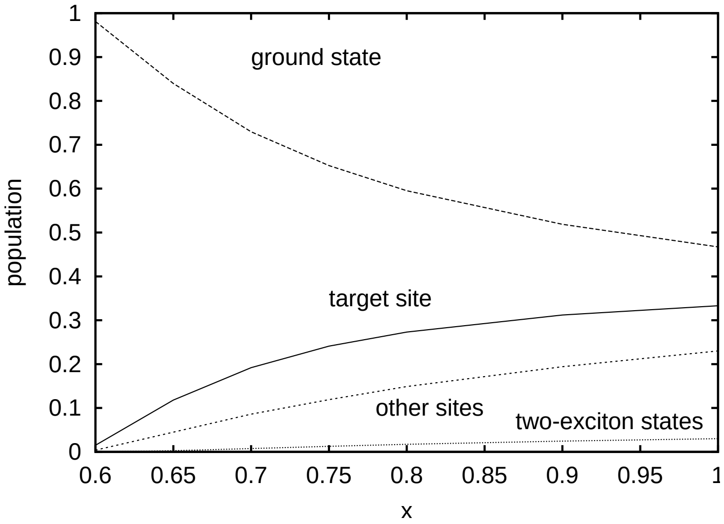

Figure 7.14: Populations including the two-exciton states versus the mixing parameter introduced in Eq. 7.2 (the target state is a linear combination of the ground state and the state, where only BChl No. 7 is excited, with the respective weights $1 - x$ and x). (τ_C =600 fs, T=4K, $\lambda = 0.25$). Population of the target site, BChl No. 7, the ground state, the sum over all other one-exciton site populations and the maximum of the two exciton population. The renormalized target state population, Eq. 7.1 drops from 0.76 at $x = 0.6$ to 0.59 at $x = 1.0$.

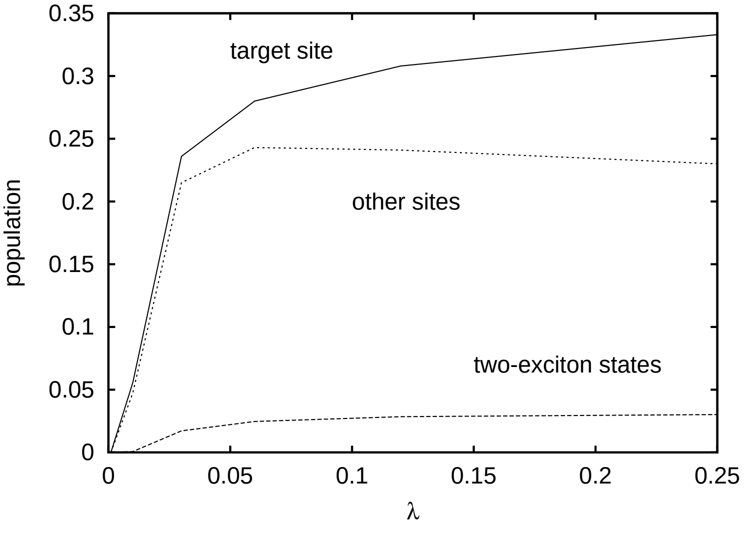

Figure 7.15: Populations including the two-exciton states, the target site $m_{tar} = 7$ population, and the one-exciton population of all other sites in dependency of the penalty factor λ (τ_C =600 fs, T = 4 K). The renormalized target state population. Eq. 7.1 rises from 0.51 at $\lambda = 0.03$ to 0.59 at $\lambda = 0.25$.

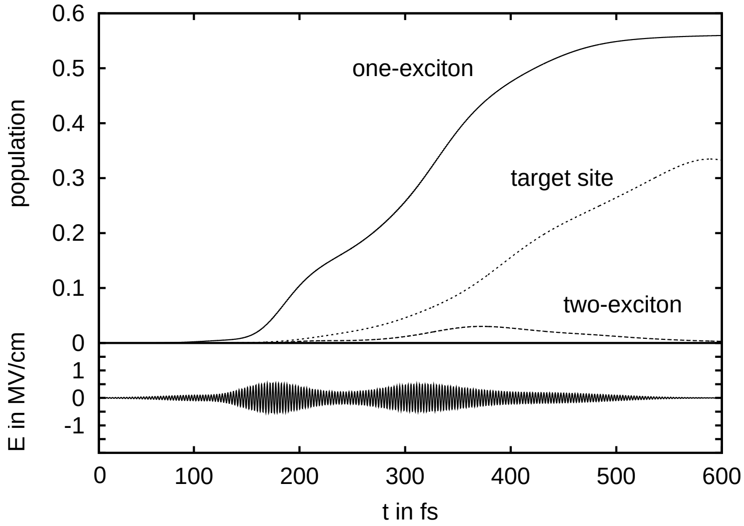

Figure 7.16: Population of the target site $m_{tar} = 7$, the whole one-exciton population and the two exciton population versus time together with the optimal pulse (lower panel, τ_C =600 fs, T = 4 K, $\lambda = 0.25$).

recombination this population is strongly decreased at time t_f.

7.3.4 Influence of Disorder and Orientational Averaging

All the given results demonstrate that laser pulse localization of exciton energy becomes possible even if higher exciton manifolds are discussed. At the end of the present discussion the influence of energetic and structural disorder will be studied. This represents a numerically very expensive task as it has been explained in Section 4.3. Therefore, only a restricted number of disorder configurations could be included and it became necessary to neglect the two–exciton states. Some preliminary results are shown in Fig. 7.17, where the disorder averaged population of the target state has been drawn versus time up to t_f. The considered type of disorder includes random orientation of the single FMO–complexes in space and a Gaussian distribution of the BChl site–energies (diagonal disorder). As it has to be expected disorder decreases the target state population. But this influence does not completely alter the results, and it seems that the actual number of different configurations does not play an crucial role. The temporal evolution of all site populations are given in Fig. 7.18. It shows that, even averaged over 15 disorder configurations (which gave the worst result in Fig 7.17) a coherent population of the target state is possible.

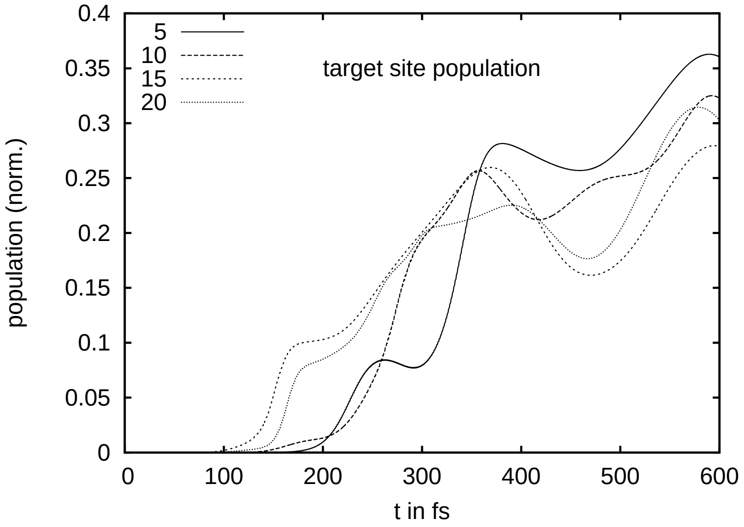

Figure 7.17: Effect of disorder, i. e. random orientations of the complexes and Gaussian disorder of the site energies of 100 cm^{-1}(FWHM), on the renormalized population, Eq. 7.1 of the target site $m_{tar} = 7$ versus time (τ_C =600 fs, T $=$ 4 K, $\lambda = 0.25$). The optimization has been done simultaneously for 5, 10, 15 and 20 disorder realizations.

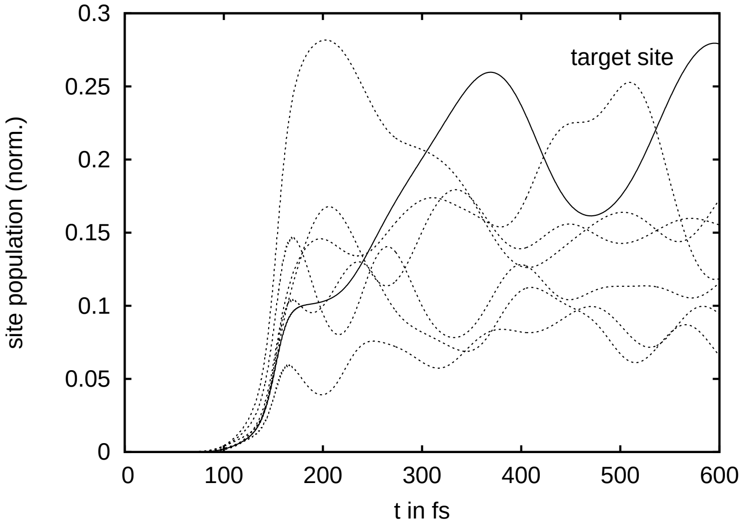

Figure 7.18: The same as 7.17 for 15 disorder realizations but all site populations are shown (population of the target state $m_{tar} = 7$, solid line, and of all other sites, dashed lines).

7.4 Controlling Excitons in the PS1

Another possible candidate for studies on exciton control would be the Photosystem 1 (PS1) of *Synechococcus elongatus* since its structure has been resolved recently anew [JFK$^+$01] resulting in a detailed knowledge on the spatial position as well as mutual orientation of all pigments. Concentrating on the 96 chlorophyll *a* molecules (Chl*a*) of the PS1 a model for the Q_y excitations of these chromophores has been presented in Chapter 6. Most of the Chls are arranged in a pseudo–ring structure around the reaction center. The latter is positioned in the center of the PS1 and includes the special pair P700 which consists of two strongly coupled Chls. Further, most of the excitonic eigenstates can be reached by the laser field, since a particular symmetry of the pigment arrangement is absent in this complex. For example, due to the high symmetry, the LH2 antenna of purple bacteria cannot be used for the present discussion (cf. Chapter 5). It is known that the exciton motion and relaxation takes place on an ultrafast timescale of a few hundred fs up to about twenty ps [GvG01]. Thus exciton motion has a fast component avoiding the dominance of energy relaxation and dephasing when trying to control the dynamics in this time region. And, finally, compared with other antenna systems spectral inhomogeneity is relatively weak.

Due to the size of the antenna several restrictions with respect to the foregoing Section 7.3 have been necessary. Here, only the one exciton manifold is taken into account. Furthermore, orientational and structural disorder has been disregarded, providing well oriented samples and weak inhomogeneous broadening, respectively. However, exciton vibrational coupling is considered and, in this way, one may show how laser pulse control remains possible when entering room temperature conditions.

Using the iterative scheme as discussed in Chapter 4 the optimal pulse is calculated which drives the system from the electronic ground state (present at $t = t_0$) into the target state at $t = t_f$. However, a complete solution of the control task cannot be expected. Caused by the presence of dissipation, $\hat{\rho}$ does not match the pure state density operator $|\phi_{\text{tar}}\rangle\langle\phi_{\text{tar}}|$, i.e. the control yield $\langle\phi_{\text{tar}}|\hat{\rho}(t_f)|\phi_{\text{tar}}\rangle$ remains smaller than 1 in any case. However, to maximize this yield it is advisable to decrease the temperature. But it would be also reasonable to change t_f, and in this manner to adapt the possible pulse duration to the internal dynamics of the PS1.

The target state which is used here is given by a superposition of delocalized eigenstates, which corresponds to a localized population of one of the Chls in the special pair. One example for the optimal pulse as well as the population dynamics is given in Fig. 7.19, for a temperature of 77 K and a optimization time of $\tau_c = t_f - t_0 = 200$ fs. Since the localized excitonic wavepacket is not an eigenstate of the system, it oscillates between the strongly coupled Chls of the special pair, as it can be seen in Fig. 7.19 (solid and dotted line). If t_f is reached the maximal population of the target state is achieved (solid line). Additionally,

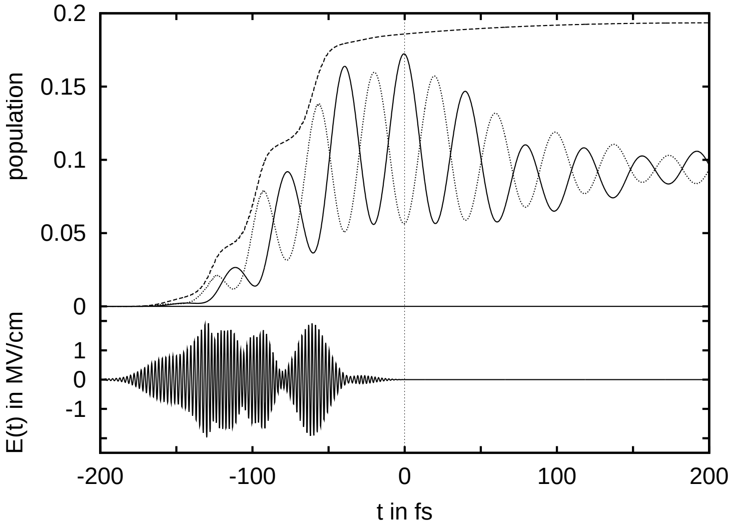

Figure 7.19: Time evolution of the populations for the optimal field at 77K, optimization time is $\tau_c = 200$ fs, and target time is t_f =0 fs. Population of the two single Chls in the P700 (solid and dotted), and population of one low-lying excitonic eigenstate (dashed) which is mostly localized on the P700. In the lower panel the electric field is given.

the population of the lowest contributing eigenstate is given (dashed). This is the state, where both Chls are equally populated. The vanishing of the coherences between this eigenstate and other eigenstates related to the special pair damps the oscillations.

Different from other approaches where a stable population of a certain target state is wished (cf. Section 7.3), here one benefits from the oscillations, since they can be detected experimentally. The dipole moments of the two Chls in the special pair have different and not collinear directions, so that the population oscillation will show up in the time dependent anisotropy [AMDS99]. Following that approach the efficiency of the pulse is defined as the population difference between the two localized states at either molecule of the special pair. The so defined efficiency is given in Fig. 7.20 for different optimization times and temperatures from 4K up to room temperature. With rising temperature there is an exponential decrease in the maximal efficiency with a temperature constant of 113 K.

The optimization time for the maximal efficiency also decays exponential with a temperature constant of 620 K. According to these dependencies, the position of the maximum follows a power law $\sim \tau_c^{5.33}$(dotted line in Fig. 7.20). At higher temperatures shorter pulses are necessary to reach the decreased maximal efficiency. For comparison, also Gaussian pulses of different frequencies and durations have been used, giving the maximal efficiency of 0.02 at 4K. This is also the

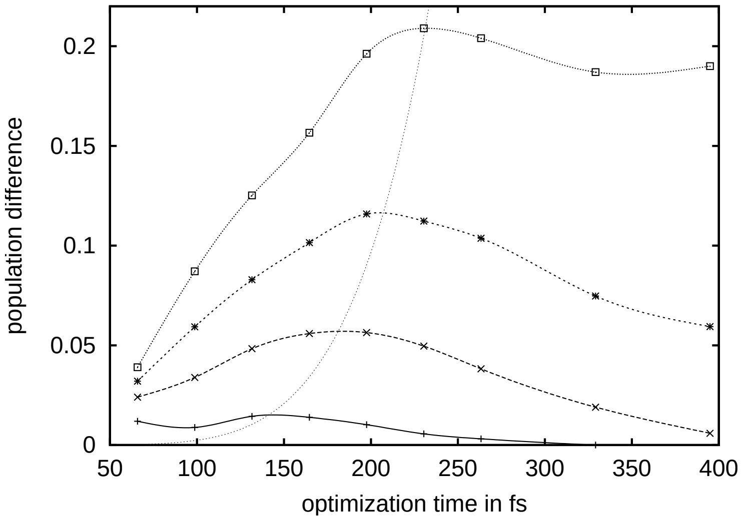

Figure 7.20: Difference of the populations of the two P700 Chl for the optimal pulse at the target time. The x-axis gives the used optimization time τ_c. The temperatures are (from top to bottom) 4K (dotted), 77K (dashed), 150K (long-dashed), and 295K (solid). A dotted line connects the position of the maxima.

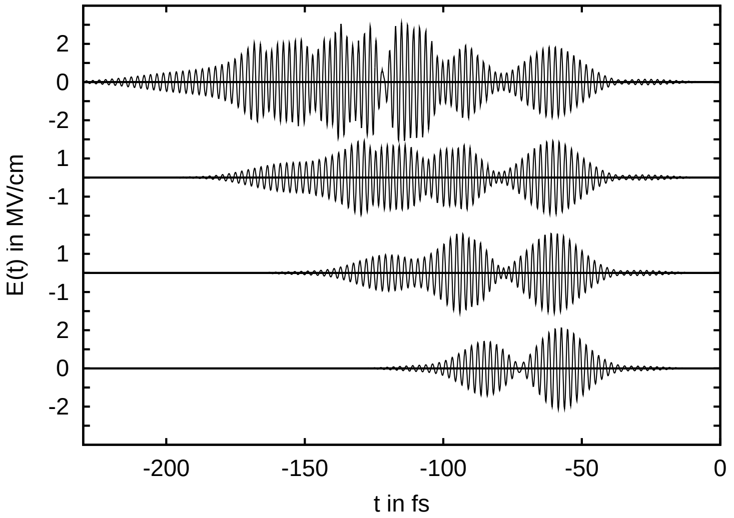

Figure 7.21: The optimal field for different temperatures, from top to bottom: 4 K, 77 K, 150 K and 295 K. For a better comparison, the target time is set to zero ($t_f = 0$). The optimal optimization time τ_c at the different temperatures is given by Fig. 7.20.

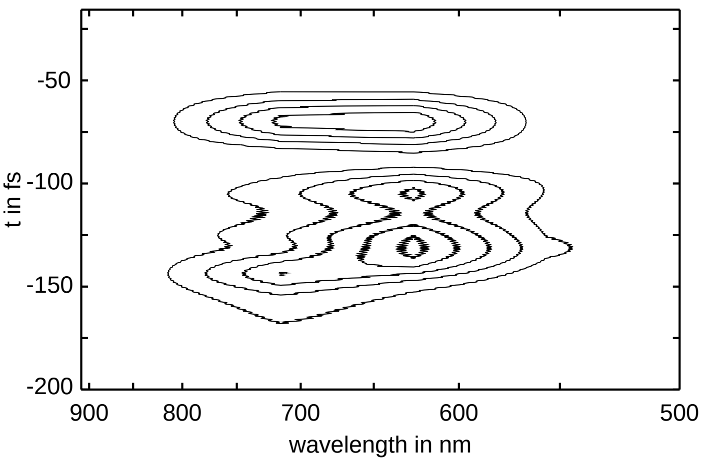

Figure 7.22: Contour plot of the time resolved spectrum of the optimal pulse for T=77 K. The contour lines are equally spaced (a.u.).

efficiency in the limit of very short pulses in Fig. 7.20, since then all structure of the pulses has vanished.

The optimal pulses for different temperatures are shown in Fig. 7.21. The time resolved spectrum of the pulse for 77 K is given as a contour plot in Fig. 7.22. All pulses have in common a spectral shift from 700 nm to 625 nm at early times. This leads to coherences between the respective eigenstates building up for the target state. Depending on the overall pulse length, some pulses at 625 nm follow. At the end of the pulse one spectrally broad peak populates the respective eigenstates at all temperatures.

7.5 Summary

In this Chapter simulations have been carried out to demonstrate the possibility of laser pulse control in chromophore complexes. It has been shown that the concept of optimal control is also applicable to excitonic states, where excitonic wavepackets can be formed in close analogy to the vibrational wavepackets usually considered. In order to do this the FMO–complex of green sulphur bacteria has been chosen since it represents a well characterized and relatively small pigment–protein complex with 7 Bacteriochlorophyll (BChl) molecules in its monomeric form. Furthermore it does not exhibit any symmetry, which would prevent certain exciton states from being addressable by the laser pulse, as it has been shown in the beginning of this Chapter. The possibility has been tested to populate a single Q_y–state of one of the seven BChl of the FMO–complex by a tailored femtosecond laser pulse. The success to reach this control task depends on temperature and on the pulse length, and at each temperature an optimal pulse length can be found. With rising temperature the control yield becomes smaller and the optimal pulse length shorter. Even under realistic conditions like the inclusion of two–exciton states, the influence of energy relaxation and dephasing, or the presence of structural and energetic disorder such a spatial localization of excitation energy is possible within a time interval of some hundreds of femtoseconds.

The same approach has been applied, with some restrictions, to the larger core-antenna system PS1 using the excitonic model developed in Chapter 6. For selected chromophores as the special pair P700, the control scenario works in this system. Furthermore, it seems to be possible to detect the excitonic wavepackets by an experiment similar to the time dependent anisotropy measurement of Ref. [AMDS99]. If the experimental verification can be obtained, a new method to discover the energy transfer pathways and thus the structure-function relationship in photosynthetic antenna systems has been introduced.

Chapter 8

Conclusion and Outlook

This work dealt with the further development of the multi-exciton density matrix theory and its application to photosynthetic antenna systems. After a short introduction into photosynthesis in Chapter 1 the theoretical description of excitons in photosynthetic antenna systems has been presented. The process of exciton-exciton annihilation has been successfully integrated into the multi-exciton density matrix theory of Ref. [RMK01] in Chapter 2 (cf. Ref. [BM03]). The theoretical background for the calculation of optical properties and the Optimal Control theory have been given in Chapter 3 and 4, respectively. The further development of the theory of photosynthetic antenna systems has to address two main fields. On the one hand the integration of a proper microscopic theory for the temperature dependence of the pure dephasing is necessary. On the other hand, certain vibrational modes have to be included into the system part to describe vibrational coherences which have been seen in low temperature transient absorption experiments.

Simulations for intensity dependent transient absorption spectra of the B850 ring of LH2 in Chapter 5 revealed the internal conversion time of a single BChl, as well as the general spectral signature of the exciton-exciton annihilation process (cf. Ref. [BHS$^+$01, MB02, BM04a]). Including energetic disorder, simulations of single molecule behavior (cf. Ref. [MB02]) as well as ensemble averages have been done (cf. Ref. [BM04a]). The comparison with experimental data showed the general validity of the method and parameters like the variance of the energetic disorder could be determined. The development of theory of exciton-exciton annihilation in Chapter 2 makes further experiments with a variation of the pulse intensity valuable, because using the respective simulations relaxation pathways and times can now be extracted.

An exciton model for the chlorophylls of the Photosystem I of *Synechococcus elongatus* has been set up in Chapter 6 (cf. Ref. [BSN$^+$04]). Using the structural data of Ref. [JFK$^+$01] to extract the dipole moments of the lowest excited state of the chlorophylls the energies of the chromophores have been determined by fitting the low temperature linear spectra with the help of an evolutionary algorithm. The resulting PS1 model was successfully used to describe time resolved fluorescence experiments. The approach of Chapter 6 to set up a model system for the photosystem I can easily be applied to other photosynthetic antenna system. A prominent example would be the photosystem II of the same cyanobacterium whose structure has been recently refined in Ref. [FIM$^+$04].

The general aim of Chapter 7 is to control the localization and motion of excitations in photosynthetic antenna systems by structured ultrafast laser-pulses. The inclusion of both the exciton-exciton annihilation process in Chapter 2 and the energetic inhomogeneity have been important preparations for a realistic consideration of the possibilities to control excitons in photosynthetic antenna complexes (cf. Ref. [BM04b, BM04c]). The goal is to create an excitonic wavepacket, i.e. a coherent superposition of excitonic eigenstates, similar as it has been successfully done with the creation of vibronic wavepackets in small molecules. The possibilities to localize excitons at single chromophores in the FMO complex have been evaluated and turned out to be strongly temperature dependent. Furthermore the inclusion of energetic disorder and exciton-exciton annihilation reduced the success. However at least at low temperatures an experimental verification seems to be possible. One example of such an experiment is proposed for the PS1 complex, where the population of one chlorophyll in the special pair has been the target of the optimization. Since this would result in oscillations in the transient anisotropy caused by the population transfer between the both strongly coupled chromophores of the special pair and the different orientations of their dipole moment. The experimental detection should be feasible.

The possibility of exciton control will lead to a better understanding of energy transfer pathways, and the role of coherent processes in photosynthetic antenna systems. Among others, one of the possible applications is the switching between the active and the inactive branch in the reaction center of PS1 to clarify the specific differences between them. Since this task is very demanding, with respect to both experimental realization as well as theoretical prediction and explanation, the close cooperation of theory and experiment is crucial. One of the main aspects is an extensive study of all processes which have an negative influence on the controllability, and their dependence on experimental conditions, like temperature or sample preparation. Different schemes of controlling coherent excitonic wavepackets can be set up, using both multiple and shaped pulses. These include increasing the amplitude of the coherence between two exciton states, and detection of the coherences by transient anisotropy. Besides the creation also the maintaining of coherences, using a specially formed pulse sequence, is of interest to extend the timescale on which the control experiment can take place. Higher excited states which give rise to exciton annihilation as well as averaging over disorder and orientations have to be considered.

Another aspect is the creation of vibrational coherences and the probing of vibrational dynamics. This has to be included into the simulations, as it will also be present in the respective experiments, and should be distinguishable from the excitonic coherences. The vibrational coherences may also act as a probe of the localization of excitations. One possible experiment in this field is the creation of a higher exciton state with coherent vibrational motion and the experimental detection of the decay of both. Furthermore, the application of the theory to other systems e.g. arrays of quantum dots seems to be possible.

The theoretical background for exciton control has been developed in this work. If the experimental verification succeeds, a new and promising field both in experiment and theory has been opened.

Appendix

Appendix A

Nonadiabatic Transitions

A.1 Intra–Chromophore Nonadiabatic Transitions

For the proper description of the EEA process and the step involving the internal conversion process the general type of the nonadiabatic coupling operator (see, e.g. [MK00a]) has to be specified to the three–level chromophore model,

$$H_{\mathrm{na}} = \sum_m \Theta_{mef} |\varphi_{me}\rangle\langle\varphi_{mf}| + \mathrm{h.c.}\ . \tag{A.1}$$

The expression combines all nonadiabatic couplings at the various chromophores resulting in transitions from the higher excited state f to the first excited state e (and the reverse).

To get the correct matrix elements in the MX representation one first introduces the unity operator 1_{CC}, Eq. 2.2 of the state space of multiple excitations in the CC. Then, a change to the MX representation can be carried out to yield

$$H_{\mathrm{na}} = \sum_{N>1} \sum_{\alpha_{N-1}} \sum_{\beta_N} \Theta(\alpha_{N-1}\beta_N) |\alpha_{N-1}\rangle\langle\beta_N| + \mathrm{h.c.}\ . \tag{A.2}$$

The MX matrix elements of the nonadiabatic coupling follow as

$$\begin{aligned} \Theta(\alpha_{N-1}\beta_N) &= \sum_{\mathcal{M}=0}^{N} \sum_{\mathcal{N}=0}^{N/2,(N-1)/2} \delta_{N,\mathcal{M}+2\mathcal{N}} \\ &\times \sum_{\{me\}_{\mathcal{M}}} \sum_{\{nf\}_{\mathcal{N}}} \sum_{k\in\{nf\}_{\mathcal{N}}} \sum_{k\notin\{me\}_{\mathcal{M}}} \Theta_{kef} \\ &\times C^*_{\alpha_{N-1}}(\{me\}_{\mathcal{M}}, ke, \{nf\}^{n\neq k}_{\mathcal{N}-1}) C_{\beta_N}(\{me\}_{\mathcal{M}}, \{nf\}_{\mathcal{N}})\ . \end{aligned} \tag{A.3}$$

The notation is of more detail with respect to the MX expansion coefficients. The coefficient $C^*_{\alpha_{n-1}}$ notices that as the result of the nonadiabatic transition from state φ_f to state φ_e the number of chromophores in state φ_f is reduced by one (all n have to be different from k). At the same time there appears an additional excitation of state φ_e at site $k \neq m$. If specified to a transfer from the two-exciton to the single-exciton manifold Eq. A.3 reads

$$\Theta(\alpha_1, \beta_2) \;=\; \sum_n \Theta_{nef} C^*_{\alpha_1}(ne) C_{\beta_2}(nf) \; . \tag{A.4}$$

A.2 Coupling to the Radiation Field

The coupling to the radiation field with electric field strength $\mathbf{E}(t)$ has been given by the last term in Eq. 2.11. For any chromophore a dipole–allowed transition from the chromophore ground–state to the first excited state is provided. Furthermore, a transition from this excited state to the higher excited state becomes also possible, thus allowing for intra–molecular excited state absorption. The respective CC dipole operator can be written

$$\begin{aligned} \hat{\mu}_{\mathrm{CC}} \;&=\; \sum_m (\mathbf{d}^{(m)}_{eg} |\varphi_{me}\rangle\langle\varphi_{mg}| + \mathbf{d}^{(m)}_{fe} |\varphi_{mf}\rangle\langle\varphi_{me}|) + \mathrm{h.c.} \\ &\equiv\; \sum_N \sum_{\alpha_{N+1},\beta_N} \mathbf{d}(\alpha_{N+1}, \beta_N) |\alpha_{N+1}\rangle\langle\beta_N| + \mathrm{h.c.} \; . \end{aligned} \tag{A.5}$$

The MX dipole matrix elements given in the second part of this expression can be computed in a similar manner as it has been already done in Appendix A.1 for the nonadiabatic coupling,

$$\begin{aligned} \mathbf{d}(\alpha_{N+1}, \beta_N) \;=\; & \sum_{\mathcal{M},\mathcal{N}} \delta_{N,\mathcal{M}+2\mathcal{N}} \sum_{\{me\}_\mathcal{M}} \sum_{\{nf\}_\mathcal{N}} \\ & \Big(\sum_{k \notin \{me\}_\mathcal{M}} \sum_{k \notin \{nf\}_\mathcal{N}} \mathbf{d}^{(k)}_{eg} C^*_{\alpha_{N+1}}(\{me\}_\mathcal{M}, ke, \{nf\}_\mathcal{N}) \\ & + \sum_{k \in \{me\}_\mathcal{M}} \mathbf{d}^{(k)}_{fe} C^*_{\alpha_{N+1}}(\{me\}^{m \neq k}_{\mathcal{M}-1}, \{nf\}_\mathcal{N}, kf) \Big) \\ & \times C_{\beta_N}(\{me\}_\mathcal{M}, \{nf\}_\mathcal{N}) \; . \end{aligned} \tag{A.6}$$

The transition matrix element from the ground–state into the single–exciton manifold simply follows as

$$\mathbf{d}(\alpha_1, 0) \;=\; \sum_k \mathbf{d}^{(k)}_{eg} C^*_{\alpha_1}(ke) \; , \tag{A.7}$$

and for the transition from the single–exciton to the two–exciton manifold one gets

$$\begin{aligned}\mathbf{d}(\alpha_2,\beta_1) &= \sum_k \sum_{m\neq k} \mathbf{d}^{(k)}_{eg} C^*_{\alpha_2}(me,ke) C_{\beta_1}(me) \\ &\quad + \sum_n \mathbf{d}^{(n)}_{fe} C^*_{\alpha_2}(nf) C_{\beta_1}(ne)\,. \end{aligned} \tag{A.8}$$

A.3 The Hamiltonian of Intra–Chromophore Vibrations

This section gives the detailed analysis of the Hamiltonian of intra-molecular vibrations, as it is discussed in the main part in Section 2.5.1. First, it is noted that any chromophore has its own set R_m of intra–molecular coordinates, i.e. $R_{\text{intra}} = \{R_m\}$. This will be accounted for in a modified notation of the diagonal part of the intra–molecular contributions to H_{vib}, Eq. 2.12. The respective part is generated by the $\Delta U_{\text{intra}}(\{me,nf\}_N; R_{\text{intra}})$ which, according to Eq. 2.8 have to be defined via a certain difference of the chromophore excitation energies. The difference $\Delta\epsilon_k(ag;R_k) = \epsilon_k(ag;R_k) - \epsilon_k(ag;R_k^{(g)})$ $(a = e, f)$ is introduced where the latter energy refers to the transition energy at the electronic ground–state equilibrium configuration $R_k^{(g)}$ of the intra–molecular coordinates. Before giving the complete expression of the vibrational Hamiltonian the separation of the ground–state part $H_{\text{vib}}^{(\text{intra})}$ into a sum of single–chromophore vibrational Hamiltonian H_{mg} is noted. If one incorporates $H_{\text{vib}}^{(\text{intra})} \equiv \sum_m H_{mg}$ into the summation with respect to the various excited states one may write (cf. Eq. 2.12, $N > 0$)

$$\begin{aligned} H_{\text{vib}}^{(\text{intra})}(\alpha_N,\alpha_N) &= \sum_{\{me,nf\}_N} \mid C_{\alpha_N}(\{me,nf\}_N) \mid^2 \Big\{ \sum_{k\notin\{me\}_{\mathcal{M}},\{nf\}_{\mathcal{N}}} H_{kg} + \\ &\quad \Big[\sum_{k\in\{me\}_{\mathcal{M}}} H_{ke} + \sum_{k\in\{nf\}_{\mathcal{N}}} H_{kf} \Big]_{N=\mathcal{M}+2\mathcal{N}} \Big\}\,. \end{aligned} \tag{A.9}$$

The newly introduced vibrational Hamiltonian referring to the excited chromophore states read $H_{ka} = H_{kg} + \Delta\epsilon_k(ag;R_k)$.

To have more concrete expressions at hand the single and two–exciton version of the general coupling expression of MX levels to intra–molecular vibrations is presented, Eq. A.9. In the case of single–exciton states it reads (note $H_{ka} = H_{kg} + \Delta\epsilon_k(ag;R_k)$),

$$H_{\text{vib}}^{(\text{intra})}(\alpha_1,\alpha_1) = \sum_m \mid C_{\alpha_1}(me) \mid^2 \Big\{ \sum_{k\neq m} H_{kg} + H_{mg} + \Delta\epsilon_m(eg;R_m) \Big\} \tag{A.10}$$

This expression can be rearranged to give

$$H_{\text{vib}}^{(\text{intra})}(\alpha_1,\alpha_1) \;=\; \sum_m h_m(\alpha_1)\,, \tag{A.11}$$

with

$$h_m(\alpha_1) \;=\; H_{mg}+\mid C_{\alpha_1}(me)\mid^2 \Delta\epsilon_m(eg;R_m)\,. \tag{A.12}$$

According to the presence of a superposition state of singly excited chromophores (the single exciton state) a superposition of ground and excited state contributions appears. A similar result follows for the two-exciton vibrational Hamiltonian,

$$\begin{aligned}
H_{\text{vib}}^{(\text{intra})}(\alpha_2,\alpha_2) = &\sum_{m_1>m_2} \mid C_{\alpha_2}(m_1e,m_2e)\mid^2 \\
\times&\Big\{\sum_{k\neq m_1,m_2} H_{kg}+H_{m_1g}+\Delta\epsilon_{m_1}(eg;R_{m_1})+H_{m_2g}+\Delta\epsilon_{m_2}(eg;R_{m_2})\Big\} \\
+&\sum_n \mid C_{\alpha_2}(nf)\mid^2 \Big\{\sum_{k\neq n} H_{kg}+H_{ng}+\Delta\epsilon_n(fg;R_n)\Big\}
\end{aligned} \tag{A.13}$$

which can be rearranged to give

$$H_{\text{vib}}^{(\text{intra})}(\alpha_2,\alpha_2) \;=\; \sum_m h_m(\alpha_2)\,, \tag{A.14}$$

with

$$\begin{aligned}
h_m(\alpha_2) \;=\; & H_{mg}+\sum_n \mid C_{\alpha_2}(me,ne)\mid^2 \Delta\epsilon_m(eg;R_m) \\
&+\sum_n \mid C_{\alpha_2}(mf)\mid^2 \Delta\epsilon_m(fg;R_m)\,.
\end{aligned} \tag{A.15}$$

Again a superposition of excited state contributions appears.

A.3.1 Limit of Vanishing Inter–Chromophore Electronic Coupling

To derive the approximate version of the EEA rate in Sec. 2.5.4 one need $h_m(\alpha_1)$ and $h_m(\alpha_2)$, Eqs. A.12 and A.15, respectively, in the limit of vanishing electronic inter–chromophore coupling ($V_{\text{el-el}}^{(N)} \to 0$). Taking this limit for the single-exciton coefficients one obtains $C_\alpha(me) \to \delta_{m,m_0}$. A single excited chromophore at site m_0 remains and the single-exciton quantum number $\alpha_1$degenerates to this particular chromophore index m_0. This behavior results in

$$h_m(\alpha_1) \quad \to \quad H_{mg} + \delta_{m,m_0} \Delta\epsilon_{m_0}(eg; R_{m_0}) \,. \tag{A.16}$$

In the case of the two-exciton state one has to distinguish between the limit leading to two single excitations or a single double-excitation. In the first case one gets (note that per definition the order of m and n in the expansion coefficient is unimportant) $C_{\alpha_2}(me, ne) \to \delta_{m_0,m}\delta_{n_0,n}$. The latter case results in $C_{\alpha_2}(mf) \to\delta_{m,k_0}$. Accordingly one obtains

$$h_m(\alpha_2) \quad \to \quad H_{mg} + (\delta_{m_0,m} + \delta_{n_0,n})\Delta\epsilon_m(eg; R_m) \,, \tag{A.17}$$

or

$$h_m(\alpha_2) \quad \to H_{mg} \quad + \delta_{k_0,m}\Delta\epsilon_m(fg; R_m) \,. \tag{A.18}$$

A more intuitive notation is achieved if one combines H_{mg} with $\Delta\epsilon_m(ag; R_m)$ ($a = e, f$). This combination can be rewritten as $H_{ka} - \lambda_{ka}$, where the excited state vibrational Hamiltonian $H_{ka} = H_{kg} - (\epsilon_k(g; R_k) - \epsilon_k(g; R_k^{(g)})) + (\epsilon_k(a; R_k) - \epsilon_k(a; R_k^{(a)}))$ is introduced as well as the related reorganization energy $\lambda_{ka} = \epsilon_k(a; R_k^{(g)}) - \epsilon(a; R_k^{(a)})$. Here, the $R_k^{(a)}$denote the equilibrium configuration which belongs to the the electronic state φ_a at chromophore k. The PES corresponding to the vibrational Hamiltonian H_{ka} are defined in a way to have their minimum at zero energy (as it has already been done for the quantities H_{kg}). Therefore the minimum energy $\epsilon_k(g; R_k^{(g)})$ of the ground-state PES has been removed and replaced by the energy $\epsilon_k(a; R_k^{(a)})$ of the excited state.

All this allows to write the Hamiltonian Eqs. A.11 and A.14 in the limit of vanishing electronic inter–chromophore coupling in the form

$$H_{\text{vib}}^{(\text{intra})}(\alpha_1, \alpha_1) \quad = \quad \sum_{m \neq m_0} H_{mg} + H_{m_0e} - \lambda_{m_0e} \,, \tag{A.19}$$

and

$$H_{\text{vib}}^{(\text{intra})}(\alpha_2, \alpha_2) \quad = \quad \sum_{m \neq m_0, n_0} H_{mg} + H_{m_0e} + H_{n_0e} - \lambda_{m_0e} - \lambda_{n_0e} \,, \tag{A.20}$$

as well as

$$H_{\rm vib}^{\rm (intra)}(\alpha_2,\alpha_2) \;=\; \sum_{m\neq k_0} H_{mg} + H_{k_0 f} - \lambda_{k_0 f}\,. \qquad \text{(A.21)}$$

If both Hamiltonians are combined with the associated electronic excitation energy (in the limit of vanishing electronic inter–chromophore coupling, cf. Eq. 2.4) one obtains the correct Hamiltonian of electron intramolecular vibrational interaction valid for decoupled chromophores.

The respective time-evolution operator (restricted up to the presence of double excitations) can be rewritten as

$$\begin{aligned} U_0(t) \;=\; & \prod_m U_{mg}(t)|0\rangle\langle 0| + \sum_m e^{-i\omega_{meg}t} U_{me}(t) \prod_{n\neq m} U_{ng}(t)|me\rangle\langle me| \\ & + \sum_{m,n} e^{-i(\omega_{meg}+\omega_{neg})t} U_{me}(t) U_{ne}(t) \prod_{k\neq m,n} U_{kg}(t)|me,ne\rangle\langle me,ne| \\ & + \sum_m e^{-i\omega_{mfg}t} U_{mf}(t) \prod_{n\neq m} U_{ng}(t)|mf\rangle\langle mf|\,. \qquad \text{(A.22)} \end{aligned}$$

The single-chromophore time-evolution operators are defined via the vibrational Hamiltonian H_{ma}, and the transition frequencies have been already introduced in Eq. 2.28.

A.3.2 Linear Coupling to Intra–Molecular Vibrations

The formulas given in the preceeding section will be put into a form of PES belonging to the intra–molecular vibrations. Therefore, one proceeds as in the case of the coupling to inter–molecular vibrations in Appendix C (cf. [RMK01]). First, as a result of a normal–mode analysis the ground–state PES should be described by a set of uncoupled harmonic vibrational coordinates with mode index ζ (note the difference to the inter–molecular normal modes). Second, a linear expansion of the quantities $\Delta\epsilon_m(ag;R_m)$ with respect to the deviations $\Delta R_{mj} = R_{mj} - R_{mj}^{(0)}$ (j labels all Cartesian coordinates of chromophore m). Remember that the $R_{mj}^{(0)}$ refer to the CC electronic ground–state. If the normal modes coordinates Q_ζ are introduced the desired linear coupling to intra–molecular vibrations has been derived. One may write (note the replacement of $\Delta\epsilon_m$ by ϵ_m on the right–hand side)

$$\Delta\epsilon_m(ag;R_m) \;\approx\; \sum_j \left(\frac{\partial}{\partial \Delta R_{mj}} \epsilon_m(ag;R_m)\right)_{|R_m=R_m^{(0)}} \sum_\zeta a_{j\zeta} Q_\zeta\,. \qquad \text{(A.23)}$$

Here, the $a_{j\zeta}$ mediate the linear transformation between the Cartesian intra–molecular coordinates and the normal–mode coordinates (written in a dimensionless form based on the use of harmonic oscillator operators). Since the coupling expression is linear in the vibrational coordinates the single chromophore coupling constant follows as

$$g_\zeta^{(\text{intra})}(ma) \quad = \quad \frac{1}{\hbar\omega_\zeta^{(\text{intra})}} \sum_j \Big(\frac{\partial}{\partial \Delta R_{mj}} \epsilon_m(ag;R) \Big)_{|R=R_0} a_{mj\zeta} \; . \tag{A.24}$$

Once these local coupling constants have been introduced it can be written

$$\Delta\epsilon_m(ag;R_m) \quad = \quad \sum_\zeta \hbar\omega_\zeta g_\zeta^{(\text{intra})}(ma) Q_\zeta \; . \tag{A.25}$$

This enables to introduce the coupling of MX states to intra–molecular vibrations via simple shifted harmonic oscillator PES. For the coupling to the single–exciton state one obtains from Eq. A.12 and A.16

$$\begin{aligned} h_m(\alpha_1) \quad &= \quad T_m^{(\text{intra})} + \sum_\zeta \hbar\omega_\zeta \{ - g_\zeta^{(\text{intra})2}(m,\alpha_1) \\ &\qquad + \frac{1}{4}(C_\zeta - C_\zeta^+ + 2g_\zeta^{(\text{intra})}(m,\alpha_1))^2 \} \; . \end{aligned} \tag{A.26}$$

The new coupling constant reads

$$g_\zeta^{(\text{intra})}(m,\alpha_1) \quad = \quad | \, C_{\alpha_1}(me) \, |^2 \, g_\zeta^{(\text{intra})}(me) \; . \tag{A.27}$$

In a similar manner one may derive the expression valid for the two–exciton manifold

$$\begin{aligned} h_m(\alpha_2) \quad &= \quad T + \sum_\zeta \hbar\omega_\zeta \{ - g_\zeta^{(\text{intra})2}(m,\alpha_2) \\ &\qquad + \frac{1}{4}(C_\zeta - C_\zeta^+ + 2g_\zeta^{(\text{intra})}(m,\alpha_2))^2 \} \; , \end{aligned} \tag{A.28}$$

but now with the coupling constant

$$\begin{aligned} g_\zeta^{(\text{intra})}(m,\alpha_2) \quad &= \quad 2 \sum_{k \neq m} | \, C_{\alpha_2}(me,ke) \, |^2 \, g_\zeta^{(\text{intra})}(me) \\ &\qquad + | \, C_{\alpha_2}(mf) \, |^2 \, g_\zeta^{(\text{intra})}(mf) \; . \end{aligned} \tag{A.29}$$

The energy shifts $\hbar\Delta\Omega(\alpha_N)$ at the particular MX level introduced, for example in Eq. 2.22 can simply be deducted from Eqs. A.26 and A.28 as the so-called polaron shift.

A.4 Reduced Density Matrix

The reduced density matrix (RDM), Eq. 2.17 cannot be directly related to observables like, for example, the expectation value of the CC dipole operator. To get such a quantity a RDM has to be defined in taking the trace $tr_{\mathrm{vib}}\{...\}$ with respect to the vibrational (reservoir) states. It follows

$$\bar{\rho}_{\alpha\beta}(t) \;=\; \mathrm{tr}\{\hat{W}(t)|\beta\rangle\langle\alpha|\} \equiv \langle\alpha|tr_{\mathrm{vib}}\{\hat{W}(t)\}|\beta\rangle \; . \qquad \text{(A.30)}$$

This RDM is of primary interest and it will be clarified in the following how $\rho_{\alpha\beta}(t)$, Eq. B.2 can be related to $\bar{\rho}_{\alpha\beta}$, Eq. A.30. Since the vibrational states depend on the excitonic (system) quantum numbers α there is no unique way to calculate the trace. Taking the state $\bar{\chi}_{\alpha\mu}$ which belongs to the exciton state $|\alpha\rangle$, one obtains

$$\bar{\rho}_{\alpha\beta}(t) \;=\; \sum_{\mu}\langle\alpha|\langle\bar{\chi}_{\alpha\mu}|\hat{W}(t)|\bar{\chi}_{\alpha\mu}\rangle|\beta\rangle \; , \qquad \text{(A.31)}$$

what is essentially different from $\rho_{\alpha\beta}(t)$, Eq. B.2 . If the displacement operator $D^{+}_{\alpha\beta} \equiv D^{+}_{\alpha}D_{\beta}$ (see, e.g. [MK00a]) is applied which moves the (harmonic oscillator) state $\bar{\chi}_{\beta\mu}$ to $\bar{\chi}_{\alpha\mu}$ it follows

$$\bar{\rho}_{\alpha\beta}(t) \;=\; \sum_{\mu}\langle\alpha|\langle\bar{\chi}_{\alpha\mu}|\hat{W}(t)D^{+}_{\alpha\beta}|\bar{\chi}_{\beta\mu}\rangle|\beta\rangle \; , \qquad \text{(A.32)}$$

To have a simple interrelation between $\bar{\rho}_{\alpha\beta}$ and $\rho_{\alpha\beta}$ in the spirit of a mean–field approximation the expectation value of $D^{+}_{\alpha\beta}$ is taken and one can write

$$\bar{\rho}_{\alpha\beta}(t) \;\approx\; \sum_{\mu} < D^{+}_{\alpha\beta} > \langle\alpha|\langle\bar{\chi}_{\alpha\mu}|\hat{W}(t)|\bar{\chi}_{\beta\mu}\rangle|\beta\rangle \equiv < D^{+}_{\alpha\beta} > \rho_{\alpha\beta}(t) \; , \qquad \text{(A.33)}$$

This expression offers the required interrelation between both types of RDM. In the following it is demonstrated how to calculate $\rho_{\alpha\beta}(t)$. Once this has been done $\bar{\rho}_{\alpha\beta}(t)$ can be computed in using the above given formula.

It remains to fix the definition of the expectation value $< ... >$. A reasonable way to define the expectation value of the displacement operator would be the thermal average with respect to those vibrational states $\bar{\chi}_{\mu}$ to which D_{α} and D_{β} refer. Therefore, one notes $D_{\alpha}|\bar{\chi}_{\mu}\rangle = |\bar{\chi}_{\alpha\mu}\rangle$ and obtains $< D^{+}_{\alpha\beta} >= \sum_{\mu} f(\mu)$ $\langle\bar{\chi}_{\alpha\mu}|\bar{\chi}_{\beta\mu}\rangle$. This quantity will also be used in Sec. 2.5.3. If the given RDM–theory is applied to the MX–vibrational system discussed in the main part of this paper it has to be defined for the intra–molecular (intra–chromophore) vibrations. However, it becomes equal to one for the protein vibrations since for those vibrations any shift of the equilibrium position has been neglected.

A.5 Multi-exciton Vibrational State Representation of the Density Matrix Theory

The state–representation explained here is based on the MX vibrational states introduced in Sec. 2.4. The respective representation of the complete CC Hamiltonian, Eq. 2.4 reads

$$H_{\rm CC} = \sum_{A,B} H_{A,B} |A\rangle\langle B| \tag{A.34}$$

with the Hamiltonian matrix

$$H_{A,B} = \delta_{A,B} E_A + V_{A,B}(t) \ . \tag{A.35}$$

The energies E_A correspond to the complete state $|A\rangle = |\alpha_M\rangle|\chi_\mu\rangle|\bar{\chi}_{\alpha\bar{\mu}}\rangle$ and split off into excitonic and vibrational contributions (cf. Eq. 2.22)

$$E_A/\hbar = E(\alpha_M) + \Delta\Omega(\alpha_M) + \Omega_\mu + \bar{\Omega}_{\bar{\mu}} \ , \tag{A.36}$$

and the coupling matrix elements incorporate different contributions.

$$V_{A,B} = V_{A,B}^{(\rm mx-pro)} + V_{A,B}^{(\rm mx-intra)} + V_{A,B}^{(\rm na)} + V_{A,B}^{(\rm field)}(t) \tag{A.37}$$

The elements resulting from the coupling to the protein vibrations follow as (note the presence of the intramolecular Franck-Condon factor which will be discussed elsewhere)

$$\begin{aligned} V_{A,B}^{(\rm mx-pro)} &= \delta_{M,N}(1-\delta_{N,0})\langle\bar{\chi}_{\alpha_N\bar{\mu}}|\bar{\chi}_{\beta_N\bar{\nu}}\rangle \\ &\quad \times \sum_\xi \hbar\omega_\xi g_\xi(\alpha_N\beta_N)\langle\chi_\mu|[C_\xi^+ + C_\xi]|\chi_\nu\rangle \ . \end{aligned} \tag{A.38}$$

The off-diagonal matrix elements of $H_{\rm vib}^{(\rm intra)}(\alpha_M, \beta_N)$, contained in Eq. 2.12 are used to introduce a coupling, which is combined with the part following from intramolecular vibrations. It reads

$$\begin{aligned} V_{A,B}^{(\rm mx-intra)} &= \delta_{M,N}(1-\delta_{N,0})(1-\delta_{\alpha_N,\beta_N})\delta_{\mu,\nu} \\ &\quad \times\langle\bar{\chi}_{\alpha_M\bar{\mu}}|\Delta H_{\rm vib}^{(\rm intra)}(\alpha_M,\beta_M)|\bar{\chi}_{\beta_M\bar{\nu}}\rangle \ . \end{aligned} \tag{A.39}$$

Finally, the matrix element of the nonadiabatic transition follow as ($N > 1$)

$$V_{A,B}^{(\rm na)} = (\delta_{M,N-1} + \delta_{M,N+1})\delta_{\mu,\nu}\Theta(\alpha_M\beta_N)\langle\bar{\chi}_{\alpha_M\bar{\mu}}|\bar{\chi}_{\beta_N\bar{\nu}}\rangle \ . \tag{A.40}$$

A.6 EEA Rate with an Exact Account for MX–Effects

In this Appendix it is demonstrated how to fully cover excitonic effects into the DOS of the EEA rate $k^{(\text{EEA})}(\alpha_2 \to \beta_1)$. Most appropriate would be the use of the coupling Hamiltonian based on a linear expansion with respect to the intra–molecular vibrational coordinates introduced in Appendix A.3.2. Now the Hamiltonian describing intra–molecular dynamics in the two–exciton manifold as well as in the single exciton manifold are characterized by the same harmonic oscillators only displaced one to another. For such a case it is well–known (see e.g. [MK00a, Muk95]) that the trace in Eq. 2.30 can be expressed by the so–called line–shape function appearing in the exponent. As a result the combined density of states reads

$$\begin{aligned}&\mathcal{D}(\alpha_2, \beta_1; \Omega(\alpha_2, \beta_1)) \\ &= \frac{1}{2\pi\hbar} \int dt \ \exp\left(i\Omega(\alpha_2, \beta_1)t - G(\alpha_2, \beta_1; 0) + G(\alpha_2, \beta_1; t)\right) .\end{aligned} \tag{A.41}$$

The G–function is defined as

$$\begin{aligned}&G(\alpha_2, \beta_1; t) \\ &= \int d\omega (e^{-i\omega t} - 1)(1 + n(\omega))(J(\alpha_2\beta_1; \omega) - J(\alpha_2\beta_1; -\omega)) ,\end{aligned} \tag{A.42}$$

where $n(\omega)$ denotes the Bose–Einstein distribution and the spectral density reads

$$J(\alpha_2, \beta_1; \omega) = \sum_m \sum_\zeta (g_\zeta^{(\text{intra})}(m, \alpha_2) - g_\zeta^{(\text{intra})}(m, \beta_1))^2 \delta(\omega - \omega_\zeta). \tag{A.43}$$

The coupling constants $g_\zeta^{(\text{intra})}$ are given in Appendix A.3.2.

The general structure of Eq. A.41 is standard and a general treatment can be found e.g. in Ref.[Muk95]. Note that the MX effects enter the expressions in a direct way via MX transition energies, but also in a more indirect way via the coupling constants to the vibrational DOF.

Appendix B

The Equation of Motion of the Reduced Density Matrix

To explain the main idea of the used density matrix theory it is applied in the following to a system of exciton–vibrational states $|A\rangle \equiv |\alpha\rangle|\bar{\chi}_{\alpha\mu}\rangle$ which are somewhat reduced as compared to those introduced in Section 2.4. Here, α reminds on the MX quantum number but to have a sufficient simple notation any hind on the given manifold is suppressed. The μ denote the vibrational quantum numbers of the vibrational states $\bar{\chi}_{\alpha\mu}$, which in addition *may* depend on the (excitonic) quantum number α. This Appendix is quite general and accounts for both the intra-chromophore vibrations and the protein vibrations. The more specialized versions will be given in the main text.

The states $|A\rangle$ are characterized by energies $E_A = \hbar\omega_\alpha + \hbar\bar{\omega}_\mu$ (including excitonic and vibrational contributions) and coupled one to another via the matrix elements $V_{AB} = \hbar v_{AB}$. The density matrix in the state representation reads

$$W_{AB}(t) \quad = \quad \langle A|\hat{W}(t)|B\rangle \, . \tag{B.1}$$

It is defined by the time–dependent non-equilibrium statistical operator $\hat{W}(t)$. The reduced density matrix (RDM) is introduced by taking the trace with respect to the vibrational quantum numbers

$$\rho_{\alpha\beta}(t) \quad = \quad \sum_\mu W_{\alpha\mu,\beta\mu}(t) \equiv \sum_\mu \langle\alpha|\langle\bar{\chi}_{\alpha\mu}|\hat{W}(t)|\bar{\chi}_{\beta\mu}\rangle|\beta\rangle \tag{B.2}$$

Following Ref. [KMS94] this RDM can be calculated in a standard way by applying the projection superoperator $\mathcal{P}$ which acts on an arbitrary matrix as follows

$$\mathcal{P}A_{\alpha\mu,\beta\nu} \quad = \quad \delta_{\mu,\nu} f(\mu) \sum_\kappa A_{\alpha\kappa,\beta\kappa} \tag{B.3}$$

$$\mathcal{P}W_{\alpha\mu,\beta\nu}(t) \quad = \quad \delta_{\mu,\nu} f(\mu) \rho_{\alpha\beta}(t) \tag{B.4}$$

The expression includes the thermal distribution $f(\mu)$ with respect to the vibrational levels. Its independency on the excitonic quantum number α is essential for the whole approach and may follow directly from the assumption of a linear exciton–vibrational coupling (cf. A.23).

The density matrix theory will be formulated in such a manner that an equation of motion for the RDM Eq. B.2 is obtained in the second order with respect to the coupling matrix v [KMS94]. To get an equation of motion for the RDM one starts with the Liouville von Neumann equation. It results the following equation of motion for the density matrix Eq. B.1:

$$\begin{aligned}\frac{\partial}{\partial t}W_{\alpha\mu,\beta\nu}(t) &= -i\omega_{\alpha\mu,\beta\nu}W_{\alpha\mu,\beta\nu}(t)\\ &\quad -i\sum_{\gamma\sigma}\left(v^{(l)}_{\alpha\mu,\gamma\sigma}W_{\gamma\sigma,\beta\nu}(t)-v^{(r)}_{\gamma\sigma,\beta\nu}W_{\alpha\mu,\gamma\sigma}(t)\right)\end{aligned} \tag{B.5}$$

with the transition frequencies $\omega_{\alpha\mu,\beta\nu}=\omega_{\alpha\beta}+\bar{\omega}_{\mu\nu}=\omega_\alpha+\bar{\omega}_\mu-\omega_\beta-\bar{\omega}_\nu$. The upper indices (l) and (r) determine, if the coupling operator acts at the left or the right index of the density matrix (Note that in the moment if one calculates the effect of the projection operator $\mathcal{P}$, the coupling operators have top be ordered in the ordinary way, i.e. the left ones on the left, the right ones on the right of the density matrix, and the ones earlier applied nearer to it). Now one applied the projection operators $\mathcal{P}$ and $\mathcal{Q}=1-\mathcal{P}$ after Eq. B.3 to Eq. B.5. It gives

$$\begin{aligned}&\frac{\partial}{\partial t}\rho_{\alpha\beta}(t)=-i\omega_{\alpha\beta}\rho(t)\\ &-i\sum_{\gamma}\left(<v^{(l)}_{\alpha\gamma}>\rho_{\gamma\beta}(t)-<v^{(r)}_{\gamma\beta}>\rho_{\alpha\gamma}(t)\right)\\ &-i\frac{1}{f(\mu)}\sum_{\gamma\sigma}\left(\mathcal{P}v^{(l)}_{\alpha\mu,\gamma\sigma}\mathcal{Q}W_{\gamma\sigma,\beta\mu}(t)-\mathcal{P}v^{(r)}_{\gamma\sigma,\beta\mu}\mathcal{Q}W_{\alpha\mu,\gamma\sigma}(t)\right),\end{aligned} \tag{B.6}$$

and

$$\begin{aligned}&\frac{\partial}{\partial t}\mathcal{Q}W_{\alpha\mu,\beta\nu}(t)=-i\omega_{\alpha\mu,\beta\nu}\mathcal{Q}W_{\alpha\mu,\beta\nu}(t)\\ &-i\sum_{\gamma}\left(\mathcal{Q}v^{(l)}_{\alpha\mu,\gamma\nu}f(\nu)\rho_{\gamma\beta}(t)-\mathcal{Q}v^{(r)}_{\gamma\mu,\beta\nu}f(\mu)\rho_{\alpha\gamma}(t)\right).\end{aligned} \tag{B.7}$$

In the Eq. B.7 the parts containing $\mathcal{Q}v\mathcal{Q}W$ have been neglected, because they lead to terms higher than second order in v. The averaging with respect to the vibrational (reservoir) DOF has been abbreviated by

$$<\ v_{\alpha\beta}>=\sum_{\mu}f(\mu)v_{\alpha\mu,\beta\mu}\,. \tag{B.8}$$

Note that if a linear exciton-vibrational coupling is provided, the coupling elements diagonal in the vibrational index vanish, and one gets $< v_{\alpha\beta} >= 0$. The integration of Eq. B.7 gives (neglecting initial correlations $\mathcal{Q}W(0)$)

$$\begin{aligned} &\mathcal{Q}W_{\alpha\mu,\beta\nu}(t) = \\ &-i\int_0^t d\tau\, e^{i\omega_{\alpha\mu,\beta\nu}\tau}\sum_\gamma \Big(\mathcal{Q}v^{(l)}_{\alpha\mu,\gamma\nu}f(\nu)\rho_{\gamma\beta}(t-\tau) - \mathcal{Q}v^{(r)}_{\gamma\mu,\beta\nu}f(\mu)\rho_{\alpha\gamma}(t-\tau)\Big) \end{aligned} \tag{B.9}$$

The result is then inserted into Eq. B.6

$$\begin{aligned} \frac{\partial}{\partial t}\rho_{\alpha\beta}(t) \;=\; & -i\omega_{\alpha\beta}\rho_{\alpha\beta}(t) - i\sum_\gamma\Big(< v_{\alpha\gamma} > \rho_{\gamma\beta}(t) - < v_{\gamma\beta} > \rho_{\alpha\gamma}(t)\Big) \\ & -\frac{1}{f(\mu)}\sum_{\gamma\sigma}\Big(\mathcal{P}v^{(l)}_{\alpha\mu,\gamma\sigma}\int_0^t d\tau\, e^{i\omega_{\gamma\sigma,\beta\mu}\tau}\sum_\delta(1-\mathcal{P})v^{(l)}_{\gamma\sigma,\delta\mu}f(\mu)\rho_{\delta\beta}(t-\tau) \\ & -\mathcal{P}v^{(l)}_{\alpha\mu,\gamma\sigma}\int_0^t d\tau\, e^{i\omega_{\gamma\sigma,\beta\mu}\tau}\sum_\delta(1-\mathcal{P})v^{(r)}_{\delta\sigma,\beta\mu}f(\sigma)\rho_{\gamma\delta}(t-\tau) \\ & -\mathcal{P}v^{(r)}_{\gamma\sigma,\beta\mu}\int_0^t d\tau\, e^{i\omega_{\alpha\mu,\gamma\sigma}\tau}\sum_\delta(1-\mathcal{P})v^{(l)}_{\alpha\mu,\delta\sigma}f(\sigma)\rho_{\delta\gamma}(t-\tau) \\ & +\mathcal{P}v^{(r)}_{\gamma\sigma,\beta\mu}\int_0^t d\tau\, e^{i\omega_{\alpha\mu,\gamma\sigma}\tau}\sum_\delta(1-\mathcal{P})v^{(r)}_{\delta\mu,\gamma\sigma}f(\mu)\rho_{\alpha\delta}(t-\tau)\Big) \end{aligned} \tag{B.10}$$

Introducing the second order autocorrelation function

$$< \; v_{\alpha\beta}(t)v_{\gamma\delta} >= \sum_{\mu,\nu} f(\mu)e^{i\bar{\omega}_{\mu\nu}t}v_{\alpha\mu,\beta\nu}\; v_{\gamma\nu,\delta\mu} - < v_{\alpha\beta} >< v_{\gamma\delta} > \,, \tag{B.11}$$

and rearranging of the coupling terms results in

$$\begin{aligned} \frac{\partial}{\partial t}\rho_{\alpha\beta}(t) \;=\; & -i\omega_{\alpha\beta}\rho_{\alpha\beta}(t) - i\sum_\gamma\Big(< v^{(l)}_{\alpha\gamma} > \rho_{\gamma\beta}(t) - < v^{(r)}_{\gamma\beta} > \rho_{\alpha\gamma}(t)\Big) \\ & -\sum_{\gamma\delta}\int_0^t d\tau\Big(e^{i\omega_{\gamma\beta}\tau} < v^{(l)}_{\alpha\gamma}(-\tau)v^{(l)}_{\gamma\delta} > \rho_{\delta\beta}(t-\tau) \\ & -\{e^{i\omega_{\gamma\beta}\tau} < v^{(r)}_{\delta\beta}(\tau)v^{(l)}_{\alpha\gamma} > + e^{i\omega_{\alpha\delta}\tau} < v^{(r)}_{\delta\beta}(-\tau)v^{(l)}_{\alpha\gamma} >\}\rho_{\gamma\delta}(t-\tau) \\ & +e^{i\omega_{\alpha\gamma}\tau} < v^{(r)}_{\delta\gamma}(\tau)v^{(r)}_{\gamma\beta} > \rho_{\alpha\delta}(t-\tau)\Big)\,. \end{aligned} \tag{B.12}$$

Now the fast varying factor $\exp(-i\omega_{\alpha\beta}\tau)$ is split off the respective density matrix $\rho_{\alpha\beta}(t-\tau)$ within the integrals, and the Markov approximation is applied, i.e. evaluating the slowly varying density matrix at time t and setting its upper limit of the integral to infinity (cf. Ref. [KMS94]).

$$\int_0^t d\tau\, A(\tau)\rho_{\alpha\beta}(t-\tau) \rightarrow \rho_{\alpha\beta}(t)\int_0^\infty d\tau\, A(\tau)e^{-i\omega_{\alpha\beta}\tau} \tag{B.13}$$

Note that after all projection operators have been removed, the upper indices (r) and (l) can be neglected. Using the following abbreviation

$$\Gamma(\alpha\beta,\gamma\delta;\omega) \;=\; Re\int\limits_0^\infty d\tau e^{i\omega\tau} < v_{\alpha\beta}(\tau)v_{\gamma\delta} > \tag{B.14}$$

the equation of motion can be rewritten as

$$\begin{aligned}\frac{\partial}{\partial t}\rho_{\alpha\beta}(t) \;=\;& -i\omega_{\alpha\beta}\rho_{\alpha\beta}(t) - i\sum_\gamma\Big(< v_{\alpha\gamma} > \rho_{\gamma\beta}(t) - < v_{\gamma\beta} > \rho_{\alpha\gamma}(t)\Big)\\ &-\sum_{\gamma\delta}\Gamma(\alpha\gamma,\gamma\delta;\omega_{\delta\gamma})\rho_{\delta\beta}(t)\\ &+\{\Gamma(\delta\beta,\alpha\gamma;\omega_{\delta\beta})+\Gamma(\delta\beta,\alpha\gamma;\omega_{\gamma\alpha})\}\rho_{\gamma\delta}(t)\\ &-\Gamma(\delta\gamma,\gamma\beta;\omega_{\delta\gamma})\rho_{\alpha\delta}(t)\Big)\,.\end{aligned} \tag{B.15}$$

For the applications within this paper one changes to the so–called Bloch model in decoupling the dynamics of the diagonal elements of the RDM from that of the off–diagonal ones. The $< v_{\alpha\gamma} >$ vanish for the case of linear exciton-vibrational interaction as it is provided for the protein vibrations, but may become important for the intra-chromophore vibrational coupling.

Population Transfer

The dissipative part related to the transfer between different populations $P_\alpha = \rho_{\alpha\alpha}$, Eq. B.15 simplifies to

$$\begin{aligned}\frac{\partial}{\partial t}P_\alpha(t) \;&=\; \sum_\beta 2\Gamma(\beta\alpha,\alpha\beta;\omega_{\beta\alpha})P_\beta(t) - 2\Gamma(\alpha\beta,\beta\alpha;\omega_{\alpha\beta})P_\alpha(t)\\ &=\; \sum_\beta k(\beta\rightarrow\alpha)P_\beta(t) - k(\alpha\rightarrow\beta)P_\alpha(t)\,,\end{aligned} \tag{B.16}$$

where the transition rates are given by

$$k(\alpha \to \beta) \;=\; 2\Gamma(\alpha\beta, \beta\alpha; \omega_{\alpha\beta})\,. \tag{B.17}$$

Coherence Dephasing

Next, the decay of the coherences ($\alpha \neq \beta$) is considered. Note that all transfer components between different coherences or coherences and populations have been neglected. It is written as

$$\begin{aligned}
\frac{\partial}{\partial t}\rho_{\alpha\beta} &= -i\omega_{\alpha\beta}\rho_{\alpha\beta}(t) - i(< v_{\alpha\alpha} > - < v_{\beta\beta} >)\rho_{\alpha\beta}(t) \\
&\quad -\sum_{\gamma}(\Gamma(\alpha\gamma, \gamma\alpha; \omega_{\alpha\gamma}) + \Gamma(\beta\gamma, \gamma\beta; \omega_{\beta\gamma}))\rho_{\alpha\beta} \\
&\quad +2\Gamma(\alpha\alpha, \beta\beta; 0)\rho_{\alpha\beta} \\
&= \Big(- i\tilde{\omega}_{\alpha\beta} - \tilde{\Gamma}(\alpha, \beta) - \Gamma(\alpha) - \Gamma(\beta)\Big)\rho_{\alpha\beta}\,,
\end{aligned} \tag{B.18}$$

giving an oscillatory part with the frequency $\tilde{\omega}_{\alpha\beta} = \omega_{\alpha\beta} + (< v_{\alpha\alpha} > - < v_{\beta\beta} >)$, the dephasing due to relaxation to all other excitonic states,

$$\begin{aligned}
\Gamma(\alpha) &= \sum_{\gamma\neq\alpha}\Gamma(\alpha\gamma, \gamma\alpha; \omega_{\alpha\gamma}) \\
&= \frac{1}{2}\sum_{\gamma\neq\alpha} k(\alpha \to \gamma)
\end{aligned} \tag{B.19}$$

and the so called pure dephasing part

$$\begin{aligned}
\tilde{\Gamma}(\alpha, \beta) &= \Gamma(\alpha\alpha, \alpha\alpha; 0) - 2\Gamma(\alpha\alpha, \beta\beta; 0) + \Gamma(\beta\beta, \beta\beta; 0) \qquad \text{(B.20)} \\
&= \int_0^\infty d\tau \sum_{\mu,\nu} f(\mu) e^{i\bar{\omega}_{\mu\nu}\tau}(v_{\alpha\mu,\alpha\nu} - v_{\beta\mu,\beta\nu})^2 - (< v_{\alpha\alpha} > - < v_{\beta\beta} >)^2,
\end{aligned}$$

which is responsible for dephasing due to elastic scattering without energy transfer. When using linear exciton-vibrational coupling, this expression simplifies to

$$\tilde{\Gamma}(\alpha, \beta) = \int_0^\infty d\tau \sum_{\mu,\nu} f(\mu) e^{i\bar{\omega}_{\mu\nu}\tau}(v_{\alpha\mu,\alpha\nu} - v_{\beta\mu,\beta\nu})^2 \tag{B.21}$$

and $\tilde{\omega}_{\alpha\beta} = \omega_{\alpha\beta}$.

Appendix C

Protein Spectral Densities

To motivate the coupling of the MX–states to protein vibrations as well as the related rate $k^{(\mathrm{mx-pro})}(\alpha_N \to \beta_N)$, Eq. 2.27 together with the approximation for the spectral density $\mathcal{J}(\alpha_N\beta_N, \beta_N\alpha_N; \omega)$ a short derivation which generalizes the one of Ref. [RMK01] is presented. In order to account for low–frequency protein vibrations it is sufficient to consider all deviations from the electronic ground–state vibrations as perturbations. Modulations of the inter–chromophore electronic coupling may also be included, however in the following only modulations of the chromophore electronic excitation energies are taken into account.

C.1 Hamiltonian of the Protein Vibrations

According Eq. 2.12 the protein contribution to the MX–state vibrational coupling, Eq. 2.11 can be written as

$$H_{\mathrm{vib}}^{(\mathrm{pro})}(\alpha_N, \beta_N) = \delta_{N,0} H_{\mathrm{vib}}^{(0,\mathrm{pro})} + (1-\delta_{N,0})\Big(T_{\mathrm{pro}} + \sum_{\{me,nf\}_N} \times C^*_{\alpha_N}(\{me,nf\}_N) \Delta U_{\mathrm{pro}}(\{me,nf\}_N; R)\, C_{\beta_N}(\{me,nf\}_N)\Big) \,. \quad \text{(C.1)}$$

The MX expansion coefficients have been introduced in Eq. 2.10. Moreover,

$$\Delta U_{\mathrm{pro}}(\{me,nf\}_N; R) = U_{\mathrm{pro}}(\{me,nf\}_N; R) - U_{\mathrm{pro}}(\{me,nf\}_N; R_0) \,. \quad \text{(C.2)}$$

Adding $(1-\delta_{N,0})\Delta U_{\mathrm{pro}}^{(0)}(R)$ to the first term and subtracting it from the last one gets

$$H_{\mathrm{vib}}^{(\mathrm{pro})}(\alpha_N, \beta_N) = H_{\mathrm{vib}}^{(0,\mathrm{pro})} + (1-\delta_{N,0}) \sum_{\{me,nf\}_N} \quad \text{(C.3)}$$

$$\times C^*_{\alpha_N}(\{me,nf\}_N)(\Delta U_{\mathrm{pro}}(\{me,nf\}_N; R) - \Delta U_{\mathrm{pro}}^{(0)}(R))\, C_{\beta_N}(\{me,nf\}_N)\Big) \,.$$

The expression for the potential energy surface (PES, Eq. 2.8) referring to the actual chromophore excited state $|\{me,nf\}_N\rangle$ of the CC reads

$$
\begin{aligned}
&U_{\rm pro}(\{me,nf\}_N;R) - U^{(0)}_{\rm pro}(R) \\
&= (1-\delta_{N,0})\Big(\sum_{k\in\{me\}_{\mathcal{M}}} \epsilon_k(eg;R) + \sum_{k\in\{nf\}_{\mathcal{N}}} \epsilon_k(fg;R)\Big)_{|N=\mathcal{M}+2\mathcal{N}} \ , \qquad \text{(C.4)}
\end{aligned}
$$

The PES $U_{\rm pro}$ appears for an arbitrary set $R \equiv \{R_j\}$ of protein coordinates and for the set R_0 which describes the equilibrium configuration for the unexcited state of the CC.

Since the MX–state protein coupling will be considered to be weak a linearization of $\Delta U_{\rm pro}$ with respect to the protein coordinate differences $\Delta R_j = R_j - R_{0j}$ will be sufficient. For $N > 0$ (presence of at least a single excitation) it follows

$$
\begin{aligned}
U_{\rm pro}(\{me,nf\}_N;R) \quad -U^{(0)}_{\rm pro}(R) \approx \ & U_{\rm pro}(\{me,nf\}_N;R_0) - U^{(0)}_{\rm pro}(R_0) \\
&+\sum_j \Big(\sum_{k\in\{me\}_{\mathcal{M}}} \frac{\partial\epsilon_k(eg;R)}{\partial R_j} \,|_{R=R^{(0)}} \\
&+ \sum_{k\in\{nf\}_{\mathcal{N}}} \frac{\partial\epsilon_k(fg;R)}{\partial R_j} \,|_{R=R^{(0)}} \Big)_{|N=\mathcal{M}+2\mathcal{N}} \\
&\times \Delta R_j \ . \qquad \text{(C.5)}
\end{aligned}
$$

The $\epsilon_k(eg;R)$ and $\epsilon_k(fg;R)$ are excitation energies from the chromophore electronic ground–state into the S_1-state and the higher excited state S_n, respectively, and the summations account for all those chromophores which have been excited in one of these two states.

If one changes from the Cartesian coordinates R_j to dimensionless normal–mode coordinates Q_ξ (with mode index ξ) the ground–state part $H^{(0,\rm pro)}_{\rm vib}$ of Eq. C.1 becomes the normal–mode harmonic oscillator Hamiltonian

$$
H^{(\rm pro)}_{\rm vib}(\alpha_N,\beta_N) \ = H^{(0,\rm pro)}_{\rm vib} \ + \sum_\xi \hbar\omega_\xi g^{(\rm pro)}_\xi(\alpha_N,\beta_N) Q_\xi \ . \qquad \text{(C.6)}
$$

The dimensionless vibrational coordinates are given by oscillator operators according to $Q_\xi = c_\xi + c^+_\xi$. The related vibrational frequencies are denoted by ω_ξ and $g^{(\rm pro)}_\xi(\alpha_N,\beta_N)$ is the dimensionless MX protein vibration coupling matrix

$$
\begin{aligned}
&g_\xi(\alpha_N,\beta_N) = \\
&\quad \sum_{\{me,nf\}_N} C^*_{\alpha_N}(\{me,nf\}_N) g_\xi(\{me,nf\}_N) C_{\beta_N}(\{me,nf\}_N) \ , \qquad \text{(C.7)}
\end{aligned}
$$

with

$$g_\xi(\{me,nf\}_N) \;=\; \Big(\sum_{k\in\{me\}_\mathcal{M}} g_\xi(ke) + \sum_{k\in\{nf\}_\mathcal{N}} g_\xi(kf)\Big)_{|N=\mathcal{M}+2\mathcal{N}} . \qquad \text{(C.8)}$$

Obviously, $g_\xi(0) = 0$ holds. The coupling constants related to single chromophore read ($a = e, f$)

$$g_\xi(ka) \;=\; \sum_j \frac{A_{j\xi}}{\sqrt{2\hbar M_j \omega_\xi^3}} \frac{\partial \epsilon_m(ag;R)}{\partial R_j} \,|_{R=R^{(0)}} \;, \qquad \text{(C.9)}$$

where the coefficients $A_{j\xi}$ describe the linear transformation from the Cartesian protein coordinates R_j to mass–weighted normal–mode coordinates (M_j are the related mass–coefficients).

C.2 Spectral Density of the Protein Vibrations

According to Eq. 2.27 details of the MX intra–manifold relaxation are governed by spectral densities of type (cf. [RMK01])

$$\mathcal{J}(\alpha_N,\beta_N;\gamma_N,\delta_N;\omega) \;=\; \sum_\xi g_\xi(\alpha_N,\beta_N) g_\xi(\gamma_N,\delta_N)\delta(\omega-\omega_\xi) \qquad \text{(C.10)}$$

Noting Eqs. C.7 and C.8 the MX spectral densities can be expressed by spectral densities referring to localized BChl excitations. One obtains

$$\begin{aligned}\mathcal{J}(\alpha_N,\beta_N;\gamma_N,\delta_N;\omega) \;=\; & \sum_{\{ke,lf\}_N} \sum_{\{me,nf\}_N} C^*_{\alpha_N}(\{ke,lf\}_N) C_{\beta_N}(\{ke,lf\}_N) \\ & \times C^*_{\gamma_N}(\{me,nf\}_N) C_{\delta_N}(\{me,nf\}_N) \\ & \times \mathcal{J}(\{ke,lf\}_N;\{me,nf\}_N;\omega) \qquad \text{(C.11)}\end{aligned}$$

with the spectral density

$$\begin{aligned}\mathcal{J}(\{ke,lf\}_N;\{me,nf\}_N;\omega) \;=\; & \Big(\sum_{p\in\{ke\}_\mathcal{K}} \sum_{q\in\{me\}_\mathcal{M}} J(pe,qe;\omega) \\ & + \sum_{p\in\{lf\}_\mathcal{L}} \sum_{q\in\{me\}_\mathcal{M}} J(pf,qe;\omega) \\ & + \sum_{p\in\{ke\}_\mathcal{K}} \sum_{q\in\{nf\}_\mathcal{N}} J(pe,qf;\omega) \qquad \text{(C.12)} \\ & + \sum_{p\in\{lf\}_\mathcal{L}} \sum_{q\in\{nf\}_\mathcal{N}} J(pf,qf;\omega)\Big)^{|N=\mathcal{K}+2\mathcal{L}}_{|N=\mathcal{M}+2\mathcal{N}} .\end{aligned}$$

The newly introduced spectral densities refer to the multiple chromophore excitations of the CC and contain the following types of two–site spectral densities

$$J(pe,qe;\omega) = \sum_\xi g_\xi(pe)g_\xi(qe)\delta(\omega-\omega_\xi)\ , \tag{C.13}$$

$$J(pf,qe;\omega) = \sum_\xi g_\xi(pf)g_\xi(qg)\delta(\omega-\omega_\xi)\ , \tag{C.14}$$

and

$$J(pf,qf;\omega) = \sum_\xi g_\xi(pf)g_\xi(qf)\delta(\omega-\omega_\xi)\ . \tag{C.15}$$

The quantity $J(pe,qf;\omega)$ can be easily deduced from $J(pf,qe;\omega)$.

The derived expressions look nice, but nothing is known on details of the MX–protein coupling in the LH2. Therefore, different additional assumptions are necessary to further proceed. In Ref. [RMK01] it has been suggested how to treat the nonlocal character of $J(pe,qe;\omega)$ (what can be easily adopted to the two other types of spectral densities used here). For the computations in the present work a somewhat different assumption has been made, i.e. that of sufficiently localized protein vibrations. Then, all the quantities of the Eqs. C.13, C.14, and C.15 become diagonal with respect to the site–indices p and q. Now it is consequent to let become the single–site spectral densities independent on th e local BChl. Furthermore, since an efficient IC–process from the S_n state to the Q_y–state is present only a vibrational modulation of the Q_y–state will be considered.

Having all these simplifications in mind the single–exciton spectral density and the two–exciton one both entering the relaxation rate, Eq. 2.27 are obtained as

$$\mathcal{J}(\alpha_1\beta_1,\beta_1\alpha_1;\omega) = \sum_m \mid C_{\alpha_1}(me)C_{\beta_1}(me)\mid^2 J_e(\omega)\ , \tag{C.16}$$

and as

$$\begin{aligned}\mathcal{J}(\alpha_2\beta_2,\beta_2\alpha_2;\omega) &= \sum_{k,m,n} C^*_{\alpha_2}(ke,me)C_{\beta_2}(ke,me)\\ &\quad \times C^*_{\beta_2}(ke,ne)C_{\alpha_2}(ke,ne)\ J_e(\omega)\ .\end{aligned} \tag{C.17}$$

Appendix D

Weak Probe Field

To linearize $\tilde{P}_{\rm pr}$ of Eq. 3.3 with respect to the probe field and, in this way to let become $\Delta A_{\rm pr}$ independent on the probe field one starts with the complete time–dependence of the MX density operator including all fields

$$\hat{\rho}(t;\mathbf{E}) \;\; = \;\; \mathcal{U}(t,t_0;\mathbf{E})\hat{\rho}(t_0)\;. \tag{D.1}$$

The time evolution superoperator has been denoted by $\mathcal{U}$ and follows via the solution of Eq. 2.20. To carry out the linearization the total electric field–strength is separated into the pump field $\mathbf{E}_{\rm pu}(t)$ and into the probe field $\mathbf{E}_{\rm pr}(t)$. The Liouvillian $L_{\rm pr}(t)$ is introduced which exclusively describes the interaction with the probe field. The expression for $\hat{\rho}(t)$ linearized with respect to the probe field follows as (note that the field dependence will be indicated in the following by denoting the dependence on the pulse envelopes $E_{\rm pu}$ and $E_{\rm pr}$)

$$\hat{\rho}(t;\mathbf{E}) \;\; \approx \;\; \hat{\rho}(t;\mathbf{E}_{\rm pu}) - i\int\limits_{t_0}^{t} d\bar{t}\,\mathcal{U}(t,\bar{t};\mathbf{E}_{\rm pu})L_{\rm pr}(\bar{t})\hat{\rho}(\bar{t};\mathbf{E}_{\rm pu})\;. \tag{D.2}$$

Here, $\rho(t;E_{\rm pu})$ denotes the density operator which has been propagated at the presence of the pump field only. Noting Eq. D.2 the polarization after Eq. 3.5 reads

$$\begin{aligned}\mathbf{P}_{\rm pr}(\mathbf{r},t) \;\; &= \;\; \frac{i}{\hbar\Delta V(\mathbf{r})}\sum_{CC\in\Delta V(\mathbf{r})}\int\limits_{t_0}^{t} d\bar{t} \\ &\quad \times {\rm tr}_{\rm mx}\{(\hat{\mu}_{\rm CC}\mathcal{U}(t,\bar{t};\mathbf{E}_{\rm pu})[\mathbf{E}_{\rm pr}(t)\hat{\mu}_{\rm CC},\hat{\rho}(\bar{t};\mathbf{E}_{\rm pu})]_{-}\}.\end{aligned} \tag{D.3}$$

This expression simplifies considerable if the pump and the probe pulse do not overlap and if the duration of the probe pulse is short compared to any characteristic time of the MX–dynamics. The first assumption allows to exclude the pump pulse dependency of the time evolution superoperator $\mathcal{U}(t, \bar{t}; E_{\rm pu})$. The latter property allows to replace the probe field under the time integral by $\mathbf{E}_{\rm pr}(\bar{t}) \approx \delta(\bar{t} - t_{\rm pr})\ \bar{\mathbf{E}}_{\rm pr}$, i. e. by a δ–function localized at time $t_{\rm pr}$. From the experimental point of view, this mimics the action of an ideal white-light pulse. Using $\bar{\mathbf{E}}_{\rm pr} = \mathbf{e}_{\rm pr}\bar{E}_{\rm pr}$ and $\mathbf{P}_{\rm pr}(t) = \mathbf{e}_{\rm pr}P_{\rm pr}(t)$ the respective polarization follows from Eq. D.3 as

$$\begin{aligned} P_{\rm pr}(t) &= \frac{i\Theta(t - t_{\rm pr})}{\hbar \Delta V(\mathbf{r})} \bar{E}_{\rm pr} \sum_{\rm CC \in \Delta V(\mathbf{r})} \\ &\quad \times {\rm tr}_{\rm mx}\{\mathbf{e}_{\rm pr}\hat{\mu}_{\rm CC}\mathcal{U}(t - t_{\rm pr})[\mathbf{e}_{\rm pr}\hat{\mu}_{\rm CC}, \hat{\rho}(\tau_{\rm del}; \mathbf{E}_{\rm pu})]_-\} \ . \end{aligned} \tag{D.4}$$

The unit–step function guarantees that the expression vanishes for times before the probe pulse acts. Note that the time–evolution superoperator describes a field–free evolution as discussed above. In contrast, the density operator $\hat{\rho}(\tau_{\rm del}; \mathbf{E}_{\rm pu})$ characterizes the full evolution of the MX–system induced by the interaction with the pump–pulse. If the pump–pulse passes the excitations relaxes until the actual distribution is monitored by the probe–pulse at time $t_{\rm pr}$. Since it is of interest to draw the probe–pulse absorption versus the delay–time $\tau_{\rm del} = t_{\rm pr} - t_{\rm pu}$ (here,$t_{\rm pu}$ is the time at which the pump–pulse reaches its maximum), the MX–density operator has been indicated by $\tau_{\rm del}$ instead of $t_{\rm pr}$. (Since the pump–pulse does not vanish for t comparable to $t_{\rm pu}$ the computed $A_{\rm pr}$ for $\tau_{\rm del} = 0$ or for small $\tau_{\rm del}$ is not valid when using Eq. D.3.)

To carry out the Fourier transformation necessary to get the differential absorption Eq. 3.3 one has to compute the time–dependence induced by $\mathcal{U}(t - t_{\rm pr})$. To do this, first it is noted that in the present type of density matrix equations diagonal and off–diagonal elements are decoupled. So one may discuss the action of $\mathcal{U}(t - t_{\rm pr})$ separately for both cases (what becomes necessary since already $\hat{\rho}(t_{\rm pr}; \mathbf{E}_{\rm pu})$ leads to diagonal and off–diagonal matrix elements). If acting on diagonal elements of $[(e_{\rm pr}\hat{\mu}_{\rm CC}), \hat{\rho}(t_{\rm pr}; \mathbf{E}_{\rm pu})]_-$ the resulting matrix elements are still diagonal, and caused by the dipole operator positioned left from $\mathcal{U}(t - t_{\rm pr})$ in Eq. D.3 the whole expression becomes off–diagonal (in the manifold index). As a consequence the complete trace vanishes. Turning to the off–diagonal matrix elements of $[(e_{\rm pr}\hat{\mu}_{\rm CC}), \hat{\rho}(t_{\rm pr}; \mathbf{E}_{\rm pu})]_-$ the action of $\mathcal{U}(t - t_{\rm pr})$ is reduced to terms oscillating with the complex transition frequencies $\tilde{\Omega}(\alpha_M, \beta_N) = \Omega(\alpha_M, \beta_N)$ $-i\Gamma(\alpha_M) - i\Gamma(\beta_N)$ $-i\tilde{\Gamma}(\alpha_M, \beta_N)$, where the various dephasing rates are given by Eqs. B.19 and B.20.

Furthermore, two approximations are taken in the following which allow to concentrate on the leading contributions to $\Delta A_{\rm pr}$. The first approximation covers the restriction to resonance contributions (in the frequency domain) to $\Delta A_{\rm pr}$. Therefore, only terms of the trace have been taken which oscillate like $\exp(-i\Omega t)$ (with $\Omega > 0$). The second approximation neglects off–diagonal density matrix elements of the type $\rho(\alpha_{M\pm2}, \beta_M)$, i. e. those quantities which connect non–

neighboring exciton manifolds (the highly oscillatory behavior of these matrix elements justifies their disregard). Accordingly the MX–trace of Eq. D.3 is obtained as (note $d(\alpha_N, \beta_{N-1})$ $=\mathbf{d}(\alpha_N, \beta_{N-1})\mathbf{e}_{\mathrm{pr}}$)

$$
\begin{aligned}
&\mathrm{tr}_{\mathrm{mx}}\{\mathbf{e}_{\mathrm{pr}}\hat{\mu}_{\mathrm{CC}}\mathcal{U}(t-t_{\mathrm{pr}})[(\mathbf{e}_{\mathrm{pr}}\hat{\mu}_{\mathrm{CC}}), \hat{\rho}(t_{\mathrm{pr}}, \mathbf{E}_{\mathrm{pu}})]_{-}\} \\
&= \sum_{M} \sum_{\alpha_M \beta_{M+1}} d(\alpha_M, \beta_{M+1}) e^{-i\tilde{\Omega}(\beta_{M+1},\alpha_M)(t-t_{\mathrm{pr}})} \\
&\quad \times \sum_{\gamma_M} d(\beta_{M+1}, \gamma_M)\rho(\gamma_M, \alpha_M; t_{\mathrm{pr}}; E_{\mathrm{pu}})\,. \qquad \text{(D.5)}
\end{aligned}
$$

The given arrangement of the MX quantum numbers follows if one calculates $tr_{\mathrm{mx}}\{...\}$ via a summation with respect to the MX–states $|\alpha_M\rangle$. The β_{M+1}–summation results from introducing a complete MX–state set left from $\mathcal{U}(t - t_{\mathrm{pr}})$. The remaining summations with respect to γ_M and γ_{M+1} are related to the expression which are propagated by $\mathcal{U}(t - t_{\mathrm{pr}})$. Note the absence of any inter–manifold off–diagonal density matrix elements.

If one inserts the trace expression into Eq. D.3 the Fourier transformation necessary to get the transient absorption signal Eq. 3.3 can be carried out. One obtains from Eq. 3.3

$$
\begin{aligned}
A_{\mathrm{pr}}(\omega) &= \frac{4\pi\omega}{\hbar c \Delta V(\mathbf{r})} \sum_{\mathrm{CC}\in\Delta V(\mathbf{r})} \sum_{M} \sum_{\alpha_M \beta_{M+1}} \mathrm{Im} \\
&\Big(\sum_{\gamma_M} \frac{d(\alpha_M, \beta_{M+1}) d(\beta_{M+1}, \gamma_M)}{\omega - \tilde{\Omega}(\beta_{M+1}, \alpha_M)} \rho(\gamma_M, \alpha_M; \tau_{\mathrm{del}}, \mathbf{E}_{\mathrm{pu}}) \qquad \text{(D.6)} \\
&- \sum_{\gamma_{M+1}} \frac{d(\gamma_{M+1}, \alpha_M) d(\alpha_M, \beta_{M+1})}{\omega - \tilde{\Omega}(\beta_{M+1}, \alpha_M)} \rho(\beta_{M+1}, \gamma_{M+1}; \tau_{\mathrm{del}}, \mathbf{E}_{\mathrm{pu}}) \Big).
\end{aligned}
$$

According to the presence of diagonal and off–diagonal MX density matrix elements, i.e. $\rho(\gamma_M, \alpha_M) = \delta_{\gamma_M,\alpha_M} P(\gamma_M)$ $+(1 - \delta_{\gamma_M,\alpha_M})\Delta\rho(\gamma_M, \alpha_M)$ the absorption A_{pr} can be separated into a term $A_{\mathrm{pr}}^{(\mathrm{pop})}$ governed by the populations $P(\gamma_M)$ and a term $A_{\mathrm{pr}}^{(\mathrm{coh})}$ governed by the (intra–manifold) coherences $\Delta\rho(\gamma_M, \alpha_M)$. The latter describes intra–manifold dephasing and vanishes on the respective time–scale. In contrast $A_{\mathrm{pr}}^{(\mathrm{pop})}$ covers the relaxation of the MX–distribution to an equilibrium distribution of the single–exciton manifold (higher manifolds are depopulated because of the presence of EEA processes). One obtains for the absorption signal determined by the MX–population

$$
\begin{aligned}
A_{\mathrm{pr}}^{(\mathrm{pop})} &= \frac{4\pi\omega}{\hbar c \Delta V(\mathbf{r})} \sum_{\mathrm{CC}\in\Delta V(\mathbf{r})} \sum_{M} \sum_{\alpha_M \beta_{M+1}} \mid d(\alpha_M, \beta_{M+1}) \mid^2 \qquad \text{(D.7)} \\
&\times G(\beta_{M+1}, \alpha_M; \omega) \Big(P(\alpha_M; \tau_{\mathrm{del}}, \mathbf{E}_{\mathrm{pu}}) - P(\beta_{M+1}; \tau_{\mathrm{del}}, \mathbf{E}_{\mathrm{pu}} \Big).
\end{aligned}
$$

Here the Lorentzian line–shape function

$$\begin{aligned} G(\alpha_M, \beta_N; \omega) &= \operatorname{Im} \frac{1}{\omega - \tilde{\Omega}(\alpha_M, \beta_N)} \\ &= \frac{\Gamma(\alpha_M) + \Gamma(\beta_N) + \tilde{\Gamma}(\alpha_M, \beta_N)}{(\omega - \Omega(\alpha_M, \beta_N))^2 + (\Gamma(\alpha_M) + \Gamma(\beta_N) + \tilde{\Gamma}(\alpha_M, \beta_N))^2} \end{aligned} \tag{D.8}$$

is introduced. The quantity $A_{\mathrm{pr}}^{(\mathrm{coh})}$ follows from A_{pr} given in Eq. D.6 in replacing, ρ by $(1 - \delta)\Delta\rho$. It is easy to reduce $A_{\mathrm{pr}}^{(\mathrm{pop})}$ to an expression which only accounts for the first and the second exciton–manifold. The respective expression is given in the main part.

Appendix E

Evolutionary Algorithm

Following Ref. [BS93] there are three main groups of Evolutionary Algorithms, which are called Evolution Strategies, Evolutionary Programming, and Genetic Algorithms. Here, an algorithm is needed to adjust the energies of the chromophores. While Genetic Algorithms only work for binary numbers, both Evolution Strategies and Evolutionary programming use real numbers for the parameters, which should be optimized. Since in Ref. [BS93] the Evolution Strategy turned out to fulfill the optimization task best, that approach has been used in a slightly simplified and adopted way, as it will be described here.

Evolution Strategy

The starting point is given by λ sets $\mathbf{a}_1(0)...\mathbf{a}_\lambda(0)$ of N_C randomly chosen energy differences $\mathbf{a}_i(0) = \{\triangle\varepsilon_{i,1}...\triangle\varepsilon_{i,N_C}\}$ of the chromophores $1...N_C$ from the mean chromophore energy. The energy differences are given by a Gaussian random distribution $N(\sigma_0)$ with standard deviation σ_0, this can be written as $\triangle\varepsilon_{i,k} = N(\sigma_0)$. Additionally the sets of standard deviations are used, starting with the same value for all sets and sites, $\boldsymbol{\sigma}_i(0) = \{\sigma_{i,1}...\sigma_{i,N_C}\}$ and $\sigma_{i,k}(0) = \sigma_0$. In each set i each chromophore k has two values, the energy $\triangle\varepsilon_{i,k}$, and the standard deviation $\sigma_{i,k}$ of the Gaussian random distribution, both will be changed during the fitting process.

Now, the fitness value $f(\mathbf{a}_i)$ is evaluated, which has been chosen to be the sum of quadratic deviations of the simulated spectra to the measured. Beside the absorption and LD spectra at 4K and the CD spectra at 77K also their respective first deviations have been used, this results in a better fit of the structural features in the spectra. The μ best sets are chosen to become the “parent” generation, using different mechanisms as described below, they are used to produce a set of $\lambda > \mu$ children. There are now two different possibilities to proceed, either one takes the parent and children generation together (which is called ES$(\mu + \lambda)$), or only the children generation is used ES(μ, λ). The first approach assures that the best solution stays in the set, but the later is less probably trapped in a local minimum. Now again the fitness value is evaluated, and the best μ sets out of the λ children are used to become the parents of the next generation. This process is repeated until a certain convergence criterion has been fulfilled, or the number of generations exceeds a given number N_{gen}.

The processes which lead from the parent generation to the children generation are the following.

Mutation

For mutations the following scheme has been used for all sets and chromophores with a general chance of 20% for the mutation (cf. Ref. [BS93])

$$\begin{aligned} \sigma'_{i,k} &= \sigma_{i,k} \cdot \exp(N_i(\tau') + N(\tau)) && \text{(E.1)} \\ \triangle\varepsilon'_{i,k} &= \triangle\varepsilon_{i,k} + N(\sigma'_{i,k})\,, && \text{(E.2)} \end{aligned}$$

where $N_i(\sigma)$ is evaluated only once for each set, and $N(\sigma)$is evaluated for every single chromophore. The parameters τ and τ'have been suggested (cf. Ref. [BS93]) to be

$$\begin{aligned} \tau &\sim (\sqrt{2\sqrt{N_C}})^{-1} && \text{(E.3)} \\ \tau' &\sim (\sqrt{2N_C})^{-1}\,. && \text{(E.4)} \end{aligned}$$

Double-Mutation

Double mutation has been introduced to shift two strongly coupled chromophores into the same direction at one time. Note that this process would have a very low probability using only single mutations as in the previous section. The following process will be done for every set separately. First a certain chromophore k is chosen by chance. Then the chromophore l which has the strongest dipole-dipole coupling to chromophore k is searched and one uses the following parameters

$$\begin{aligned} c'_{i,k} &= \exp(N_i(\tau') + N(\tau)) && \text{(E.5)} \\ c_{i,k} &= N(\sigma'_{i,k}) && \text{(E.6)} \end{aligned}$$

to shift both the energies and the standard derivations

$$\begin{aligned} \sigma'_{i,k} &= \sigma_{i,k} \cdot c'_{i,k} && \text{(E.7)} \\ \triangle\varepsilon'_{i,k} &= \triangle\varepsilon_{i,k} + c_{i,k}\,, && \text{(E.8)} \end{aligned}$$

and

$$\begin{aligned} \sigma'_{i,l} &= \sigma_{i,l} \cdot c'_{i,k} && \text{(E.9)} \\ \triangle\varepsilon'_{i,l} &= \triangle\varepsilon_{i,l} + c_{i,k} \, , && \text{(E.10)} \end{aligned}$$

in the same way for chromophore k and l.

Recombination

The process of recombination, sometimes also called crossover is given in the following. Two of the parents i and j are chosen by chance, and for each chromophore the value of either parent is chosen again by chance.

$$\begin{aligned} \sigma'_{i,k} &= \sigma_{i,k} \text{ or } \sigma_{j,k} && \text{(E.11)} \\ \triangle\varepsilon'_{i,k} &= \triangle\varepsilon_{i,k} \text{ or } \triangle\varepsilon_{j,k} && \text{(E.12)} \end{aligned}$$

The Parameters for the PS1

It turned out for the described task, the ES(μ,λ) gives better results, and therefore has been used throughout the calculations. For the determination of the energies of the 96 Chls of the PS1 ($N_C = 96$) the ES(20,5) algorithm is used, with up to 200 generations. The children are reproduced by mutation (10), double mutation (5) and recombination (5).

Bibliography

[AMDS99] D. C. Arnett, C. C. Moser, P. L. Dutton, and N. F. Scherer. *J. Phys. Chem. B*, 103:2014, 1999.

[ANM00a] R. E. Blankenship A. N. Melkozernov, S. Lin. *Biochem.*, 39:1489, 2000.

[ANM00b] R. E. Blankenship A. N. Melkozernov, S. Lin. *J. Phys. Chem. B*, 104:1651, 2000.

[BDKG03] T. Brixner, N. H. Damrauer, B. Kiefer, and G. Gerber. *J. Chem. Phys.*, 118:3692, 2003.

[Bed98a] G. S. Beddard. *J. Phys. Chem. B*, 102:10966, 1998.

[Bed98b] G. S. Beddard. *Phil. Trans. R. Soc. Lond. A*, 356:421, 1998.

[BHS$^+$01] B. Brüggemann, J. L. Herek, V. Sundström, T. Pullerits, and V. May. *J. Phys. Chem. B.*, 105:11391, 2001.

[BJK$^+$02] M. Byrdin, P. Jordan, N. Krauss, P. Fromme, D. Stehlik, and E. Schlodder. *Biophys. J.*, 83:433, 2002.

[BJvM$^+$95] S. E. Bradforth, R. Jimenez, F. van Mourik, R. van Grondelle, and G. R. Fleming. *J. Phys. Chem.*, 99:16179, 1995.

[BK99] L. D. Bakalis and J. Knoester. *J. Phys. Chem.*, 103:6620, 1999.

[Blu96] K. Blum. *Density Matrix Theory and Applications.* Plenum Press, New York, 1996.

[BM03] B. Brüggemann and V. May. *J. Chem. Phys.*, 118:746, 2003.

[BM04a] B. Brüggemann and V. May. *J. Chem. Phys.*, 120:2325, 2004.

[BM04b] B. Brüggemann and V. May. *J. Phys. Chem. B*, submitted, 2004.

[BM04c] B. Brüggemann and V. May. *Chem. Phys. Lett.*, submitted, 2004.

[BNP13] M. Becker, V. Nagarajan, and W. W. Parson. *J. Am. Chem. Soc.*, 1991:6840, 113.

[Bri04a] Encyclopaedia Britannica. *Bacteria.* Encyclopaedia Britannica Inc., 2004.

[Bri04b] Encyclopaedia Britannica. *Blue-green algae.* Encyclopaedia Britannica Inc., 2004.

[BRS$^+$00] M. Byrdin, I. Rimke, E. Schlodder, D. Stehlik, and T. A. Roelofs. *Biophys. J.*, 79:992, 2000.

[BS86] P. Brumer and M Shapiro. *Chem. Phys. Lett.*, 126:541, 1986.

[BS93] T. Bäck and H.-P. Schwefel. *Evolutionary Computation*, 1:1–23, 1993.

[BSFN03] A. Ben-Shem, E. Frolow, and N. Nelson. *Nature*, 426:630, 2003.

[BSH$^+$99] M. A. Bopp, A. Sytnik, T.D. Howard, R. J. Cogdell, and R. M. Hochstrasser. *Proc. Natl. Acad. Sci. USA*, 96:11271, 1999.

[BSN$^+$04] B. Brüggemann, K. Sznee, V. Novoderezhkin, R. van Grondelle, and V. May. *J. Phys. Chem. B*, submitted, 2004.

[CABA03] A Camara-Artigas, R. Blankenship, and J. P. Allen. *Photosynth. Res.*, 49:49, 2003.

[CMW96] J. Cao, M. Messina, and K. R. Wilson. *J. Chem. Phys.*, 106:5239, 1996.

[Dav62] A. S. Davydov. *Theory of Molecular Excitons.* McGraw-Hill, New York, 1962.

[DKKS02] A. Damjanovic, I. Kosztin, U Kleinekathöfer, and K. Schulten. *Phys. Rev. E*, 65:031919, 2002.

[DMC$^+$00] M. Dahlbom, T. Minami, V. Chernyak, T. Pullerits, V. Sundström, and S. Mukamel. *J. Phys. Chem. B*, 104:3976, 2000.

[DVFF02] A. Damjanović, H. M. Vaswani, P. Fromme, and G. R. Fleming. *J. Phys. Chem. B*, 106:10251, 2002.

[dVRRe01] R. de Vivie-Riedle, H. Rabitz, and K. Kompa (eds.). Laser control of quantum dynamics. *special issue, Chem. Phys.*, 267:1, 2001.

[Fan63] U. Fano. *Phys. Rev.*, 131:259, 1963.

[(Fe99] K. Wilson (Festschrift). *J. Chem. Phys. A*, 103:10021, 1999.

[FIM+04] K. N. Ferreira, T. M. Iverson, K. Maghlaoui, J. Barber, and S. Iwata. *science*, page 1093087, 2004.

[FJLW98] A. Freiberg, J.A. Jackson, S. Lin, and N.W. Woodbory. *J. Phys. Chem. A*, 102:4372, 1998.

[FKD+02] G. Fritzsch, J. Koepke, R. Diem, A. Kuglstatter, and L. Baciou. *Acta Crystallogr.*, D58:1660, 2002.

[FNK88] M. Fragata, B. Nordén, and T. Kurucsev. *Photochem. Photobio.*, 47:133, 1988.

[För48] Th. Förster. *Ann. Physik*, 2:55, 1948.

[Fre31a] Ya. I. Frenkel. *Phys. Rev.*, 37:17, 1931.

[Fre31b] Ya. I. Frenkel. *Phys. Rev.*, 37:1276, 1931.

[GFG95] E. Gaižauskas, K.-H. Feller, and R. Gadonas. *Opt. Com.*, 118:360, 1995.

[GvAM+94] B. Gobets, H. van Amerongen, R. Monshouwer, J. Kruip, M. Rögner, R. van Grondelle, and J. P. Dekker. *Biochim. Biopys. Act*, 1188:75, 1994.

[GvG01] B. Gobets and R. van Grondelle. *Biochim. Biophys. Act.*, 1507:80, 2001.

[GVK+96] V. Gulbinas, L. Valkunas, D. Kuciauskas, E. Katilius, V. Liuolia, W. Zhou, and R. E. Blankenship. *J. Phys. Chem.*, 100:17950, 1996.

[GvSR+01] B. Gobets, I. H. M. van Stokkum, M Rögner, J. Kruip, E. Schlodder, N. V. Karapetyan, J. P. Dekker, and R. van Grondelle. *Biophys. J.*, 81:407, 2001.

[GvSvM+03] B. Gobets, I.H.M. van Stokkum, F. van Mourik, M. Rögner, J. Kruip, E. Schlodder, J.P. Dekker, and R. van Grondelle. *Biophys. J*, 85:3883, 2003.

[HRD+02] X. Hu, T. Ritz, A. Damjanovic, F. Autenrieth, and K. Schulten. *Quarterly Reviews of Biophysics*, 35:1, 2002.

[HS70] C. Houssier and K. Sauer. *J. Am. Chem. Soc.*, 92:779, 1970.

[HSBB93] A. R. Holzwarth, G. Schatz, H. Brock, and E. Bittersmann. *Biophys.J.*, 64:1813, 1993.

[HWC$^+$02] J. L. Herek, W. Wohlleben, R.J. Cogdell, D. Zeidler, and M. Motzkus. *Nature*, 417:533, 2002.

[JFK$^+$01] P. Jordan, P. Fromme, O. Klukas, W. Saenger, and N. Krauß. *Nature*, 411:909, 2001.

[JTG$^+$00] F. Jelezko, C. Tietz, U. Gehrken, J. Wrachtrup, and R. Bittl. *J. Phys. Chem. B*, 34:8093, 2000.

[KAS02] P. Král, Z. Amitay, and M Shapiro. *Phys. Rev. Lett.*, 89:063002, 2002.

[KGvS$^+$01] J. T. M. Kennis, B. Gobets, I. H. M. van Stokkum, J. P. Dekker, R. van Grondelle, and G. R. Fleming. *J. Phys. Chem. B*, 105:4485, 2001.

[KHG$^+$00] F. J. Kleima, E. Hofmann, B. Gobets, I. H. M. van Stokkum, R. van Grondelle, K. Diederichs, and H. van Amerongen. *Biophys. J.*, 78:344, 2000.

[KM04] A. Kaiser and V. May. 2004. to be submitted.

[KMS94] O. Kühn, V. May, and M. Schreiber. *J. Chem. Phys.*, 101:10404, 1994.

[Kno63] R. S. Knox. *Theory of Excitons.* Acad. Press., New York, 1963.

[KPV$^+$96] R. Kumble, S. Palese, R. W. Visschers, P. L. Dutton, and R. M. Hochstrasser. *Chem. Phys. Lett.*, 261:396, 1996.

[KS96] J. Knoester and F. C. Spano. *in T. Kobayashhi (ed.): J-Aggregates.* World Scientific, Singapore, 1996.

[KS97] O. Kühn and V. Sundström. *J. Chem. Phys.*, 107:4154, 1997.

[KS03] N. Kamiya and J.-R. Shen. *PNAS*, 100:98, 2003.

[LAI$^+$91] S.H. Lin, R. Alden, R. Islampour, H. Ma, and A. A. Villaeys. *Density Matrix Method and Femtosecond Processes.* World Scientific Singapore, 1991.

[LZBA97] Y. F. Li, W. Zhou, R. E. Blankenship, and J. P. Allen. *J. Mol. Biol.*, 271:456, 1997.

[MB02] V. May and B. Brüggemann. *in A. Douhal and J. Santamaria (eds.): Femtochemistry and Femtobiology.* World Scientific, Singapore, 2002.

[MCG97] Y.-Z. Ma, R. J. Cogdell, and T. Gillbro. *J. Phys. Chem. B*, 101:1087, 1997.

[MCM97] T. Meier, V. Chernyak, and S. Mukamel. *J. Phys. Chem. B*, 101:7332, 1997.

[MGF99] V. A. Malyshev, H. Glaeske, and K.-H. Feller. *Chem. Phys. Lett.*, 305:117, 1999.

[MK00a] V. May and O. Kühn. *Charge and Energy Transfer Dynamics in Molecular Systems.* Wiley-VCH Berlin, 2000.

[MK00b] M. V. Mostovoy and J. Knoester. *J. Phys. Chem. B*, 104:12355, 2000.

[MKM02] T. Mancal, U. Kleinekathöfer, and V. May. *J. Chem. Phys.*, 117:636, 2002.

[MKvO$^+$01] M. Matsushita, M. Ketelaars, A. M. van Oijen, J. Köhler, J. T. Aartsma, and J. Schmidt. *Biophys. J.*, 80:1604, 2001.

[MM01a] T. Mancal and V. May. *Chem. Phys.*, 268:201, 2001.

[MM01b] T. Mancal and V. May. *Europ. Phys. J. D*, 14:173, 2001.

[MM02] T. Mancal and V. May. *Chem. Phys. Lett.*, 362:407, 2002.

[Mot38] N. F. Mott. *Trans. Farad. Soc.*, 34:500, 1938.

[MR01] Z. Murtha and H. Rabitz. *Eur. Phys. J. D*, 14:141, 2001.

[Muk95] S. Mukamel. *Nonlinear Optical Spectroscopy.* Oxford University Press, 1995.

[Nak58] S. Nakajima. *Progr. Theor. Phys. 20*, 20:948, 1958.

[NAWP96] V. Nagarajan, R. G. Allen, J. C. Williams, and W. W. Parson. *Proc. Natl. Acad. Sci. USA*, 93:13774, 1996.

[NFK92] B. Nordén, M. Fragata, and T. Kurucsev. *Aust. J. Chem.*, 45:1559, 1992.

[NJWP99] V. Nagarajan, E. T. Johnsson, J. C. Williams, and W. W. Parson. *J. Phys. Chem. B*, 103:2297, 1999.

[NSvAvG03] V. Novoderezhkin, J. M. Salverda, H. van Amerongen, and R. van Grondelle. *J. Phys. Chem. B.*, 107:1893, 2003.

[NvG02] V. Novoderezhkin and R. van Grondelle. *J. Phys. Chem. B*, 106:6025, 2002.

[NWvG03] V. Novoderezhkin, M. Wendling, and R. van Grondelle. *J. Phys. Chem. B.*, 107:11534, 2003.

[OKP02] V. Sundström O. Kühn and T. Pullerits. *Chem. Phys.*, 15:275, 2002.

[OZR99] Y. Ohtsuki, W. Zhu, and H. Rabitz. *J. Chem. Phys.*, 110:9825, 1999.

[PDR88] A. P. Pierce, M. A. Dahleh, and H. Rabitz. *Phys. Rev. A*, 37:4950, 1988.

[PDS+96] L.-O. Pålsson, J. P. Dekker, E. Schlodder, R. Monshouwer, and R. van Grondelle. *Photosynth. Res.*, 48:239, 1996.

[PG00] A. B. J. Parusel and S. Grimme. *J. Phys. Chem. B*, 104:5395, 2000.

[PPF+97] S. M. Prince, M. Z. Papiz, A. A. Freer, G. McDermott, A. M. Hawthornthwaite-Lawless, R. J. Cogdell, and N. W. Isaacs. *J. Mol. Biol.*, 268:412, 1997.

[PPH+03] M. Z. Papiz, S. M. Prince, T. Howard, R. J. Cogdell, and N. W. Isaacs. *J. Mol. Biol.*, 362:1523, 2003.

[PPvGvA97] E.J.G. Peterman, T. Pullerits, R. van Grondelle, and H. van Amerongen. *J. Phys. Chem. B*, 101:4448, 1997.

[PTAG95] L.-O. Pålsson, S. E. Tjus, B. Andersson, and T. Gillbro. *Chem. Phys.*, 194:291, 1995.

[PTVF92] W. H. Press, S. A. Teukolsky, W. T. Vetterling, and B. P. Flannery. *Numerical Recipies in Fortran.* Cambridge University Press, 1992.

[RCS+99] R.Simonetto, M. Crime, D. Sandonà, R. Croce, G. Cinque, J. Breton, and R. Bassi. *Biochem*, 38:12974, 1999.

[Red63] A. Redfield. *Adv. Magn. Res.*, 1:1, 1963.

[RHS+03] A. W. Roszak, T. D. Howard, J. Southall, A. T. Gardiner, C. J. Law, N. W. Isaacs, and R. J. Cogdell. *science*, 302:1969, 2003.

[RKMK01] I. V. Ryzhov, G. G. Kozlov, V. A. Malyshev, and J. Knoester. *J. Chem. Phys.*, 114:5322, 2001.

[RM97a] Th. Renger and V. May. *Phys. Rev. Lett.*, 78:3406, 1997.

[RM97b] Th. Renger and V. May. *J. Phys. Chem. B*, 101:7232, 1997.

[RM97c] Th. Renger and V. May. *Photochem. Photobiol*, 66:618, 1997.

[RMK01] Th. Renger, V. May, and O. Kühn. *Phys. Rep*, 343:137, 2001.

[RMSK00] Th. Renger, V. May, V. Sundström, and O. Kühn. *J. Chinese Chem. Soc.*, 47:807, 2000.

[RZ00] S. A. Rice and M. Zhao. *Optical Control of Molecular Dynamics.* Wiley, New York, 2000.

[SB03] M. Shapiro and P. Brumer. *Principles of Quantum Control of Molecular Processes.* Wiley, New Yersey, 2003.

[SBRM02] J. Schütze, B. Brüggemann, Th. Renger, and V. May. *Chem. Phys.*, 275:333–354, 2002.

[SBS97] S. Savikhin, D. R. Buck, and W. S. Struve. *Chem. Phys.*, 223:303, 1997.

[SDT88] H. Stiel, S. Daehne, and K. Teuchner. *J. Lumin.*, 39:351, 1988.

[SdVR99] K. Sundermann and R. de Vivie-Riedle. *J. Chem. Phys.*, 110:1896, 1999.

[SFS$^+$01] H. Stahlberg, D. Fotiadis, S. Scheuring, Hervé Rémigy, T. Braun, K. Mitsuoka, Y. Fujiyoshi, and A. Engel. *FEBS Lett.*, 504:166, 2001.

[SGGP88] V. Sundström, T. Gillbro, R. A. Gadonas, and A. Piskarskas. *J. Chem. Phys.*, 89:2754, 1988.

[si02] special issue. *Photoprocesses in Multichromophoric Molecular Assemblies.* Chemical Physics 275, 2002.

[SJF01] G. D. Scholes, X. J. Jordanides, and G. R. Fleming. *J. Phys. Chem. B*, 105:1640, 2001.

[SLR$^+$02] M. K. Sener, D. Lu, T. Ritz, S. Park, P. Fromme, and K. Schulten. *J. Phys. Chem. B*, 106:7948, 2002.

[SM95] F. C. Spano and E. S. Manas. *J. Chem. Phys*, 103:5939, 1995.

[SPvG99] V. Sundström, T. Pullerits, and R. van Grondelle. *J. Phys. Chem. B*, 103:2327, 1999.

[SR90a] S. Shi and H. Rabitz. *J. Chem. Phys.*, 92:364, 1990.

[SR90b] S. Shi and H. Rabitz. *J. Chem. Phys.*, 92:2927, 1990.

[SSD95] L. Seidner, G. Stock, and W. Domcke. *J. Chem. Phys*, 103:3998, 1995.

[Sun70] A. Suna. *Phys. Rev. B*, 1:1716, 1970.

[SWR88] S. Shi, A Woody, and H. Rabitz. *J. Chem. Phys.*, 88:6870, 1988.

[TCD+99] C. Tietz, O. Chekhlov, A. Dräbenstedt, J. Schuster, and J. Wrachtrup. *J. Phys. Chem. B*, 103:6328, 1999.

[TGJW00] C. Tietz, U. Gerken, F. Jelezko, and J. Wrachtrup. *J. Single Mol.*, 1:67, 2000.

[THP+01] G. Trinkunas, J. L. Herek, T. Polívka, V. Sundström, and T. Pullerits. *Phys. Rev. Lett.*, 86:4167, 2001.

[TKR86] D. J. Tannor, R. Kosloff, and S. A. Rice. *J. Chem. Phys.*, 85:5805, 1986.

[TM93] D. E. Tronrud and B. W. Matthews. *in J. Deisenhofer and J. R. Norris (eds.): Photosynthetic reaction center.* Academic Press, New York, 1993.

[TM+00] S. Tretiak, C. Middleton, , V. Chernyak, and S. Mukamel. *J. Phys. Chem. B*, 104:4519, 2000.

[VAPS96] L. Valkunas, E. Akesson, T. Pullerits, and V. Sundström. *Biophys. J.*, 70:2373, 1996.

[vAVvG00] H. van Amerongen, L. Valkunas, and R. van Grondelle. *Photosynthetic Excitons.* World Scientific Singapore, 2000.

[vOKK+99] A. M. van Oijen, M. Ketelaars, J. Köhler, T. J. Aartsma, and J. Schmidt. *Science*, 285:400, 1999.

[vOKK+00] A. M. van Oijen, M. Ketelaars, J. Köhler, T. J. Aartsma, and J. Schmidt. *Biophys. J.*, 78:1570, 2000.

[vZWL+95] M. A. M. J. van Zandvoort, D. Wróbel, P. Lettinga, G. van Ginkel, and Y. K. Levine. *Photochem. Photobiol.*, 62:299, 1995.

[Wan37] G. H. Wannier. *Phys. Rev.*, 52:191, 1937.

[WH95] K. Wynne and R.M. Hochstrasser. *J. Raman Spectrosc.*, 26:561, 1995.

[WPG$^+$02] M. Wendling, M. A. Przyjalgowski, D. Gülen, S. I. E. Vilto, T. J. Aartsma, R. van Grondelle, and H. van Amerongen. *Photosynth. Res.*, 71:99, 2002.

[WSSD97] B. Wolfseder, L. Seidner, G. Stock, and W. Domcke. *Chem. Phys.*, 217:275, 1997.

[YDVF03] M. Yang, A. Damjanovic, H. M. Vaswani, and G. R. Fleming. *Biophys. J.*, 85:140, 2003.

[YF02] M. Yang and G. R. Fleming. *Chem. Phys.*, 275:355, 2002.

[ZBR97] W. Zhu, J. Botina, and H. Rabitz. *J. Chem. Phys.*, 108:1953, 1997.

[ZFW$^+$02] D. Zeidler, S. Frey, W. Wohlleben, M. Motzkus, F. Busch, T.Chen, W. Kiefer, and A. Materney. *J. Chem. Phys.*, 116:5231, 2002.

[ZMCM98] W. M. Zhang, T. Meier, V. Chernyak, and S. Mukamel. *J. Chem. Phys.*, 108:7763, 1998.

[ZMJ$^+$02] V. Zazubovich, S. Matsuzaki, T.W. Johnsson, J.M. Hayes, P.R. Chitnis, and G.J. Small. *Chemical Physics*, 275:47, 2002.

[Zwa64] R. Zwanzig. *Physica*, 30:1109, 1964.

[ZWK$^+$01] A. Zouni, H.-T. Witt, J. Kern, P. Fromme, N. Krauss, W. Saenger, and P. Orth. *Nature*, 409:739, 2001.

Danksagung

An erster Stelle möchte ich meinem Betreuer Priv.-Doz. Dr. Volkhard May danken für die Möglichkeit, an diesem interessanten Thema der Photosynthetischen Antennensysteme zu arbeiten. Die Einführung in die Dichtematrixtheorie und die Theorie der Optimalen Kontrolle waren essentiell für den Erfolg dieser Arbeit. Nicht zuletzt danke ich Dr. May auch für die Sicherstellung des materiellen Rahmens meiner Dissertation.

Allen Mitarbeitern der Arbeitsgruppe Halbleitertheorie sowie Prof. Dr. Zimmermann möchte ich für Unterstützung und Begleitung während der 4 Jahre am Hausvogteiplatz und in Adlershof danken. Insbesondere Dr. Tomáš Mančal für viele nützliche Diskussionen über die Theorie und deren Umsetzung in Computerprogramme, und Dr. Axel Esser für Einblicke in die Theorie von Quantengräben sowie die gute Zusammenarbeit bei der Installation und Wartung der Computer gebührt mein Dank. Auch Priv.-Doz. Dr. Erich Runge und Prof. Dr. Vincenzo Savona möchte ich für nette Gespräche und ihre prompte Hilfe bei einigen Computerproblemen danken, sowie Gianandrea Mannarini für die Betreuung der Windows Rechner und Dr. Andreas Kaiser für Diskussionen zu mathematischen Grundlagen.

Für die motivierenden jährlichen Exkursionen möchte ich Prof. Dr. Jörn Manz und seiner Gruppe danken.

The stays in the experimental groups in Amsterdam and Lund were very motivating and helpfull, much thanks to Prof. Dr. Villy Sundström and Dr. Tõnu Pullerits in Lund and to Prof. Dr. Rienk van Grondelle, Dr. Vladimir Novoderezhkin, Dr. Delmar S. Larsen, Kinga Sznee and Dr. Lavanya L. Premvardhan in Amsterdam. Thanks also to Dr. Jennifer L. Herek for nice discussions at both places.

Viel Dank geht an meine Eltern, Antje und Volker Brüggemann für die kontinuierliche Unterstützung, sowie an Swantje Meier für das geduldige Lesen dieser Arbeit.

Die Arbeit wurde durch die DFG u.a. durch den Sonderforschungsbereich 450 “Analyse und Steuerung ultraschneller photoinduzierter Redaktionen” gefördert, die Aufenthalte in Amsterdam und Lund durch das ESF-ULTRA Programm.

Lebenslauf

Persönliches:

Name:	Ben Brüggemann
23. Januar 1973	geboren in Bad Hersfeld
Nationaltität:	deutsch
Familienstand:	ledig

Ausbildung:

Sep. 1979 - Aug. 1983	Grundschule Schenklengsfeld
Sep. 1983 - Aug. 1989	Gesamtschule Obersberg, Bad Hersfeld
Sep. 1989 - Juli 1992	Modellschule Obersberg, Bad Hersfeld
13.06.1992	Allgemeine Hochschulreife (Abitur)
Aug. 1992 - Okt. 1993	Zivildienst
Okt. 1993 - Juli 1999	Studium der Physik an der Freien Universität Berlin
30.07.1999	Physik Diplom, Thema der Diplomarbeit: *Energie und Ladungstransfer in biologischen Modellsystemen* bei Prof. Dr. Helmut Gabriel.
Dez. 1999 - Jan. 2004	Promotion an der Humboldt-Universität zu Berlin, Thema: *Theory of Ultrafast Exciton Dynamics in Photosynthetic Antenna Systems* unter der Betreuung von Priv.-Doz. Dr. Volkhard May.

Beschäftigung:

Okt. 1996 - Sep. 1999	Tutor im Physikalischen Praktikum für Naturwissenschaftler, Freie Universität Berlin
Dez. 1999 - Jan. 2004	Wissenschaftlicher Mitarbeiter an der Humboldt Universität zu Berlin, Institut für Physik

Gastaufenthalte:

Apr. 2000, Apr.2001	in der Gruppe von Prof. V. Sundström, Lund, Schweden (2+1 Wochen), gefördert durch das ESF-ULTRA Programm.
Mai 2002, Mai 2003, Nov. 2003	in der Gruppe von Prof. R. van Grondelle, Amsterdam, Niederlande (4+1+1 Wochen), gefördert durch das ESF-ULTRA Programm.

Aufstellung der wissenschaftlichen Veröffentlichungen

Zeitschriftenartikel im Rahmen der Dissertation

- B. Brüggemann, J. L. Herek, V. Sundström, T. Pullerits and V. May:
  "Microscopic Theory of Exciton Annihilation: Application to the LH2 Antenna System",
  J. Phys. Chem. B 105, 11391 (2001).

- J. Schütze, B. Brüggemann, Th. Renger, and V. May:
  "Theory of Linear Absorption Spectra of Biological and Non-Biological Chromophore Complexes",
  Chem. Phys.275, 333-354 (2002).

- B. Brüggemann and V. May:
  "Exciton Exciton Annihilation Dynamics in Chromophore Complexes: 1. Multiexciton Density Matrix Formulation",
  J. Chem. Phys. 118, 746 (2003).

- B. Brüggemann and V. May:
  "Exciton Exciton Annihilation Dynamics in Chromophore Complexes: 2. Application to the LH2 Antenna",
  J. Chem. Phys. 120, 2325 (2004).

- B. Brüggemann, K. Sznee, V. Novoderezhkin, R. van Grondelle, and V. May:
  "From Structure to Dynamics: Modeling Exciton Dynamics in the Photosynthetic Antenna PS1",
  submitted to J. Phys. Chem. B

- B.Brüggemann, and V. May:
  "Excitonic Wavepacket Motion in the PS1 Core-Antenna System",
  submitted to Chem. Phys. Lett.

- B.Brüggemann, and V. May:
  "Coherent Control of the Spatial Exciton Localization in FMO",
  submitted to J. Phys. Chem. B

Tagungsbeiträge im Rahmen der Dissertation

- B. Brüggemann and V. May,
  Exciton Annihilation Dynamics in Biological and Artificial Antenna Systems,
  CLEO/Europe - IQEC 2000,
  Nice, France, 10.-15. September 2000: poster contribution.

- B. Brüggemann and V. May,
  Energietransfer im Antennensystem LH2 der bakteriellen Photosynthese
  Frühjahrstagung der DPG, Potsdam, 13.-16. March 2000: poster contribution.

- B. Brüggemann and V. May,
  Disordered Frenkel-Excitons in Biological and Artificial Antenna Systems,
  ESF Winterschool:
  Ultrafast Spectroscopy in Chemistry and Biology,
  Börgafjäll, Sweden, 9.-15. April 2000: poster contribution.

- B. Brüggemann and V. May,
  Exciton Annihilation in Biological Antenna Systems
  Frühjahrstagung der DPG, Berlin, 2001: poster contribution.

- V. May and B. Brüggemann:
  "Microscopic Theory of Exciton Annihilation: Application to the LH2 Antenna System"
  in "Femtochemistry and Femtobiology" , A. Douhal, J. Santamaria (eds.)
  (World Scientific: Singapore, 2002)

- B. Brüggemann and V. May,
  Exciton Annihilation in Antenna Systems: Single Molecule Dynamics,
  Frühjahrstagung der DPG, Regensburg, 11.-15. March 2002: poster contribution.

- B. Brüggemann and V. May,
  From Structure to Dynamics: Modeling of the Photosystem I
  ESF ULTRA Workshop:
  Femtosecond Dynamics in Photosynthetic Light Harvesting Complexes,
  Belek-Antalya, Turkey, 5.-9. October 2002: oral contribution.

Selbständigkeitserklärung

Hiermit erkläre ich, die vorliegende Arbeit selbständig ohne fremde Hilfe verfasst zu haben und nur die angegebene Literatur und Hilfsmittel verwendet zu haben.

Ben Brüggemann

1. April 2004